CRANFIELD INSTITUTE OF TECHNOLOGY

COLLEGE OF AERONAUTICS

Ph.D.THESIS

1985

J. MATHEWS

The theory and application of heated films for the measurement of skin friction

Supervisor: Dr. D.I.A. Poll

September 1985

ABSTRACT

The use of hot surface films for measuring skin friction is examined. It is shown that all existing theories, which neglect heat conduction within the substrate, are inadequate in predicting the variation of heat loss from the film with skin friction. A more physically realistic theory is presented which accounts for the conductive and convective heat transfer into the flow and also heat conduction within the substrate. This leads to a more general relationship between skin friction and heat loss from the film. Experiments conducted in flat plate laminar and turbulent boundary layer flow show that this relationship is more accurate than previous forms.

The time and temperature dependence of the heat loss from the hot film are also explored theoretically and experimentally. The effect of surface misalignment of the film is shown to alter significantly the convective heat transfer. This effect is more pronounced in laminar flow than in turbulent flow.

Using a glue-on hot film probe,calibrations relating the heat loss to skin friction were found to be different in laminar and turbulent flow.

An experimental operating procedure for the use of hot surface films for measuring skin friction is proposed which significantly increases the accuracy of the technique.

CONTENTS

PAGE

Abstract

Chapter 1 Review of the heat transfer technique for the measurement of skin friction

1.1 Introduction. 1
1.2 Historical development of the technique. 4
1.3 Disadvantages and problems of the technique 9

Chapter 2 Survey of theoretical solutions

2.1 Basic theories. 12
2.2 Heat convection to a quadratic velocity profile. 16
2.3 Effect of turbulence. 19
2.4 Effect of longitudinal diffusion and compressibility. 22
2.5 Solutions with a specified heat flux distribution. 23
2.6 Conclusions. 24

Chapter 3 The steady heat conduction/convection problem

3.1 The heat conduction/convection equations. 25
  3.1.1 Statement of the two-dimensional problem. 25
  3.1.2 Boundary conditions. 26
  3.1.3 Dimensionless parameters. 27
3.2 Solution procedure. 28
3.3 Solution assuming $\frac{\partial^2 T_F}{\partial x^2} = 0$ 29
  3.3.1 Solution in the transformed plane. 29
  3.3.2 Determination of $\overline{q}(\alpha)$. 31
  3.3.3 Inversion. 32
3.4 Evaluation of the integrals. 33
3.5 Results. 34
  3.5.1 Variation of Nu with Pe and K. 34
  3.5.2 Wall temperature distributions. 36
  3.5.3 Heat transfer to the fluid. 37
3.6 Effect of longitudinal diffusion. 38
3.7 Evaluation of the integrals. 40

CONTENTS (contd.) PAGE

3.8 Results. 41
  3.8.1 Variation of Nu with Pe and K. 41
  3.8.2 Wall temperature distributions. 41
  3.8.3 Heat transfer to the fluid. 42
3.9 The effect of varying the heat flux distribution. 42
3.10 Temperature profiles in the fluid. 44
3.11 Conclusions. 47

Chapter 4 Further consequences of substrate conduction

4.1 Introduction. 48
4.2 The one-dimensional heat conduction model. 48
4.3 Experimental investigation into the effects of substrate conduction for the glue-on probe. 50
  4.3.1 Probe details. 50
  4.3.2 Suspended probe. 51
  4.3.3 Effect of backing material. 52
4.4 Theoretical explanation for the non-linear variation of i^2R with ΔT. 53
4.5 Further experiments. 53
4.6 Conclusions. 55

Chapter 5 Flat plate laminar flow experiments

5.1 Plate design and wind tunnel. 56
5.2 Measurement of the laminar boundary layer properties. 57
  5.2.1 Hot-wire measured velocity profiles. 57
    5.2.1.1. Data selection. 58
  5.2.2 Analysis of the velocity profiles. 58
  5.2.3 Traversing Pitot tube measurements. 60
5.3 Calculation of the integral properties of the boundary layer. 61
5.4 Prediction of skin friction. 62
5.5 Hot Film Experiments - Laminar Flow. 62
  5.5.1 Experimental procedure. 62
  5.5.2 Effect of surface misalignment. 63

CONTENTS (contd.) PAGE

5.5.3 Calibrations. 65
5.5.4 Note on the form of the calibration at very low τ_w. 66

Chapter 6 Flat plate turbulent flow experiments

6.1 Introduction. 67
6.2 Experimental set-up. 68
6.3 Preston tube results. 68
6.3.1 Choice of calibration. 69
6.3.2 Use of a universal velocity profile. 70
6.4 Mean velocity profile measurements. 72
6.4.1 Calculation of the boundary layer integral properties. 72
6.4.2 Mean velocity profiles. 73
6.4.3 Application of the momentum integral equation. 73
6.5 Velocity profiles near the wall. 75
6.5.1 Estimation of C_f based on Clauser's method. 75
6.5.2 Estimation of C_f using Bradshaw's method. 77
6.5.3 Sensitivity of C_f upon κ, C and y^+. 79
6.6 Comparison of C_f predictions. 80
6.7 Hot Film Experiments - Turbulent Flow. 80
6.7.1 Effect of surface misalignment. 80
6.7.2 Response due to a change in flow. 81
6.7.3 Detailed calibrations. 82
6.8 Laminar and turbulent calibrations. 83
6.9 Effect of wall material. 84
6.10 Effect of ΔT upon calibration. 84

Chapter 7 Suggested operating procedure for the use of hot film probes for the measurement of skin friction 87

Principal conclusions 89

Acknowledgements. 90

CONTENTS (contd.) PAGE

References 91

Appendices

A Effect of compressibility upon the calibration 101
B Solution for a specified wall temperature distribution neglecting longitudinal diffusion and substrate conduction. 102
C Pope's method for relating the turbulent calibration to the laminar calibration. 107
D Application of the Fourier inverse transformation. 109
E Solution for the wall temperature distribution for K = 0, neglecting longitudinal diffusion. 112
F Notes on the Airy function, Ai, and its derivative. 116
G Solution to the one-dimensional heat conduction equation for a semi-infinite composite solid. 120
H Generation of heat in a wire conducting an electric current. 124
I Estimation of the integral properties from the laminar boundary layer velocity profiles. 126
J Outline of Pfeil and Sticksel's law of the wall. 128
K Estimation of the integral properties from the turbulent boundary layer velocity profiles. 131
L Numerical application of Clauser's technique. 133

Figures.

FIGURES

FIGURE NO.	TITLE
1.1	Details of Ludwieg's probe and the Murthy-Rose probe.
1.2	Typical calibrations in air flows.
1.3	Inverted calibration from Poll and Watson, 1984.
1.4	$\lvert\%\rvert$ error in $\rho\tau_W$ due to $\frac{1}{3}$ and $\frac{1}{6}$ power law calibrations fitted to Rubesin's results.
3.1	The heat conduction/convection problem.
3.2	Integration contour for application of the Fourier inverse transformation.
3.3	Variation of Nu with $Pe^{1/3}$ and K.
3.4	Wall temperature distribution - Effect of Pe.
3.5	Wall temperature distribution - Effect of K.
3.6	Surface heat flux distribution - Effect of Pe.
3.7	Surface heat flux distribution - Effect of K.
3.8	Variation of Nu with $Pe^{1/3}$ and K (including longitudinal diffusion).
3.9	Effect of longitudinal diffusion upon the Nu-$Pe^{1/3}$ relationship.
3.10	Wall temperature distribution - Effect of Pe (including longitudinal diffusion).
3.11	Wall temperature distribution - Effect of K (including longitudinal diffusion).
3.12	Surface heat flux distribution - Effect of Pe (including longitudinal diffusion).
3.13	Surface heat flux distribution - Effect of K (including longitudinal diffusion).
3.14	Effect of varying q upon the Nu-$Pe^{1/3}$ relationship (including longitudinal diffusion).
3.15	Streamwise variation of the temperature profile in the fluid.
3.16	Effect of Pe upon the fluid temperature profile at $x^*/a^* = 1$.
3.17	Effect of K upon the fluid temperature profile at $x^*/a^* = 1$.

FIGURES (contd)

FIGURE NO. TITLE

3.18 Variation of δ_T^*/a^* with $Pe^{-\frac{1}{2}}$ and $K^{\frac{1}{2}}$ at $x^*/a^* = 1$.
3.19 Variation of $\delta_T^+\sqrt{Pr}$ with $Pe^{\frac{1}{2}}$ and $K^{\frac{1}{2}}$ at $x^*/a^* = 1$.

4.1 Details of the flush mounting and glue-on probes.
4.2 Variation of probe resistance with temperature.
4.3 Power (V^2) variation with time - suspended probe.
4.4 Variation of power (i^2R) with ΔT - suspended probe.
4.5 Power (V^2) variation with time - probe on tufnol plate.
4.6 Variation of power (i^2R) with ΔT at 2 times - probe on tufnol plate.
4.7 Predicted variation of power (i^2R) with ΔT for the nickel film alone.
4.8 Variation of Nu with time - Wind on and wind off.

5.1 Sketch of the flat plate model.
5.2 Sketch of the low turbulence, low speed wind tunnel.
5.3 Schematic drawing of the data acquisition system.
5.4 Laminar velocity profiles - hot wire measurements.
5.5 Variation of Δx with unit Reynolds number (based on hot wire measurements).
5.6 Laminar velocity profiles - Pitot tube measurements.
5.7 Variation of Δx with unit Reynolds number (based on Pitot tube measurements).
5.8 Variation of shape factor (H) with Reynolds number.
5.9 Variation of R_θ with Rx_B.
5.10 Effect of surface misalignment upon Nu.
5.11 Series of laminar calibrations (probe flush).
5.12 Variation of τ_M/τ_W with h^+ (laminar flow)
5.13 Laminar calibration showing correction for the surface misalignment error.
5.14 Laminar calibration at low Pe (probe flush).

6.1 Turbulent boundary layer mean velocity profile.
6.2 Measurement of C_f using the Preston tube technique.

FIGURES (contd.)

FIGURE NO.	TITLE
6.3	Variation of C_f with R_{x_m} deduced from the Preston tube and surface Pitot tube.
6.4	Variation of C_f with R_{x_m} deduced from the Preston tube and surface Pitot tube.
6.5	Variation of C_f with R_{x_m} deduced from the Preston tube and surface Pitot tube.
6.6	Variation of C_f with R_{x_m} deduced from the Preston tube and surface Pitot tube.
6.7	Variation of shape factor with Reynolds number.
6.8	Variation of veolcity profile with Reynolds number.
6.9	Variation of R_θ with Rx_m.
6.10	Comparison between various $C_f \sim R_\theta$ relationships.
6.11	Application of Clauser's method.
6.12	Application of Bradshaw's method.
6.13	Variation of C_f with Rx_m.
6.14	Effect of surface misalignment upon Nu.
6.15	Series of turbulent calibrations (probe flush).
6.16	Variation of τ_M/τ_w with h^+ (turbulent flow).
6.17	Turbulent calibration for ascending and descending speeds.
6.18	Time variation of Nu following a step change in U_∞.
6.19	Time variation of Nu after stopping the flow.
6.20	Detailed turbulent calibration.
6.21	Laminar and turbulent calibrations.
6.22	Turbulent calibration on copper block.
6.23	Series of turbulent calibrations - effect of ΔT.
6.24	Variation of i^2R with ΔT (Pe = 0).
6.25	Collapsed turbulent calibrations.
6.26	Series of laminar calibrations - effect of ΔT (probe on copper block).
6.27	Variation of $\frac{i^2R}{kw}$ with ΔT (Pe = 0) (probe on copper block).
6.28	Collapsed laminar calibrations (probe on copper block).

PRIMARY NOTATION

A,a	a constant
Ai, Ai'	Airy function and its derivative
B,b	a constant
Bi	Airy function
C,c	a constant
C_f	skin friction coefficient
Cp	specific heat
d	Preston tube diameter
E	a constant
erf	error function
H	shape factor
h	step height
i	electric current
I_ν, J_ν, K_ν	Bessel functions of order ν
K	thermal conductivity ratio
k	thermal conductivity
ker_ν, kei_ν	Kelvin functions of order ν
L	streamwise length of the film
L_{eff}	effective streamwise heating length of the film
M	Mach number
m	a constant
n	a constant
Nu	mean Nusselt number per unit width $\frac{Q}{k\Delta T}$ or $\frac{i^2R}{wk\Delta T}$
p	pressure
Pe	Péclet number $({PrL^2\tau_w}/{\rho\nu^2})$
Pr	Prandtl number $(\frac{\mu C_p}{k})$
Q	heat flux per unit width
q	local heat flux
R	electrical resistance
Rx_B etc	Reynolds number based on x_B $(\frac{U_\infty x_B}{\nu})$
t	time
T	temperature
U_∞	free-stream velocity
u	streamwise velocity component
u_τ	friction velocity: $\sqrt{\frac{\tau_w}{\rho}}$

u^+	u/u_τ
V	anemometer output voltage
v	normal velocity component
W	spanwise width of the film
x	streamwise coordinate
y	normal coordinate
y^+	$\frac{yu_\tau}{\nu}$

Greek symbols

α	thermal diffusivity
α_2	a constant
β	a constant
Γ	gamma function
γ	a constant
Δ	an increment of
δ	mean boundary layer thickness
δ_L	viscous sub-layer thickness
δ_T	thermal boundary layer thickness
δ^*	displacement thickness
ε_m	eddy viscosity
κ	von Kármán's constant
θ	momentum thickness
λ	a constant
μ	viscosity
ν	kinematic viscosity
ρ	density
τ_w	wall shear stress

Superscripts

*	dimensional quantity (in chapter 3)
-	transformed variable

Subscripts

e	effective value in turbulent flow
F	fluid quantity
I	imaginary part
m	measured value
max	maximum value
MF	mean value over the film
R	real part
s	substrate quantity
w	value at the wall
o	initial value, value at $\tau_W = 0$
∞	value at infinity

Units

Unless otherwise stated the S.I. system of units is used.

CHAPTER 1

Review of the heat transfer technique for the measurement of skin friction

1.1 Introduction

The drag force exerted on a vehicle moving through a fluid is one of the dominant factors determining the performance of the body. As the cost of extracting the earth's finite fossil fuel reserves grows, the incentive for minimising the drag and hence the fuel consumption increases.

Drag arises through the action of pressure forces and shearing forces, or skin friction, upon the body. Approximately 50% of the cruise drag on current civil aircraft may be attributed to skin friction. Since the success of new aircraft projects is dependent upon accurate performance predictions it is essential that the skin friction drag is accurately known. Skin friction also leads to energy 'losses' in internal flows. To maintain the flow a pressure difference is necessary between the inlet and outlet of the system. Thus the shearing stress of a fluid at a wall, or skin friction, is a parameter of fundamental engineering importance.

Knowledge of the shear stress over a surface is also important in understanding the nature of the flow. The wall shear stress is an important scale parameter in the study of turbulent flows. For a Newtonian fluid the shear stress at the wall is by definition

$$\tau_W = \mu \left.\frac{\partial u}{\partial y}\right|_W \qquad (1.1)$$

i.e. the product of viscosity and velocity gradient at the wall.

Although the measurement of skin friction is a problem of central importance in the field of applied fluid mechanics, it is notoriously difficult to obtain reliable wall shear stress data experimentally. The only method available for the direct measurement of τ_W involves measuring the drag force on a surface element mounted on a balance. Typically the total force acting on the element is measured either by a spring displacement mechanism or by an electro-mechanical force balancing system. To maximise the force for accurate measurement implies bulky devices with large surface elements and so an average value of τ_w (force/area) is measured and not a local value. Furthermore, the effects of misalignment of the surface element with the body and flow pressure gradients cannot be readily accounted for.

The wall shear stress may be determined if the velocity profile within the boundary layer is known. Obviously, if the variation of u(y) as $y \to 0$ is known then by using equation (1.1) τ_w may be deduced. However, in general the accurate measurement of u(y) as the wall is approached is extremely difficult and so the method has little practical application. Alternatively, if the streamwise variation of the complete velocity profile is known, τ_w may be deduced by application of the momentum integral equation. For two-dimensional, incompressible flow this may be approximated[†] by the expression

$$\frac{\tau_w}{\rho} = \frac{d}{dx}(U^2\theta) + \delta^* U \frac{dU}{dx} \qquad (1.2)$$

where θ represents the momentum thickness and δ^* the displacement thickness of the boundary layer. The accuracy of the momentum integral approach is severely limited as θ varies slowly with x and hence the determination of $^{d\theta}/_{dx}$ is generally unreliable.

For turbulent boundary layer flows, it has been observed in a large number of cases that for a region close to the wall the velocity profile may be expressed as

$$\frac{u}{u_\tau} = f\left(\frac{yu_\tau}{\nu}\right) \qquad (1.3)$$

or

$$u^+ = f(y^+)$$

where u_τ is the friction velocity defined as $\sqrt{\frac{\tau_w}{\rho}}$.

[†] Under adverse pressure gradient conditions additional terms may become significant and hence ought to be included in equation (1.2).

This relation, which may be derived using dimensional arguments, takes the form

$$u^+ = y^+ \tag{1.4}$$

inside the viscous sublayer ($y^+ \lesssim 10$). For $y^+ \gtrsim 30$ and $y \lesssim 0.15\delta$ equation (1.3) assumes the form

$$u^+ = \frac{1}{\kappa} \ln y^+ + C \tag{1.5}$$

where κ is von Karman's mixing length constant.
Between these two regions a buffer or blending zone exists.

It has been suggested by many authors that for equilibrium turbulent flows κ and C are 'universal constants'. However, a brief comparison between various published experimental results indicates the difficulty involved in actually determining their true values. Although there would appear to be considerable differences in the various suggested values of κ and C the actual scatter of each pair when used in equation (1.5) is not so large. Possibly the most widely accepted values are

$$\kappa = 0.41$$
$$C = 5.0$$

Thus if u(y) is known within the region for which equation (1.5) is applicable then u_τ and hence τ_w may be deduced.

A more convenient method for estimating τ_w that also relies upon the universal nature of the velocity profile in turbulent flows is the Preston tube technique. By measuring the Pitot pressure recorded by a circular tube in contact with the wall, along with the wall static pressure, the shear stress may be estimated using various proposed calibrations. Other techniques based upon pressure measurement include the Stanton tube, sub-layer fences, blocks, etc. A comprehensive review of the techniques available for the measurement of skin friction is given by Winter (1977).

Clearly the use of any technique that depends upon the 'universal' nature of the flow in the wall region will be inaccurate in non-equilibrium flows, e.g. in flows where the turbulent boundary layer has been manipulated in an attempt to reduce the skin friction. Recent work by Poll, Mathews and Stewart (1985,a) has questioned the use of Preston tubes for estimating τ_w along the attachment line of a swept cylinder.

The relationship between the heat convected from a hot surface element and the local skin friction may also be used as the basis of a technique for estimating τ_w. In practice the electrical power required to maintain a surface element at a constant elevated temperature is measured. The power (i^2R) supplied to the hot element must balance the rate at which energy (heat) is convected into the flow and also that which is conducted into the substrate[†]. Since the effects of substrate conduction are not explicitly known, probes using this technique require calibration in a flow where the skin friction is known.

This thesis examines the use of the heat transfer technique for the measurement of skin friction.

1.2 Historical development of the technique.

The foundation to the current knowledge of convective heat transfer appears to have been laid towards the end of the 19th century and early 20th century - see Eckert (1980). In 1931, Fage and Falkner examined the relationship between the heat convected from a hot surface element and the skin friction. Their experimental results obtained from a nickel strip on a circular cylinder confirmed a variation of heat loss from the strip with skin friction. However, they did not suggest that such a dependence could be used to measure τ_w. Ludwieg (1950) specifically designed, constructed and demonstrated the use of a gauge based on the heat transfer technique for measuring skin friction. His gauge, see figure 1.1(a) consisted of a hollow brass casing across the end of which a thin celluloid diaphragm 0.1mm thick was attached. A copper block (2 x 9 x 6 mm), with an attached electric heater and thermocouple, was cemented onto the diaphragm inside the brass housing. The brass housing was

---

[†] For the moment, the heat conducted into the wires providing the electrical connection to the film is ignored. It is shown later that this is negligible relative to the heat conduction within the substrate.

then mounted with the celluloid end flush with the surface of a flat plate over which the skin friction was known. The air gap around the copper block provided good thermal insulation from the brass housing, whilst the celluloid skin offered minimal resistance to the heat transferred from the hot copper block to the airflow.

Ludwieg's theoretical study suggested that under favourable circumstances[†] the heat convected from the copper block ought to be proportional to the cube root of skin friction, or explicitly

$$\frac{Q}{k\Delta T} = 0.807 \left(\frac{L^2 Pr \tau_W}{\rho \nu^2}\right)^{1/3} \tag{1.6}$$

where Q is the total convected heat transfer rate per unit width, L is the streamwise length of the heating element, ΔT is the mean temperature rise of the copper block and k, Pr, ρ, ν represent the usual fluid properties. His experimental results, see figure 1.2(a), supported the rectilinear variation of Q with $\tau_W^{1/3}$. The curvature of the results was largely attributed to the presence of the celluloid diaphragm which he assumed interfered with the flow in the viscous sublayer of the turbulent boundary layer. Ludweig assumed that the total heat dissipated from the copper block consisted of two independent portions - the heat convected by the flow which scales with $\tau_W^{1/3}$ and that which is conducted to the wall as a result of the imperfect heat insulation. This second portion he assumed to be dependent upon the instrument itself and not the flow. Since it is the total heat loss that is measured (i^2R), then equation (1.6) becomes:

$$\frac{i^2 R}{wk\Delta T} = 0.807\left(\frac{L^2 Pr \tau_W}{\rho \nu^2}\right)^{1/3} + B \tag{1.7}$$

where w is the spanwise width of the heating element.

[†] see Chapter 2.

or

$$Nu = 0.807\ Pe^{1/3} + B \qquad +$$

where the 'constant' B represents the heat conducted into the substrate.

Liepmann and Skinner (1954) measured the heat loss from a 0.0005 inch platinum wire cemented in a groove cut on the surface of an ebonite plate. Their results indicated that the convected heat transfer per unit rise in temperature of the wire was proportional to $\tau_W^{1/3}$. However, they found that the slope of the calibration did not correspond with that of equation (1.7). They therefore suggested that another consequence of substrate conduction is to increase the effective heating length of the wire in the streamwise direction. Thus, in order to account for the effects of substrate conduction equation (1.7) is modified to:

$$\frac{i^2R}{wk\Delta T} = 0.807\left(\frac{L_{eff}^2 Pr\tau_w}{\rho\nu^2}\right)^{1/3} + B \qquad (1.8)$$

Since the increase in L to L_{eff} is due to substrate conduction, i.e. independent of τ_w, then

$$Nu = APe^{1/3} + B \qquad (1.9)$$

where for a given probe, the 'constants' A and B represent the effects of substrate conduction. Liepmann and Skinner also suggested that

---

+ In the theory of heat transfer a Péclet number is defined as the product of Prandtl number and Reynolds number. In the current case

$$\frac{L^2Pr\tau_W}{\rho\nu^2} = \frac{PrL^2 \left.\frac{du}{dy}\right|_W}{\nu}$$

$$= Pr.\left(\frac{L.L \left.\frac{du}{dy}\right|_W}{\nu}\right)$$

which is the product of a Prandtl number and a Reynolds number (based on the characteristic velocity $L\left.\frac{du}{dy}\right|_W$). Thus $\frac{L^2Pr\tau_W}{\rho\nu^2}$ may be considered as a Péclet number.

if L_{eff} was sufficiently small so that the thermal layer over the heating element remained within the viscous sub-layer of the turbulent boundary layer, then the probe would have identical calibrations in laminar and turbulent flows.

Bellhouse and Schultz (1966) constructed a probe consisting of a platinum film baked onto a Pyrex-glass substrate. Their results appeared to agree with equation (1.8). However, they obtained different calibrations in laminar and turbulent flows. They suggested that the probe may be moved from one location to another with no effect upon the calibration and that for an error of less than 5% in terms of τ_w the calibration may be fixed by two points. They demonstrated the use of the probe in flows where the boundary layer was undergoing transition and also separation. Geremia's results (1972) also indicated that the probe's calibration carried out in one apparatus can be used for skin friction measurements in another apparatus, provided the calibration covers the same range.

Experiments by Owen (1969) and Pope (1971), using the same gauge design as Bellhouse and Schultz, indicated that to within a 5% error in terms of τ_w, identical calibrations for laminar and turbulent flow could be obtained. Bellhouse and Schultz (1965) demonstrated that the calibration is independent of Mach number, at least up to $M = 3$, provided the fluid properties are calculated at the appropriate film temperature (see also Appendix A). Owen and Bellhouse (1970) apparently obtained a unique calibration for laminar and turbulent boundary layers up to $M = 4.5$.

Brown (1967) showed that if the effective heating length of the film is small then the calibration is relatively insensitive to pressure gradients $(\frac{dp}{dx})$ except when $\tau_w \to 0$. Furthermore, Spence and Brown (1968) and also Bellhouse and Schultz (1966) proposed the form of the calibration when pressure gradients are significant (see Chapter 2).

Murthy and Rose (1977) constructed a probe consisting of a platinum-rhodium wire, 5-10μm diameter, solvent bonded onto a polystyrene substrate, see figure 1.1(b). They also proposed the use of two points for fixing the calibration and suggested that the no-flow reading Nu_0 may be used. Rubesin et al (1975) examined a range of probe designs and suggested that the substrate ought to have the lowest possible thermal conductivity so as to reduce the effective length of the heating element. They therefore proposed a gauge consisting of a heating wire (0.025mm diameter) embedded in a Polyester resin film on a styrene copolymer substrate. From their experiments it appeared that such probes have identical calibrations in laminar and turbulent boundary layer flows and also that the interference on a probe due to the operation of another one further upstream is negligible when their spacing is greater than 10mm.

Using a photo-etching process McCroskey and Durbin (1972) manufactured a probe consisting of two mutually perpendicular heating films. By considering the response of both films, they demonstrated that such a probe could be used to determine both the magnitude and direction of the skin friction vector, thus suggesting that the dual film probe may be used to measure skin friction in three-dimensional flows. McCroskey and Fisher (1972) applied the technique for measuring the skin friction distribution on a model helicopter rotor. Higuchi and Peake (1978) and Kreplin and Meier (1979) also demonstrated the use of dual sensor probes for estimating the skin friction vector in complex three-dimensional flows.

Poll and Watson (1984) suggested that because the technique does not require the mean velocity profile to exhibit any special features (e.g. a universal law of the wall), it may be applied in flows where the velocity profile has been manipulated, possibly through the use of large eddy break up devices, etc.

The technique has also been applied by Armistead and Keyes (1968a,b) for measuring the fluctuating component of the wall shear stress in turbulent flow. Owen (1969) proved the technique as a useful tool in studying transition.

From the above discussion, it would therefore appear that the use of heated films for measuring skin friction has the following advantages:

(i) Possibility of a unique calibration in laminar and turbulent flows.

(ii) Calibration is independent of Mach number.

(iii) Calibration is reasonably insensitive to pressure gradients.
(iv) Calibration is relatively insensitive to flow alignment.
(v) Probe may be mounted flush with the surface, i.e. no flow disturbance.
(vi) Probes are generally small and robust.
(vii) Calibration may be fixed by any 2 points - one of which may be the no flow measurement.
(viii) Calibration may be transportable from one test rig to another.
(ix) Probe may be used in a wide range of flows.
(x) Interference from upstream gauges is small.
(xi) Probe may be used to measure fluctuating skin friction.
(xii) Technique is easy to operate, requiring only basic hot wire control equipment.
(xiii) Technique does not rely upon the apparent universality of the law of the wall.

1.3 Disadvantages and problems of the technique.

A major drawback of the heat transfer technique is that the accuracy of the method is severely limited by the extremely weak dependence of the total heat loss from the film upon the wall shear stress. During calibration any errors in determining τ_w have little effect upon the calibration line, equation (1.9). However, when the calibration is used to determine τ_w, any small error in measuring Nu will give a larger error in τ_w. This point is graphically demonstrated in figure 1.3 where a calibration from Poll and Watson (1984) is plotted in the direct wall shear measuring mode. As shown, a 1% error in the measured value of $V^2/\Delta T$ (which is proportional to Nu) can result in a 20% error in the deduced value of τ_w.

Since Nu requires ΔT to be known, any change in ΔT, if not properly accounted for, could lead to large errors in estimating τ_w. Reichert and Azad (1977) found that the calibration varied with the temperature of the fluid even when the corresponding changes in ΔT were included in the calculation of Nu. Similar trends were observed by Cousteix and Juillen (1982). Hulton and Gammon (1976) also found that the calibration was sensitive to changes in the substrate temperature.

From the literature there appears to be some confusion concerning the measured no-flow value of Nu, Nu_0, relative to the calibration intercept B. Murthy and Rose (1977) suggest that $B = Nu_0$ whilst McCroskey and Durbin (1972) found Nu_0 to be less than B. Kreplin and Meier (1977) found that in some instances Nu_0 was greater than B.

Ramaprian and Tu (1983) and Sandborn (1979) considered the effect of turbulence upon the calibration when obtained in a turbulent flow. Equation (1.9) strictly relates the instantaneous heat flux to the instantaneous wall shear stress. Hence, they argue, using mean values of $Pe(\tau_W)$ and Nu to fix the calibration may give rise to significant errors in determining the constants A and B owing to the nonlinear relation between heat transfer and shear stress.

Bellhouse and Schultz (1968) showed that the dynamic calibration of a probe differed from the static calibration and was frequency dependent. Baines and Keffer (1976) using a probe consisting of a nickel film deposited on a quartz rod found, by suddenly exposing the hot film to a shear stress, that the response was unacceptably slow (the time constant, T_C, being of order 0.2 seconds). (Application of a low amplitude square wave test signal in the electrical circuit containing the probe had suggested that $T_C < 0.001$ seconds.) They suggested that the probable cause of the poor frequency response of the probe was due to the large thermal inertia of the substrate.

In practice, it is found that the heat conducted into the substrate is significantly greater than that convected by the flow and thus only a small proportion of the measured value of Nu (possibly less than 10%) is flow dependent. Hence any small change in the heat conduction within the substrate could give rise to a large wall shear stress error. A similar point was made by Reichert and Azad (1977) who found that the calibration shifted when the probe was moved from one test location to another. They suggested that this was probably due to a small change in the amount of contact between the probe body and mounting which seemed to significantly alter the heat conduction through the substrate.

A more fundamental discrepancy exists within the literature concerned with the application of the heat transfer technique for measuring skin friction. There appears to be some uncertainty about the form of the basic relationship between the heat loss from the film and the wall shear stress. Calibrations involving the cube root of τ_w have been extensively used, whereas, Kreplin, Meier and Maier (1978) used the fourth root of τ_w. No theoretical justification was given for using $\tau_w^{1/4}$ except that it seemed to fit their experimental results better than $\tau_w^{1/3}$.

Reviewing many of the published calibrations in terms of $\tau_w^{1/3}$, it is found that the experimental data are often curved, or 'bowed', indicating a 'rolling-off' of Nu with increasing $\tau_w^{1/3}$, see figure 1.2 for examples. (Pope (1971) noted this from his own experiments.) The curvature of the published results is such that it implies a higher root of τ_w (i.e. $\tau_w^{1/n} : n > 3$) ought to have been used to achieve linearity. Any departure of the experimental results from the $Nu \sim Pe^{1/3}$ calibration may lead to significant errors when the calibration is used to measure τ_w. This is illustrated in figure 1.4 where the % error in τ_w due to fitting the best $1/3$ rd power law calibration to Rubesin's results (see figure 1.2(d)) is plotted. Also shown is the % error in τ_w when a calibration curve involving $\tau_w^{1/6}$ is fitted to the results.

The following disadvantages may be cited against the technique -

(i) Requires calibration in a known τ_w flow.
(ii) Inherent inaccuracy due to ill conditioned calibration curve.
(iii) Uncertainty of the actual form of the calibration.
(iv) Calibration is very sensitive to changes in the fluid or substrate temperature.
(v) The applicability of the calibration effected in a two-dimensional flow to three-dimensional flows is unproven.
(vi) The effects of τ_w fluctuations and the ability to measure them is unclear.
(vii) The effects of substrate conduction upon the probe's response are uncertain.
(viii) The repeatability of the calibration is suspect.
(ix) The effects of not flush mounting the probe are unknown.

CHAPTER 2

Survey of theoretical solutions

This chapter examines the historical development of various theories used in the application of heated films for the measurement of skin friction.

2.1 Basic Theories

Fage and Falkner (1931) derived a relationship between skin friction and the heat convected from a hot surface element. They recognised that the heat convected from the surface depends not only upon the fluid skin friction but also upon the velocity profile in the neighbourhood of the wall. By considering the heat balance for an element in the flow field, and ignoring second order terms, they derived the linear, steady heat convection equation:

$$\frac{\partial^2 T}{\partial y^2} - \frac{\rho C_p}{k}\left(v\frac{\partial T}{\partial y} + u\frac{\partial T}{\partial x}\right) = 0 \qquad (2.1)$$

A series solution was then obtained by restricting the problem to cases where

(i) The surface temperature distribution could be expressed in the form $T_w = T_\infty + Ex^p$ where E, T_∞ and p are constants.
(ii) The free-stream velocity is given by $U_\infty = Fx^m$ (F,m constants) thus allowing the use of the Falkner-Skan similarity solution for the viscous boundary layer.
(iii) A uniform velocity gradient (normal to the wall) may be assumed to exist over the region through which the heat transfer is taking place.

In particular, they found that the relationship between the local heat flux q(x) and $\tau_w(x)$ was given by

$$\frac{q(x)}{k} = (T_w(x) - T_\infty)\lambda_1(-2\alpha_2)^{-1/3}\left(\frac{\tau_w(x)}{\rho\nu^2}\right)^{1/3}\left(\frac{L}{x}\right)^{1/3} \qquad (2.2)$$

where λ_1 and α_2 are constants for a given Pr, m and p and L is the length of the hot wall.

Implicit in the solution leading to equation (2.2) is the assumption that the viscous and thermal boundary layers start from the same origin. However, equation (2.2) may also be used for an isolated hot surface element if the skin friction is constant over the region for which $T_w > T_\infty$. Thus, for example, if it is assumed that the heat transfer is from an isothermal surface element (i.e. $p = 0$) over which the skin friction is constant (which from the Falkner-Skan solution implies $m = {}^1/_3$) then Fage and Falkner determined $\lambda_1 = 0.45$ and $\alpha_2 = -0.378$. Hence by integrating equation (2.2) over the heated surface length L the total heat flux Q is

$$\frac{Q}{k\Delta T} = 0.808\left[\frac{Pr\tau_w L^2}{\rho\nu^2}\right]^{1/3} \qquad (2.3)$$

where $\Delta T = T_w - T_\infty$.

To validate the theory an electrically heated nickel strip was embedded in the surface of an ebonite block carried in a metal casing within a hollow steel cylinder. Mounting the cylinder across the working section of a wind tunnel, the wall temperature distribution $T_w(x)$ was measured over a range of speeds for various angular positions of the strip. Their results suggested little variation of $T_w(x)$ with speed or angular position. By fitting appropriate forms of $T_w = T_0 + Ex^p$ to the measured wall temperature distribution it was possible to estimate the relationship between the total heat flux to the flow and the mean skin friction over the heated segment. For example, assuming constant skin friction over the hot surface, they predicted that for the measured wall temperature distribution the heat flux to the flow was

$$\frac{Q}{k\Delta T_e} = 1.044\left[\frac{PrL^2\bar{\tau}_w}{\rho\nu^2}\right]^{1/3} \qquad (2.4)$$

where $\bar{\tau}_w$ is the mean skin friction over the heated region and ΔT_e is the estimated mean temperature rise of the nickel strip.

Ludwieg (1950) appears to have been the first to suggest that the variation of heat transfer with skin friction could be used as the basis of a technique for measuring skin friction. He argued that since the velocity profile in the near wall region of a turbulent boundary layer is related to τ_W then the heat transferred from a hot surface film to the flow ought to be related to τ_W. Assuming that the thermal layer generated by the heating element remains within the viscous sub-layer of the turbulent boundary layer then the energy equation (2.1) may be further simplified to

$$\frac{\tau_W}{\mu} y \frac{\partial T}{\partial x} = \frac{\nu}{Pr} \frac{\partial^2 T}{\partial x^2} . \qquad (2.5)$$

since $u^+ = y^+$ (i.e. $u = \frac{\tau_W}{\mu} y$) and $v = 0$. (Assuming $v = 0$ implies τ_W is constant over the heated surface.)

Introducing the parameters

$$\xi = x\sqrt{\frac{\tau_W Pr}{\rho\nu^2}} \quad \text{and} \quad \eta = y\sqrt{\frac{\tau_W Pr}{\rho\nu^2}} \qquad (2.6)$$

the governing equation (2.5) becomes

$$\eta\frac{\partial T}{\partial \xi} - \frac{\partial^2 T}{\partial \eta^2} = 0 \qquad (2.7)$$

The assumption of an isothermal film on an otherwise adiabatic wall determines the boundary conditions

$$\begin{array}{llll} T = T_W & 0 \leq \xi \leq L^+ & & \text{for } \eta = 0 \\ \frac{\partial T}{\partial \eta} = 0 & -\infty \leq \xi \leq 0 & L^+ \leq \xi \leq \infty & \text{for } \eta = 0 \end{array} \qquad (2.8)$$

where

$$L^+ = \sqrt{\frac{\tau_W L^2}{\rho\nu^2}}$$

Ludwieg proposed that provided L^+ was not too small then the boundary conditions may be simplified to

$$\begin{array}{llll} T = T_W & \text{for} & 0 \leq \xi \leq \infty & \text{and } \eta = 0 \\ \frac{\partial T}{\partial \eta} = 0 & \text{for} & -\infty \leq \xi \leq 0 & \text{and } \eta = 0 \end{array} \qquad (2.9)$$

Equations (2.7) and (2.9) were originally solved by Lévêque (1928) giving the solution

$$T = T_W - (T_W - T_\infty)F(\gamma)$$

where

$$\gamma = \left(\frac{\eta}{9\xi}\right)^{1/3} , \quad F(\gamma) = \frac{\int_0^\gamma e^{-\gamma^3} d\gamma}{\int_0^\infty e^{-\gamma^3} d\gamma} \tag{2.10}$$

Thus using Lévêque's solution, Ludwieg obtained the relationship

$$\frac{Q}{k\Delta T} = \frac{9^{2/3}}{6\int_0^\infty e^{-\gamma^3} d\gamma} \left\{ \frac{L^2 \tau_w Pr}{\rho \nu^2} \right\}^{1/3} \tag{2.11}$$

or $\quad Nu = 0.807 Pe^{1/3}$

Defining the thermal boundary layer thickness, δ_T, as the distance from the wall where the tangent to the temperature profile at the surface intersects with $\frac{T_W - T}{T_W - T_\infty} = 1$ then at the downstream edge of the film

$$\delta_T = 1.86 L \; Pe^{-1/3} \; . \tag{2.12}$$

Assuming the viscous sublayer thickness δ_L may be defined $\delta_L = \frac{C\nu}{u_\tau}$ where C is a constant then the necessary condition $\delta_T < \delta_L$ implies that

$$Pe < \left(\frac{C}{1.86}\right)^6 Pr^3 \tag{2.13}$$

In 1954 Liepmann and Skinner also obtained the $Nu \sim Pe^{1/3}$ relationship using dimensional and similarity arguments. They examined the effect of pressure gradient upon the heat convected from an isothermal film by assuming a velocity profile of the form

$$u = \frac{1}{2\mu} y^2 \frac{dP}{dx}^{+} \tag{2.14}$$

+ The velocity profile near the wall may be approximated as $u \approx \frac{\tau_W}{\mu} y + \frac{1}{2\mu} \frac{dP}{dx} y^2$. At separation $\tau_W \to 0$ (2-dimensional flow) so the profile becomes $u \approx \frac{1}{2\mu} \frac{dP}{dx} y^2$.

and showed that Nu is proportional to $\left(\frac{PrL^3}{\rho\nu^2}\frac{dP}{dx}\right)^{1/4}$. To justify the assumption $\frac{\partial^2T}{\partial x^2} << \frac{\partial^2T}{\partial y^2}$ they imposed the condition that Nu ought to be large (Nu >> 1). Using an order of magnitude analysis an upper limit for Nu was also obtained, $Nu < \frac{Pr}{C_f}$, to ensure that the thermal boundary layer remains within the viscous sub-layer. They proposed that under these conditions a unique calibration for both laminar and turbulent boundary layers would be obtained.

Appendix B outlines a simple solution procedure for the energy equation assuming a uniform sheared flow with a prescribed wall temperature distribution. It is shown that if the effects of longitudinal diffusion are ignored then the solution is given by

$$Nu = aPe^{1/3} \tag{2.15}$$

where the constant a is a function of the wall temperature.

2.2 Heat convection to a quadratic velocity profile

Bellhouse and Schultz (1966) considered the combined effects of pressure gradient and skin friction upon the heat convected from the film. They obtained a solution to the thermal energy integral equation

$$\frac{d}{dx}\int_0^\infty u(T - T_\infty)dy = \frac{q}{\rho C_p} \tag{2.16}$$

for a velocity profile of the form

$$u = \frac{\tau_w}{\mu} y + \frac{1}{2\mu}\frac{dP}{dx} y^2 \tag{2.17}$$

The solution follows the method proposed by Curle (1962) who assumed that the temperature profiles are self similar i.e.

$$\frac{T - T_\infty}{T_w - T_\infty} = f\left(\frac{y}{\delta_T}\right) = f(\eta) \tag{2.18}$$

Using Fourier's conduction law $q = -k \left.\frac{\partial T}{\partial y}\right|_{y=0}$, Curle evaluated the integral in equation (2.16) and found

$$\frac{d}{dx}\left\{a\frac{\tau_w}{\mu}\frac{\Delta T^3 k^2}{q^2} + \frac{b}{2\mu}\frac{dP}{dx}\Delta T\frac{k^3}{q^3}\right\} = \frac{q}{\rho C_p} \tag{2.19}$$

where

$$\begin{aligned} a &= \int_0^1 \eta f(\eta) f'(0)^2 d\eta \simeq 0.2226 \\ b &= -\int_0^1 \eta^2 f(\eta) f'(0)^3 d\eta \simeq 0.1046 \end{aligned} \tag{2.20}$$

Using the Falkner-Skan similarity solutions, Curle computed a and b and found that they were reasonably constant (variation less than 1%) over the whole range of pressure gradients from stagnation ($m = 1$) to separation ($m = -0.0904$) and Prandtl number range from order 1 to order 10.

To evaluate equation (2.19) Bellhouse and Schultz made the following assumptions

(i) Over the heated film τ_w and dP/dx are constant.

(ii) $T_w(x)$ and $q(x)$ are step functions, both constant along the film and zero everywhere else.

Thus integrating equation (2.19) they obtained

$$a k^2 \tau_w \left(\frac{\Delta T}{q}\right)^3 + \frac{b}{2}\frac{dP}{dx}\left(\frac{\Delta T}{q}\right)^4 k^3 = \frac{\mu^2 L}{\rho k Pr} \tag{2.21}$$

or

$$Nu^3 = aPe + \frac{b}{2}\frac{L}{\tau_w}\frac{Pe}{Nu}\frac{dP}{dx}$$

However, examination of equation (2.19) immediately reveals that ΔT and q cannot both be constant over the film as the differential on the left hand side would then be zero. Bellhouse (1965) showed that if ΔT and τ_w were both constant over the gauge then for $dP/dx = 0$, $q(x)$ varies like $x^{-1/3}$ over the film. Assuming $q(x) \sim x^{-1/3}$, equation (2.19) yields

$$Nu^3 = \frac{9}{4} aPe + \frac{27}{8}\frac{b}{2}\frac{dP}{dx}\frac{L}{\tau_w}\frac{Pe}{Nu} \tag{2.22}$$

Since the temperature field is dependent upon the velocity field, the assumption of a universal temperature profile independent of pressure gradient seems suspect and so the existence of single values for a and b is doubtful. Spence and Brown (1968) therefore sought a solution to the thermal energy equation (2.1) for a quadratic velocity profile, equation (2.17), assuming a 'top-hat' temperature distribution over the film. The solution consisted of two series relating the total convective heat loss from the isothermal film to the skin friction and pressure gradient for the limiting cases of $\frac{\tau_w^3}{(dP/dx)^2}$ tending to zero and tending to infinity.

For $\frac{\tau_w^3}{(dP/dx)^2} \to \infty$ i.e. $\frac{dP}{dx} \to 0$ then

$$Nu = 0.8072\, Pe^{1/3} + 0.1 \frac{L\, dP/dx}{\tau_w} - 0.02869\, Pe^{-1/3} \left(\frac{L\, dP/dx}{\tau_w}\right)^2 + \ldots \tag{2.23}$$

whilst for $\frac{\tau_w^3}{(dP/dx)^2} \to 0$ i.e. $\tau_w \to 0$

$$Nu = 0.6184 \left(Pe \frac{L dP}{\tau_w dx}\right)^{\frac{1}{4}} + 0.3649 \left(Pe \frac{L}{\tau_w} \frac{dP}{dx}\right)^{\frac{1}{2}} \frac{\tau_w}{L\, dP/dx}$$
$$- 0.1457 \left(Pe \frac{L}{\tau_w} \frac{dP}{dx}\right)^{\frac{3}{4}} \left(\frac{\tau_w}{L\, dP/dx}\right)^2 \tag{2.24}$$

Fortunately these series may be accurately represented by the single equation

$$Nu^3 = \frac{10}{19} Pe + \frac{25}{171} \frac{dP}{dx} \frac{L}{\tau_w} \frac{Pe}{Nu} \tag{2.25}$$

i.e. the leading term of each series.

Clearly this is of the same form as the integral solution, equation (2.22). Brown(1967b) noted that the assumption that the thermal boundary layer thickness is negligible relative to the viscous boundary layer implies that the Prandtl number is very large. Thus Brown recomputed the values of a and b using Curle's method for Pr → ∞

and obtained

$$a = \frac{1}{6\left[\Gamma(4/3)\right]^3} \quad , \qquad b = \frac{64}{3}\,\frac{1}{\left[\Gamma(\tfrac{1}{4})\right]^4} \tag{2.26}$$

where Γ signifies the Gamma function (Abramowitz and Stegun, 1968).

Hence putting $dP/dx = 0$, and therefore $q(x) \sim x^{-1/3}$, Brown showed that the integral solution, equation (2.22), became

$$Nu = 0.8072\ Pe^{1/3} \tag{2.27}$$

Similarly, assuming $\tau_w = 0$ implies, from equation (2.19), that $q(x) \sim x^{-\frac{1}{4}}$ and hence

$$Nu = 0.6184\left(\frac{PrL^3}{\rho\nu^2}\,\frac{dP}{dx}\right)^{\frac{1}{4}} \tag{2.28}$$

which corresponds to the limiting results of Spence and Brown.

Spence and Brown (1968) point out that the assumption $\frac{\partial^2 T}{\partial x^2} << \frac{\partial^2 T}{\partial y^2}$ is invalid at the leading and trailing edges of the film with a 'top-hat' temperature distribution. However, the error of the current solution will be negligible if the thermal boundary layer thickness is small compared to the length of the film. They therefore proposed the requirement that for $Pe > 44$ the effects of longitudinal diffusion are negligible and thus Nu is proportional to $\tau_w^{1/3}$ for $\frac{dP}{dx} = 0$. They also derived an upper limit for Pe:

$$Pe > 64^2 Pr^3 \tag{2.29}$$

supposedly to ensure a unique calibration in both laminar and turbulent flows. (This limit is based on the criterion that less than 1% of the surface heat flux crosses the plane $y^+ = 12$.)

2.3 Effect of turbulence

The previous analyses assume that if the thermal boundary layer is confined to the viscous sub-layer of a turbulent boundary layer then calibrations in laminar and turbulent flows ought to be identical since heat transfer is taking place into identical velocity profiles. Owen (1969) recognised that even within the viscous sublayer the velocity is not steady. He proposed that, to the first order, the effect of the velocity fluctuations upon the heat convected from the hot wall element may be accounted for by using the concept of eddy viscosity. Using Deissler's formula (1955)

$$\varepsilon_m = n^2uy(1 - e^{-n^2uy/\nu}) \tag{2.30}$$

where n = 0.124 , Owen assumes that for Prandtl and Schmidt numbers of order unity a good approximation for the eddy viscosity close to the wall is

$$\varepsilon_m = n^2uy \tag{2.31}$$

Introducing an effective fluid viscosity, $\mu_e = \mu + \rho\varepsilon_m$, Owen suggests that the effect of eddying in the sub-layer may be accounted for by replacing the quadratic velocity profile, equation (2.17), by

$$u = \frac{\tau_w}{\mu_e} y + \frac{1}{2\mu_e}\frac{dP}{dx} y^2 \ . \tag{2.32}$$

To obtain the appropriate solution for turbulent flow, Owen simply replaces μ by its effective value, μ_e, in the previous solutions. For example, assuming $dP/dx = 0$, then from Spence and Brown

$$Nu^3 = 0.526\ \rho\frac{PrL^2}{\mu^2}\tau_w$$

becomes

$$Nu^3 = 0.526\ \rho\frac{PrL^2}{\mu_e^2}\tau_w \tag{2.33}$$

Thus, Owen suggests that equivalence between laminar and turbulent calibrations may be obtained by using the effective fluid viscosity in turbulent flow. Unfortunately he does not give details on how the effective value of μ_e is determined.

This approach is highly suspect as Owen appears to have neglected the variation of μ_e with y by simply replacing μ by μ_e in the final result. Substituting Owen's proposed velocity profile into the thermal energy integral equation (2.16) gives

$$\frac{d}{dx}\int_0^\infty (T - T_\infty)\frac{\tau_w}{\mu_e}y + (T - T_\infty)\frac{1}{2\mu_e}\frac{dP}{dx}y^2dy = \frac{q}{\rho C_p} \qquad (2.34)$$

Since μ_e is a function of y, see equation (2.30), it must be included within the integral. Furthermore, equation (2.31) is also suspect in that it does not satisfy the requirement that close to the wall ε_m must be at least of order y^3, see Reichardt (1951). It is noted that a simple expansion of Deissler's formula for y small gives $\varepsilon_m \sim y^4$.

Pope (1971) also considered the effect of turbulence within the viscous sub-layer in an attempt to reduce the turbulent calibration to the laminar one. If it is assumed that the result for turbulent flow may be deduced from the laminar solution by replacing μ and k by their effective turbulent values then, for $dP/_{dx} = 0$, the ratio of the turbulent to laminar calibration slopes would be

$$\frac{(\text{Cal.slope})_T}{(\text{Cal.slope})_L} = \left(\frac{k_e^2\,\mu}{k^2\mu_e}\right)^{1/3} \qquad (2.35)$$

Hence, assuming linear variations of the effective properties:

$$\begin{aligned} \mu_e &= \mu(1 + \alpha y) \\ k_e &= k(1 + \beta y) \end{aligned} \qquad (2.36)$$

gives

$$\frac{(\text{Cal.slope})_T}{(\text{Cal.slope})_L} \simeq 1 + \frac{2\beta - \alpha}{3}\bar{\delta} \qquad (2.37)$$

where $\bar{\delta}$ is some relevant length scale in the y direction. Pope therefore suggested that if the change in conductivity due to turbulence is neglected ($\beta = 0$) the turbulent slope would be less than the laminar slope. However, if a turbulent Prandtl number of 0.93 is assumed the opposite holds. The assumption of a linear variation of μ with y implies that for $y \to 0$

$$u \simeq \frac{\tau_w}{\mu}y(1 - \gamma y) \qquad (2.38)$$

where $\gamma = 0.5\alpha$. Pope was therefore able to use the solution of Spence and Brown (1968) to show that if the variation of viscosity and conductivity are small then, for a top-hat temperature distribution, the solution to the energy equation becomes

$$Nu = 0.8072\ Pe^{1/3} + 0.10(2\beta - \alpha)L - 0.02869\ Pe^{-1/3}\left[L(2\beta - \alpha)\right]^2 \tag{2.39}$$

Equation (2.39) may also be used to predict the convective heat transfer to a quadratic velocity profile by putting $\beta = 0$ and $\alpha = 2\gamma$. Reviewing measured mean velocity profiles in the near wall region of turbulent flows, Pope proposed that for $y^+ < 20$ the profile could be accurately represented by the quadratic equation

$$u^+ = y^+(1 - 0.0208y^+) \tag{2.40}$$

Recognising that this suggests a ε_m variation of $0.0416 \frac{yu_\tau}{\nu}$, which does not satisfy Reichardt's requirements $\varepsilon_m \sim O(y^3)$, Pope defends equation (2.40) by pointing out that although the velocity profile at the wall fluctuates with time no eddies actually reach the wall itself. Hence the various eddy-viscosity theories must break down as the wall is approached.

Using equations (2.38) and (2.39) Pope derived a procedure which appeared to shift the turbulent calibration (heat transferred to a quadratic profile) onto the laminar calibration (heat convected to essentially a linear sheared velocity profile). This method is outlined in Appendix C.

2.4 Effect of longitudinal diffusion and compressibility

Ling (1963) and Springer and Pedley (1973, 1974) have examined the effect of retaining the term $\frac{\partial^2 T}{\partial x^2}$ in the solution of the linear, steady, temperature convection equation for the problem of an isothermal film on an otherwise adiabatic wall with a uniform sheared flow. The effects of longitudinal diffusion $(\frac{\partial^2 T}{\partial x^2})$ are shown to be significant at the leading and trailing edges of the film. Using a numerical technique to solve the complete temperature equation, Ling demonstrated that the thermal boundary layer has a finite thickness at the leading edge of the film. (Heat is conducted upstream in the fluid and finally convected downstream.) His results suggest that the thermal boundary layer diffuses to about $\frac{4.1L}{\sqrt{Pe}}$ ahead of the film. In terms of the total heat flux to the flow, Ling proposed the more accurate solution

$$Nu = 0.807\ Pe^{1/3} + 0.19\ Pe^{-1/6} \qquad (2.41)$$

Clearly, the second term is only significant for small values of Pe.

Diaconis (1954) examined the effect of compressibility upon the heat transferred from an isothermal film on an otherwise insulated plate. If the size of the heating element is sufficiently small so that the thermal boundary layer remains within the viscous sub-layer over the film, then the governing equation may be taken as the laminar, compressible, energy equation. Assuming Cp and Pr to be constant and the viscosity-temperature relation to be linear, Diaconis found that, although the temperature field is Mach number dependent, the total heat flux from the hot film is independent of Mach number. Thus he concluded that the Nu ∿ Pe relationship for compressible flow is identical to the incompressible form - providing the fluid properties are evaluated at the temperature of the film.

2.5 Solutions with a specified heat flux distribution

Tanner (1967) noted that there is a marked difference between the predicted convective heat transfer using adiabatic substrate theories and that measured in experiments. He suggested that a substantial increase in the heat transfer could occur by an increase in the effective area of the heating film due to the effects of substrate conduction. By specifying a heat flux over the film the steady state heat conduction equation in the substrate and the forced heat convection equation for a uniform sheared flow were solved. His three-dimensional analysis permitted the examination of anisotropic substrates although he assumed that the effects of spanwise and streamwise diffusion in the flow were negligible. His results confirmed an increase in heat transfer due to substrate conduction.

However, he did not suggest any modification to the Nu $\sim$ Pe relationship.

Rotem (1967) also considered the problem of a film with a specified heating flux although he assumed an adiabatic substrate. For the case of a uniform sheared flow with constant skin friction over the film, he showed that the convective heat transfer was proportional to $Pe^{1/3}$.

2.6 Conclusions

The theoretical basis for relating the wall shear to the convective heat loss from a hot surface element has undergone little development over the years. All those relations derived for use with practical gauges assume that the substrate is a perfect insulator (i.e. adiabatic) and consequently lead to the basic result

$$Nu = a\ Pe^{1/3} \tag{2.42}$$

where the constant a depends upon the prescribed form of the wall temperature distribution. In practice, however, substrate conduction does occur so it is implicitly suggested that the appropriate form of equation (2.42) is

$$Nu = A\ Pe^{1/3} + B$$

or

$$Nu = a\left[\frac{Pr(\lambda L)^2\tau_W}{\rho\nu^2}\right]^{1/3} + B$$

where λL is the effective heating length of the film.

Until now it has been assumed that the 'constants' A (or λ) and B represent the necessary modification to equation (2.42) in order to account for the effects of substrate conduction.

CHAPTER 3

The steady heat conduction/convection problem

Chapter 2 outlined the development of theoretical work seeking to relate the heat lost from a hot surface element to the skin friction. To date, all the theoretical relationships used in determining the form of the calibration of a hot film gauge for the measurement of skin friction are based on the assumption of adiabatic substrates. In practice, however, it is found that the heat conduction within the substrate greatly exceeds the convective heat transfer. (In some cases less than 10% of the total heat loss from the probe is due to the flow.) It is therefore considered that any realistic theoretical approach should include the effects of substrate conduction. This chapter presents such a theory which leads to a more physically realistic yet simple form of the Nu ∿ Pe relationship.

3.1 The heat conduction/convection equations.

3.1.1 Statement of the two-dimensional problem.

Consider a heating film on the interface between a constant property, semi-infinite solid and fluid as sketched in figure 3.1. For incompressible flow ($y^* > 0$) the energy equation may be written

$$\rho^* C_p^* \left(\frac{\partial T^*}{\partial t^*} + u^* \frac{\partial T^*}{\partial x^*} + v^* \frac{\partial T^*}{\partial y^*}\right) - k^* \left(\frac{\partial^2 T^*}{\partial x^{*2}} + \frac{\partial^2 T^*}{\partial y^{*2}}\right) = 0 \qquad (3.1)$$

where * denotes dimensional quantities.

The heat conduction equation in the solid, $y^* < 0$ is

$$\frac{\partial^2 T^*}{\partial x^{*2}} + \frac{\partial^2 T^*}{\partial y^{*2}} = \left(\frac{\rho^* C_p^*}{k^*}\right) \frac{\partial T^*}{\partial t^*} \qquad (3.2)$$

(Note the effects of natural convection and radiation are ignored.)

For incompressible, constant property flow, the temperature and momentum equations in the flow are de-coupled and so the velocity field is independent of the temperature field. Since the typical streamwise length of the film is of order 10^{-4}m, the flow field is defined as

$$u^* = \frac{\tau_W^*}{\mu^*}.y^* \tag{3.3}$$

where τ_W^* is assumed to be constant over the heated wall region. Therefore from the continuity equation,

$$\text{since } \frac{\partial u^*}{\partial x^*} = 0 \Rightarrow v^* = 0$$

i.e. Couette flow is assumed. Such a simple flow model will not be physically realistic in the region of a stagnation point or a separation point.

Clearly the heat conduction/convection problem is time dependent. However, in order to simplify the solution the quasi-steady problem is solved by putting $\partial T^*/\partial t^* = 0$. (The time dependence of the total heat loss from the heating film is examined in Chapter 4.)

The governing temperature differential equations for the proposed heat conduction/convection problem are therefore

$$\text{Fluid } y^* > 0 : \quad \frac{\partial^2 T_F^*}{\partial x^{*2}} + \frac{\partial^2 T_F^*}{\partial y^{*2}} - \frac{P_r \tau_W^*}{\rho^* \nu^{*2}} y^* \frac{\partial T_F^*}{\partial x^*} = 0 \tag{3.4}$$

$$\text{Solid } y^* < 0 : \quad \frac{\partial^2 T_S^*}{\partial x^{*2}} + \frac{\partial^2 T_S^*}{\partial y^{*2}} = 0 \tag{3.5}$$

where the subscripts F and S refer to the fluid and solid respectively.

3.1.2 Boundary conditions.

There would appear to be 2 alternative boundary conditions that may be specified along the interface $y^* = 0$.

(i) A specified temperature distribution.
(ii) A specified heat flux distribution.

Previous solutions (see Chapter 2) typically assume a constant temperature over the film on an adiabatic substrate. In reality, the substrate is not adiabatic and so the actual wall temperature distribution must be continuous and smooth. (In air flows, the thermal conductivity of the substrate relative to the air may be very large.) However, it does not appear to be possible to specify the wall temperature 'a priori'.

Alternatively, a specified heat flux distribution over the film on a conducting substrate does lead to a smooth, realistic temperature distribution. Indeed, it may be argued that at a particular instant in time, the electric current flowing in the film generates a heating flux. (This point is discussed further in Section 3.9.) Thus the solution to the quasi-steady problem with a specified heat flux distribution is sought for the following boundary conditions:

On the interface, $y^* = 0$, the temperature of the fluid must equal that of the solid,

$$\text{i.e.} \qquad T_F^*(x^*,0) = T_S^*(x^*,0) \tag{3.6}$$

Furthermore, there must be a heat flux balance along the interface, i.e.

$$k_S^* \frac{\partial T_S^*}{\partial y^*} - k_F^* \frac{\partial T_F^*}{\partial y^*} = q^*(x^*,0) = q^*(x^*) \tag{3.7}$$

where $q^*(x^*)$ is the specified heat flux distribution.

Finally, it is assumed that at infinity, the temperature vanishes, i.e.

$$T^* \rightarrow 0 \text{ as } |r^*| \rightarrow \infty , \quad r^* = \sqrt{x^{*2} + y^{*2}} . \tag{3.8}$$

This condition implies that at infinity the solid and the fluid are at the same temperature T_∞^*. Therefore, T^* represents the temperature rise above T_∞^*.

3.1.3 Dimensionless parameters.

The governing equations and boundary conditions are made dimensionless by introducing the following parameters.

A characteristic length scale may be defined

$$L^* = \sqrt{\frac{\rho^* {\nu^*}^2}{P_r \tau_W^*}} \tag{3.9}$$

Thus $x = \frac{x^*}{L^*}$, $y = \frac{y^*}{L^*}$.

Let the total heat flux be $Q^* = \int_{-\infty}^{\infty} q^*(x^*)dx^*$ (3.10a)

Thus a dimensionless heat flux distribution may be defined

$$q(x) = \frac{q^*(x).L^*}{Q^*} \tag{3.10b}$$

Also $T = \frac{T^* k_F^*}{Q^*}$ and let $K = \frac{k_S^*}{k_F^*}$ (3.11)

Therefore, in dimensionless form, the temperature equations become

$$y \geqslant 0 \qquad \frac{\partial^2 T_F}{\partial x^2} + \frac{\partial^2 T_F}{\partial y^2} - y\frac{\partial T_F}{\partial x} = 0 \tag{3.12}$$

$$y \leqslant 0 \qquad \frac{\partial^2 T_S}{\partial x^2} + \frac{\partial^2 T_S}{\partial y^2} = 0 \tag{3.13}$$

whilst the boundary conditions become

$$T_S(x,0) = T_F(x,0) \tag{3.14}$$

$$K\frac{\partial T_S}{\partial y}(x,0) - \frac{\partial T_F}{\partial y}(x,0) = q(x) \tag{3.15}$$

$$r \to \infty \qquad T \to 0 \tag{3.16}$$

Note that as $\tau_W^* \to 0$ (i.e. stopping the flow) then $L^* \to \infty$ so $x,y \to 0$. Thus the solution for the no flow case cannot be obtained using these equations.

3.2 Solution procedure.

Equations (3.12) and (3.13) describing the heat conduction/convection problem subject to the boundary conditions (3.14) to (3.16) may be solved by application of the theory of Fourier transforms.

Let the Fourier transform of $T(x,y)$ be $\overline{T}(\alpha,y)$ which may be defined by

$$\overline{T}(\alpha,y) = \int_{-\infty}^{\infty} T(x,y)e^{2\pi i\alpha x}dx \ . \qquad (3.17)$$

N.B. The vanishing of T at infinity is a necessary condition (although not sufficient) to ensure the existence of $\overline{T}(\alpha,y)$.

Thus taking Fourier transforms, equation (3.12) becomes

$$\frac{d^2\overline{T}_F}{dy^2} - 4\pi^2\alpha^2\overline{T}_F + 2\pi i\alpha y\overline{T}_F = 0 \qquad (3.18)$$

Similarly equation (3.13) in the transformed plane becomes

$$\frac{d^2\overline{T}_S}{dy^2} - 4\pi^2\alpha^2\overline{T}_S = 0 \qquad (3.19)$$

3.3 Solution assuming $\frac{\partial^2 T_F}{\partial^2 x} = 0$.

3.3.1 Solution in the transformed plane.

In order to simplify the solution, we shall first assume that the effects of longitudinal diffusion are small. Hence upon dropping the term $\frac{\partial^2 T_F}{\partial x^2}$ in equation (3.12) the transformed equation (3.18) becomes

$$\frac{d^2\overline{T}_F}{dy^2} + 2\pi i\alpha y\overline{T}_F = 0 \ . \qquad (3.20)$$

Introducing the transformation $s = (2\pi\alpha)^{1/3}ye^{-\pi/6 i}$ equation (3.20) may be rewritten

$$\frac{d^2\overline{T}_F}{ds^2} - s\overline{T}_F = 0 \qquad (3.21)$$

which is Airy's Equation, see Abramowitz and Stegun (1968). The general solution to equation (3.20) is therefore,

$$\overline{T}_F(\alpha,y) = a(\alpha)\,\mathrm{Ai}\{s\} + b(\alpha)\mathrm{Bi}\{s\} \qquad (3.22)$$

where Ai{s} , Bi{s} are the Airy functions.

If the argument of s is restricted to the range

$$-\pi/3 < \mathrm{Arg}\{s\} < \pi/3$$

then, since $\overline{T}_F$ must vanish at infinity (the Fourier transform of equation (3.16)), Bi{s}is not an admissible solution. However, since y is real

$$\mathrm{Arg}\{s\} = \frac{1}{3}\mathrm{Arg}\{\alpha\} - \frac{\pi}{6}$$

so it is necessary to place a cut along the negative imaginary axis of the α-plane, i.e.

$$-\frac{\pi}{2} < \mathrm{Arg}\{\alpha\} < \frac{3\pi}{2}$$

Thus the solution equation (3.22) becomes

$$y \geq 0 : \qquad \overline{T}_F(\alpha,y) = a(\alpha)\mathrm{Ai}\{e^{-i\pi/6}(2\pi\alpha)^{1/3}y\} \qquad (3.23)$$

The general solution to equation (3.19) is

$$\overline{T}_s(\alpha,y) = c(\alpha)e^{-\sqrt{4\pi^2\alpha^2}.y} + d(\alpha)e^{+\sqrt{4\pi^2\alpha^2}.y} \qquad (3.24)$$

Again, since $\overline{T}_s \to 0$ as $y \to -\infty$, $c(\alpha) = 0$

Hence equation (3.24) reduces to

$$y \leq 0 : \qquad \overline{T}_s(\alpha,y) = d(\alpha)e^{+\sqrt{4\pi^2\alpha^2}.y} \qquad (3.25)$$

The functions a(α) and d(α) are found by applying the Fourier transformation (3.17) to the boundary conditions, i.e.

$$y = 0 \qquad \overline{T}_s = \overline{T}_F \qquad (3.26)$$

and $y = 0$

$$K\frac{d\overline{T}_s}{dy} - \frac{d\overline{T}_F}{dy} = \overline{q}(\alpha) \tag{3.27}$$

where $\overline{q}(\alpha)$ is the Fourier transform of the specified heat flux distribution $q(x)$.

Thus from equations (3.23) and (3.25) it may be shown that

$$a(\alpha) = \frac{\overline{q}(\alpha)}{+\sqrt{4\pi^2\alpha^2}\,K\,Ai\{o\} - (2\pi\alpha)^{1/3}\,e^{-\pi/6\,i}\,Ai'\{o\}} \tag{3.28}$$

and

$$d(\alpha) = a(\alpha).Ai\{o\} \tag{3.29}$$

where $Ai'\{o\}$ denotes the derivative of the Airy function.

Putting $y = 0$ in either equation (3.25) or (3.23), the surface temperature distribution in the transformed plane may be found

$$\overline{T}(\alpha,o) = \frac{\overline{q}(\alpha)C_1}{+\sqrt{4\pi^2\alpha^2}\,K\,C_1 + (2\pi\alpha)^{1/3}\,e^{-\pi/6\,i}\,C_2} \tag{3.30}$$

where $C_1 = Ai\{o\} = 0.35503$

$C_2 = -Ai'\{o\} = +0.25882$

3.3.2 Determination of $\overline{q}(\alpha)$.

For the present a 'top-hat' heat flux distribution over the film may be assumed, i.e.

$$q^*(x^*) = q^*H\{a^* - |x^*|\} \qquad \text{(dimensional quantities)} \tag{3.31}$$

where a^* is half the streamwise length of the film (see figure 3.1).

From the definition of Q^*,

$$Q^* = 2a^*q^* \tag{3.32}$$

Using the definition of L^*, equation (3.9), it is clear that

$$Pe = \left(\frac{2a^*}{L^*}\right)^2 \tag{3.33}$$

Thus $$q(x) = \frac{1}{\sqrt{Pe}} H\{\frac{\sqrt{Pe}}{2} - |x|\} \qquad (3.34)$$

which upon application of the Fourier transform gives

$$\bar{q}(\alpha) = \frac{\text{Sin}(\pi\sqrt{Pe}\alpha)}{\pi\sqrt{Pe}\alpha} \qquad (3.35)$$

Note: The temperature field is completely specified for a given K and Pe.

3.3.3 Inversion

The surface temperature for a 'top-hat' heat flux distribution is therefore

$$\bar{T}(\alpha,0) = \frac{\frac{\text{Sin}(\pi\sqrt{Pe}\alpha)}{\pi\sqrt{Pe}\alpha}.C_1}{+\sqrt{4\pi^2\alpha^2}\,K\,C_1 + e^{-i\pi/6}(2\pi\alpha)^{1/3}C_2} \qquad (3.36)$$

or

$$\bar{T}(\alpha,0) = \bar{T}_R(\alpha) + i\bar{T}_I(\alpha)$$

Application of the inverse theorem gives the temperature distribution in the real plane

$$T(x,0) = \int_{-\infty+i\varepsilon}^{\infty+i\varepsilon} \bar{T}(\alpha,0).e^{-2\pi i\alpha x}d\alpha \qquad (3.37)$$

As shown in Appendix D, this may be converted to the sum of 2 real integrals

$$T(x,0) = 2\int_0^\infty \bar{T}_R(r)\text{Cos}2\pi rx +.\bar{T}_I(r)\text{Sin}2\pi rx\ dr \qquad (3.38)$$

The mean temperature over the film may be calculated from equation (3.38)

$$T_{mean} = \frac{1}{\sqrt{Pe}}\int_{-\frac{\sqrt{Pe}}{2}}^{\frac{\sqrt{Pe}}{2}} 2\int_0^\infty \bar{T}_R(r)\text{Cos}2\pi rx + \bar{T}_I(r)\text{Sin}2\pi rx\ dr\ dx \qquad (3.39)$$

Inverting the order of integration gives

$$T_{mean} = 2\int_0^\infty \overline{T}_R(r)\,\frac{\mathrm{Sin}(\pi r\sqrt{Pe})}{\pi r\sqrt{Pe}}\,dr \qquad (3.40)$$

3.4 Evaluation of the integrals.

Except for the case K = 0 (adiabatic substrate) numerical evaluation of the integrals is necessary. This was carried out on a VAX 11-750 digital computer using an integrating routine obtained from the Numerical Algorithms Group (Nag). The numerical technique used first transformed the infinite integration range to (0,1) using the identity

$$\int_\delta^\infty F(r)dr = \int_0^1 F(\delta + \frac{1-t}{t})\,\frac{1}{t^2}\,dt \qquad (3.41)$$

where δ represents the lower finite limit of integration. In order to avoid the singularity of $\overline{T}(r)$ at $r = 0$, δ was assigned the value 0.00001. An approximation of the integral value over the range $(0,\delta)$ was determined by analytically integrating the expression for $\overline{T}(r)$ as $r \to 0$. It may be shown that the contribution to either integral (3.38) or (3.40) due to integration over the range $(0,\delta)$ is approximately

$$1.28756\delta^{2/3} + \frac{1}{4\pi K}\ln(8.08996K\delta^{2/3} + 1) \qquad (3.42)$$

or if K = 0 the contribution is

$$1.93134\delta^{2/3}$$

The numerical evaluation of the transformed integral (3.41) was obtained using an adaptive procedure based on the Gauss 7-point and Kronrod 15-point rules.

3.5 Results

3.5.1 Variation of Nu with Pe and K.

Of particular interest is the variation of T_{mean}^{-1} with Pe and K. From the definition of T*, see equation (3.11)

$$\frac{1}{T_{mean}} = \left(\frac{Q^*}{k_F^* T^*}\right)_{mean} \tag{3.43}$$

Since T* actually represents a temperature rise above T_∞^*, i.e. $T^* \equiv \Delta T^* = (T^* - T_\infty^*)$, then the reciprocal of the dimensionless mean film temperature is the mean Nusselt number, Nu.

If K = 0 (adiabatic wall), then from equation (3.36)

$$\bar{T}_R(r) = \frac{\sqrt{3}}{2H} \frac{\bar{Q}(r)}{(2\pi r)^{1/3}}$$

where $$H = -\frac{Ai'\{0\}}{Ai\{0\}} = 3^{1/3}\frac{\Gamma(2/3)}{\Gamma(1/3)} = 0.7290$$

Thus

$$T_{mean} = \frac{\sqrt{3}}{H}\left(\frac{\sqrt{Pe}}{2}\right)^{1/3}\int_0^\infty \frac{Sin^2(\pi\sqrt{Pe}r)}{(\pi\sqrt{Pe}r)^{7/3}}\,dr$$

Let $\theta = \pi\sqrt{Pe}r$,

$$\Rightarrow \quad T_{mean} = \frac{\sqrt{3}}{\pi H}\left(\frac{1}{2Pe}\right)^{1/3}\int_0^\infty \frac{Sin^2\theta}{\theta^{7/3}}\,dr$$

Now $\int_0^\infty \theta^{-7/3}\,Sin\theta d\theta = \frac{3}{4}\int_0^\infty \theta^{-4/3}\,Sin2\theta d\theta$

which from Gradshteyn and Ryzhik (1980) gives the result

$$\int_0^\infty \theta^{-7/3}\,Sin\theta d\theta = \frac{\sqrt{3}.\pi}{2^{5/3}\,\Gamma(4/3)}$$

Thus

$$Nu = \frac{1}{T_{mean}} = \frac{4H\Gamma(4/3)Pe^{1/3}}{3}$$

or $$Nu \simeq 0.868Pe^{1/3} \tag{3.44}$$

This result agrees in form with previous adiabatic substrate theories although the constant differs from the isothermal solution. The actual wall temperature distribution for the current problem is considered in section 3.5.2.

For $K > 0$ numerical evaluation of integral (3.40) is necessary. Figure 3.3 shows the effect of K upon the $Nu \sim Pe^{1/3}$ relationship.

The theoretical results indicate that Nu is not directly proportional to $Pe^{1/3}$ for $K > 0$, although for small values of K, the proposed relationship

$$Nu = A\,Pe^{1/3} + B$$

may be adequate for a limited Pe range. The curvature or 'bow' of the results in figure 3.3 indicates that a higher root of Pe is required to achieve proportionality with Nu. Finding the best fitting curve, in the least square error sense, of the form

$$Nu = A\,Pe^{1/n} + B \tag{3.45}$$

to the theoretical results over the range $1 \leqslant Pe \leqslant 100$ gives the following values for A, B and n

K	n	A	B	rms error	rms error n=3
0	3.0	0.868	0	0	0
5	3.9	1.759	2.259	0.005	0.054
15	4.9	3.580	5.008	0.006	0.129
45	6.2	8.344	11.527	0.008	0.277

The rms values (root mean square error in terms of Nu) clearly indicate that a considerable improvement in accuracy is obtained by using equation (3.45) with $n > 3$.

The result $Pe = 0$ $Nu = 0$ cannot be obtained directly from the present theory. Since Pe is proportional to (streamwise length of the film)^2, then Pe = 0 may simply imply that the film length is zero so obviously Nu must be zero. Computations down to Pe = 10^{-9} for various values of K do indicate that the curves pass through the origin. This result may be further confirmed by considering the simplified problem of a semi-infinite solid, initially at a uniform temperature, with a constant heat flux, q_0^*, along the surface, ($y^* = 0$). From Carslaw and Jaeger (1959) the solution for the rise in temperature ΔT^* is

$$\Delta T^*(y^*,t^*) = \frac{2q_0^*}{k^*}\left\{\left(\frac{\alpha^* t^*}{\pi}\right)^{\frac{1}{2}} e^{-y^{*2}/4\alpha^* t^*} - \frac{y^*}{2}\operatorname{erfc}\left(\frac{y^*}{2\sqrt{\alpha^* t^*}}\right)\right\}$$

where α^* is the thermal diffusivity of the solid and t^* is time.

Putting $y^* = 0$ gives the surface temperature

$$\Delta T^*(0,t) = \frac{2q_0^*}{k^*}\sqrt{\frac{\alpha^* t^*}{\pi}}$$

A local Nusselt number may be defined $\quad Nu = \frac{q_0^*}{k^* \Delta T^*}$

Thus $\quad Nu = \frac{1}{2}\sqrt{\frac{\pi}{\alpha^* t^*}}$

Hence the steady state solution may be obtained by putting $t^* \to \infty$ i.e. $Nu \to 0$. The similarity between this simplified problem and that where the flow is stopped ($\tau_w^* = 0$) confirms the result Pe = 0, Nu = 0.

3.5.2 Wall temperature distributions

Using equations (3.36) and (3.38) the dimensionless wall temperature distribution has been computed. By factoring T(x,0) by the appropriate value of Nu then the product T.Nu may be considered as the ratio:

$$T.Nu = \frac{T_w^* - T_\infty^*}{T_{MF}^* - T_\infty^*} \qquad (3.46)$$

where T_{MF}^* is the mean film temperature. Figures 3.4 and 3.5 show the effect of Pe and K for a 'top-hat' heat flux distribution upon the wall temperature normalised with respect to the mean film temperature. The results clearly indicate that the wall temperature distribution is not symmetrical about the centre line of the film although increasing K or decreasing Pe reduces the asymmetry. The wall temperature distributions are discussed further in section 3.8.2.

For the particular case K = 0 the appropriate integrals may be evaluated analytically.

The results, derived in Appendix E , are:

$$\text{For } -1 < \frac{x^*}{a^*} < 0 \qquad \frac{T_W^* - T_\infty^*}{T_{MF}^* - T_\infty^*} = 1.0583\left\{1 - \left|\frac{x^*}{a^*}\right|\right\}^{1/3}$$

$$\text{For } \; 0 < \frac{x^*}{a^*} < 1 \qquad \frac{T_W^* - T_\infty^*}{T_{MF}^* - T_\infty^*} = 1.0583\left\{1 + \frac{x^*}{a^*}\right\}^{1/3} \tag{3.47}$$

$$\text{For } \qquad \frac{x^*}{a^*} > 1 \qquad \frac{T_W^* - T_\infty^*}{T_{MF}^* - T_\infty^*} = 1.0583\left\{\left(\frac{x^*}{a^*} + 1\right)^{1/3} - \left(\frac{x^*}{a^*} - 1\right)^{1/3}\right\}$$

Note: The case K = 0 was used as a check upon the routines used to evaluate the integrals.

3.5.3 Heat transfer to the fluid.

Using equations (3.23) and (3.28) it may be shown that

$$\left.\frac{\partial \bar{T}}{\partial y}\right|_{y=0} = \frac{-\bar{q}(\alpha)(2\pi\alpha)^{1/3} e^{-i\,\pi/6} C_2}{+\sqrt{4\pi^2\alpha^2 K}\, C_1 + (2\pi\alpha)^{1/3} e^{-i\,\pi/6} C_2} \tag{3.48}$$

$$= \dot{\bar{T}}_R + i\dot{\bar{T}}_I$$

As in section 3.3.3 application of the inverse transformation gives the result

$$\frac{\partial T}{\partial y}(x,0) = 2\int_0^\infty \dot{\bar{T}}_R \operatorname{Cos} 2\pi r x + \dot{\bar{T}}_I \operatorname{Sin} 2\pi r x \, dr \tag{3.49}$$

Factoring $\frac{\partial T}{\partial y}$ by Nu.$\sqrt{Pe}$ gives

$$\frac{\partial T}{\partial y} \cdot Nu\sqrt{Pe} = \frac{2a^*}{\Delta T^*_{MF}} \frac{\partial T^*}{\partial y^*} \qquad (3.50)$$

Figures 3.6 and 3.7 show the effect of Pe and K upon heat flux into the fluid: $\frac{2a^*}{\Delta T_{MF}} \frac{q^*_F}{k^*_F}$

The trends observed are discussed in section 3.8.3.

3.6 Effect of longitudinal diffusion

The Fourier transform of the complete conduction/convection equation (3.12) is (from equation (3.18))

$$\frac{d^2\overline{T}_F}{dy^2} - 4\pi^2\alpha^2\overline{T}_F + 2\pi i\alpha y\overline{T}_F = 0 \qquad (3.51)$$

Introducing the transformation

$$s = e^{-\frac{\pi}{6} i}(2\pi\alpha)^{\frac{1}{3}}(y + 2\pi i\alpha) \qquad (3.52)$$

reduces equation (3.51) to Airy's equation -

$$\frac{d^2\overline{T}_F}{ds^2} - s\overline{T}_F = 0$$

with the general solution as indicated in equation (3.22).

As before, restricting the argument of s to $-\frac{\pi}{3} < \mathrm{Arg}\{s\} < \frac{\pi}{3}$ and thus requiring a cut along the negative imaginary axis of the α plane, disqualifies the function Bi{s}. Hence the appropriate solution to equation (3.41) is

$$y \geqslant 0 \qquad \overline{T}_F(\alpha,y) = a(\alpha)\mathrm{Ai}\{e^{-\frac{\pi}{6} i}(2\pi\alpha)^{\frac{1}{3}}(y + 2\pi i\alpha)\} \qquad (3.53)$$

The solution for the region $y \leqslant 0$ is as before i.e.

$$y \leqslant 0 \qquad \overline{T}_s(\alpha,y) = d(\alpha)e^{+\sqrt{4\pi^2\alpha^2}\cdot y}$$

Enforcing the transformed boundary conditions (equations 3.26 and 3.27) gives

$$a(\alpha) = \frac{\overline{q}(\alpha)}{+\sqrt{4\pi^2\alpha^2}\,K\,\mathrm{Ai}\{g\} - e^{-\pi/6\,i}\,(2\pi\alpha)^{1/3}\,\mathrm{Ai}'\{g\}} \qquad (3.54)$$

$$d(\alpha) = a(\alpha).\mathrm{Ai}\{g\} \qquad (3.55)$$

where $g = e^{\pi/3\,i}\,(2\pi\alpha)^{4/3}$.

Thus the surface temperature distribution in the transformed plane is

$$\overline{T}(\alpha,0) = \frac{\overline{q}(\alpha)\ \mathrm{Ai}\{g\}}{+\sqrt{4\pi^2\alpha^2}\,K\,\mathrm{Ai}\{g\} - e^{-\pi/6\,i}\,(2\pi\alpha)^{1/3}\,\mathrm{Ai}'\{g\}} \qquad (3.56)$$

$$= \overline{T}_R + i\overline{T}_I$$

As outlined in Appendix D, application of Fourier's inverse theorem gives

$$\overline{T}(x,0) = 2\int_0^\infty \overline{T}_R(r)\mathrm{Cos}(2\pi rx) + \overline{T}_I(r)\mathrm{Sin}(2\pi rx)dr\ . \qquad (3.57)$$

and as before the mean film temperature is

$$T_{MF} = 2\int_0^\infty \overline{T}_R(r)\ \frac{\mathrm{Sin}(\pi r/Pe)}{\pi r/Pe}\ dr \qquad (3.58)$$

The heat flux to the fluid along the interface $y = 0$ may also be determined using the relation

$$\frac{\partial\overline{T}}{\partial y}(\alpha,0) = \frac{\overline{q}(\alpha)(2\pi\alpha)^{1/3}\,e^{-i\pi/6}\,\mathrm{Ai}'\{g\}}{+\sqrt{4\pi^2\alpha^2}\,K\,\mathrm{Ai}\{g\} - e^{-i\pi/6}\,(2\pi\alpha)^{1/3}\,\mathrm{Ai}'\{g\}} \qquad (3.59)$$

3.7 Evaluation of the integrals.

For all values of K numerical evaluation of the appropriate integrals is necessary. As outlined in Section 3.2 use was made of a 'Nag' integrating routine. The contribution due to the integral over the limit $(0,\delta)$ where $\delta \ll 1$ was found to be identical to the previous results, i.e. equation (3.42). As an independent check, the integrals were estimated using Simpson's rule and Weddle's rule over a finite interval (δ,Δ). The residual due to the integral over the range (Δ,∞) was estimated by analytically integrating the appropriate asymptotic expansion of the integrand. (A suitable value of Δ was found to be 4.) The agreement between the 2 methods was very good (difference < 2%). Due to the oscillatory behaviour of the integrand a very large number of intervals were required when using Simpson's rule. The Nag routine returned the integral value to within a specified accuracy in typically $^1/_{10}$th of the CPU time required when using Simpson's rule.

The values of the Ai{g} and Ai'{g} were computed using the ascending series definitions for Ai and Ai' when $|g| < 4.1$. For $|g| \geq 4.1$ the asymptotic expansions for Ai and Ai' were used (see Abramowitz and Stegun,1968). In each case the relevant series was truncated after 10 terms, (see Appendix F for details). All computer calculations were conducted using Double Precision.
Using the results

$$\mathrm{Ai}\{re^{i\pi/3}\} = \frac{\sqrt{r}}{3}\{J_{-1/3}\,(2/3\,r^{3/2}) - e^{\pi/3\,i}\;J_{1/3}(\,2/3\,r^{3/2}\,)\} \qquad (3.60)$$

and

$$\mathrm{Ai}'\{re^{i\pi/3}\} = -\,\frac{r}{3}\{J_{-2/3}\,(2/3\,r^{3/2}) - e^{2\pi i/3}\;J_{2/3}\,(2/3\,r^{3/2})\} \qquad (3.61)$$

(derived in Appendix F) it was possible to check the computed values of Ai{g} and Ai'{g} using the series definitions. The values of the Bessel functions $J_{1/3}$, $J_{-1/3}$, $J_{2/3}$ and $J_{-2/3}$ were obtained from U.S.N.B.S. tables (1948). Agreement was demonstrated to at least 6 significant figures.

3.8 Results

3.8.1 Variation of Nu with Pe and K.

The value of Nu for a given Pe and K may be determined from the mean temperature over the film. Figure 3.8 shows the effect of K upon the Nu $\sim Pe^{1/3}$ relationship assuming a 'top-hat' heat flux distribution over the film. The curves are clearly 'bowed' indicating that Nu is not porportional to $Pe^{1/3}$.

Fitting the curve

$$Nu = APe^{1/n} + B$$

the best values of A, B and n were determined over the range $1 < Pe < 100$.

K	n	A	B	rms error	rms error n=3
0	2.6	0.594	0.627	0.003	0.024
5	3.8	1.646	2.526	0.005	0.048
15	4.9	3.545	5.138	0.006	0.122
45	6.2	8.310	11.625	0.008	0.274

Comparing these values to those obtained previously, it is clear that the effect of longitudinal diffusion is to increase B and decrease A with little effect upon the value of n, except at small values of K. The changes in A and B appear to be only significant at small values of K. A direct comparison between the current results and those obtained with $\frac{\partial^2 T_E}{\partial x^2} = 0$ is shown in figure 3.9. Clearly the effects of longitudinal diffusion are only significant for small values of K and Pe.

3.8.2 Wall temperature distributions.

Figures 3.10 and 3.11 show the effect of Pe and K upon the wall temperature $\frac{T^*_W - T^*_\infty}{T^*_{MF} - T^*_\infty}$ assuming a 'top-hat' heat flux distribution.

Clearly the temperature field is not symmetrical about the centre of the film. The results for $K = 0$ clearly show the diffusion of heat upstream from the film. Increasing K from 0 to 45 dramatically alters the wall temperature distribution. Conversely, the wall temperature seems to be comparatively insensitive to changes in Pe (i.e. τ_w). This is in agreement with the measurements of Fage and Falkner (1931) and Pope (1971). Increasing K decreases the skewness but increases the flatness of the distribution. Similarly, it may be observed that increasing Pe increases the skewness but decreases the flatness of the distribution. Such trends seem to be intuitively correct.

3.8.3 Heat transfer to the fluid.

Applying the inverse theorem to equation (3.59) and factoring the results by $Nu.\sqrt{Pe}$, the heat transfer rate to the fluid may be computed. Figures 3.12 and 3.13 show the variation of $\frac{2a^*}{\Delta T^*_{MF}} \frac{q_F^*}{k_F^*}$ with Pe and K for the 'top-hat' heat flux over the film.

The results clearly show that as $K \to 0$ the 'top-hat' heating distribution is approached. The maximum rate seems to occur in the leading edge region of the film. A rather interesting result is that the heat flow seems always to be in the direction from the solid to the fluid. This, however, would appear to be contradictory to Pope's assertion (1971) that downstream of the film the hot fluid would heat the wall. He therefore suggested that the increase in the effective heating length of the film is solely due to substrate conduction occuring upstream of the film.

3.9 The effect of varying the heat flux distribution

In section 3.1.2 it was suggested that the consequence of electrical dissipation in the film would be the generation of a heating flux. Assuming the electrical power dissipated is $i^{*2}r^*$, (where i^* is the local electric current and r^* is the local electrical resistance) then the variation of $i^{*2}r^*$ across the film would give the heat flux distribution. If it is assumed that the current density is constant and the electrical resistance varies inversely proportional to the local film 'thickness', then $i^{*2}r^*$(or the heat flux distribution) will be directly proportional to the film thickness distribution. Hence, a 'top-hat' $q^*(x^*)$ corresponds to a film of constant thickness. The fact that the electrical resistance of the film material (usually an alloy of nickel or platinum) is temperature dependent suggests that the actual heat flux distribution cannot be known 'a priori'. However, the results show that for $K > 0$ the variation of temperature over the film is not very large and since the rate of change of resistance with temperature of the film alloy is usually small (0.035Ω/°C) then the heat flux-temperature dependence will be small.

To investigate the effect of varying the heat flux distribution upon the results, a cosine distribution was assumed.

i.e. $$q^*(x^*) = q^*_{max}\mathrm{Cos}\left(\frac{\pi x^*}{2a^*}\right)\,H\{a^* - |x^*|\} \qquad (3.62)$$

or in dimensionless form

$$q(x) = \frac{\pi}{2\sqrt{Pe}}\,\mathrm{Cos}\left(\frac{\pi x}{\sqrt{Pe}}\right)\,H\{\frac{\sqrt{Pe}}{2} - |x|\} \qquad (3.63)$$

Applying the Fourier transformation, equation (3.17), gives

$$\overline{q}(\alpha) = \frac{\mathrm{Cos}(\pi\alpha\sqrt{Pe})}{1 - 4\alpha^2 Pe} \qquad (3.64)$$

Hence substituting for $\overline{q}(\alpha)$ in equation (3.56) the wall temperature may be computed as previously outlined.

A comparison between the 'top-hat' and cosine heat flux solutions upon the Nu, $Pe^{1/3}$ relationship is shown in figure 3.14, where the effects of longitudinal diffusion are included in the solution. Clearly, the trends are very similar. Determining the best power law fit of the form

$$Nu = APe^{1/n} + B$$

to the results it was found that the values of n agreed with those obtained previously.

Note: If the effects of longitudinal diffusion are ignored and $K = 0$

then it may be shown that

$$Nu = 0.842Pe^{1/3} \tag{3.65}$$

i.e. the Nu $\sim$ $Pe^{1/3}$ law is recovered.

An investigation by Busing (1965) into platinum films baked on to glass, suggested that the thickness distribution of such films is parabolic. However, since the results between the 'top-hat' and cosine heat flux distributions are sufficiently similar it would seem that the general relationship

$$Nu = APe^{1/n} + B$$

where $n(>3)$ increases with K ought to apply for a wide range of film geometries.

3.10 Temperature profiles in the fluid.

If the effects of longitudinal diffusion are included, then from equation (3.53) the temperature profiles in the fluid may be computed if the Airy function $Ai(z)$, where

$$z = e^{-i\pi/6} (2\pi\alpha)^{1/3} (y + 2\pi\alpha e^{i\pi/2})$$

is known. Clearly as y increases the argument of z (in the complex sense) will vary from $\pi/3$(at $y = 0$) to $\sim -\pi/6$. The computation of $Ai\{z\}$ where the argument of z is varying may present difficulties. However, if the effects of longitudinal diffusion are ignored, then from equations (3.23) and (3.28)

$$\overline{T}(\alpha,y) = -\frac{\overline{q}(\alpha)Ai\{e^{-i\pi/6}\, y(2\pi\alpha)^{1/3}\}}{+\sqrt{4\pi^2\alpha^2}\,KC_1 + (2\pi\alpha)^{1/3}\, e^{-i\pi/6}\, C_2} \tag{3.66}$$

or

$$\overline{T}(\alpha,y) = \overline{T}_R(\alpha,y) + i\overline{T}(\alpha,y)$$

As shown previously, application of the Fourier inverse transformation gives

$$\overline{T}(x,y) = 2\int_0^{\infty} \overline{T}_R(r,y)\mathrm{Cos}2\pi rx + \overline{T}_I(r,y)\mathrm{Sin}2\pi rx \, dr$$

where r is real.

Thus the calculation of T(x,y) requires Ai{z}, where

$$z = y(2\pi r)^{1/3} e^{-i\pi/6}$$

Note: z now has constant argument $(-\pi/6)$ for all y.

Using the ascending series definition and the asymptotic expansion Ai(z) was computed. (See Appendix V) In order to check the complex arithmetic operations (in the imaginary sense!) used for evaluating the Airy function it is shown in Appendix V that Ai(z) $(\arg(z) = -\pi/6)$ may be expressed in terms of Kelvin functions with real arguments i.e.

$$\mathrm{Ai}(re^{-i\pi/6}) = \frac{1}{\pi}\sqrt{\frac{r}{3}}\, e^{-i\pi/4}\left\{\mathrm{ker}_{1/3}\left(\tfrac{2}{3}r^{3/2}\right) - i\,\mathrm{kei}_{1/3}'\left(\tfrac{2}{3}r^{3/2}\right)\right\} \tag{3.67}$$

Using the asymptotic expansions for the modulus and phase of the Kelvin functions the calculation of $\mathrm{Ai}\{re^{-i\pi/6}\}$ was checked for both the ascending series and asymptotic expansion of the Airy function.

Figure 3.15 shows the typical streamwise variation of the temperature profile $\frac{T^* - T^*_\infty}{T^*_{MF} - T^*_\infty}$ vs $\frac{y^*}{a^*}$ where a* is the semi-streamwise length of the film. These results indicate that the wall temperature is greater than the fluid temperature and thus the heat flow is from the wall to the fluid.

Figures 3.16 and 3.17 show the effect of Pe and K upon the wall temperature profile at the trailing edge of the film. Increasing K increases the thickness of the thermal boundary layer whilst increasing Pe has the opposite effect. Figure 3.18 shows the effect of K and Pe upon the thermal boundary layer thickness δ_T^* at the trailing edge of the film where δ_T^* is defined:

$$\frac{y^*}{a^*} = \frac{\delta_T^*}{a^*} \quad \text{when} \quad \frac{T^* - T^*_\infty}{T^*_{MF} - T^*_\infty} = 0.05 \tag{3.68}$$

The results suggest that δ_T^*/a^* is proportional to $\sqrt{K}$ and $\frac{1}{\sqrt{Pe}}$.

These results may be used to estimate under what conditions the current theory may be applicable in turbulent flow. The assumption of a uniform sheared flow is only realistic in the immediate vicinity of the wall for turbulent boundary layer flow. Clearly if K is large or Pe small then the thermal boundary layer may interact with a higher order velocity profile. From the definition of Pe

$$Pe = \frac{L^{*2} Pr \tau_W^*}{\rho^* \nu^{*2}}$$

$$\Rightarrow \quad \frac{u_\tau^*}{\nu^*} = \frac{\sqrt{Pe}}{L^* \sqrt{Pr}} \quad .$$

Let $$\delta_T^+ = \frac{\delta_T^* u_\tau^*}{\nu^*}$$

Thus $$\delta_T^+ = \frac{\delta_T^*}{L^*} \cdot \frac{\sqrt{Pe}}{\sqrt{Pr}}$$

<u>or</u> $$\delta_T^+ \sqrt{Pr} = \frac{\delta_T^*}{L^*} \cdot \sqrt{Pe}$$

A carpet plot of $\delta_T^+\sqrt{Pr}$ with K and Pe is shown in figure 3.19. The variation of δ_T^+ with Pe is small (assuming the effects of longitudinal diffusion are negligible) and for practical purposes may be ignored. The requirement for δ_T to remain within the viscous sub-layer may therefore be expressed as an upper limit of K. Hence, assuming the outer limit of the viscous sub-layer is given by $\frac{y^* u_\tau^*}{\nu^*} = 12$ then for $Pr = 0.71$ implies $\delta_T^+\sqrt{Pr} < 10$ which from figure 3.19 suggests K must be less than 30. For K > 30 the previous results may still be applicable as the interaction of the outer edge of the thermal layer with a higher order velocity profile may be reasonably expected to have little effect upon the heat transfer at the wall.

The requirement K < 30 does not necessarily imply the existence of a unique calibration in laminar and turbulent flows. Since the flow within the viscous sublayer is unsteady and three-dimensional, (see Smith and Metzler, 1983) the assumption of a single calibration for both laminar and turbulent flows, provided the thermal layer remains within the viscous sublayer, is unwarranted.

3.11 Conclusions

The effect of substrate conduction upon the heat loss from a surface film with a specified heat flux distribution has been examined theoretically. Using the linear, steady, two-dimensional heat conduction and forced convection equations it has been shown that for a uniform sheared flow the adiabatic $Nu \sim Pe$ relationship is altered. The results may be represented approximately by the relation

$$Nu = APe^{1/n} + B$$

where $n(>3)$ increases with the substrate-to-fluid thermal conductivity ratio. Therefore, the non-linearity of Nu with $Pe^{1/3}$ observed in many of the published hot film calibrations (see figure 1.2) appears to be primarily due to substrate conduction.

CHAPTER 4

Further consequences of substrate conduction

4.1 Introduction

This chapter considers further effects of substrate conduction upon the modified Nusselt number $\sim$ Péclet number relationship -

$$Nu = APe^{1/n} + B \tag{4.1}$$

as derived from the quasi-steady heat conduction/convection problem.

As noted in chapter 3 the heat conduction/convection problem is, in general, time dependent. In order to obtain a 'first-order' estimate of the dependence of Nu upon time, the variation of B (or more precisely the measured value of Nu when Pe = 0, Nu_0) with time is considered. This is justified on the grounds that the term $APe^{1/n}$ is normally smaller than B and B is approximately equal to Nu_0.

4.2 The one-dimensional heat conduction model

To examine the consequences of heat conduction within the substrate consider the one-dimensional heat conduction equation for a semi-infinite solid initially at a uniform temperature

$$\frac{\partial^2 T}{\partial x^2} - \frac{1}{\alpha}\frac{\partial T}{\partial t} = 0 \tag{4.2}$$

where $\alpha = \frac{k}{\rho C}$

Since the film is normally operated at a constant temperature it would seem reasonable to assume that the appropriate boundary condition for equation (4.2) is a constant temperature along the surface of the solid. This problem has the well known solution (see Carslaw and Jaeger, 1959)

$$\Delta T(x,t) = \Delta T_0\left(1 - \text{erf}\,\frac{x}{2\sqrt{\alpha t}}\right) \tag{4.3}$$

where erf signifies the error function, ΔT_0 is the temperature rise of the surface (x=0) and ΔT is the temperature increase from the initial temperature. The heat flux at any point is therefore

$$q(x,t) = \frac{\Delta T_0 k}{\sqrt{\pi \alpha t}} e^{-\left(\frac{x}{2\sqrt{\alpha t}}\right)^2} \tag{4.4}$$

In particular, the heat flux at the surface, x = 0, is

$$q(0,t) = \frac{\Delta T_0 k}{\sqrt{\pi \alpha t}} \quad . \tag{4.5}$$

For a probe with a substrate consisting of 2 or more layers of different materials the heat conduction process will be dependent upon the thermal properties of the various strata. (e.g. For the glue-on probe, see section 4.3, the solid heat conduction will be governed by the thermal properties of the foil onto which the heating film is deposited and also the properties of the wall onto which the probe is attached.) Appendix G outlines the solution to the one-dimensional heat conduction equation for a semi-infinite solid consisting of 2 layers. Assuming a constant temperature along the surface of the solid, the solution for the heat flux at the surface is

$$q(0,t) = \frac{\Delta T_0 k_1}{\sqrt{\pi \alpha_1 t}} \left(\frac{k_2 \rho_2 c_2}{k_1 \rho_1 c_1}\right)^{\frac{1}{2}} \quad . \tag{4.6}$$

where the subscript 1 refers to the layer of finite thickness.

Thus from equations (4.5) and (4.6) it is clear that

(i) q decays with time like $t^{-\frac{1}{2}}$

(ii) q is proportional to ΔT_0.

Therefore, the above analysis implies that B, or Nu_0, will be -

(i) time dependent, possibly decaying like $t^{-\frac{1}{2}}$

(ii) independent of ΔT, where ΔT is the mean temperature rise of the film.

4.3 Experimental investigation into the effects of substrate conduction for the glue-on probe

4.3.1 Probe details

There are basically two types of hot film probes commercially available - a glue-on probe or a flush mounting probe, see figure 4.1. The flush mounting type typically consists of a nickel film deposited on the end of a cylindrical quartz rod. The glue-on probe consists of a heating element, usually nickel, deposited on a plastic foil which is then glued directly onto the wall. In the subsequent experiments the glue-on probe was used because of its better thermally insulative substrate and lower cost relative to the quartz based flush mounting probe.

The glue-on probe, manufactured by DISA (Probe number 55R47), is sketched in detail in figure 4.1. The nickel heating film (0.9mm x 0.1mm x 0.001mm) is deposited on a kapton foil (8mm x 16mm x 0.05mm). A thin layer of silicon dioxide is deposited over the film to provide a protective coating. The film is connected to two nickel/silver plates onto which the copper wires (0.1mm diameter, 55mm long) are soldered. The kapton foil is glued directly onto the wall at the required measuring point.

Before a probe can be used, it is necessary to know the variation of the probe's electrical resistance with temperature. Initially this was determined by placing a probe in an oven and measuring the probe's resistance over a range of temperatures (15^oC to 50^oC). It was later found that a more accurate resistance-temperature calibration could be obtained by placing the probe in a container of water due to the improved temperature control of the fluid. A typical resistance-temperature calibration is shown in figure 4.2 indicating the adequacy of the linear relationship

$$R = R_0 + \frac{dR}{dT} . \Delta T \qquad (4.7)$$

where R_0 is the probe's resistance at a given datum temperature, ΔT is the change in temperature relative to the datum and dR/dT is a constant. dR/dT was typically found to be $\simeq 0.03\ \Omega/^oC$. The measured value of dR/dT for each probe tested agreed to within 5% of the manufacturer's figure.

4.3.2 Suspended probe

Two DISA glue-on probes (55R47) were taken and their resistance-temperature relationship determined as outlined in section 4.3.1. Both probes were suspended in a Torr-Plan pressure vessel in which the absolute pressure was reduced to less than 5mm of mercury. One probe was connected to a DISA constant temperature anemometer unit (type 55D01) whilst the second probe, used as a resistance thermometer, was connected to a Thurbly multimeter set in the resistance measuring mode. Setting the required resistance on the anemometer (and thus the mean film temperature), the anemometer output voltage (which may be related to the current flowing through the probe) was monitored for typically 60 minutes after switching the probe into the heating circuit. The experiment was repeated on successive days with the probe at different operating temperatures (resistances).

Figure 4.3 shows the variation of $V^2 \sim \frac{1}{\sqrt{t}}$ where V is the anemometer output voltage and t is seconds from switch on. The base $t = 0$ is uncertain as the probe requires a gradual build-up of electric current till the probe's resistance balances that demanded by the anemometer. (The warming up period is typically less than 10 seconds.) Clearly V^2 is time dependent and, to the first order, decays like $t^{-\frac{1}{2}}$. Figure 4.3 also shows the increase in V^2 due to conduction and natural convection to the surrounding air when the pressure in the vessel is at atmospheric pressure. The increment in V^2 appeared to be independent of probe attitude indicating that the effects of natural convection are small.

The corresponding variation of i^2R with ΔT is shown in figure 4.4. (On the scale of figure 4.4 the decay of i^2R with time is not observable.) The current flowing through the probe is related to the anemometer output voltage by the relation

$$i = \frac{V}{50 + R_L + R} \tag{4.8}$$

where R_L and R are the electrical resistances of the cables and the probe respectively. The variation of i^2R with ΔT is such that $\frac{i^2R}{\Delta T}$

is not constant. Over the range $\Delta T = 40$ to $120^{\circ}C$, $\frac{i^2R}{\Delta T}$ decreases approximately 8%. This contradicts conclusion (ii) in section 4.2. A plausible theoretical explanation to the observed nonlinear variation of i^2R with ΔT is given in section 4.4.

4.3.3 Effect of backing material

Two DISA glue-on probes were stuck[†] to the under surface of a tufnol plate which was mounted horizontally across the working section of a low speed wind tunnel. (For a description of the plate and wind tunnel see chapter 5, section 5.1.) The probes were placed approximately 0.2m laterally apart so as to ensure that the thermal field generated by the hot probe would not affect the cold probe which was used as a resistance thermometer. The time variation of the voltage supplied by the anemometer to maintain the hot probe at a constant temperature (resistance) was recorded (wind off). The experiment was repeated with the probe operating at various resistances (ΔT's). A period of at least 24 hours elapsed between each run (with both probes unheated) to allow the heat to dissipate out of the probe and plate. The variation of V^2 with $t^{-\frac{1}{2}}$ for each run (i.e. ΔT) is shown in figure 4.5.

The results clearly show that the electrical power supplied to the probe decays with time in a manner like $t^{-\frac{1}{2}}$. Comparing these results with those for the suspended probe (figure 4.3), it is clear that the effects of heat conduction within the tufnol plate are

(i) Approximately double the electrical power supplied to the probe for the same ΔT

(ii) Increase the $V^2 \sim t^{-\frac{1}{2}}$ gradient.

These trends are consistent with the theoretical solution, equation (4.6), as the thermal properties of tufnol are greater than those of kapton.

Using the results of figure 4.5 the variation of i^2R with ΔT at a constant time may be deduced. Figure 4.6 shows the predicted variation of i^2R with ΔT at two constant values of t. In actual

---

[†] Durafix glue was used as this is soluble in Acetone thus permitting the probe to be removed from the wall.

operation the variation of ΔT is not likely to be more than 20°C. Over such a range the relationship between i^2R and ΔT may be reasonably approximated by the expression (see figure 4.6)

$$i^2R = b_s\Delta T + b_I \tag{4.9}$$

where $b_I \neq 0$. Clearly $\frac{i^2R}{\Delta T}$ is not a constant. Fitting a straight line over the range $80 < \Delta T < 100^\circ C$ for each time level in figure 4.6 it appears that b_s, the slope, decreases with time although b_I, the intercept, remains constant. Thus from equation (4.9)

$$\frac{i^2R}{\Delta T} = b_s(t) + \frac{b_I}{\Delta T} \tag{4.10}$$

i.e. $$B = B_S(t) + {}^{B_I}/_{\Delta T}$$

4.4 Theoretical explanation for the non-linear variation of i^2R with ΔT

Appendix H presents a solution for the generation of heat in a wire conducting an electric current i. The solution is applied to the nickel film giving the results:

$$i^2R = 0.0538i \tan 65i \tag{4.11}$$

$$\Delta T = \frac{\tan 65i - 65i}{0.351i} \tag{4.12}$$

The theoretical variation of i^2R with ΔT is shown in figure 4.7. These results indicate the same trends as shown in figures 4.4 and 4.6. For example, fitting a straight line over the range $80 < \Delta T < 100^\circ C$, as shown in figure 4.7, clearly gives an intercept which is greater than zero so $\frac{i^2R}{\Delta T}$ is not a constant.

It is also demonstrated in appendix H that the heat conducted into the nickel/silver plates is small relative to that conducted into the substrate.

4.5 Further experiments

Using the 2 probes glued on to the tufnol plate the effect of air flow over the plate upon the power loss-time dependence was examined. A series of wind-on and wind-off experiments were carried out on consecutive days. Before heating the probe the wind tunnel was started and run at a constant speed (17m/s) for about 40 minutes.

This was to allow a condition of thermal equilibrium to be established. The cold probe, being used as a resistance-thermometer indicates a temperature which is related to the temperature of the air flow and also that of the tufnol plate. It was found that shortly after starting the tunnel this reference temperature changed by about 2^oC. For both cases (wind-on and wind-off), the variation of V with time was recorded for several runs with the period between each run varying from 10 minutes to 60 minutes. ΔT was maintained at a constant value throughout the experiments. The variation of Nu with time is shown in figure 4.8 where Nu is defined:

$$Nu = \frac{i^2 R}{wk\ \Delta T}$$

The results show that in both cases the rate at which Nu (i.e. i^2R) decreases is most rapid for the first run. Furthermore, the rate at which Nu decreases is greater with the flow off than in the flow on case. In both cases the first run is significantly above subsequent runs (even when the period between successive runs is greater than 60 minutes). The variation of Nu with time appears to be reasonably repeatable for the second and subsequent runs.

For the first run of the day it would seem reasonable to assume that the substrate of the nickel film is at a uniform temperature. Upon turning the probe on, clearly a large temperature difference will exist between the nickel film (very large thermal conductivity) and the substrate (kapton, which has a very low thermal conductivity). After turning the probe off, it is observed that the original resistance of the film is obtained after a brief period of time indicating that the film has returned to its original temperature. (The residual heat in the nickel film will be quickly removed by conduction into the relatively large nickel/silver plates and copper wires.) The heat conducted into the substrate however requires many hours to dissipate due to the small temperature gradients and low thermal conductivity of the substrate material. Upon reheating the probe, since the substrate has not returned to its original thermal equilibrium state, the heat conduction process will be different from the first occasion where the system was initially at a uniform temperature.

In order to increase the ratio of heat convected by the flow to that conducted into the substrate (and therefore increase the sensitivity of the probe) it is necessary to use substrates that are insulative. As shown in figure 4.6 and equations (4.5) and (4.6) this will also reduce the time dependence of the total heat transferred from the probe. However, because of the insulative properties of the substrate, the time taken to dissipate the heat when the probe is turned off will be very long. This may result in the probe's $Nu \sim Pe^{1/n}$ calibration being unrepeatable. (For calibrations to be repeatable it is necessary for the substrate at the start of each calibration to be at the same thermal equilibrium state.)

4.6 Conclusions

From the simple theoretical models and experiments it has been established that

(i) $\frac{i^2R}{\Delta T}$ is time dependent

(ii) $\frac{i^2R}{\Delta T}$ varies with ΔT.

Thus, in order to account for these effects, it is necessary to further modify the calibration relationship. Using equation (4.10) the following relationship is proposed

$$Nu = APe^{1/n} + \left[\frac{B_I}{\Delta T} + B_S(t)\right] \quad . \qquad (4.13)$$

CHAPTER 5

Flat plate laminar flow experiments

In order to provide further evidence for the theory proposed in chapters 3 and 4 a detailed experimental study of the calibration for the glue-on probe was conducted in laminar, flat plate, boundary layer flow.

5.1 Plate design and wind tunnel

The plate was manufactured from a tufnol sheet (Carp brand) 10mm thick. Tufnol was selected for its machinability and good thermal insulating properties. In order to minimise the likelihood of local flow separation at the leading edge of the plate an elliptical nose profile was selected. The higher the axis ratio of the elliptical nose the smaller is the resulting adverse pressure gradient. However, increasing the axis ratio increases the distance along the surface over which the pressure gradient is non zero. Using Davis' results (1980) an axis ratio of 5 was selected as this represented a reasonable compromise between the conflicting requirements of a small adverse pressure gradient and short region over which the pressure gradient acts.

Holes were drilled (0.5 mm diameter) along the longitudinal axis of the plate. Over the elliptical nose section 3 static pressure tappings were located at corresponding positions from the leading edge on both the upper and lower surfaces. A hinged flap was attached along the trailing edge of the plate. By careful adjustment of the flap angle, the static pressures over the upper and lower surfaces at the nose could be matched thus ensuring the locating of the stagnation line at the leading edge and zero pressure gradient along the main length of the plate. At 1m downstream from the leading edge an adjustable rectangular block (16mm x 8mm) was located. The block, also made from tufnol, could be traversed up and down relative to the surface of the plate. (Minimum stepping distance was 0.0025mm.) Details of the plate and block are shown in figure 5.1.

The plate was mounted horizontally along the centre line of a low turbulence, low speed, wind tunnel. The leading edge of the plate was positioned 0.16m downstream from the start of the tunnel's working section as experiments by Latiff (1981) indicated a slight pressure gradient existed downstream of the nozzle exit. Previous measurements in the wind tunnel indicated that the turbulence level of the free-stream was approximately

$$\sqrt{\frac{\overline{u'^2}}{U_\infty^2}} \sim 0.1\%$$

where $\overline{u'^2}$ is the mean squared fluctuating velocity component. The general arrangement of the wind tunnel is shown in figure 5.2.

The tunnel free-stream velocity was measured using an ellipsoidal head N.P.L. standard Pitot-static probe (see Salter et al, 1965). The static pressure in the tunnel was measured by a Betz manometer. A mercury in glass thermometer mounted inside the wind tunnel was used to determine the air temperature. Traversing probes (a hot wire or Pitot tube) could be mounted on the floor of the tunnel with access to the flow through sealable ports. The development of the boundary layer along the lower surface of the plate could be examined at 0.3m intervals.

5.2 Measurement of the laminar boundary layer properties

5.2.1 Hot-wire measured velocity profiles

Mean boundary layer velocity profiles were measured with a DISA 55D01 constant temperature anemometer and linearizer. The hot-wire was mounted in a DISA traversing mechanism under the floor of the wind tunnel. The minimum stepping distance of the traversing mechanism was 0.01mm over a range of 10mm. The wire was traversed from the free-stream towards the surface of the tufnol plate in steps of 0.1mm till the measured velocity ratio $^u/U_\infty \sim 0.4$. (This was to avoid damaging the hot wire by accidental contact with the plate.)

All the experimental results were recorded using the digital data acquisition system as sketched in figure 5.3. The gains on the D.C. voltage amplifier and linearizer were adjusted so that the full range of the 12 bit analogue-to-digital converter (A/D) could be used.

5.2.1.1 Data selection

Four mean values were read alternatively from the traversing probe (u) and the free-stream (U_∞) channels of the A/D. Each mean value was the average of typically 5 consecutive samples. Using the 4 mean pairs, the variation of the velocity ratio $^u/_{U_\infty}$ was examined. Determining the average velocity ratio, the r.m.s. error of the 4 $^u/_{U_\infty}$ values was computed and if this was greater than some limiting value (typically 0.0015) the readings were discarded and a new set taken. When suitable values were obtained the mean values of u and U_∞ along with the reading on the traversing mechanism were stored.

This technique was used in an attempt to filter out any spurious non-steady results such as the passage of a burst of turbulence across the hot wire in transitional flow. Although this method cannot be assumed to be a completely reliable technique for the measurement of laminar velocity profiles in transitional flows, the results at high Reynolds number did appear to be of full laminar quality. During the experiment, the time taken to obtain results by this method increased dramatically as the Reynolds number increased.

5.2.2 Analysis of the velocity profiles

Assuming two-dimensional flow, the velocity profiles may be compared with the theoretical solution for the laminar boundary layer equations with zero pressure gradient as given by Blasius, (see Schlichting, 1979). Blasius' solution may be written as

$$\frac{u}{U_\infty} = f'(\eta) \qquad (5.1)$$

where $\eta = y\sqrt{\frac{U_\infty}{\nu x}}$ and f satisfies the differential equation $2f''' + ff'' = 0$. Since the absolute value of y cannot be measured then let

$$y = y_m - y_0 \qquad (5.2)$$

where y_m is the reading on the traversing gear and y_0 is the value of y_m for which the measured velocity would be zero. Thus to compare the measured velocity profiles with the Blasius solution y_0 is required. There would appear to be 2 techniques for estimating y_0:

(i) Using Maclaurin's series, the velocity profile may be expressed as

$$\frac{u}{U_\infty}(\eta) = f'(o) + \eta f''(o) + \frac{\eta^2}{2} f'''(o) + \ldots$$

or

$$\frac{u}{U_\infty}(\eta) = 0.33206\eta - 0.0023\eta^4 + \ldots \qquad (5.3)$$

hence for $\eta < 1.0$, u is approximately proportional to y (error < 1%). Thus if the measured velocity data close to the wall are assumed to lie inside the region corresponding to $\eta < 1.0$ then by simple extrapolation to $u = 0$, y_0 may be found.

(ii) From the measured values of $^u/_{U_\infty}$ the corresponding values of η may be deduced. If the flow has Blasius profile, then a plot of $y_m \sim \eta$ will be a straight line, the intercept ($\eta = 0$) of which equals y_0. i.e.

$$\eta = (y_m - y_0)\sqrt{\frac{U_\infty}{\nu x}}$$

$$\Rightarrow \qquad y_m = \eta\sqrt{\frac{\nu x}{U_\infty}} + y_0 \qquad (5.4)$$

The first method is generally unreliable as the extrapolation to $u = 0$ is based on a few points. Furthermore, since the points used must be close to the wall, they most probably will contain errors due to wall proximity effects on the measuring probe. The second technique however does not suffer from these drawbacks and therefore is believed to be more accurate.

Using the tabulated Blasius solution appearing in Schlichting (1979) (η vs $^u/_{U_\infty}$: η in steps of 0.2) the value of η was determined from the measured $^u/_{U_\infty}$ by application of the three-point Lagrange interpolation formula†. A typical plot of $y_m \sim \eta$ at various Reynolds

---

† The three-point formula effectively fits a quadratic equation, $\eta = a + b\, u/U_\infty + c(u/U_\infty)^2$, through three neighbouring points. The results were checked graphically.

numbers is shown in figure 5.4. These results clearly show that over the main body of the profile y_m varies linearly with η indicating the general agreement with Blasius' solution. (Near the outer edge of the boundary layer, η varies rapidly with $^u/_{U_\infty}$, hence any small error in the measurement of $^u/_{U_\infty}$ will lead to a greatly magnified error in η. Also, near the wall the measurement of $^u/_{U_\infty}$ is unreliable and therefore η may be in error.) Ignoring the points at the inner and outer extremities of the profile, the best straight line (in the least square error sense) was fitted to the y_m,η results typically over the range $1.3 < \eta < 3.8$. (i.e. $0.4 < {}^u/_{U_\infty} < 0.9$). The intercept ($\eta = 0$) therefore gave y_0 - see equation (5.4).

From equation (5.4) the slope of the line ought to be $\sqrt{\frac{\nu x}{U_\infty}}$. Knowing ν and U_∞ it is therefore possible to calculate x. The results suggest that the calculated value of x is greater than the measured length from the leading edge, x_m. Defining $x = x_m + \Delta x$, figure 5.5 shows the variation of Δx with unit Reynolds number as calculated from the velocity profiles measured over a range of x_m. The fact that the computed Blasius value of x is greater than the measured length is not surprising as the flat plate boundary layer solution is not applicable near the leading edge of the plate due to the low Reynolds number and pressure gradient[†]. However, the experimental results show that downstream of the nose section the boundary layer relaxes to Blasius flow.

5.2.3 Traversing Pitot tube measurements

As an independent check upon the hot wire profile measurements, the experiment was repeated using a traversing Pitot tube. The Pitot tube was made from circular steel tubing 1.07mm diameter. The mouth of the tube was flattened to form, approximately, a rectangular opening,

---

[†] Using a laminar boundary layer computer programme, based on Beasley's work (1973), the flow over the plate was predicted. The results confirmed that as the pressure gradient tends to zero downstream of the nose region the boundary layer relaxes to Blasius' flow with a virtual origin ahead of the leading edge of the plate.

0.7mm high by 1.3mm wide. The profiles were analysed using the same technique as that used for the hot wire profiles. No corrections were applied to the Pitot tube readings and thus the reliability of the velocity data near the wall must be suspect[†]. Figure 5.6 shows typical plots of $y_m \sim \eta$. These results show that in the near wall region the deduced value of η appears to be less than expected, i.e. u is under-read. The variation of Δx as calculated from the Pitot tube profile measurements is shown in figure 5.7. Using the results in figures 5.5 and 5.7 the mean value of Δx is approximately 0.06m.

5.3 Calculation of the integral properties of the boundary layer

It may be shown that a significant contribution to the displacement thickness, δ^*, is due to the flow near the wall. Hence any error in the measurement of $^u/U_\infty$ close to the wall may lead to a significant error in δ^*. For example, the contribution to δ^* from the wall out to $^u/U_\infty \simeq 0.4$ is about 56% and the contribution to θ is approximately 27%. Appendix I outlines the procedure used to calculate the values of θ and δ^* from the measured profiles. (Initial attempts using simple trapezoidal integration from the wall to the outer edge of the boundary layer gave values of H significantly greater than the Blasius value of 2.59.)

Figure 5.8 shows the variation of H with Rx_m. Over the measured Reynolds number range 0.3×10^6 to 1.7×10^6, H remains sensibly constant and agrees very closely with the Blasius value of 2.59. The variation of R_θ $(= \frac{U_\infty \theta}{\nu})$ with Rx_B where

$$Rx_B = \frac{U_\infty}{\nu}(x_m + 0.06) \qquad (5.5)$$

is shown in figure 5.9, x_m being the measured distance from the leading edge. The agreement with the Blasius solution

$$R_\theta = 0.6641\, R_{x_B}^{0.5} \qquad (5.6)$$

is very good.

[†] MacMillan (1957) suggests 3 corrections for Pitot tubes in wall proximity - a displacement effect (the effective centre of the tube does not correspond to the geometric centre), a viscous correction and a velocity correction.

5.4 Prediction of skin friction

The detailed experimental study has indicated that the flow is accurately described by Blasius' solution provided x is defined as

$$x = x_m + 0.06 \text{ m}$$

Therefore, it is concluded that the skin friction may be estimated using the modified Blasius formula

$$\tau_w = 0.3321\mu\, U_\infty \sqrt{\frac{U_\infty}{\nu(x_m + 0.06)}} \qquad (5.7)$$

or

$$C_f = 0.6641\; Rx_B^{-0.5} \qquad (5.8)$$

An estimation of the accuracy with which τ_w may be predicted using equation (5.7) can be obtained from the plots of Δx vs ${}^{U_\infty}/_{\nu}$. The observed uncertainty in Δx leads to an uncertainty in τ_w. The scatter of Δx is such that the error in τ_w is probably less than 4%.

5.5 Hot Film Experiments - Laminar Flow

5.5.1 Experimental procedure

The DISA glue-on probe was operated in the constant temperature mode using a DISA 55D01 anemometer. The mean temperature of the hot probe may be related to the selected operating resistance of the probe. As pointed out by Poll and Watson (1984), a small change in ΔT if not correctly accounted for, may lead to large errors in the prediction of skin friction (see section 1.3). Defining ΔT as:

$$\Delta T = T_{hot} - T_{cold}$$

$$= \frac{(R_{hot} - R_{cold})}{{}^{dR}/_{dT}} \qquad (5.9)$$

implies that the measurement of ΔT requires measurement of $(R_{hot} - R_{cold})$ assuming $\frac{dR}{dT}$ is known. Since the anemometer bridge holds R_{hot} constant, any change in ΔT may be considered as a change in R_{cold} which is dependent on both the fluid temperature and the substrate temperature. In all of the following experiments, R_{cold} was estimated by monitoring the resistance of a second probe glued onto the surface of the plate. This method for calculating ΔT ought to be more accurate than methods based upon changes in the fluid temperature alone (or substrate temperature).

To maximise the resolution of the data acquisition system the anemometer output voltage, which is related to the current flowing through the probe, was off-set by approximately the no-flow reading using a high precision constant voltage supply. The remaining voltage was then amplified (x 40) and the resulting voltage read by the computer via the analogue-to-digital converter.

In order to minimise the time dependence of the heat loss, the probe was switched on at least 30 minutes prior to any run.

5.5.2 Effect of surface misalignment

Since the glue-on probe is simply stuck to the plate surface the exposed surface of the probe will not be flush with the wall. To examine what effect this surface misalignment has upon the convective heat transfer, a probe was glued onto the rectangular block located at $x_m = 1.0m$. The rectangular block, which has the same surface dimensions as the probe, was traversed up and down relative to the surface of the plate over a range of free-stream velocities. Figure 5.10 shows the variation of Nu with step height where Nu is defined

$$Nu = \frac{i^2 R}{k_F . \Delta T . w} \qquad (5.10)$$

where

$$i = \frac{V}{50 + R_L + R} \qquad (5.11)$$

and w is the spanwise width of the heating film.

In an attempt to normalise the results the following series of experiments were conducted:

First, a calibration of Nu $\sim$ Pe (i.e. τ_w) was performed with the probe flush. (For the kapton substrate in air K $\approx$ 7 so from chapter 3,

$n \approx 4$). Then, at a series of constant speeds, the probe was traversed and the variation of Nu with h recorded. At periodic intervals the calibration was repeated with the probe set flush with the wall.

Figure 5.11 shows the calibrations obtained with the probe flush with the wall. Clearly significant shifts have occurred between some of the calibrations although the slope, A, seems to be reasonably repeatable. (The anemometer output was observed on an oscilloscope to ensure that laminar flow was maintained at the higher speeds.) The shifts in the calibration appear to be a 'time effect' as the changes in ΔT between the runs were very small (see chapter 4).

It would seem reasonable to assume that the change in Nu caused by traversing the probe is due to a change in the heat convected into the flow. The effect of using the flush calibration when the probe is not flush with the wall may be estimated in the following manner.

Assume the flush calibration is

$$\mathrm{Nu}_F = A\,\mathrm{Pe}_W^{\frac{1}{4}} + B \tag{5.12}$$

and when the probe is not flush

$$\mathrm{Nu}_M = A\,\mathrm{Pe}_M^{\frac{1}{4}} + B$$

Hence $$\mathrm{Nu}_M - \mathrm{Nu}_F = A(\mathrm{Pe}_M^{\frac{1}{4}} - \mathrm{Pe}_W^{\frac{1}{4}})$$

Therefore $$\mathrm{Pe}_M = \left(\frac{\mathrm{Nu}_M - \mathrm{Nu}_F}{A} + \mathrm{Pe}_W^{\frac{1}{4}}\right)^4 \tag{5.13}$$

From the traversing experiments Nu_F, $\mathrm{Pe}_W^{\frac{1}{4}}$ are known (i.e. conditions at $h = 0$) and A is obtained from figure 5.11. Thus ${}^{\mathrm{PeM}}/_{\mathrm{Pe}_W}\left(= {}^{\tau M}/_{\tau_W}\right)$ may be calculated. Figure 5.12 shows the variation of ${}^{\tau M}/_{\tau_W}$ with h^+ where $h^+ = \frac{hu_\tau}{\nu}$, $u_\tau = \sqrt{\frac{\tau_W}{\rho}}$, for a range of u_τ. A reasonable collapse of the results has been obtained with the mean trends given by

$$0 < h^+ < 15 \qquad \frac{\tau M}{\tau_W} = 1 + 0.075\,h^+ \tag{5.14}$$

$$-8 < h^+ < 0 \qquad \frac{\tau M}{\tau_W} = 1 + 0.085\,h^+ \tag{5.15}$$

In view of the sensitivity of the laminar calibration upon surface misalignment the suggestion that the calibration of a probe determined in one apparatus may be used to measure τ_W in another seems ill-founded.

5.5.3 Calibrations

The calibrations shown in figure 5.11 were obtained at $x_m = 1.0$m with a maximum wall shear stress $\simeq 0.08$ N/m^2. (The Reynolds number at the start of transition was about 10^6.) In order to examine the Nu $\sim$ Pe calibration in more detail over a larger Pe(τ_W) range, a probe was glued onto the plate at $x_m = 0.243$m. A typical calibration is shown in figure 5.13 plotted as Nu $\sim \tau_W^{1/3}$, where the film is not flush with the surface. Except at very low speeds[†], Nu initially appears to be proportional to $\tau_W^{1/3}$. From the theoretical study of chapter 3, one would have expected these results to have been 'bowed', however it would appear that the rate of increase of Nu does not 'roll off' with increasing $\tau_W^{1/3}$.

Equation (5.14) indicates that as h^+ (i.e. τ_W) increases then Nu will be increasingly over estimated. Thus the fact that the probe is glued onto the wall (i.e. not flush mounted) will tend to mask any roll off in Nu. Using equation (5.14), the results in figure 5.13 may be corrected to estimate the calibration for the probe flush with the wall. For the probe glued onto the plate the step height was estimated to be about 0.09mm. Over the range $0.4 \lesssim \tau_W^{1/3} \lesssim 0.9$ the calibration shown in figure 5.13 may be approximated by

$$\mathrm{Nu} = 3.12\tau_W^{1/3} + 15.50 \qquad (5.16)$$

With h = 0.09mm, then for the conditions of the experiment, equation (5.14) becomes

$$\frac{\tau_M}{\tau_W} = 1 + 0.4\sqrt{\tau_W} \qquad (5.17)$$

For a given τ_W, Nu and τ_M may be computed which then may be used to

---

[†] see section 5.5.4.

predict the form of the calibration with the probe flush. The computed variation of Nu with τ_M is also shown in figure 5.13. Performing a least square error analysis on the deduced data the best power law fit was found to be

$$Nu = 3.0307\ \tau_M^{1/3.6} + 15.2958 \qquad rms \approx 0.0007 \qquad (5.18)$$

Fitting the best $1/3$ power law gave

$$Nu = 2.6913\ \tau_M^{1/3} + 15.6505 \qquad rms \approx 0.011 \qquad (5.19)$$

Note the large reduction in the rms error using $\tau_M^{1/3.6}$ as opposed to $\tau_M^{1/3}$.

5.5.4 Note on the form of the calibration at very low τ_W

In all the calibrations obtained for the glue-on probe the measured value of Nu at $\tau_W = 0$ was greater than the intercept (B) of the calibration curve. Therefore, a single calibration relationship of the general form

$$Nu = A\ Pe^{1/n} + B \qquad (5.20)$$

will not be adequate for relating Nu to τ_W for all τ_W. From figure 5.13 the lower limit for which the calibration equation (5.18) applies is approximately $\tau_W \approx 0.06$ N/m^2.

To determine the form of the calibration for $\tau_W < 0.06$ N/m^2 a second series of experiments were performed using the probe glued onto the rectangular block at $x_m = 1.0$. Setting the probe flush with the wall several calibrations were performed. Fitting a curve of the general form, equation (5.20), to the results, suggested that the most appropriate value of n was approximately 2. A typical calibration is shown in figure 5.14. Within the scatter of the results the value of B now agrees with the measured no-flow value of Nu.

CHAPTER 6

Flat Plate turbulent flow experiments

6.1 Introduction

From mean velocity profile measurements, there are basically 2 independent techniques that may be used to estimate C_f. The first method, based on the momentum integral equation, requires complete mean velocity profiles to be measured over a range of Reynolds number. The second technique is based upon the observation that the velocity profile adjacent to the wall (see figure 6.1) may be expressed as

$$\frac{u}{u_\tau} = f\left(\frac{yu_\tau}{\nu}\right)$$

or $$u^+ = f(y^+) \qquad (6.1)$$

where f is very similar for a wide range of flows with modest pressure gradients. For example, within the viscous sublayer equation (6.1) takes the form

$$\text{for } y^+ \lesssim 8 \;:\; u^+ = y^+ \qquad (6.2)$$

whilst further out from the wall but still in close proximity to it

$$\text{for } y^+ \gtrsim 30,\; y \lesssim 0.2\delta \;:\; u^+ = \frac{1}{\kappa}\ln y^+ + C \qquad (6.3)$$

where κ and C appear to be universal constants.
Between these regions a buffer zone exists.
Clearly, if the functional form of f is known, then u_τ may be estimated given u and y.

Of the several methods, based on equation (6.1), that have been developed for estimating skin friction in turbulent flow, the following techniques are applied in the subsequent experiments.

(i) Preston tube - a one point measurement applicable within the viscous sub-layer, buffer zone or semi-logarithmic layer.

(ii) The Clauser chart - a multi-point technique based on equation (6.3).

(iii) Bradshaw's method - essentially based on one point within the semi-logarithmic layer.

6.2 Experimental set-up

The flat plate model described in Chapter 5 was used for the turbulent boundary layer experiments. To ensure fully turbulent flow, a wire of diameter 0.5mm was taped to the lower surface of the plate about 30mm downstream from the leading edge. The location of the wire was selected so as to be in a region of adverse pressure gradient. Gibbings (1959) has reviewed various criteria for determining the minimum wire diameter to ensure that transition occurs at the wire and suggests that for low turbulence, incompressible flow over a flat plate, transition occurs at the wire when

$$\frac{U_\infty k}{\nu} \geqslant 826$$

This criterion therefore implies that for the trip wire used ($k = 0.5$mm) transition would only occur at the wire when $U_\infty > 25$ m/s. However, in practice the coupled effects of adverse pressure gradient and the trip wire seemed to be adequate in fixing transition as the integral properties of the boundary layer displayed fully turbulent characteristics.

The data acquisition system as described previously was again used in all the following experiments. Each point recorded was the mean of 40 samples.

6.3 Preston tube results

Possibly one of the most convenient means of estimating the local skin friction in two-dimensional turbulent boundary layer flow is by the use of Preston tubes. Two circular steel tubes of outside diameters d = 1.47mm and 0.89mm were fixed to the plate surface at the point of measurement. Care was taken to ensure that the open mouth of each tube was in contact with the wall and that the axes of the tubes were aligned with the sides of the wind tunnel. The tubes were placed 30mm apart, slightly offset from the centre line of the plate. (In regions close to the centre line of the plate the spanwise variation of τ_w across the plate was found to be negligible.) The static pressure was taken from the mean of two neighbouring upstream wall pressure tappings.

6.3.1 Choice of calibration

The use of Preston tubes to estimate skin friction is based upon the assumption of universality of the velocity profile in the near wall region of a turbulent boundary layer. McAllister, Pierce and Tennant (1982) have reviewed various calibrations for relating τ_w to d and Δp, where Δp is the total pressure read by the Preston tube less the wall static pressure. Using a floating element balance in a two-dimensional turbulent boundary layer along with a range of Preston tubes ($0.46 \leqslant d \leqslant 2.11$mm) they concluded that Patel's calibration seemed to give best agreement between the predicted wall shear and that measured directly. Patel's original calibration (1965) consisted of 3 algebraic expressions in terms of the parameters

$$y^* = \log_{10}\left(\frac{\tau_w d^2}{4\rho\nu^2}\right), \quad x^* = \log_{10}\left(\frac{\Delta p d^2}{4\rho\nu^2}\right) \qquad (6.4)$$

These expressions are

For $x^* < 2.9$ $\qquad y^* = 0.5x^* + 0.037$ (6.5)

For $2.9 \leqslant x^* < 5.6$ $\qquad y^* = 0.8287 - 0.1381x^* + 0.1437x^{*2} - 0.006x^{*3}$ (6.6)

For $5.6 \leqslant x^* < 7.6$ $\qquad x^* = y^* + 2\log_{10}(1.95y^* + 4.10)$ (6.7)

Head and Vasanta Ram (1971) found that Patel's expressions gave values of y^* that did not match at the points where a change over is made from one equation to another. They found that the discontinuity at the higher change over point gave an error in τ_w of approximately 3%. Fitting a smooth curve through the change over regions, they presented a tabulated form of Patel's calibration equations. Poll (1983a) derived polynomials in terms of x^* that effectively bridged Patel's change over points. He proposed the following algebraic expressions

For $x^* \leqslant 2.86 \quad y^* = 0.5x^* + 0.037$ (6.8)

For $2.86 < x^* \leqslant 2.9165 \quad y^* = 0.57387x^* - 0.1743$ (6.9)

For $2.9165 < x^* \leqslant 5.00 \quad y^* = 0.8287 - 0.1381x^* + 0.1437x^{*2} - 0.006x^{*3}$ (6.10)

For $5.00 < x^* \leqslant 6.00 \quad y^* = -534.7713 + 495.5094x^* - 182.8383x^{*2} + 33.6758x^{*3} - 3.0908x^{*4} + 0.1131x^{*5}$ (6.11)

For $6.00 < x^* < 7.95 \quad x^* = y^* + 2\log_{10}(1.95y^* + 4.10)$ (6.12)

For d = 0.89mm it was found that x^* varied between 3.2 to 5.6, whilst for d = 1.47mm; $4.1 < x^* < 6.1$ thus indicating the use of the smoothing polynomial (equation (6.11)) for both tube sizes.

Skin friction measurements were made at four different locations x_m = 0.178, 0.397, 0.702 and 1.007m. The results for both Preston tubes are shown in figure 6.2. There would appear to be a slight difference (about 3%) between the τ_w predictions for the 2 tubes at the higher Reynolds number range. However, this is within the overall accuracy of the method.

6.3.2 Use of a universal velocity profile (surface Pitot tube)

An equivalent method for estimating τ_w from the Preston tube results is to convert (Δp,d) to (u,y). If a universal velocity profile is assumed, than τ_w may be deduced from (u,y).

Since circular Pitot tubes are used, various corrections may be applied in converting (Δp,d) to (u,y). MacMillan (1957) has examined the effects of wall proximity, viscosity and sheared flow across the mouth of a circular Pitot tube. Poll (1983,b) suggests that for a Pitot tube in contact with the wall MacMillan's corrections may be summarised -

$$u = u_m\left\{1.015 - \frac{85}{\left(\frac{u_m d}{\nu}\right)^2}\right\} \qquad (6.13)$$

at an effective height y = 0.65d, where u_m is the measured velocity.

Adopting these corrections, the surface Pitot tube (Preston tube) results were analysed to give (u,y).

Of the various laws of the wall that describe the flow from the wall to the outer edge of the semi-logarithmic region (equation 6.3), one of the most recent formulations is that due to Pfeil and Sticksel (1981) (see appendix J):

$$u^+ = \frac{1}{\kappa} \ln(1 + a_1 y^+) + C_1\left[1 - e^{-a_2 y^+}(1 + a_3 y^+)\right] \qquad (6.14)$$

where the 'constants' a_1, a_2, a_3 and C_1 are related to κ and C for flat plate flow.

By definition

$$\frac{u}{U_\infty} = \frac{u^+ y^+}{\frac{yU_\infty}{\nu}} \qquad (6.15)$$

Hence, combining equations (6.14) and (6.15)

$$\frac{y^+}{\kappa} \ln(1 + a_1 y^+) + C_1 y^+\left[1 - e^{-a_2 y^+}(1 + a_3 y^+)\right] = \frac{u}{U_\infty} \cdot \frac{yU_\infty}{\nu} \qquad (6.16)$$

This implicit equation was solved for y^+ given ($^u/_{U_\infty}$, $^{yU_\infty}/_\nu$) using the Newton-Raphson method, Knowing y^+, C_f follows:

$$C_f = 2\left\{\frac{y^+}{\frac{yU_\infty}{\nu}}\right\}^2 \qquad (6.17)$$

and hence τ_w. Assuming $\kappa = 0.41$ and $C = 5.0$ (thus fixing a_1, a_2, a_3, C_1 - appendix J) the values of τ_w were computed. These results are compared with those derived using Poll's modification to Patel's calibration equations for both Preston tubes on figures 6.3 and 6.4. The results clearly show a consistent discrepancy between the values of τ_w estimated using the two techniques. The values of τ_w deduced using Patel's calibration are typically 3 - 4% less than those obtained directly by assuming Pfeil and Sticksel's universal law of the wall with $\kappa = 0.41$ and $C = 5.0$.

Patel showed that the calibration equation (6.7) could be used to derive the value of the constants κ and C appearing in the logarithmic law of the wall. Using MacMillan's correction for the displacement of the effective centre of the Pitot tube from its geometric centre, he obtained the values $\kappa = 0.42$, $C = 5.45$.

However, as shown by Poll, Mathews and Stewart (1985,b) if both MacMillan's velocity and displacement corrections are assumed then equation (6.7) implies $\kappa = 0.41$, $C = 5.25$. Using these values, the constants appearing in Pfiel and Sticksel's law of the wall were estimated as outlined in Appendix J. Equation (6.16) was then re-solved for the Preston tube readings (u,y). The comparison between Patel's predicted τ_w and that deduced using Pfeil and Sticksel's law of the wall based on $\kappa = 0.41$ and $C = 5.25$ is shown in figures 6.5 and 6.6. The agreement in the predicted τ_w between the two methods is considerably improved.

6.4 Mean velocity profile measurements

Using the flattened Pitot tube, mean velocity profiles were measured over a range of Reynolds number. The Pitot tube was initially placed firmly against the plate surface and slowly retracted from the wall. The point at which the Pitot tube was just touching the wall (y_{wall}) was estimated from the response of the Pitot tube. No corrections were applied to the deduced velocity from the traversing Pitot. It was assumed that the effective centre of the Pitot tube coincided with the tube's geometric centre.

6.4.1 Calculation of the boundary layer integral properties.

The combined effects of viscosity and wall proximity may be expected to distort the flow around the Pitot tube and therefore cause errors in the measured velocity profile near the wall. This in turn will introduce errors in the estimation of θ and δ^*. In order to overcome this difficulty, the computation of θ and δ^* was completed as outlined in Appendix K.

The shape parameter, H, seems to be the most suitable quantitative criterion for characterising the boundary layer. The variation of H with R_θ is shown in figure 6.7. For comparison the results of Purtell, Klebanoff and Buckley (1981) are shown. These results suggest that H is solely dependent upon R_θ. The agreement between the current results and those from Purtel et al is particularly good, thus implying the effectiveness of the tripping wire at low Reynolds number.

6.4.2 Mean velocity profiles

Figure 6.8 shows typical mean velocity profiles in terms of $^{u}/_{U_\infty} \sim {^{y}/_{\delta^*}}$ over the full range of Reynolds number for the experiment. The variation of $^{u}/_{U_\infty} \sim {^{y}/_{\delta^*}}$ appears to be reasonably independent of Reynolds number, except at the lower extreme ($R_x = 0.34 \times 10^6$) where the wake region of the profile appears to be slightly underdeveloped.

6.4.3 Application of the momentum integral equation

The incompressible, zero pressure gradient form of the momentum integral equation may be written as

$$\frac{C_f}{2} = \frac{d\theta}{dx} \tag{6.18}$$

or

$$\frac{C_f}{2} = \frac{dR_\theta}{dR_x} \tag{6.19}$$

Thus if the $R_\theta \sim R_x$ relationship is known, then C_f may be estimated. It was decided that the most reliable way to differentiate the experimental results was to determine the best power law relationship between R_θ and R_{x_m} (where R_{x_m} is the Reynolds number based on the measured length from the leading edge, x_m). Assuming the general form

$$R_\theta = c(R_{x_m} + R_o)^n \;\dagger \tag{6.20}$$

the best values of c, n and R_o were determined using a least square error criterion for the R_θ, R_{x_m} values. The best fitting curve of the form (6.20) was found to be

---

† The concept of a virtual origin, independent of Reynolds number, would imply that a more suitable power law relationship between R_θ and R_{x_m} ought to be

$$R_\theta = c\left(\frac{U_\infty}{\nu}\right)^n (x_m + \Delta x)^n$$

$$\approx c\, R_{x_m}^n \left(1 + n\frac{\Delta x}{x_m}\right) \qquad \text{assuming } \frac{\Delta x}{x} \ll 1.$$

However, since transition is Reynolds number dependent it does not seem reasonable to assume Δx is constant.

$$R_\theta = 0.02689(R_{x_m} + 74100)^{0.81694} \qquad (6.21)$$

Hence using equation (6.14)

$$C_f = 0.04394(R_{x_m} + 74100)^{-0.18306} \qquad (6.22)$$

or $$C_f = 0.01954\ R_\theta^{-0.22408} \qquad (6.23)$$

Figure 6.9 shows the variation of R_θ with R_{x_m} along with equation (6.21).

Putting $R_0 = 0$ the best power fit was found to be

$$R_\theta = 0.06859 R_x^{0.75388} \qquad (6.24)$$

Hence by differentiation

$$C_f = 0.10342\ R_x^{-0.246} \qquad (6.25)$$

or $$C_f = 0.04314\ R_\theta^{-0.3263} \qquad (6.26)$$

Equations (6.23) and (6.26) are shown in figure 6.10. These results are compared with the following

(i) Schlichting (1979) $C_f = 0.0256\ R_\theta^{-0.24}$ (6.27)

(ii) Ludweig-Tillman law(1949) $C_f = 0.246\ 10^{-0.678H}\ R_\theta^{-0.268}$ (6.28)
where $H \sim R_\theta$ is determined from figure 6.7.

(iii) Squire and Young (1938) $C_f = 2\left[5.89 \log_{10}(4.075R_\theta)\right]^{-2}$ (6.29)

(iv) Data from Purtell, Klebanoff and Buckly (1981)

(v) Karmon-Schoenherr (see Bertram, 1961)

$$C_f = \frac{0.0586}{[\log_{10}(2R_\theta)]^2 + 0.8686 \log_{10}(2R_\theta)} \qquad (6.30)$$

Equation (6.23) gives the best overall comparison with the above formulations. It is noted that the Ludweig-Tillman law and Schlichting's formula appear to deviate from equation (6.23) at low R_θ.

6.5 Velocity profiles near the wall

In order to obtain more detailed velocity profiles, the gear ratio of the traversing mechanism was adjusted to give a minimum stepping displacement of 0.01mm over a maximum traversing length of 10mm. At this setting, complete velocity profile traverses could not be performed as δ was typically greater than 10mm. Using the flattened Pitot tube, the probe was traversed in steps of 0.1mm away from the wall. (The tube was initially set in firm contact with the wall.) No corrections were applied to the measured velocity distribution.

6.5.1 Estimation of C_f based on Clauser's method

Clauser (1954) suggested a simple graphical technique whereby a measured velocity profile could be used to estimate C_f.

The semi-logarithmic law of the wall is written as

$$\frac{u}{u_\tau} = \frac{1}{\kappa} \ln \frac{yu_\tau}{\nu} + C \tag{6.31}$$

for some range of $\frac{yu_\tau}{\nu}$

Replacing u_τ by $\frac{u_\tau}{U_\infty} \cdot U_\infty$

$$\frac{u}{U_\infty} \cdot \frac{U_\infty}{u_\tau} = \frac{1}{\kappa} \ln\left\{\frac{yU_\infty}{\nu} \cdot \frac{u_\tau}{U_\infty}\right\} + C \tag{6.32}$$

$$\Rightarrow \quad \frac{u}{U_\infty} = \frac{u_\tau}{U_\infty}\frac{1}{\kappa} \ln \frac{yU_\infty}{\nu} + \frac{u_\tau}{U_\infty}\left\{C + \frac{1}{\kappa} \ln \frac{u_\tau}{U_\infty}\right\} \tag{6.33}$$

$$\text{i.e.} \quad \frac{u}{U_\infty} = A' \ln \frac{yU_\infty}{\nu} + C' \tag{6.34}$$

Thus if equation (6.31) holds, then a plot of $\frac{u}{U_\infty}$ vs $\ln(\frac{yU_\infty}{\nu})$ ought to have a straight line segment, the slope of which is:

$$\text{slope} = \frac{u_\tau}{U_\infty}\frac{1}{\kappa} = \sqrt{\frac{C_f}{2}}\frac{1}{\kappa} \tag{6.35}$$

and

$$\text{intercept} = \frac{u_\tau}{U_\infty}\left\{C + \frac{1}{\kappa} \ln \frac{u_\tau}{U_\infty}\right\} = \sqrt{\frac{C_f}{2}}\left\{C + \frac{1}{2\kappa} \ln(\frac{C_f}{2})\right\} \tag{6.36}$$

For a specified range of points that conform to equation (6.31), there would appear to be 2 methods by which the above analysis may be applied:

(i) specify both κ and C and hence determine C_f using equation (6.35). (Clauser's original method)

(ii) specify κ and from the slope of the straight line determine C_f.

Clauser's originally proposed method requires plotting the profile $\frac{u}{U_\infty}$ vs $\ln\frac{yU_\infty}{\nu}$ on a chart based on equation (6.33) with lines of constant C_f drawn. In the current work, it was felt that the accuracy of this graphical technique could be improved upon by a numerical analysis of the results. Appendix L outlines the numerical technique used to find the best value of C_f for a specified κ and C from a set of data points selected from the profile.

Application of (ii) is based upon the best fitting straight line through selected data points $^u/_{U_\infty}$, $\ln\frac{yU_\infty}{\nu}$. This approach has the advantage that the value of C need not be specified to determine C_f. (Using the intercept, C may be calculated for a given κ and C_f.)

For both methods, the deduced value of C_f will be dependent upon the assumed value of κ. Simpson (1970) suggested that for $R_\theta < 6000$, von Karman's constant κ ought to be replaced by the function

$$\Omega = \frac{\kappa}{\left(\frac{R_\theta}{6000}\right)^{\frac{1}{8}}} \qquad (6.37)$$

Thus over the range of the current experiments $1000 < R_\theta < 6000$, Simpson's criterion therefore implies that κ varies from 0.51 to 0.41. However, more recently, Purtell et al (1981) found κ and C to be constant (to within the accuracy of their experiments) down to $R_\theta = 1340$. The work of Andrepoules et al (1984) also confirmed the constancy of κ, although they found a slight decrease in C (5.0 to 4.5) with increasing R_θ over the range 3600 → 15400.

One might reasonably expect the accuracy and reliability in the predicted value of C_f to increase as the number of points used in defining the line increases. However, the range of points is restricted in that both techniques may only be applied to points that lie within the semi-logarithmic region. It seems to be generally accepted that the lower limit of this region corresponds to y^+ of approximately 30. However, since the accuracy of the measurements very close to the wall is dubious, it would seem prudent to select as the lower limit a point corresponding to a higher value of y^+. The upper limit of the semi-logarithmic region is dependent upon C_f and also (although not applicable in this case) pressure gradient. (Purtell et al suggest that for flat plate flow, the thickness of the semi-logarithmic region is approximately 0.15 of the total boundary layer thickness.)

As an aid for the selection of the widest possible range of applicable data points, the profile was plotted as $^u/_{U_\infty}$ vs $\ln \frac{yU_\infty}{\nu}$ with equation (6.33) drawn assuming $\kappa = 0.41$, $C = 5.0$ and C_f determined using equation (6.22). Examples are shown on figure 6.11. Upon examining the fit of the line to the data, it was then possible to select as wide a range of points that seemed to lie on a straight line. Using these points, C_f was then estimated using both techniques as outlined. The results are given in table 3 in the following section.

6.5.2 Estimation of C_f using Bradshaw's method

Bradshaw (1959) also proposed a procedure for estimating C_f using velocity profile measurements inside the semi-logarithmic region. Replacing u^+ by the log-law relation, equation (6.15) becomes

$$\frac{u}{U_\infty} = \frac{y^+(\frac{1}{\kappa}\ln y^+ + C)}{y\frac{U_\infty}{\nu}} \tag{6.38}$$

Bradshaw suggests that if y^+ is assigned some value that would be expected to lie within the log-law region, then, assuming κ and C are known, the intersection of a mean curve through the experimental points ($^u/_{U_\infty}$, $\frac{yU_\infty}{\nu}$) with equation (6.38) gives a predicted value of $\frac{yU_\infty}{\nu}$ for the particular value of y^+. Hence, since by definition,

$$C_f = 2\left\{\frac{y^+}{\frac{yU_\infty}{\nu}}\right\}^2 \tag{6.39}$$

C_f may be calculated.

Bradshaw's method was applied using the following numerical procedure:

> Using the $C_f \sim R_{x_m}$ relationship (equation (6.22)) an initial estimate of C_f was used to select a number of data points (typically 6) which bridged the predicted intersection with equation (6.38) for an assumed y^+ value (e.g. $y^+ = 100$). The best fitting quadratic equation through the points was determined i.e.
>
> $$\frac{u}{U_\infty} = a + b\,\frac{yU_\infty}{\nu} + c\left(\frac{yU_\infty}{\nu}\right)^2 \qquad (6.40)$$
>
> Combining with equation (6.38) gives
>
> $$\frac{y^+\left(\frac{1}{\kappa}\ln y^+ + C\right)}{y\,\frac{U_\infty}{\nu}} = a + b\,\frac{yU_\infty}{\nu} + c\left(\frac{yU_\infty}{\nu}\right)^2 \qquad (6.41)$$

This equation was then solved for $\frac{yU_\infty}{\nu}$ (using the Newton-Raphson method) and hence C_f using equation (6.39).

The method is graphically shown in figure 6.12. The results are compared with the previous C_f estimates in Table 3.

$R_{x_m}.10^6$	Predicted C_f ($\times 10^3$)				C
	Momentum Integral method see equation 6.22 (a)	$\kappa = 0.41$, $C = 5.0$		$\kappa = 0.41$	($\kappa = 0.41$)
		Bradshaw's Method (b)	Full Clauser Line (c)	Best Straight Line (d)	(e)
2.697	2.91	2.88	2.90	3.04	4.54
1.344	3.29	3.30	3.31	3.20	5.32
0.942	3.49	3.55	3.57	3.56	5.00
0.656	3.71	3.71	3.74	3.89	4.64
0.439	3.96	4.07	4.09	4.05	5.10
.0.303	4.19	4.48	4.50	4.40	5.20

Table 3. Comparison in C_f predictions using the various techniques

As expected, the full Clauser method and Bradshaw's method give essentially the same estimated C_f. The agreement with the momentum integral solution is very good except at the lowest Reynolds number where the error is about 5%. The values of C_f predicted by method (ii) of section 6.5.1 (column (d) in table 3) agree well with the other predictions. Using equation (6.36), the corresponding values of C are shown in column (e) using the values of C_f as given in column (d) and $\kappa = 0.41$. Overall, the results do not show any consistant trend between C and Reynolds number. (The mean value of C from column (e) is approximately 5.0.)

6.5.3 Sensitivity of C_f upon κ, C and y^+

The advantage of the non-graphical approach in the application of Clauser's or Bradshaw's method is that the consequence of assuming various values of κ, C or y^+ upon the predicted C_f may be readily examined.

In Bradshaw's method, the value of y^+ was varied over the range 60 to 240 and the corresponding predictions for C_f examined. The results indicated that over a certain range of y^+ the deduced value of C_f remained essentially constant, however as y^+ increases beyond the outer limit of the semi-logarithmic region then the estimated value of C_f appeared to monotonically increase. i.e. If the assigned value of y^+ is greater than the outer limit of the log region then C_f will be over estimated. (A y^+ of 100 is too large for $C_f \gtrsim 4.2$.)

The effect of assuming various values for κ and C upon the predicted C_f was also examined. The results suggested the following conclusions:

(i) The % error in C_f due to an error in κ is of the same order and sign.

(ii) The % error in C_f due to an error in C is approximately half the magnitude but opposite sign.

(iii) For an error in κ and C the error in C_f may be deduced by considering separately the consequences of the error due to κ and that due to C.

i.e. Assuming $\kappa = 0.41$ and $C = 5.25$ (as implied by Patel's upper calibration for the Preston tube) would give a C_f prediction about 3%

less than that derived assuming $\kappa = 0.41$, $C = 5.0$. This agrees well with the conclusions from section 6.3.2.

The consequence of an error in the measurement of y was also examined. The results suggest that the ratio: % error $^{\Delta y}/_{\theta}$ to % error in C_f was approximately 5 to 1 where Δy is the error in y. Thus C_f appears to be relatively insensitive to the estimation of y_{WALL}.

6.6 Comparison of C_f predictions

Figure 6.13 compares the C_f predictions obtained from the Preston tube results (using Poll's modification to Patel's calibration), the momentum integral equation, and application of Clauser's or Bradshaw's method ($\kappa = 0.41$, $C = 5.0$). The agreement between the 3 methods would suggest that C_f (hence τ_W) may be predicted with an error of about 5% at low Reynolds number but at higher Reynolds number the error is probably less.

6.7 Hot Film Experiments - Turbulent Flow

6.7.1 Effect of surface misalignment.

Following the same experimental procedure as described in sections 5.5.1 and 5.5.2, the effect of the step height of the film upon the convective heat transfer was studied for a turbulent boundary layer flow. Figure 6.14 shows the effect of traversing the film, glued onto the rectangular block, vertically relative to the plate surface over a range of free-stream speeds. These results clearly show that recessing the film has the effect of increasing Nu. This is opposite to the trend observed in laminar boundary layer flow - see figure 5.10.

With the film set flush with the plate surface, a calibration was performed where τ_W was estimated using a Preston tube (d = 1.47mm). The response of Nu with h was then recorded for a range of free-stream velocities. At various intervals during the experiment the calibration was repeated with the probe set flush with the plate surface. For some of the experiments the trip wire was removed so transition was not fixed. Typical calibrations obtained with the probe flush are shown in figure 6.15 in terms of Nu vs $Pe^{\frac{1}{3}}$. As previously noted, the calibration slope is repeatable although the intercept is not always reproducible. Note also that calibrations I and III were obtained with the trip wire removed. (The anemometer output was monitored on an oscilloscope to ensure that the flow was fully turbulent.)

Using equations (5.12) and (5.13) the variation of $\frac{\tau_m}{\tau_w}$ with h^+ was computed. The results are shown in figure 6.16 along with the mean trends obtained for laminar flow. For $0.9 \leq \frac{\tau_m}{\tau_w} \leq 1.1$ (i.e. $\pm 10\%$ error in τ_w) then in turbulent flow $-25 \lesssim h^+ \lesssim 30$ whilst for laminar flow $-1.2 \lesssim h^+ \lesssim 1.4$. Figure 6.16 clearly indicates the sensitivity of Nu upon surface misalignment for laminar flow and its relative insensitivity for turbulent flow. For the current experiments in turbulent flow $h^+ < 12$ and so the effects of surface misalignment are negligible.

These results confirm the suggestion by Poll and Watson (1984) that after encountering a small forward facing step, the wall shear stress relaxes to its undisturbed value very rapidly. It appears that after the surface discontinuity the viscous sublayer is quickly re-established, however the semi-logarithmic and wake regions of the profile remain perturbed for a distance typically 25δ downstream of the step.

6.7.2 Response due to a change in flow

Further calibration experiments were conducted using probes fixed nearer the leading edge. Figure 6.17 shows a typical calibration obtained, with the trip wire on, at $x_m = 0.243$m in terms of Nu vs $\tau_w^{1/3}$. The experiment was performed by increasing the tunnel speed in small increments till the maximum speed was reached and then the speed was gradually reduced. At each constant speed, mean values of V and U_∞ were recorded, each mean being the ensembled average of 40 samples. The wall shear stress was estimated using equation (6.22). The results for the ascending and descending speed runs are clearly shown. Over the middle speed range the calibrations appear to be distinct, however, there is some evidence that the difference is due to a time effect. Experiments indicate that as the settling period at a new speed increases during the descending speed run, the calibration line approaches the ascending speed curve.

To examine this time effect further, the consequence of a step change in Pe (U_∞) upon Nu was examined. Figure 6.18 shows the variation of free-stream velocity with time and the corresponding Nu history. (Performing the experiment in turbulent flow gives a more severe change in τ_W than would be obtained in laminar flow.) The probe was operated in the constant temperature mode, at a constant U_∞, for typically 60 minutes prior to the step change in U_∞. Following a sudden increase in U_∞, Nu initially over-shoots its final 'steady' value. Similarly, a sudden decrease in U_∞ causes Nu to under-shoot followed by a gradual build up to its 'equilibrium' value.

This phenomenon would appear to be due to a time dependence in the heat conduction within the substrate. (Relative to the time scale of figure 6.18, it is reasonable to assume that the anemometer responds instantaneously to any changes in the cooling conditions thus maintaining the film at a constant mean temperature.) From figures 3.10 and 3.12 (the steady state solution) the effect of increasing Pe increases the heat flux from the wall to the fluid and lowers the wall temperature upstream and downstream of the film. Assume steady state conditions exist at the lower Pe. Suddenly increasing the flow to a higher Pe will increase the heat flux from the wall to the fluid (see figure 3.12). However, because the wall temperature is higher than the final steady state value (see figure 3.10) there will be an additional heat flux to the fluid, which will obviously decrease with time as the new 'equilibrium' conditions are approached. By similar arguments the observed behaviour for suddenly decreasing Pe may be explained.

The behaviour of the probe for the particular case of suddenly turning the flow on or off cannot be deduced using figures 3.10 or 3.12 as the substrate conduction process in the no-flow case ($Pe = 0$) is different. For example, the measured Nu history due to suddenly stopping the flow is shown in figure 6.19 which clearly is different from that observed for a sudden decrease in Pe. Clearly the power supplied to the probe does not reach a 'steady' value for some time.

6.7.3 Detailed calibrations

Various calibrations were performed with a longer settling time at each speed condition prior to recording V and U_∞. A typical calibration in terms of Nu vs $Pe^{1/3}$ is shown in figure 6.20. A mean curve through the data is clearly 'bowed' indicating that a higher root of Pe is necessary to ensure proportionality. Using the least square error criterion, a general power law relationship of the form

$$Nu = APe^{1/n} + B \tag{6.42}$$

was fitted to the data excluding the point Pe = 0. The rms error was minimised with n = 3.8. The same trend was observed in calibrations performed using a Preston tube to estimate τ_w. The values of n determined from various calibrations varied from 3.6 to 4.0 with a mean value ∿ 3.8. This value of n agrees well with that predicted by the steady state, two-dimensional theory discussed in chapter 3. However, it is noted that the measured value of Nu is significantly greater than the theoretical prediction for the corresponding value of K and Pe. This discrepancy may be due to the fact that the measured Nu is based on the total hot resistance of the probe and not that of the nickel film alone. Other departures from the theoretical model of chapter 3 are

- (i) Lack of two-dimensionality (Geometrically, the aspect ratio of the nickel film is approximately 9. However, in terms of the effective heating dimensions of the film the aspect ratio may be considerably less)
- (ii) Composite substrate.

6.8 Laminar and turbulent flow calibrations

A series of consecutive laminar and turbulent calibration experiments were conducted. Prior to the first calibration, the probe was turned on at the selected operating resistance for 30 minutes after which the probe was turned off. After a further 30 minutes the probe was re-heated. The first calibration was then performed about 30 minutes later. Subsequent calibrations were repeated at roughly half hourly intervals with the probe remaining on throughout the series of calibrations.

The calibration results are shown in figure 6.21(a). The value of Nu at Pe = 0 has remained constant throughout the experiment so a direct comparison between the calibrations may be made. As plotted, the laminar and turbulent calibrations overlap suggesting the possibility of a unique calibration. However, correcting the laminar results for the effects of surface misalignment (see section 5.5.3) it is clear that the two calibrations are distinct, see figure 6.21(b). At the upper limit of the laminar results the calibrations differ by 30% in terms of Pe. (Note that Pope's criterion for a unique calibration in laminar and turbulent flow, error < 5%, is satisfied (see Appendix C) - even when the effective heating length[†] is used in calculating Pe.)

6.9 Effect of wall material (Copper plate model)

A cylindrical copper block, diameter 50mm, was mounted flush with the surface of the tufnol plate at a distance 0.2m from the leading edge. Two glue-on probes, whose resistance-temperature variation was known, were stuck onto the copper block. (One probe was used as a resistance thermometer.) A typical turbulent calibration is shown in figure 6.22 where τ_W was deduced using a Preston tube.

Fitting the general power law relationship, equation (6.42), to the results suggested that the most appropriate value of n was 3.7. This is sufficiently similar to the value obtained for the probe glued onto the tufnol plate as to suggest that n is constant for the probe in a given fluid. i.e. The thermal properties of the material onto which the probe is attached does not seem to alter the value of n. However, comparing figures 6.20 and 6.22 it is clear that increasing the thermal conductivity of the wall material increases the value of Nu for $\tau_W = 0$. It is interesting to note that the slope of the calibration for the copper backed probe is very similar to that for the tufnol backed probe.

6.10 Effect of ΔT upon the calibration

Figure 6.23 shows a series of turbulent calibrations performed with the probe operated at various temperatures. A period of 24 hours elapsed between each run so as to ensure near thermal equilibrium

---

[†] Using equation (12) in Appendix C the effective heating length of the film was found to be approximately 20% greater than the geometric length.

conditions. The probe was turned on typically 60 minutes prior to the start of the calibration.

Clearly, the calibration is dependent upon ΔT. The fluid properties ρ, μ and k involved in the definitions of Nu and Pe have been computed at the free-stream fluid temperature, T_∞. It may be shown that evaluating the fluid properties at a temperature $T_\infty + \frac{\Delta T}{m}$, where m is any positive constant, has the effect of shifting the calibration curves further apart. Therefore no average temperature exists which will collapse the data. Thus the variation of the $Nu \sim Pe$ relationship with ΔT is not primarily due to a variation of the fluid properties with temperature. (This is in agreement with Chapter 4.)

Determining the best fitting power law relationship of the form equation (6.42), the best value of n was found to be approximately 3.8 for each calibration. (The no-flow reading was not used in determining the coefficients A, B and n.) As is clear from figure 6.23 the measured value of Nu at $Pe = 0$ decreases with increasing ΔT. For all the calibration curves the intercept, B, was found to be typically 4% less than the measured no flow value. The results also indicate that the calibration slope, A, decreases slightly with increasing ΔT. ($\sim$ 3% from $\Delta T = 70^\circ C$ to $130^\circ C$.)

From the analysis of Chapter 4 it was suggested that, for a limited range of ΔT, the variation of i^2R with ΔT could be reasonably approximated by the expression

$$i^2R = b_s \Delta T + b_I$$

where $b_I \neq 0$. Figure 6.24 shows the variation of the no-flow value of i^2R, as measured before the start of the calibration, with ΔT. Fitting the best straight line through the points gave $b_I = 0.00342$. The calibrations in figure 6.23 are replotted in figure 6.25 in terms of Nu_b vs $Pe^{1/3}$ where

$$Nu_b = \frac{i^2R - 0.00342}{k\, \Delta T . w}$$

Clearly the variation of Nu_b with ΔT at a given Pe is significantly less than that indicated in figure 6.23. Increasing b_I to 0.004 minimised the scatter of the results.

To further examine the effect of ΔT upon the calibration, various laminar calibrations were performed using the probe glued onto the copper block. Between each calibration the probe was turned off for approximately 40 minutes after which the new operating resistance was selected and the probe turned on. Each laminar calibration was performed approximately 30 minutes after switching the probe on. Prior to the first calibration, a 'dummy' run was performed with the probe operating at the resistance selected for the first calibration. The results, uncorrected for the effect of surface misalignment, are shown in figure 6.26. The results are very similar to those of figure 6.23. As previously noted, the calibration slope decreases slightly with increasing ΔT.

Figure 6.27 shows the variation of $\left.\frac{i^2R}{k\,w}\right|_{\tau_w=0}$ with ΔT. Fitting a straight line through the data gives the intercept $b_I' = 264$.† Using this value of b_I', figure 6.28 shows the variation of $\frac{\frac{i^2R}{kw} - b_I'}{\Delta T}$ with $Pe^{1/3}$ for each calibration. Comparing figures 6.26 and 6.28, the variation between the calibrations at differing ΔT is considerably reduced although the scatter of the data is still unacceptably large.

In view of the uncertainty concerning the effect of changes in ΔT upon the calibration, it would appear that the probe should be operated at a constant value of ΔT. This could be simply achieved by adjusting the hot resistance, as set on the constant temperature anemometer, by the appropriate amount corresponding to the resistance change of a cold probe being used as a resistance thermometer.

It is noted that during several of the calibration experiments the temperature, inferred by the resistance change of a cold probe, gradually increased as the speed of the wind tunnel was raised. (The maximum temperature change was approximately 3°C.) Thus during calibration ΔT decreased slightly being least at the high speed (high Pe) setting. From figures 6.23 and 6.26 is is clear that this will have the effect of increasing Nu which in turn will tend to mask the 'roll-off' of Nu with increasing $Pe^{1/3}$.

---

† $b_I' = \frac{b_I}{kw}$

CHAPTER 7

Suggested operating procedure for the use of hot film probes for the measurement of skin friction

The following operating guide lines, based on the experimental work conducted using the glue-on probe, are proposed to enable hot film probes to be used for the measurement[†] of skin friction.

(i) Two similar probes, whose resistance-temperature characteristics are known, are required. The first probe, heated by a constant temperature anemometer, is operated at a constant value of ΔT. The change in resistance of the hot probe required to maintain ΔT constant may be determined from the resistance change of the second probe which is used as a resistance thermometer. (The cold probe ought to be mounted close to, but preferably not downstream of, the heated probe.) To maximise the heat flux to the flow ΔT ought to be as large as possible.

(ii) The model onto which the probes are mounted ought to have good thermal insulating properties. For metallic models, probes should be mounted on a suitable insulating insert.

(iii) The decay of the anemometer output voltage with time may be reduced to a tolerable level (less than 1% error in τ_w) by turning the probe on at least 15 minutes prior to measurement.

(iv) In laminar flows, the calibration is very sensitive to surface misalignment so glue-on probes should only be used with caution. In turbulent flow the calibration is relatively insensitive to surface misalignment (for a 10% error in τ_w $-25 < h^+ < 30$).

(v) It has been established that for a probe operating at a constant ΔT the calibration may be accurately represented by the relationship

---

[†] The accuracy of the technique is severely limited by the extremely weak dependence of the total heat loss from the film upon the wall shear stress. An error band of ± 10% in terms of τ_w seems to be physically realistic.

$$i^2R = A\tau_w^{1/n} + B(t)$$

where $n(> 3)$ increases with the substrate-to-fluid conductivity ratio. For kapton substrate in air n is approximately 3.7. At very low values of τ_w (e.g. $\tau_w < 0.06$ N/m^2) a different form of the above calibration may be necessary.

(vi) The calibration is best performed by slowly changing the value of τ_w in one direction only, allowing several minutes to pass at each new τ_w setting before recording i^2R.

(vii) For the DISA glue-on probe the measured value of i^2R at $\tau_w = 0$ prior to a calibration is greater than the value of B deduced by extrapolation of the calibration results to $\tau_w = 0$. When the flow is stopped the anemometer output voltage initially decays rapidly with time.

(viii) Due to the time and history dependence of the heat conduction within the substrate (see figure 4.8) the calibration in general is not repeatable. However, it appears that these effects only alter the value of B. Thus the calibration may be fixed (i.e. B determined) by making a measurement at a known, non-zero, value of τ_w (assuming A and n are known). If this cannot be done, then by measuring i^2R at $\tau_w = 0$, prior to the start of a run and sufficiently long after the end of a previous run, the change in B may be assumed to equal the change in $i^2R\big|_{\tau_w=0}$ between the current value and that measured during the initial calibration.

PRINCIPAL CONCLUSIONS

(1) Adiabatic substrate theories suggest that Nu is proportional to $Pe^{1/3}$. However, examination of many of the published calibrations (particularly those performed in air) suggest that a higher root of Pe is necessary to achieve proportionality with Nu.

(2) It has been demonstrated theoretically that when substrate conduction is accounted for, Nu is approximately proportional to $Pe^{1/n}$ where $n(> 3)$ increases with the substrate-to-fluid thermal conductivity ratio. Experiments performed in air flow suggest that for Kapton substrate Nu is approximately proportional to $Pe^{1/3.7}$.

(3) The calibration for hot film probes is time and history dependent. i.e.

$$Nu = APe^{1/n} + B(t) .$$

(4) The calibration is temperature dependent. (This problem may be avoided by operating the probe at a constant ΔT.)

(5) The effect of surface misalignment of the hot film significantly alters the convective heat transfer. This effect is more pronounced in laminar flow than in turbulent flow.

(6) The calibration for the glue-on probe appears to be dependent upon the nature of the flow, i.e. the calibration in laminar flow is different from the turbulent calibration.

ACKNOWLEDGEMENTS

I would like to thank my supervisor Dr. D.I.A. Poll for the constant advice and encouragement he gave during the course of this research. I would also like to thank Professor J.F. Clarke for his invaluable guidance through much of the theoretical work.

Thanks are also due to the College of Aeronautics workshop staff for their assistance without which the experimental work could not have taken place.

My grateful thanks is also due to Mrs. F. Creckendon who typed this thesis.

Finally, I would like to express my special thanks to Lorna, my wife, for her encouragement and moral support throughout the research.

This work was funded by the Department of Education for Northern Ireland.

REFERENCES

Abramowitz, M., Stegun, I.A. (1968) Handbook of mathematical functions. Dover.

Andrepoules, J., Durst, F., Zaric, Z., Jovanovic, J. (1984) Influence of Reynolds number on characteristics of turbulent wall boundary layers. Experiments in Fluids Vol.2.pp 7-16.

Armistead, R.A., Keyes, J.J. (1968,a) Hot film sensor for the study of wall turbulence phenomena. Review of Scientific Instruments, vol.39 pp 61-68.

Armistead, R.A., Keyes, J.J. (1968,b) A study of wall-turbulence phenomena using hot film sensors. Journal of Heat Transfer. Trans.ASME, Vol.90, pp 13-21.

Baines, W.D., Keffer, J.F. (1976) Measurement of shear stress near a stagnation point. Review of Scientific Instruments, Vol.47, No.4.

Beasley, J.A. (1973) Calculation of the laminar boundary layer and prediction of transition on a sheared wing. R & M 3787.

Bellhouse, B.J. (1965) The aerodynamic uses of heated thin film gauges. Ph.D Thesis, Oxford.

Bellhouse, B.J., Schultz, D.L. (1965) The measurement of skin friction in supersonic flow by means of heated thin film gauges. A.R.C. R & M 3490.

Bellhouse, B.J.
Schultz, D.L. (1966) Determination of mean and dynamic skin friction, separation and transition in low speed flow with a thin-film heated element.
Journal of Fluid Mechanics, Vol.24, pp 379-400.

Bellhouse, B.J.
Schultz, D.L. (1968) The measurement of fluctuating skin friction in air with heated thin film gauges.
Journal of Fluid Mechanics, Vol.32, pp 675-680.

Bertram, M.H. (1961) Calculations of compressible average turbulent skin friction.
NASA Technical Report R-123.

Bradshaw, P. (1959) A simple method for determining skin friction from velocity profiles.
Journal of Aerospace Science, Vol.26, pp 841.

Brown, G.L. (1967,a) Theory and application of heated films for skin friction measurement.
Proceedings of the 1967 Heat Transfer and Fluid Mechanics Institute, Stanford University Press, pp 361-381.

Brown, G.L. (1967,b) The application of heated surface films to aerodynamic measurements in boundary layers.
PhD Thesis, Oxford.

Busing, J.R. (1965) On the joule heating method of calibrating thin film resistance thermometers.
CoA Report No 183, Cranfield Inst. of Tech., Bedford.

Carslaw, H.S.
Jaeger, J.C. (1959) Conduction of heat in solids.
2nd edition, Clarendon Press, Oxford.

Clauser, F.H. (1954) Turbulent boundary layers in adverse pressure gradients.
Journal of Aeronautical Sciences, Vol.21, pp 91-108.

Coles, D.E. (1962) The turbulent boundary layer in a compressible fluid.
Rand Corp., Report R-403-PR, Santa Monica, California.

Cousteix, J.
Juillen, J.-C. (1982) Jauges a fil chaud pour la mesure du frottement pariétal (Réalisation, Étalonnage, Applications)
La recherche Aerospatiale No.3, pp 207-218.

Curle, N. (1962) Laminar boundary layer equations.
Oxford Mathematical Monographs.

Davis, M.R. (1980) Design of flat plate leading edges to avoid flow separation.
AIAA Journal, Vol.18, pp 598-600.

Deissler, R.G. (1955) Analysis of turbulent heat transfer, mass transfer and friction in smooth tubes at high Prandtl and Schmidt numbers.
NACA TR 1210.

Diaconis, N.S. (1954) The calculation of wall shearing stress from heat-transfer measurement in compressible flows.
Journal of Aeronautical Sciences, Vol.21, pp 201-202.

Eckert, E.R.G. (1980) Pioneering contributions to our knowledge in convective heat transfer (Hundred years of heat transfer research) Joint ASME/AICLE National Heat Transfer Conference, Orlando, Florida, July 1980.

Fage, A., Falkner, V.M. (1931) Relation between heat transfer and surface friction for laminar flow. A.R.C. R & M No. 1408.

Geremia, J.O. (1972) Experiments on the calibration of flush mounted film sensors. DISA Information, No.13, pp 5-10.

Gibbings, J.C. (1959) On boundary-layer transition wires. A.R.C. Technical Report, C.P.No.462.

Gradshteyn, I.S., Ryzhik, I.M. (1980) Table on integrals, series, and products. Academic Press, INC. (LONDON)

Head, M.R., Vasanta Ram, V. (1971) Improved presentation of Preston tube calibration. Aeronautical Quarterly XXII, No.3, pp 295-300.

Higuchi, H., Peake, D.J. (1978) Bi-directional, buried wire skin friction gauge. NASA TM 78531.

Hulton, P., Gammon, L.N. (1976) The effect of probe body temperature changes on the behaviour of flush mounting film probes. DISA Information, No.20, p 4.

Kreplin, H.-P., Meier, H.U. (1977) Application of heated element techniques for the measurement of wall shear stress in three-dimensional boundary layers. DFVLR-AVA IB 251-77 A 15.

Kreplin, H.-P.
Meier, H.U.
(1979) Experimental investigation of the transition and separation phenomena on a body of revolution.
Second Symposium on Turbulent Shear Flows.

Kreplin, H.-P.
Meier, H.U.
Maier, A.
(1978) Wind tunnel model and measuring techniques for the investigation of three-dimensional turbulent boundary layers.
A.I.A.A. Paper No. 78-781.

Latiff, Z.B.A.
(1981) Development of a low turbulence wind tunnel for the investigation of boundary layer flows.
MSc Thesis, CoA, Cranfield Institute of Technology, Bedford.

Lévêque, M.A.
(1928) Les lois de la transmission de chaleur par convection.
Ann. Mines, Vol.13, pp 201-239.

Liepmann, H.W.
Skinner, G.T.
(1954) Shearing stress measurements by use of a heated element.
NACA TN 3268.

Lighthill, M.J.
(1950) Contribution to the theory of heat transfer through a laminar boundary layer.
Proceedings of the Royal Society, London. Vol.A202, pp 359-377.

Ling, S.C.
(1963) Heat transfer from a small isothermal spanwise strip on an insulated boundary.
Journal of Heat Transfer, Trans AMSE, Vol.85, pp 230-236.

Ludweig, H.
(1950) Instrument for measuring the wall shearing stress of turbulent boundary layers.
NACA TM 1284.

Ludweig, H. Tillman, W.	(1949)	Investigations of the wall shearing stress in turbulent boundary layers. NACA TM 1285.
McAllister, J.E. Pierce, F.J. Tennant, M.H.	(1982)	Preston tube calibrations and direct force floating element measurements in a two-dimensional turbulent boundary layer. Journal of Fluid Engineering, Trans. ASME, Vol.104, pp 156-161.
McCroskey, W.J. Drubin, E.J.	(1972)	Flow angle and shear stress measurements using heated films and wires. Journal of Basic Engineering, Trans. ASME, Vol.94, pp 46-52.
McCroskey, W.J. Fisher, R.K.	(1972)	Detailed aerodynamic measurements on a model rotor in blade stall regime. Journal of American Helicopter Society, Vol.17, pp 20-30.
MacMillan, F.M.	(1957)	Experiments on Pitot tubes in shear flow. A.R.C. R & M 3028.
Murthy, V.S. Rose, W.C.	(1977)	Direct measruements of wall shear stress by buried wire gauges in a shock-wave boundary layer interaction region. AIAA Paper No. 77-691.
Noble, B.	(1958)	Methods based on the Weiner-Hopf technique for the solution of partial differential equations. Pergamon Press, London.
Owen, F.K.	(1969)	The application of thin film heated elements to problems in high speed flow. PhD Thesis, Oxford.
Owen, F.K. Bellhouse, B.J.	(1970)	Skin friction measurement at supersonic speeds. AIAA Journal, Vol.8, pp 1358-1360.

Patel, V.C.	(1965)	Calibration of the Preston tube and limitations on its use in pressure gradients. Journal of Fluid Mechanics, Vol.23, pp 185-208.
Pfeil, H. Sticksel, W.J.	(1982)	Influence of the pressure gradient on the law of the wall. AIAA Journal, Vol. 20, pp 434-436.
Poll, D.I.A.	(1983,a)	A note on the algebraic representation of the Preston tube calibration. CoA Memo No. 8308, Cranfield Inst. of Tech., Bedford.
Poll, D.I.A.	(1983,b)	A note on the use of surface Pitot tubes for the measurement of skin friction in laminar boundary layers. CoA Memo No.8307, Cranfield Inst. of Tech., Bedford.
Poll, D.I.A. Mathews, J. Stewart, I.R.	(1985,a)	A cautionary note on the use of the Preston tube technique in three-dimensional boundaries. CoA Memo No.8513, Cranfield Inst. of Tech., Bedford.
Poll, D.I.A. Mathews, J. Stewart, I.R.	(1985,b)	Some evidence in support of a Reynolds number independent universal law of the wall. CoA Memo No.8514, Cranfield Inst. of Tech., Bedford.
Poll, D.I.A. Watson, R.D.	(1984)	On the relaxation of a turbulent boundary layer after an encounter with a forward facing step. AGARD Conference Proceedings, No.365.
Pope, R.J.	(1971)	The use of thin film heated elements in water flows. PhD Thesis, Oxford.

Purtell, L.P.
Klebanoff, P.S.
Buckley, F.T. (1981) Turbulent boundary layer at low Reynolds number.
Physics of Fluids, Vol.24, pp 802-811.

Ramaprian, B.R.
Tu, S.W. (1983) Calibration of a heat flux gauge for skin friction measurement.
Journal of Fluids Engineering, Trans. ASME, Vol. 105, pp 445-457.

Reichardt, H. (1951) Complete representation of the turbulent velocity distribution in smooth pipes.
Z. angen. Math. Mech. Vol.31, pp 208-219.

Reichert, J.K.
Azad, R.S. (1977) Wall shear stress measurement with a hot film in a variable temperature flow.
Review of Scientific Instruments, Vol.48, pp 341-345.

Rotem, Z. (1967) The heated surface probe for measuring shear stress at the wall in laminar boundary layers.
The Canadian Journal of Chemical Engineering, Vol.45, pp 175-178.

Rubesin, M.W.
Okuno, A.F.
Mateer, G.G.
Brosh, A. (1975) Flush mounted hot-wire gauge for skin friction and separation detection measurements.
Proceedings of the 6th International Congress on Instrumentation in Aero-Space Facilities.

Salter, C.
Warsap, J.H.
Goodman, D.G. (1965) A new design of Pitot-static tube, with a discussion of Pitot-static tubes and their calibration factors.
R & M 3365.

Sandborn, V.A. (1979) Evaluation of the time dependent surface shear stress in turbulent flow.
ASME Paper No. 79-WA/FE-17.

Schlichting, H. (1979) Boundary layer theory.
7th edition, McGraw-Hill, New York.

Simpson, R.L. (1970) Characteristics of turbulent boundary layers at low Reynolds numbers with and without transpiration.
Journal of Fluid Mechanics, Vol.42, pp 769-780.

Smith, C.R.
Metzler, S.P. (1983) The characteristics of low-speed streaks in the near-wall region of a turbulent boundary layer.
Journal of Fluid Mechanics, Vol.129, pp. 27-54.

Spence, D.A.
Brown, G.L. (1968) Heat transfer to a quadratic shear profile.
Journal of Fluid Mechanics, Vol.33, pp 753-773.

Springer, S.G.
Pedley, T.J. (1973) The solution of heat-transfer problems by the Wiener-Hopf technique.
I. Leading edge of a hot film.
Proceedings of the Royal Society, London, Vol.A333, pp 347-362.

Springer, S.G. (1974) The solution of heat-transfer problems by the Wiener-Hopf technique.
II. Trailing edge of a hot film.
Proceedings of the Royal Society, London, Vol. A337, pp 395-412.

Squire, H.B.
Young, A.D. (1938) The calculation of the profile drag of aerofoils.
ARC R & M 1838.

Tanner, R.I. (1967) Theory of a thermal fluxmeter in a shear flow.
Journal of Applied Mechanics, Vol.34, pp 801-805.

U.S.N.B.S. (1948) Tables of Bessel functions of fractional order. Vol.1.
Columbia University Press, New York.

Winter, K.G. (1977) An outline of the techniques available for the measurement of skin friction in turbulent boundary layers.
Progress in Aerospace Sciences, Vol.18, pp 1 - 57.

APPENDIX A

Effect of compressibility upon the calibration

Assume the calibration may be written as

$$Nu = APe^{1/3} + B$$

where A and B are constants.

The effect of compressibility upon the calibration may be examined by considering the temperature dependence of the fluid properties ρ, μ and k appearing in the definitions of Nu and Pe i.e.

$$\frac{Q}{\Delta Tk} \sim \left(\frac{L^2\tau_w Pr}{\rho\nu^2}\right)^{1/3}$$

$$\Rightarrow \qquad \frac{Q}{\Delta T} \sim \left(\frac{Cp^2}{Pr^2}\,\rho\mu L^2\tau_w\right)^{1/3}$$

Thus the effect of compressibility is essentially confined to the term $(\rho\mu)^{1/3}$. Bellhouse and Schultz (1965) showed that over the range 0°C to 100°C $(\rho\mu)^{1/3}$ varies only by 2% and so the effect of compressibility is negligible. (This result also confirms that the presence of the hot wall has hegligible effect upon the wall shear stress.)

APPENDIX B

Solution for a specified wall temperature distribution neglecting longitudinal diffusion and substrate conduction

Consider the problem as sketched below.

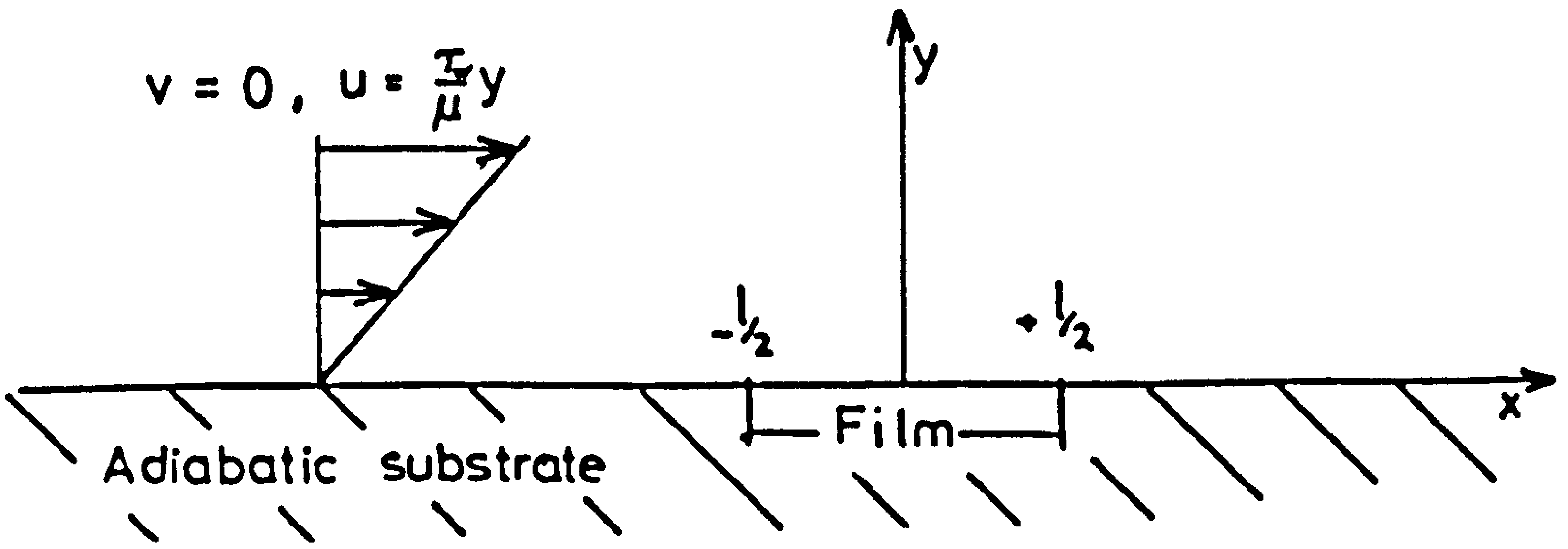

Neglecting longitudinal diffusion, the energy equation for the constant property flow may be written:

$$\frac{\tau_w}{\mu}\, y\, \frac{\partial T}{\partial x} = \frac{k}{\rho C_p}\, \frac{\partial^2 T}{\partial y^2} \qquad (1)$$

The solution to the temperature field T(x,y) is sought for a specified wall temperature distribution $T_w(x)$.

Defining the Fourier transformation as

$$\bar{T}(\alpha,y) = \int_{-\infty}^{\infty} T(x,y)e^{2\pi i\alpha x}dx \qquad (2)$$

then in the transformed plane equation (1) becomes

$$\frac{d^2\bar{T}}{dy^2} + 2\pi\alpha\, \frac{Pr\tau_w}{\rho\nu^2}\, e^{i\pi/2}\, y\bar{T} = 0 \qquad (3)$$

For convenience let $m = \frac{Pr\tau_w}{\rho\nu^2}$.

Using the substitution

$$z = m^{1/3}\, (2\pi\alpha)^{1/3}\, ye^{-i\pi/6} \qquad (4)$$

reduces equation (3) to Airy's equation - see Abramowitz and Stegun (1968).

$$\frac{d^2\overline{T}}{dz^2} - z\overline{T} = 0 \qquad (5)$$

The general solution to equation (5) may be expressed in terms of the Airy functions Ai,Bi.

$$\overline{T}(\alpha,y) = a(\alpha)\mathrm{Ai}\{z\} + b(\alpha)\mathrm{Bi}\{z\} \qquad (6)$$

Restricting the argument of z to the range $-\pi/3$ to $\pi/3$ then $\mathrm{Bi}\{z\}$ is not a valid solution since $\overline{T}(\alpha,y)$ must vanish at infinity. (Thus T represents the temperature rise above T_∞.)

From the definition of z, equation (4)

$$\mathrm{Arg}\{z\} = -\tfrac{\pi}{6} + \tfrac{1}{3}\mathrm{Arg}\{\alpha\}$$

$$\Rightarrow \quad \mathrm{Arg}\{\alpha\} = \tfrac{\pi}{2} + 3\mathrm{Arg}\{z\}$$

Therefore $-\tfrac{\pi}{3} < \mathrm{Arg}\{z\} < \tfrac{\pi}{3} \quad \Rightarrow \quad -\tfrac{\pi}{2} < \mathrm{Arg}\{\alpha\} < 3\tfrac{\pi}{2}$

i.e. a cut is placed along the negative imaginary axis of the α-plane.

Hence $\overline{T}(\alpha,y) = a(\alpha)\ \mathrm{Ai}\{m^{1/3}(2\pi\alpha)^{1/3}ye^{-i\pi/6}\}$ (7)

The function $a(\alpha)$ may be found from the boundary condition

$$T(x,0) = T_W(x)$$

i.e. $\overline{T}(\alpha,0) = \overline{T}_W(\alpha)$ (8)

where $\overline{T}(\alpha)$ is the Fourier transform of the specified wall temperature distribution.

Putting $y = 0$ in equation (7) gives

$$a(\alpha) = \frac{\overline{T}_W(\alpha)}{C_1}$$

where $C_1 = \mathrm{Ai}\{0\}$ (9)

Thus $\overline{T}(\alpha,y) = \frac{\overline{T}_W(\alpha)}{C_1}\mathrm{Ai}\{m^{1/3}(2\pi\alpha)^{1/3}ye^{-i\pi/6}\}$ (10)

Of particular interest is the heat flux into the fluid -

$$q(x) = -k_f \frac{\partial T}{\partial y}(x,0)$$

i.e. $$\bar{q}(\alpha) = -k_f \frac{\partial \bar{T}}{\partial y}(\alpha,0) \qquad (11)$$

Thus differentiating equation (10) and putting $y = 0$ gives

$$\bar{q}(\alpha) = -k_f\, m^{1/3}\,(2\pi\alpha)^{1/3}\, e^{-i\pi/6}\frac{C_2}{C_1}\,\bar{T}_w(\alpha) \qquad (12)$$

where $C_2 = Ai'\{0\}$.

Assume a 'top-hat' distribution for $T_w(x)$

$$T_w(x) = T_0 H\left\{\frac{L}{2} - |x|\right\} \qquad (13)$$

where T_0 represents the temperature rise above T_∞.

Hence

$$\bar{T}_w(\alpha) = T_0\,\frac{\mathrm{Sin}\,\pi\alpha L}{\pi\alpha} \qquad (14)$$

and

$$\bar{q}(\alpha) = -k_f\, m^{1/3}\frac{C_2}{C_1}\,T_0\, e^{-i\pi/6}\,(2\pi\alpha)^{1/3}\frac{\mathrm{Sin}(\pi\alpha L)}{\pi\alpha} \qquad (15)$$

The Fourier inverse transformation is defined

$$T(x,y) = \int_{-\infty+i\varepsilon}^{\infty+i\varepsilon} \bar{T}(\alpha,y)\, e^{-2\pi i\alpha x} d\alpha \qquad (16)$$

Thus application of the inverse transformation leads to the result

$$q(x) = -k_f\frac{C_2}{C_1}\,T_0 m^{1/3}\, 2\int_0^\infty \sqrt{3}\,\frac{\mathrm{Sin}(\pi rL)}{(2\pi r)^{2/3}}\,\mathrm{Cos}(2\pi rx)$$

$$- \frac{\mathrm{Sin}(\pi rL)}{(2\pi r)^{2/3}}\,\mathrm{Sin}(2\pi rx)\, dr\ . \qquad (17)$$

Let Q be the total heat flux over the film - i.e.

$$Q = \int_{-L/2}^{L/2} q(x)dx \tag{18}$$

Substituting for q(x) using equation (17) and inverting the order of integration gives

$$Q = -k_f T_0 \frac{C_2}{C_1} m^{1/3}\, 4/3 \int_0^\infty \frac{\text{Sin}^2(\pi rL)}{(2\pi r)^{5/3}} dr \tag{19}$$

Putting $\theta = \pi rL$ then

$$Q = -k_f T_0 (mL^2)^{1/3} \frac{2^{1/3}\sqrt{3}}{\pi} \frac{C_2}{C_1} \int_0^\infty \frac{\text{Sin}^2\theta}{\theta^{5/3}} d\theta \tag{20}$$

From Gradshteyn and Ryzhik (1980)

$$\int_0^\infty \theta^{-5/3} \text{Sin}^2\theta d\theta = \frac{3}{4} \frac{\Gamma(1/3)}{2^{1/3}}$$

and from Abramowitz and Stegun (1968)

$$\frac{C_2}{C_1} = -3^{1/3} \frac{\Gamma(2/3)}{\Gamma(1/3)}$$

Thus $Q = +k_f T_0 (mL^2)^{1/3} . \frac{3\sqrt{3}.3^{1/3}}{4} \Gamma(2/3)$

or

$$\frac{Q}{k_f T_0} = 0.807549 \left\{ \frac{PrL^2 \tau_W}{\rho \nu^2} \right\}^{1/3} \tag{21}$$

$$Nu = 0.8075\, Pe^{1/3}$$

If a Cosine wall temperature distribution is assumed i.e.

$$T_W = T_{OMAX}\, H\{\tfrac{L}{2} - |x|\}.\text{Cos}(\tfrac{\pi x}{L}) \tag{22}$$

then

$$\bar{T}_w(\alpha) = \frac{T_{mean}\ L}{1 - 4\alpha^2 L^2} \operatorname{Cos}(\pi\alpha L) \qquad (23)$$

Substituting for $\bar{T}_w(\alpha)$ in equation (12) and application of the Fourier inverse transformation leads to the result

$$Nu = 0.7233\ Pe^{1/3} \qquad (24)$$

From the form of equation (12), and as illustrated by these 2 examples, the solution will always be of the form

$$Nu = aPe^{1/3}$$

where the constant a is dependent upon the specified wall temperature distribution.

APPENDIX C

Pope's method for relating the turbulent calibration to the laminar calibration

In his thesis Pope proposed a procedure that appeared to collapse the calibration effected in turbulent flow onto the laminar calibration. In his original work several numerical errors were made and so his method is repeated here in its correct form.

From equation (2.39)

$$\begin{aligned} Nu &= 0.8072\ Pe^{1/3} + 0.10(2\beta - \alpha)L - 0.02869\ Pe^{-1/3}\left[L(2\beta - \alpha)\right]^2 \\ &= 0.8072\ Pe_m^{1/3} \qquad (1) \end{aligned}$$

where Pe_m is the value of Pe deduced using the laminar calibtation.

Defining

$$\varepsilon = \frac{0.1(2\beta - \alpha)L}{0.8072\ Pe^{1/3}} \qquad (2)$$

then

$$\left(\frac{Pe_m}{Pe}\right)^{1/3} = 1 + \varepsilon - 2.316\varepsilon^2 \qquad (3)$$

From equations (2.40) and (2.38)

$$\alpha = \frac{0.0416\sqrt{\rho\tau_w}}{\mu} = \frac{0.0416\ Pe^{\frac{1}{2}}}{LPr^{\frac{1}{2}}} \qquad (4)$$

Putting $\beta = 0$ gives

$$\varepsilon = -0.00515\left[\frac{Pe^{1/3}}{Pr}\right]^{\frac{1}{2}} \qquad (5)$$

Assuming the calibration in laminar flow is

$$Nu - Nu_o = 0.8072\ Pe^{1/3} \qquad (6)$$

then the turbulent calibration is

$$Nu_m - Nu_o = 0.8072\ Pe_m^{1/3} \qquad (7)$$

hence

$$Nu\ - Nu_m = 0.8072(Pe^{1/3} - Pe_m^{1/3}) \qquad (8)$$

From equation (3)

$$\left(\frac{Pe}{Pe_m}\right)^{1/3} - 1 = \frac{-\varepsilon + 2.316\varepsilon^2}{1 + \varepsilon - 2.316\varepsilon^2} \qquad (9)$$

$$= g(\varepsilon)$$

Thus

$$Nu = Nu_m + (Nu_m - Nu_o)g(\varepsilon) \qquad (10)$$

and

$$= \frac{-0.00574}{Pr^{\frac{1}{2}}} (Nu_m - Nu_o)^{\frac{1}{2}}(1 + g(\varepsilon))^{\frac{1}{2}} \qquad (11)$$

Thus knowing $(Nu_m - Nu_o)$ ε may be computed and hence the corrected value of Nu estimated using equation (10). (The corrected value of Nu is the value that would have been measured if a uniform sheared profile were present.)

Using equations (3) and (5) it is possible to derive a criterion in terms of $Pe/_{Pr^3}$ for the maximum error allowed in the interpreted value of Pe. Assuming a maximum error of 5% then

$$Pe < 1024\ Pr^3$$

(Pope had suggested $Pe < 900\ Pr^3$).

In practical terms, it must be noted that for equation (6) to hold then the effective heating length should be used, i.e. the value of L used in the definition of Pe should be the effective heating length of the film L_{eff} which may be estimated from the slope of the calibration: $Nu = Nu_o + m\tau_w^{1/3}$

$$L_{eff} = \left[\frac{m^3\rho\nu^2}{(.8072)^3 Pr}\right]^{\frac{1}{2}} \qquad (12)$$

APPENDIX D

Application of the Fourier Inverse Transformation

From Nobel (1958) the Fourier inverse transformation, $\overline{T}(\alpha,y)$ $T(x,y)$, may be performed along any line within a horizontal strip in the α-plane where $\overline{T}(\alpha,y)$ is analytic. A branch point exists at the origin, $\alpha = 0$, and the α-plane has been cut along the negative imaginary axis. Therefore, inversion cannot be simply performed along the real axis of α-plane due to the singularity of $\overline{T}(\alpha,y)$ at the origin.

To demonstrate the application of the inverse transformation in terms of real integrals only one case will be considered here as the principles may be readily applied to all other results.

From section 3.6 it is shown that for a 'top-hat' heat flux distribution the surface temperature in the transformed plane is

$$\overline{T}(\alpha,0) = \frac{\frac{\mathrm{Sin}(\pi\sqrt{Pe\alpha})}{\pi\sqrt{Pe\alpha}} \cdot \mathrm{Ai}\{g\}}{+\sqrt{4\pi^2\alpha^2}\,K\mathrm{Ai}\{g\} - e^{-\pi/6}(2\pi\alpha)^{1/3}\,\mathrm{Ai}'\{g\}} \qquad (1)$$

where $g = e^{i\pi/3}\,(2\pi\alpha)^{4/3}$

Application of the Fourier inverse theorem therefore gives:

$$T(x,0) = \int_{-\infty+i\varepsilon}^{\infty+i\varepsilon} \frac{\frac{\mathrm{Sin}(\pi\sqrt{Pe\alpha})}{\pi\sqrt{Pe\alpha}}}{+\sqrt{4\pi^2\alpha^2}\,K - e^{-i\pi/6}(2\pi\alpha)^{1/3}\,\frac{\mathrm{Ai}'\{g\}}{\mathrm{Ai}\,\{g\}}} . e^{-2\pi i\alpha x}\,d\alpha. \qquad (2)$$

This integral is evaluated by considering the contour of integration as shown in figure 3.2.

It may be shown that the integrand in equation (2) is analytic at all points within the contour. (Ai{z} and Ai'{z} have zeros on the negative real axis of the z-plane. Thus Ai{g} and Ai'{g} will only have zeros along the positive imaginary axis of the α-plane.)

Thus
$$\oint \overline{T}(\alpha,0)e^{-2\pi i\alpha x}\,d\alpha = 0$$

Therefore

$$T(x,0) + A_1 + A_2 + A_3 + A_4 + A_5 = 0$$

where A_2 and A_4 represent integration along the real axis, A_3 represents integration around the semi-circle at the origin with $|\alpha| = \delta$ and A_1, A_5 signify integration along the curves $|\alpha| = R$ as $R \to \infty$.

Consider integration along the arc A_1.

$$\text{On } A_1 \qquad \alpha = Re^{i\theta}$$

$$d\alpha = ie^{i\theta}Rd\theta.$$

From Abramowitz and Stegun (1968)

$$\text{As } z \to \infty \qquad \frac{Ai'\{z\}}{Ai\ \{z\}} \to -z^{\frac{1}{2}}$$

Thus the inversion integral around A_1 becomes

$$A_1 \sim - \int_0^{\theta_1} ie^{i\theta}R \, \frac{\dfrac{\text{Sin}(\pi\sqrt{Pe}Re^{i\theta})}{\pi\sqrt{Pe}Re^{i\theta}}}{2\pi R(Ke^{i\theta/2} + e^{i2\theta/3})} \, e^{-2\pi ixRe^{i\theta}} d\theta \ .$$

As $R \to \infty$, $\theta_1 \to \epsilon/R \to 0$ ($\epsilon << 1!$) so clearly $A_1 \to 0$.

Similarly for A_5.

Consider integration along A_3

$$\alpha = \delta e^{i\theta}$$

$$d\alpha = ie^{i\theta}\delta d\theta \ .$$

$$\text{As} \quad \delta \to 0 \text{ then} \quad \frac{Ai'\{g\}}{Ai\ \{g\}} \to - \frac{C_2}{C_1}$$

$$\text{and} \quad \frac{\text{Sin}\pi\sqrt{Pe\alpha}}{\pi\sqrt{Pe\alpha}} \to 1 \ .$$

$$\text{Assuming} \quad + \sqrt{4\pi^2\alpha^2}\, K << \frac{C_2}{C_1} e^{-\pi/6 i}(2\pi\alpha)^{1/3}$$

$$\text{Thus as} \quad \delta \to 0 : \overline{T}(\alpha,0) \to \frac{C_1}{C_2} e^{+i\pi/6} (2\pi\alpha)^{-1/3}$$

$$\therefore \quad A_5 \sim \int_0^{\pi} ie^{i\theta}\delta \, \frac{C_1}{C_2} e^{i\pi/6} (2\pi\delta)^{-1/3} \, e^{2\theta/3 i} \, e^{-2\pi ix\delta e^{i\theta}} d\theta \ .$$

which tends to zero as δ tends to zero.

Therefore $\qquad T(x,0) = -A_2 - A_4$.

On $A_2 \qquad \alpha = re^{i0} \therefore d\alpha = dr$

Thus along the +ve real axis A_2

$$A_2 = \int_{\infty}^{0} \frac{\frac{\text{Sin}\pi\sqrt{Per}}{\pi\sqrt{Per}}}{2\pi rK - e^{i\pi/6}\,(2\pi r)^{1/3}\frac{Ai'}{Ai}\{(2\pi r)^{4/3}\,e^{i\pi/3}} . e^{-2\pi irx}dr \; .$$

Let $\quad \overline{T}(\alpha = re^{i0},0) = \overline{T}_R + i\overline{T}_I$

Then

$$-A_2 = \int_0^{\infty} (\overline{T}_R + i\overline{T}_I)(\text{Cos}(2\pi rx) - i\text{Sin}(2\pi rx))dr \; .$$

Now consider integration along A_4

$$\alpha = re^{i\pi}$$

$$\therefore \quad d\alpha = e^{i\pi}dr \; .$$

Since

$$\frac{\text{Sin}(\pi\sqrt{Per})}{\pi\sqrt{Per}} = \frac{\text{Sin}(-\pi\sqrt{Per})}{-\pi\sqrt{Per}}$$

and

$$\frac{Ai'}{Ai}\{(2\pi r)^{4/3}\,e^{-i\pi/3}\} = \overline{\frac{Ai'}{Ai}\{(2\pi r)^{4/3}\,e^{i\pi/3}\}}$$

where the bar denotes the complex conjugate, then it can be shown that

$$\overline{T}(\alpha = re^{i\pi}) = \overline{\overline{T}(\alpha = re^{i0})}$$

Thus

$$-A_4 = \int_0^{\infty} (\overline{T}_R - i\overline{T}_I)\; e^{2\pi irx}\; dr \; .$$

$$= \int_0^{\infty} (\overline{T}_R - i\overline{T}_I)\{\text{Cos}(2\pi rx) + i\text{Sin}(2\pi rx)\}dr \; .$$

$$\therefore \quad T(x,0) = -A_2 - A_4 = 2\int_0^{\infty} \overline{T}_R\,\text{Cos}(2\pi rx) + \overline{T}_I\,\text{Sin}(2\pi rx)dr$$

APPENDIX E

Solution for the wall temperature distribution for K = 0, neglecting longitudinal diffusion

Putting K = 0 in equation (3.36), the surface temperature in the transformed plane for a 'top-hat' heat flux distribution is

$$\bar{T}(\alpha,0) = \frac{\frac{\mathrm{Sin}(\pi\sqrt{Pe}\alpha)}{\pi\sqrt{Pe}\alpha} . C_1}{(2\pi\alpha)^{1/3} e^{-i\pi/6} C_2} = \bar{T}_R(\alpha) + \bar{T}_I(\alpha) \qquad (1)$$

Hence

$$\bar{T}_R(\alpha) = \frac{\sqrt{3}}{2}\frac{C_1}{C_2}\frac{\mathrm{Sin}(\pi\sqrt{Pe}\alpha)}{(\pi\sqrt{Pe}\alpha)^{4/3}} . \left(\frac{\sqrt{Pe}}{2}\right)^{1/3}$$

$$\bar{T}_I(\alpha) = \frac{1}{\sqrt{3}}\bar{T}_R(\alpha) \qquad (2)$$

Application of the Fourier inverse transformation gives

$$T(x,0) = 2\int_0^\infty \bar{T}_R(r)\mathrm{Cos}(2\pi rx)dr + 2\int_0^\infty \bar{T}_I\mathrm{Sin}(2\pi rx)dr \qquad (3)$$

Consider the first integral:

$$2\int_0^\infty \bar{T}_R(r)\mathrm{Cos}(2\pi rx)dr = \sqrt{3}\,\frac{C_1}{C_2}\left(\frac{\sqrt{Pe}}{2}\right)^{1/3}\int_0^\infty \frac{\mathrm{Sin}(\pi\sqrt{Pe}r)\mathrm{Cos}(2\pi rx)}{(\pi\sqrt{Pe}r)^{4/3}}dr \qquad (4)$$

$$= \frac{\sqrt{3}}{\pi}\frac{C_1}{C_2}\left(\frac{1}{2}\right)^{1/3}\frac{1}{\sqrt{Pe}}\int_0^\infty \frac{\mathrm{Sin}(\sqrt{Pe}\theta)\mathrm{Cos}(2x\theta)}{\theta^{4/3}}d\theta \qquad (5)$$

From Gradshteyn and Ryzhik (1980)

$$\int_0^\infty \theta^{-4/3}\,\mathrm{Sin}(\sqrt{Pe}\theta)\mathrm{Cos}(2x\theta)d\theta = \tfrac{1}{2}\mathrm{Sin}(-\pi/6)\,\Gamma(-1/3)\Big[(\sqrt{Pe} + 2x)^{1/3}$$

$$+ |\sqrt{Pe} - 2x|^{1/3}\,\mathrm{sign}(\sqrt{Pe} - 2x)\Big] \qquad (6)$$

for $x > 0$.

Similarly the second integral of equation (3) may be written:

$$2\int_0^\infty \overline{T}_I(r)\mathrm{Sin}(2\pi rx)dr = \frac{1}{\pi}\frac{C_1}{C_2}\left(\frac{1}{2}\right)^{1/3}\frac{1}{\sqrt{Pe}}\int_0^\infty \frac{\mathrm{Sin}(\sqrt{Pe}\,\theta)\mathrm{Sin}(2x\theta)}{\theta^{4/3}}\,d\theta \qquad (7)$$

where

$$\int_0^\infty \theta^{-4/3}\,\mathrm{Sin}(\sqrt{Pe}\,\theta)\mathrm{Sin}(2x\theta)d\theta = \tfrac{1}{2}\mathrm{Cos}(\pi/6)\,\Gamma(-1/3)\left[|2x-\sqrt{Pe}|^{1/3}-(2x+\sqrt{Pe})^{1/3}\right] \qquad (8)$$

for $x > 0$ and $2x \neq \sqrt{Pe}$.

Using $\frac{C_1}{C_2} = \frac{\Gamma(1/3)}{3^{1/3}\Gamma(2/3)}$ and $\Gamma(-1/3) = -3\Gamma(2/3)$ then adding equations (7) and (8) gives

$$T(x,0) = \frac{-0.60961}{\sqrt{Pe}}\left\{|2x-\sqrt{Pe}|^{1/3} - 2(2x+\sqrt{Pe})^{1/3} - |\sqrt{Pe}-2x|^{1/3}\mathrm{sign}(\sqrt{Pe}-2x)\right\} \qquad (9)$$

for $x > 0$ and $x \neq \frac{\sqrt{Pe}}{2}$.

Using equation (3.33) the dimensionless parameter x may be replaced by $\frac{x^*}{a^*}$ where a^* is half the length of the film, i.e.

$$T(\tfrac{x^*}{a^*},0) = \frac{-0.60961}{Pe^{1/3}}\left\{\left|\frac{x^*}{a^*}-1\right|^{1/3} - 2\left(\frac{x^*}{a^*}+1\right)^{1/3} - \left|1-\frac{x^*}{a^*}\right|^{1/3}\mathrm{sign}\left(1-\frac{x^*}{a^*}\right)\right\} \qquad (10)$$

for $\frac{x^*}{a^*} > 0$, $\frac{x^*}{a^*} \neq 1$.

For $0 < \frac{x^*}{a^*} < 1$ then $\left|\frac{x^*}{a^*}-1\right| = (1-\frac{x^*}{a^*})$

$$\left|1-\frac{x^*}{a^*}\right| = (1-\frac{x^*}{a^*})$$

$$\mathrm{sign}\ (1-\frac{x^*}{a^*}) = +1 \ .$$

Thus for $0 < \frac{x^*}{a^*} < 1$ equation (10) becomes

$$T(\tfrac{x^*}{a^*},0) = \frac{0.60961}{Pe^{1/3}}\left\{2\left(\frac{x^*}{a^*}+1\right)^{1/3}\right\} \qquad (11)$$

For $\frac{x^*}{a^*} > 1$ then
$$\left|\frac{x^*}{a^*} - 1\right| = (\frac{x^*}{a^*} - 1)$$
$$\left|1 - \frac{x^*}{a^*}\right| = (\frac{x^*}{a^*} - 1)$$
$$\mathrm{sign}(1 - \frac{x^*}{a^*}) = -1$$

so for $\frac{x^*}{a^*} > 1$
$$T(\frac{x^*}{a^*},0) = \frac{0.60961}{Pe^{1/3}}\left\{2(\frac{x^*}{a^*} + 1)^{1/3} - 2(\frac{x^*}{a^*} - 1)^{1/3}\right\} \qquad (12)$$

The solution for $\frac{x^*}{a^*} < 0$ can also be deduced using equations (6) and (8). Let $x_p = |x|$. Hence equation (3) becomes

$$T(x,0) = 2\int_0^\infty \overline{T}_R(r)\mathrm{Cos}(2\pi r x_p)dr - 2\int_0^\infty \overline{T}_I(r)\mathrm{Sin}(2\pi r x_p)dr \qquad (13)$$

Using the integral solutions equations (6) and (8)

$$T(x,0) = \frac{-0.60961}{\sqrt{Pe}}\left\{- |2x_p - \sqrt{Pe}|^{1/3} - |\sqrt{Pe} - 2x_p|^{1/3}\mathrm{sign}(\sqrt{Pe} - 2x_p)\right\} \qquad (14)$$

for $x_p > 0$, $x_p \neq \sqrt{Pe}/2$.

or
$$T(\frac{x^*}{a^*},0) = \frac{0.60961}{Pe^{1/3}}\left\{\frac{x_p^*}{a^*} - 1^{1/3} + 1 - \frac{x_p^*}{a^*}^{1/3}\mathrm{sign}(1 - \frac{x_p^*}{a^*})\right\} \qquad (15)$$

Thus for $-1 < \frac{x^*}{a^*} < 0$

i.e. $0 < \frac{x_p^*}{a^*} < 1$ then
$$\left|\frac{x_p^*}{a^*} - 1\right| = (1 - \frac{x_p^*}{a^*})$$
$$\left|1 - \frac{x_p^*}{a^*}\right| = (1 - \frac{x_p^*}{a^*})$$
$$\mathrm{sign}(1 - \frac{x_p^*}{a^*}) = +1.$$

so for $-1 < \frac{x^*}{a^*} < 0$
$$T(\frac{x^*}{a^*},0) = \frac{0.60961}{Pe^{1/3}}\left\{2(1 - \left|\frac{x^*}{a^*}\right|)^{1/3}\right\} \qquad (16)$$

For $\frac{x^*}{a^*} < -1$ i.e. $\frac{x_p^*}{a^*} > 1$ then
$$\left|\frac{x_p^*}{a^*} - 1\right| = (\frac{x_p^*}{a^*} - 1)$$
$$\left|1 - \frac{x_p^*}{a^*}\right| = (\frac{x_p^*}{a^*} - 1)$$
$$\mathrm{sign}(1 - \frac{x_p^*}{a^*}) = -1$$

Therefore, for $\frac{x^*}{a^*} < -1$, $T(\frac{x^*}{a^*},0) = 0$ (17)

Thus factoring the results by Nu (= $0.868Pe^{1/3}$) gives

For $\frac{x^*}{a^*} < -1$ $$\frac{T_W^* - T_\infty^*}{T_{MF}^* - T_\infty^*} = 0$$

For $-1 < \frac{x^*}{a^*} < 0$ $$\frac{T_W^* - T_\infty^*}{T_{MF}^* - T_\infty^*} = 1.0583\left\{1 - \left|\frac{x^*}{a^*}\right|\right\}^{1/3}$$

For $0 < \frac{x^*}{a^*} < 1$ $$\frac{T_W^* - T_\infty^*}{T_{MF}^* - T_\infty^*} = 1.0583\left\{1 + \frac{x^*}{a^*}\right\}^{1/3}$$

For $\frac{x^*}{a^*} > 1$ $$\frac{T_W^* - T_\infty^*}{T_{MF}^* - T_\infty^*} = 1.0583\left\{\left(\frac{x^*}{a^*} + 1\right)^{1/3} - \left(\frac{x^*}{a^*} - 1\right)^{1/3}\right\}$$

APPENDIX F

Notes on the Airy function, Ai, and its derivative

A Representation in terms of ascending series and asymptotic expansion

In order to compute the surface temperature distribution when the effects of longitudinal diffusion are included it is necessary to evaluate the Airy functions $\mathrm{Ai}\{re^{i\pi/3}\}$ and $\mathrm{Ai}'\{re^{i\pi/3}\}$. As outlined in section (3.7) this is achieved using the ascending series and asymptotic series definitions of the Airy function. From Abramowitz and Stegun (1968) these are

Ascending series $\mathrm{Ai}(z) = C_1 f(z) - C_2 g(z)$

where
$$f(z) = 1 + \frac{1}{3!} z^3 + \frac{1.4}{6!} z^6 + \frac{1.4.7}{9!} z^9 + \ldots .$$

$$g(z) = z + \frac{2}{4!} z^4 + \frac{2.5}{7!} z^7 + \frac{2.5.8}{10!} z^{10} + \ldots .$$

$$C_1 = \frac{1}{3^{2/3}\,\Gamma(2/3)} \,, \quad C_2 = \frac{1}{3^{1/3}\,\Gamma(1/3)} \qquad \frac{C_2}{C_1} = \frac{3^{1/3}\Gamma(2/3)}{\Gamma(1/3)}$$

The derivative of the Airy function may be calculated by differentiation of the ascending series.

Asymptotic Expansion

$$\mathrm{Ai}(z) \sim \frac{1}{2\sqrt{\pi}} z^{-\frac{1}{4}} e^{-\zeta} \sum_{k=0}^{\infty} (-1)^k c_k \zeta^{-k} \qquad (|\arg z| < \pi)$$

$$\mathrm{Ai}'(z) \sim -\frac{1}{2\sqrt{\pi}} z^{\frac{1}{4}} e^{-\zeta} \sum_{k=0}^{\infty} (-1)^k d_k \zeta^{-k} \qquad (|\arg z| < \pi)$$

where
$$c_0 = 1 \,, \quad c_k = \frac{\Gamma(3k + \frac{1}{2})}{54^k k!\,\Gamma(k + \frac{1}{2})} \qquad k = 1,2,3 \ldots .$$

$$d_0 = 1 \,, \quad d_k = -\frac{6k+1}{6k-1} c_k \,, \quad \zeta = \tfrac{2}{3} z^{3/2} .$$

For the particular case of section 3.6 where $z = re^{i\pi/3}$ it was found that using the first 10 terms of each series the ascending and asymptotic expansions agreed to at least 5 significant figures where $r = 4.1$.

B Representation of the Airy function in terms of Bessel functions

In order to check the computed values of the Airy functions it is possible to represent the functions in terms of Bessel functions with real arguments.

From Abramowitz and Stegun (1968)

$$\mathrm{Ai}(z) = \frac{1}{3}\sqrt{z}\left[I_{-1/3}(\zeta) - I_{1/3}(\zeta)\right]$$

and $$\mathrm{Ai}'(z) = -\frac{z}{3}\left[I_{-2/3}(\zeta) - I_{2/3}(\zeta)\right]$$

where $$\zeta = \frac{2}{3}z^{3/2}$$

With $$z = re^{i\pi/3} \Rightarrow \zeta = \frac{2}{3}r^{3/2}e^{i\pi/2}$$ i.e. ζ is purely imaginary.

Using the result $$I_\nu(z) = e^{-\frac{\nu}{2}\pi i}J_\nu(ze^{i\pi/2}) \qquad \text{for } -\pi < \arg z \leq \pi/2$$

Thus $$\mathrm{Ai}\{re^{i\pi/3}\} = \frac{\sqrt{r}}{3}e^{i\pi/6}\left[e^{i\pi/6}J_{-1/3}(ae^{i\pi}) - e^{-i\pi/6}J_{1/3}(ae^{i\pi})\right]$$

and $$\mathrm{Ai}'\{re^{i\pi/2}\} = -\frac{re^{i\pi/3}}{3}\left[e^{i\pi/3}J_{-2/3}(ae^{i\pi}) - e^{-i\pi/3}J_{2/3}(ae^{i\pi})\right]$$

where $$a = \frac{2}{3}r^{3/2}.$$

By analytic continuation $$J_\nu(ze^{m\pi i}) = e^{m\nu\pi i}J_\nu(z) \quad : m \text{ an integer.}$$

Hence $$\mathrm{Ai}\{re^{i\pi/3}\} = \frac{\sqrt{r}}{3}\left[J_{-1/3}\left(\tfrac{2}{3}r^{3/2}\right) - e^{\frac{\pi}{3}i}J_{1/3}\left(\tfrac{2}{3}r^{3/2}\right)\right]$$

$$\mathrm{Ai}'\{re^{i\pi/3}\} = -\frac{r}{3}\left[J_{-2/3}\left(\tfrac{2}{3}r^{3/2}\right) - e^{\frac{2\pi i}{3}}J_{2/3}\left(\tfrac{2}{3}r^{3/2}\right)\right]$$

i.e. the Airy function and its derivative have been expressed in terms of Bessel functions with real arguments.

C Representation of $\mathrm{Ai}\{re^{-i\pi/6}\}$ in terms of Kelvin functions with real arguments.

From Abramowitz and Stegun (1968) the Airy function may be expressed in terms of the Bessel function K:

$$\mathrm{Ai}\{z\} = \frac{1}{\pi}\sqrt{\frac{z}{3}}\, K_{1/3}\left(\frac{2}{3} z^{3/2}\right)$$

Thus $\mathrm{Ai}\{re^{-i\pi/6}\} = \frac{1}{\pi}\sqrt{\frac{r}{3}}\, e^{-i\pi/12}\, K_{1/3}\left(\frac{2}{3} r^{3/2} e^{-i\pi/4}\right)$

For convenience let $a = \frac{2}{3} r^{3/2}$.

Using the definition of the Kelvin functions

$$e^{-\frac{1}{2}\nu\pi i}\, K_\nu(ae^{i\pi/4}) = \mathrm{ker}_\nu a + i\,\mathrm{kei}_\nu a$$

Thus $K_{1/3}(ae^{i\pi/4}) = e^{\pi/6\, i}\,(\mathrm{ker}_{1/3}\, a + i\,\mathrm{kei}_{1/3}\, a)$

Since $K_\nu(\bar{z}) = \overline{K_\nu(z)}$ where the bar denotes the complex conjugate

then $K_{1/3}(ae^{-i\pi/4}) = e^{-\pi/6\, i}\,(\mathrm{ker}_{1/3} a - i\,\mathrm{kei}_{1/3}\, a)$

Hence

$$\mathrm{Ai}\{re^{-i\pi/6}\} = \frac{1}{\pi}\sqrt{\frac{r}{3}}\, e^{-i\pi/4}\left\{\mathrm{ker}_{1/3}\left(\frac{2}{3} r^{3/2}\right) - i\,\mathrm{kei}_{1/3}\left(\frac{2}{3} r^{3/2}\right)\right\}$$

D Calculation of $\mathrm{ker}_{1/3}(a)$ and $\mathrm{kei}_{1/3}(a)$

The asymptotic expansions (a large) for the modulus and phase may be used to estimate $\mathrm{ker}_{1/3}a$ and $\mathrm{kei}_{1/3}a$. From Abramowitz and Stegun (1968) these are

$$\mathrm{ker}_\nu a = N_\nu \mathrm{Cos}\phi_\nu\ , \quad \mathrm{kei}_\nu a = N_\nu \mathrm{Sin}\phi_\nu$$

where

$$\ln N_\nu = -\frac{a}{\sqrt{2}} + \frac{1}{2}\ln\left(\frac{\pi}{2a}\right) + \frac{\mu - 1}{8\sqrt{2}}\,\frac{1}{a} + \frac{(\mu - 1)(\mu - 25)}{384\sqrt{2}}\,\frac{1}{a^3}$$

$$- \frac{(\mu - 1)(\mu - 13)}{128}\,\frac{1}{a^4} + O\left(\frac{1}{a^5}\right)$$

$$\phi_\nu = -\frac{a}{\sqrt{2}} - \left(\frac{\nu}{2} + \frac{1}{8}\right)\pi - \frac{\mu - 1}{8\sqrt{2}}\,\frac{1}{a} + \frac{\mu - 1}{16}\,\frac{1}{a^2}$$

$$+ \frac{(\mu - 1)(\mu - 25)}{384\sqrt{2}}\,\frac{1}{a^3} + O\left(\frac{1}{a^5}\right)$$

where $\mu = 4\nu^2$.

These expansions appear to be accurate (error less than 1%) for $a > 2$ (i.e. $r \gtrsim 2.1$).

APPENDIX G

Solution to the one-dimensional heat conduction equation for a semi-infinite composite solid

Consider the conduction of heat within the composite solid, initially at a uniform temperature, as sketched below.

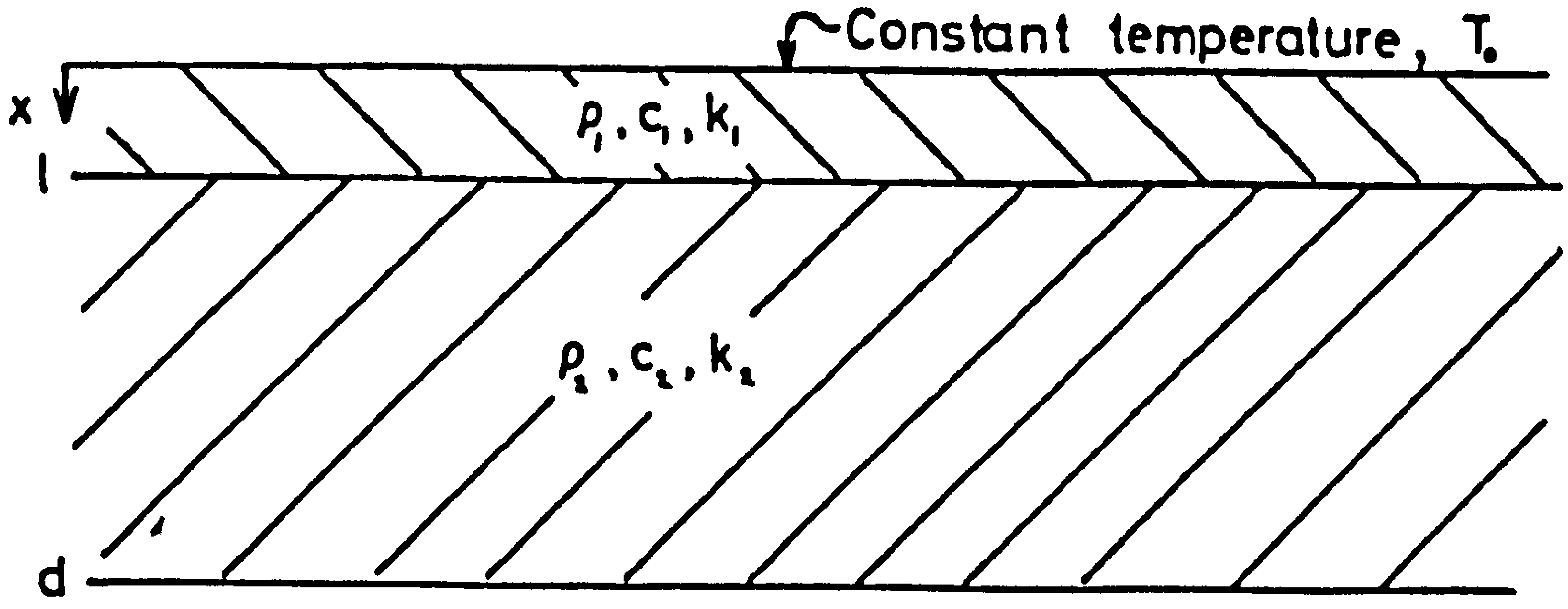

The linear heatconduction equations are

For $0 < x < \ell$
$$\frac{\partial^2 T_1}{\partial x^2} - \frac{1}{\alpha_1}\frac{\partial T_1}{\partial t} = 0 \qquad (1)$$

where $\alpha_1 = \frac{k_1}{\rho_1 c_1}$

For $\ell < x < d$
$$\frac{\partial^2 T_2}{\partial x^2} - \frac{1}{\alpha_2}\frac{\partial T_2}{\partial t} = 0 \qquad (2)$$

Equations (1) and (2) are solved subject to the following boundary conditions

(i) Since the heating film of a probe is normally maintained at a constant temperature (i.e. resistance), a constant temperature is specified along the surface -

$$T(o,t) = T_0 \qquad (3)$$

(ii) It is assumed that the media are in perfect thermal contact along the interface $x = \ell$ i.e.

$$T_1(\ell,t) = T_2(\ell,t) \tag{4}$$

$$k_1 \frac{\partial T_1}{\partial x}(\ell,t) = k_2 \frac{\partial T_2}{\partial x}(\ell,t) \tag{5}$$

(iii) In general $\ell \ll d$ so d may be treated as semi-infinite. It is assumed that initially the media are at the same temperature, so T effectively denotes the increase in temperature. Thus as $x \to \infty$ $T_2 \to 0$. (6)

The solution for $T(x,t)$ may be readily obtained by means of the Laplace transformation defined as

$$\bar{T}(x,p) = \int_0^\infty T(x,t)e^{-pt}\,dt \tag{7}$$

Hence, the governing equations and boundary conditions become

$$0 < x < \ell \qquad \frac{d^2\bar{T}_1}{dx^2} - \frac{p}{\alpha_1}\bar{T}_1 = 0 \tag{8}$$

$$x > \ell \qquad \frac{d^2\bar{T}_2}{dx^2} - \frac{p}{\alpha_2}\bar{T}_2 = 0 \tag{9}$$

$$x = 0 \qquad \bar{T}_1 = \frac{T_0}{p} \tag{10}$$

$$x = \ell \qquad \bar{T}_1 = \bar{T}_2 \;;\quad k_1 \frac{\partial \bar{T}_1}{\partial x} = k_2 \frac{\partial \bar{T}_2}{\partial x} \tag{11}$$

$$x \to \infty \qquad \bar{T}_2 \to 0 \tag{12}$$

The solution to equations (8) to (12) may be shown to be

$$0 < x < \ell \qquad \bar{T}_1(x,p) = \frac{T_0}{p}\left\{\frac{\cosh[r_1(x-\ell)] + \sigma\sinh[r_1(x-\ell)]}{\cosh r_1\ell + \sigma\sinh r_1\ell}\right\} \tag{13}$$

and

$$x > \ell \qquad \bar{T}_2(x,p) = \frac{T_0}{p}\left\{\frac{e^{-r_2(x-\ell)}}{\cosh r_1\ell + \sigma\sinh r_1\ell}\right\} \tag{14}$$

where

$$r_1 = \sqrt{\frac{p}{\alpha_1}},\; r_2 = \sqrt{\frac{p}{\alpha_2}},\; \sigma = \frac{k_2}{k_1}\sqrt{\frac{\alpha_1}{\alpha_2}} \tag{15}$$

The electrical power supplied to the hot film must balance the rate at which heat is conducted into the solid. Therefore, of particular interest is the heat flux at the plane x = 0, i.e.

$$q(0,t) = -k_1 \frac{\partial T_1}{\partial t}(0,t)$$

or

$$\overline{q}(0,p) = -k_1 \frac{\partial \overline{T}_1}{\partial t}(0,p)$$

Thus differentiating equation (13) gives

$$\overline{q}(0,p) = \frac{-k_1T_0}{2p}\left\{\frac{(1-\sigma)r_1e^{-r_1\ell} - (1+\sigma)r_1e^{r_1\ell}}{\cosh r_1\ell + \sigma\sinh r_1\ell}\right\} \quad (16)$$

From the definition of the hyperbolic functions, then

$$2\cosh r_1\ell + 2\sigma\sinh r_1\ell = (\sigma+1)e^{r_1\ell}(1 - ae^{-2r_1\ell})$$

where $a = \frac{\sigma - 1}{\sigma + 1}$

Thus equation (16) may be rewritten

$$\overline{q}(0,p) = \frac{k_1T_0r_1}{p}\left\{\frac{1 + ae^{-2r_1\ell}}{1 - ae^{-2r_1\ell}}\right\} \quad (17)$$

Since $|a| < 1$, then from the Binomial theorem

$$(1 - ae^{-2r_1\ell})^{-1} = \sum_{n=0}^{\infty} a^n e^{-2nr_1\ell}$$

Hence

$$\overline{q}(0,p) = \frac{k_1T_0r_1}{p}\left\{\sum_{n=0}^{\infty} a^n e^{-2nr_1\ell} + a\sum_{n=0}^{\infty} a^n e^{-2r_1\ell(n+1)}\right\} \quad (18)$$

The Laplace inverse transformation may now be performed - see Carslaw and Jaeger (1959)

$$q(0,t) = \frac{k_1T_0}{\sqrt{\pi\alpha_1 t}}\left\{1 + 2\sum_{n=1}^{\infty} a^n e^{-\frac{n^2\ell^2}{\alpha_1 t}}\right\} \quad (19)$$

Since $|a| < 1$ then $\sum_{n=1}^{\infty} a^n = \frac{a}{1-a}$.

If $\frac{\ell^2}{\alpha_1 t}$ is small then equation (19) may be approximated to

$$q(0,t) \simeq \frac{k_1 T_0}{\sqrt{\pi \alpha_1 t}} \left\{ 1 + \frac{2a}{1 - a} \right\}$$

or

$$q(0,t) \simeq \frac{k_1 T_0}{\sqrt{\pi \alpha_1 t}} \left(\frac{k_2 \rho_2 c_2}{k_1 \rho_1 c_1} \right)^{\frac{1}{2}}$$

APPENDIX H

Generation of heat in a wire conducting an electric current

Consider the conduction of heat in a wire, length 2ℓ and cross sectional area a, which is carrying an electric current i. Assuming the electrical resistance of the wire varies linearly with temperature, then the steady, linear, heat conduction equation may be written (see Carslaw and Jaeger, 1959)

$$\frac{d^2T}{dx^2} + \alpha \frac{i^2R_0}{2\ell ka} T = -\frac{i^2R_0}{2\ell ka}^{\dagger} \qquad (1)$$

where k is the thermal conductivity of the wire, α is the temperature coefficient of resistance at T_0 and R_0 is the resistance of the wire at temperature T_0. Assuming the ends of the wire are maintained at a constant temperature T_0, the solution to equation (1) is

$$T - T_0 = \frac{1}{\alpha}\left[\frac{\cos p(\ell - x)}{\cos p\ell} - 1\right] \qquad (2)$$

where $\qquad p^2 = \alpha \frac{i^2R_0}{2\ell ka}$.

The total resistance of the wire is

$$R = R_0 + \frac{R_0}{2\ell}\int_0^{2\ell} \alpha(T - T_0)dx\ . \qquad (3)$$

Thus integrating equation (2) gives

$$\frac{R - R_0}{R_0} = \frac{\tan p\ell}{p\ell} - 1$$

Hence the power dissipated in the wire, i^2R, is

$$i^2R = i^2R_0 \frac{\tan p\ell}{p\ell}\ . \qquad (4)$$

The mean temperature rise of the wire may also be obtained from

---

† The Thomson effect and heat loss through radiation are ignored.

equation (2) -

$$\Delta T_{mean} = \frac{\tan p\ell - p\ell}{p\ell} \qquad (5)$$

Equations (4) and (5) may be used to examine the theoretical variation of i^2R with ΔT for the nickel film of the glue-on probe. (Relative to the film the 2 nickel/silver plates are massive so it is reasonable to assume that the ends of the film are kept at a constant temperature.) From figure 4.2, $2\ell \simeq 1 \times 10^{-3}$m, $a \simeq 2 \times 10^{-11}$m^2. Assuming the resistivity of nickel at 20°C is $7 \times 10^{-8}\Omega$m then the resistance of the film = 3.5Ω (20°C). Finally, assuming the temperature coefficient of resistance at 20°C ≃ 0.0054/°C gives $p\ell \simeq 65i$. Thus for the nickel film, equations (4) and (5) become

$$i^2R = 0.0538i \tan 65i \quad , \qquad (6)$$

$$\Delta T = \frac{\tan 65i - 65i}{0.351i} \quad . \qquad (7)$$

These results may also be used to estimate how much heat is conducted laterally out of the film into the nickel/silver plates. (In the above problem this represents the only conductive heat loss path as it is assumed that the film is embedded in a perfect insulator.) From figure 4.7 at ΔT = 100°C, $i^2R \simeq 1.2 \times 10^{-3}$ watts. However, in figure 4.6 the measured value of i^2R at ΔT = 100°C is approximately 40×10^{-3} watts. Clearly the heat conducted into the end plates is small relative to that conducted into the substrate. A similar conclusion may also be obtained by simply considering the thermal conductivities of nickel and kapton and the geometry of the film.

APPENDIX I

Estimation of the integral properties from the laminar boundary layer velocity profiles

For two-dimensional, incompressible flow, the displacement thickness of the boundary layer may be defined as -

$$\delta^* = \int_0^\infty 1 - \frac{u}{U_\infty}\, dy \qquad (1)$$

and the momentum thickness -

$$\theta = \int_0^\infty \frac{u}{U_\infty}\left(1 - \frac{u}{U_\infty}\right) dy \,. \qquad (2)$$

The following procedure was adopted for determining δ^* and θ from the laminar velocity profiles.

Consider the momentum thickness. Equation (2) may be rewritten

$$\theta = \sqrt{\frac{\nu x}{U_\infty}}\left\{\int_0^{\eta_{min}} v(1 - v)d\eta + \int_{\eta_{min}}^{\eta_{max}} v(1 - v)d\eta + \int_{\eta_{max}}^{\infty} v(1 - v)d\eta\right\} \qquad (3)$$

where $v = \frac{u}{U_\infty}$ and $\eta = y\sqrt{\frac{U_\infty}{\nu x}}$.

The first and last integrals in equation (3) were estimated by numerically integrating (using Simpson's rule) the tabulated Blasius solution. (η_{min} and η_{max} may be replaced by v_{min} and v_{max}.) The middle integral was estimated (using trapezoidal integration) from the main 'body' of the measured velocity profile. (y_0 is not required.)

The contribution to θ due to the first integral for $0.25 < v_{min} < 0.6$ was then approximated by the best fitting quadratic (in terms of v_{min}):

$$\int_0^{y_{min}} v(1 - v)d\eta \simeq - 0.05656 + 0.4428v_{min} + 0.3766v_{min}^2 \qquad (4)$$

For the range of v_{min}, the contribution to the displacement thickness was estimated as

$$\int_0^{v_{min}} 1 - v \, d\eta \simeq 0.0232 + 2.8446v_{min} - 1.172v_{min}^2 \qquad (5)$$

For $v_{max} > 0.95$ the contribution to θ due to third integral in equation (3) was approximated by the expression

$$\int_{v_{max}}^{1} v(1 - v)d\eta \simeq 2.3846 - 4.2513v_{max} + 1.8663v_{max}^2 \qquad (6)$$

Equation (6) was also found to be adequate for estimating the corresponding contribution to δ^*.

The contribution to θ and δ^* estimated by equations (4), (5) and (6) must be factored by $\sqrt{\frac{\nu x}{U_\infty}}$. From figures 5.5 and 5.7 the value of x may be approximated by the expression

$$x = x_m + 0.06 \qquad (7)$$

where x_m is the measured length from the leading edge (in metres).

APPENDIX J

Outline of Pfeil and Sticksel's law of the wall

By examining the influence of pressure gradient upon the velocity profile near the wall of a turbulent boundary layer, Pfeil and Sticksel (1982) introduce a single explicit algebraic relationship describing the velocity profile from the wall to the outer edge of the semi-logarithmic region. By considering fully developed turbulent channel flow they show that the velocity profile is not only a function of y^+ but also of pressure gradient. At the wall, and in the immediate vicinity of the wall, they suggest that the pressure forces must balance the viscous forces.

If the changes in longitudinal and transverse velocity fluctuations in the streamwise direction (x) for fully developed channel flow may be neglected then

$$\frac{dP}{dx} = \frac{d\tau}{dy} \qquad (1)$$

Assume $\tau = \tau_i - \rho\overline{u'v'}$ and let $P^+ = \frac{\nu}{\rho u_\tau^3}\frac{dP}{dx}$

where τ_i is the viscous shear stress

Then dividing equation (1) by τ_w gives

$$P^+ = \frac{\partial}{\partial y^+}\left(\frac{\partial u^+}{\partial y^+} - \frac{\rho\overline{u'v'}}{\tau_w}\right) \qquad (2)$$

Upon integrating (the constant of integration = -1) and rearranging

$$-\frac{\rho\overline{u'v'}}{\tau_w} = 1 + P^+y^+ - \frac{\partial u^+}{\partial y^+} \qquad (3)$$

Pfeil and Sticksel propose that the velocity profile from the wall to the outer edge of the semi-logarithmic layer may be described by the following expression

$$u^+ = \frac{1}{\kappa}\ln(1 + a_1y^+) + C_1\left[1 - e^{-a_2y^+}(1 + a_3y^+)\right] \qquad (4)$$

Differentiating equation (4) with respect to y^+ and inserting into equation (3) gives

$$-\frac{\rho\overline{u'v'}}{\tau_w} = 1 + P^+y^+ - \frac{a_1}{\kappa}\,\frac{1}{1 + a_1y^+} - C_1e^{-a_2y^+}(a_2 - a_3 + a_2a_3y^+) \qquad (5)$$

Expanding $(1 + a_1y^+)^{-1}$ and $e^{-a_2y^+}$ and using Reichardt's criterion that the Reynolds stress in the immediate vicinity of the wall must be at least proportional to y^3 gives the following relations

$$1 - \frac{a_1}{\kappa} - C_1(a_2 - a_3) = 0 \qquad (6)$$

$$P^+ + \frac{a_1^2}{\kappa} + C_1a_2(a_2 - 2a_3) = 0 \qquad (7)$$

$$\frac{a_1^3}{\kappa} + \tfrac{1}{2}C_1a_2^2(a_2 - 3a_3) = 0 \qquad (8)$$

A fourth relationship is obtained by ensuring that at large y^+ the new law, equation (5), merges with the semi-logarithmic law. This gives the condition

$$C - C_1 - \frac{1}{\kappa}\ln a_1 = 0 \qquad (9)$$

For the current experiments $P^+ = 0$ so the constants a_1, a_2, a_3, C_1 appearing in equation (5) depend solely upon the constants appearing in the semi-logarithmic law - κ and C.

Solution

From equation (9) C_1 may be expressed in terms of a_1, κ and C and equations (6), (7) and (8) used to find a_1, a_2 and a_3. The resulting non-linear equations are solved using the Newton-Raphson technique - i.e.

$$f_i(a_1^{k-1},a_2^{k-1},a_3^{k-1}) + \sum_{j=1}^{3} \left.\frac{\partial f}{\partial a_i}\right|_{a_i^{k-1}} \cdot (a_j^k - a_j^{k-1}) = 0 \qquad i = 1,2,3.$$

Results

κ	C	a_1	a_2	a_3	C_1
0.40	5.5	0.2251	0.1739	0.1266	9.2217
0.41	5.0	0.2385	0.1862	0.1369	8.4966
0.42	5.45	0.2354	0.1809	0.1314	8.8944
0.41	5.25	0.2342	0.1814	0.1327	8.7905

APPENDIX K

Estimation of the integral properties from the turbulent boundary layer velocity profiles

The following procedure was used for the calculation of δ^* and θ from the turbulent boundary layer profile measurements.

Consider the momentum thickness:

$$\theta = \int_0^\infty \frac{u}{U_\infty} \left(1 - \frac{u}{U_\infty}\right) dy \tag{1}$$

The integral may be considered in 2 parts:

$$\theta = \frac{\nu}{U_\infty} \int_0^{y^+_{min}} u^+\left(1 - \sqrt{\frac{C_f}{2}}\, u^+\right)dy^+ + \int_{y_{min}}^{y_{max}} \frac{u}{U_\infty}\left(1 - \frac{u}{U_\infty}\right)dy. \tag{2}$$

where $y^+_{min} = \frac{y_{min}\, u_\tau}{\nu}$, y_{min} is a measured point in the profile corresponding to $y^+ \sim 70$ and y_{max} was judged to correspond with the mean boundary layer thickness defined as $y = \delta$ at $\frac{u}{U_\infty} = 0.995$.

Similarly, the displacement thickness may be written as

$$\delta^* = \frac{\nu}{U_\infty} \int_0^{y^+_{min}} \sqrt{\frac{2}{C_f}} - u^+ dy^+ + \int_{y_{min}}^{y_{max}} 1 - \frac{u}{U_\infty}\, dy \quad . \tag{3}$$

The integrals over the range $0 \rightarrow y^+_{min}$ in equations (2) and (3) were evaluated using the universal velocity profile, $u^+ = f(y^+)$, of Pfeil and Sticksel (1982). The integrals $\int_0^{y^+_{min}} u^+ dy^+$ and $\int_0^{y^+_{min}} u^{+2} dy^+$ were evaluated and the results approximated by the following:

$$\int_0^{y^+_{min}} u^+ dy^+ \simeq -107.155 + 12.391 y^+_{min} + 0.02081 y^{+2}_{min} \tag{4}$$

$$\int_0^{y^+_{min}} u^{+2} dy^+ \simeq -1891.32 + 149.128 y^+_{min} + 0.61546 y^{+2}_{min} \tag{5}$$

for $15 < y^+_{min} < 120$.

The integrals over the range y_{min} to y_{max} in equations (2) and (3) were estimated using trapezoidal integration on the measured velocity profile. The value of C_f (and hence u_τ) was estimated using the Preston tube results. The deduced values of δ^* and θ were found to be relatively insensitive to the assumed value of C_f.

At $y^+_{min} \simeq 70$ the contribution to δ^* was approximately 20% whilst the contribution to $\theta \simeq 12\%$.

APPENDIX L

Numerical application of Clauser's technique

Assuming the semi-logarithmic law of the wall, then from equation (6.33) we have

$$\frac{u}{U_\infty} = \sqrt{\frac{C_f}{2}}\,\frac{1}{\kappa}\ln\frac{yU_\infty}{\nu} + \sqrt{\frac{C_f}{2}}\,C + \sqrt{\frac{C_f}{2}}\,\frac{1}{\kappa}\ln\sqrt{\frac{C_f}{2}}\,. \qquad (1)$$

For convenience let $v = \frac{u}{U_\infty}$, $r = \ln\frac{yU_\infty}{\nu}$, $\alpha = \sqrt{\frac{C_f}{2}}$

Then $$v = \frac{\alpha r}{\kappa} + \alpha C + \frac{\alpha}{\kappa}\ln\alpha\,. \qquad (2)$$

Assuming values for κ and C, then, given a data set of $(v_i, r_i)_{i=1,n}$ the best value of α may be determined based on the least square error criterion:

The total squared error for a given value of α will be

$$E^2 = \sum_{i=1}^{n} (u_i - \alpha A r_i - \alpha B - \alpha A \ln\alpha)^2$$

Minimising this with respect to α

$$\text{i.e.}\quad \frac{\partial E^2}{\partial \alpha^2} = 0$$

$$\Rightarrow \quad A\sum_1^n ur + (A + B)\Sigma u + A\ln\alpha\Sigma u = \alpha\{A^2\sum_1^n y^2 r + (A^2 + 2AB)\sum_1^n r$$

$$+ n(AB + B^2)\}$$

$$+ \alpha\ln\alpha\{n(A^2 + 2AB) + 2A^2\sum_1^n r + nA^2\ln\alpha\}$$

This equation may be solved for $\alpha(\sqrt{\frac{C_f}{2}})$ using the Newton-Raphson method.

(a) LUDWIEG'S PROBE

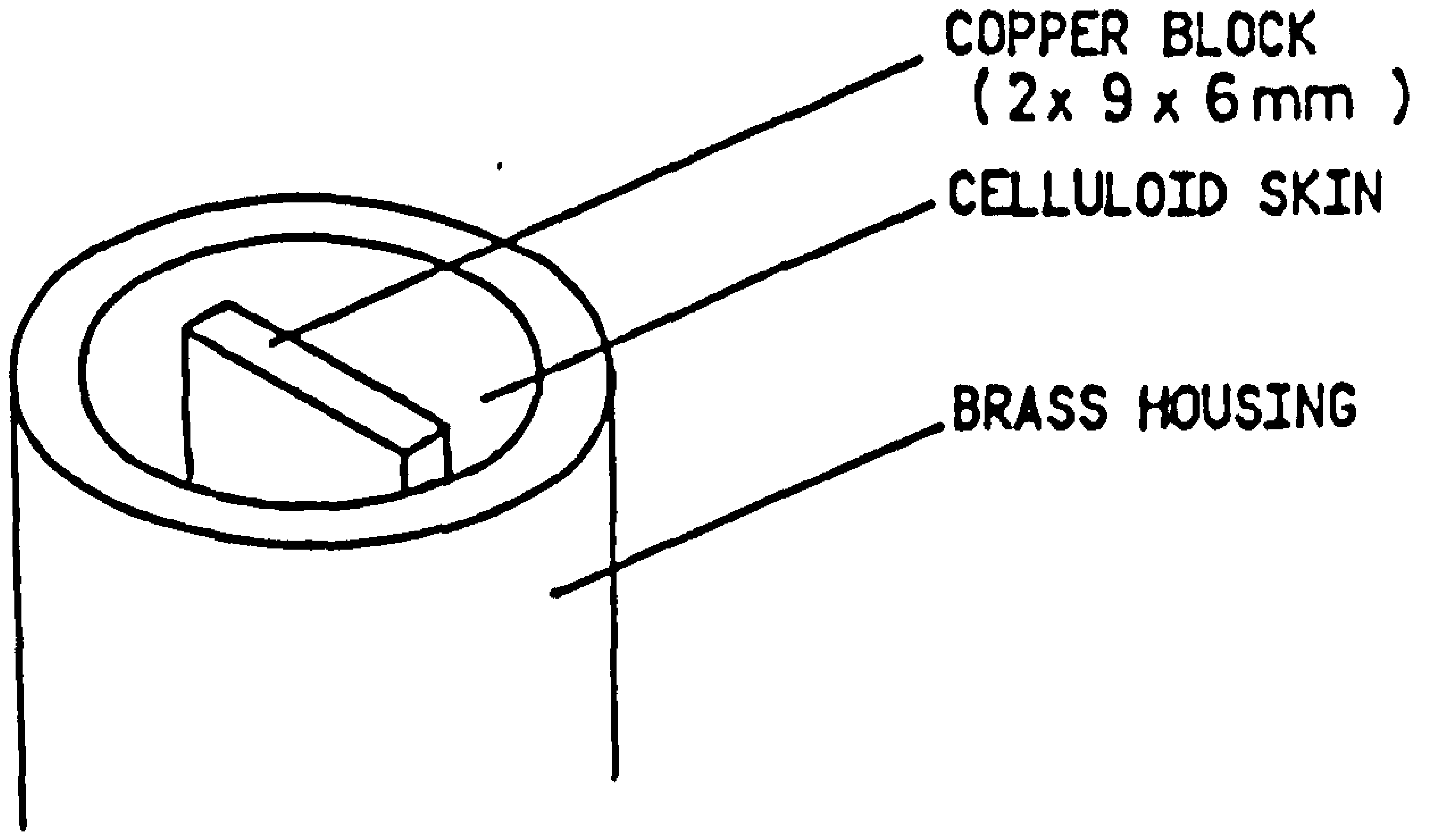

(b) THE MURTHY-ROSE PROBE

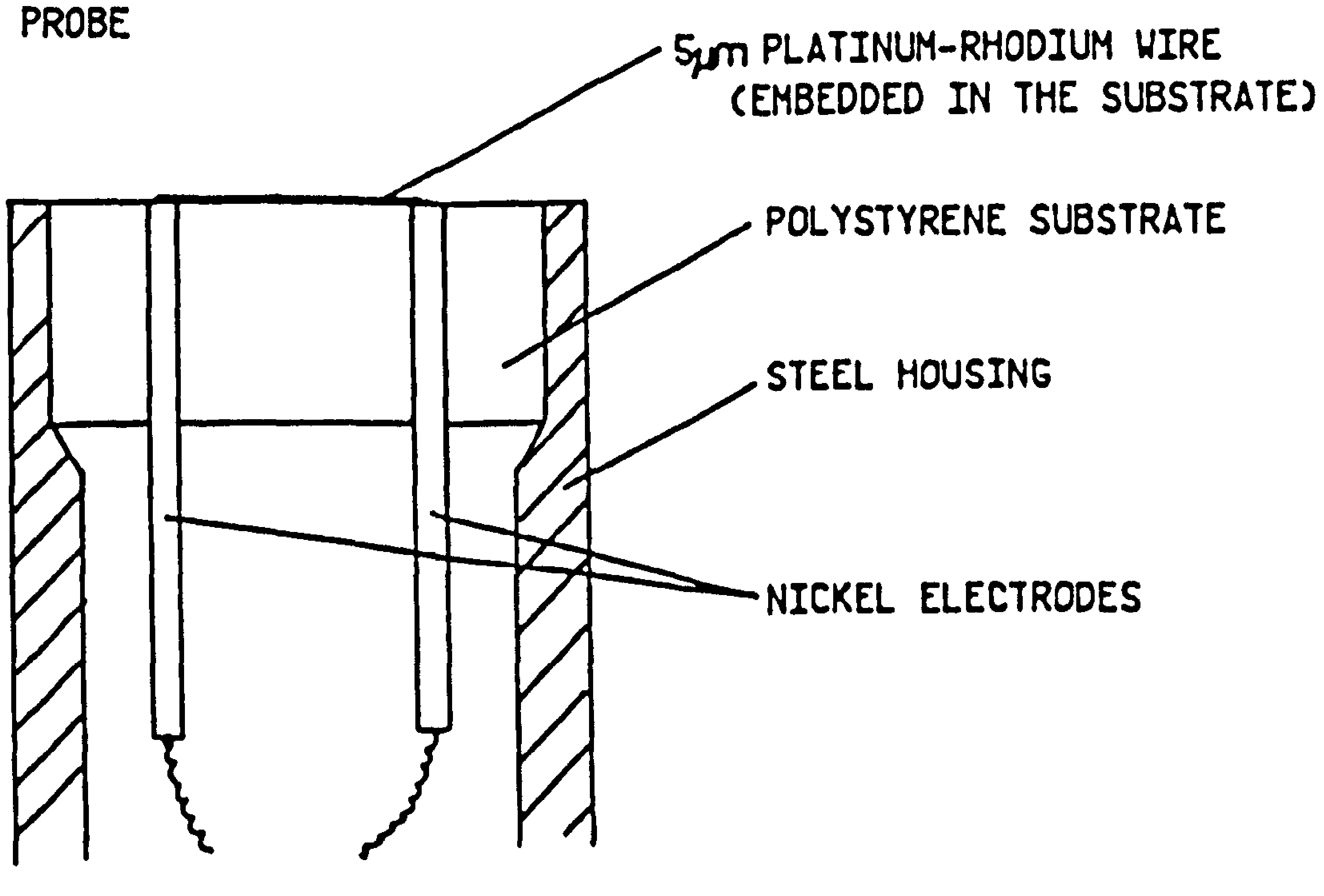

FIG. 1.1 DETAILS OF LUDWIEG'S PROBE AND THE MURTHY-ROSE PROBE

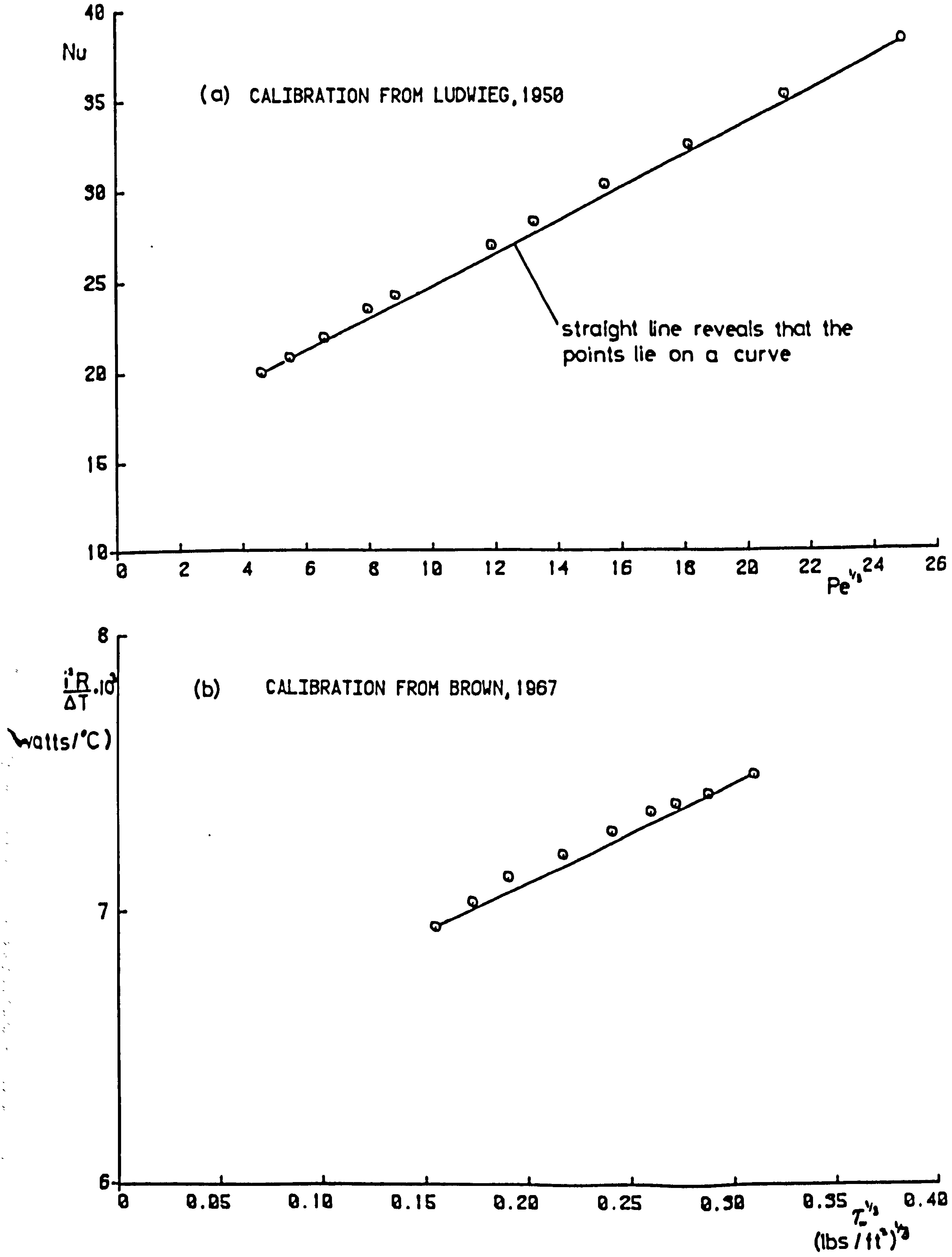

FIG. 1.2 TYPICAL CALIBRATIONS IN AIR FLOWS

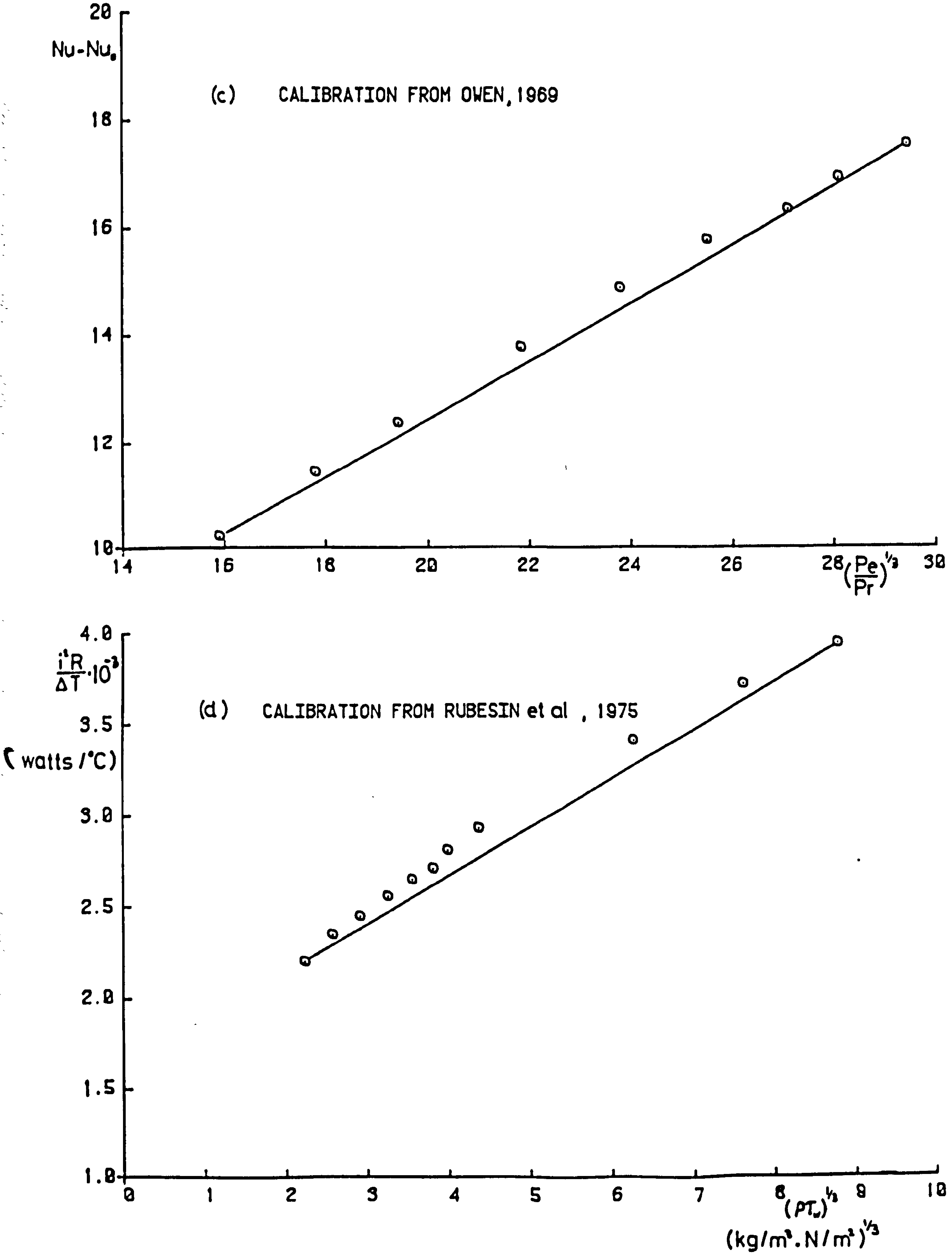

FIG. 1.2 TYPICAL CALIBRATIONS IN AIR FLOWS

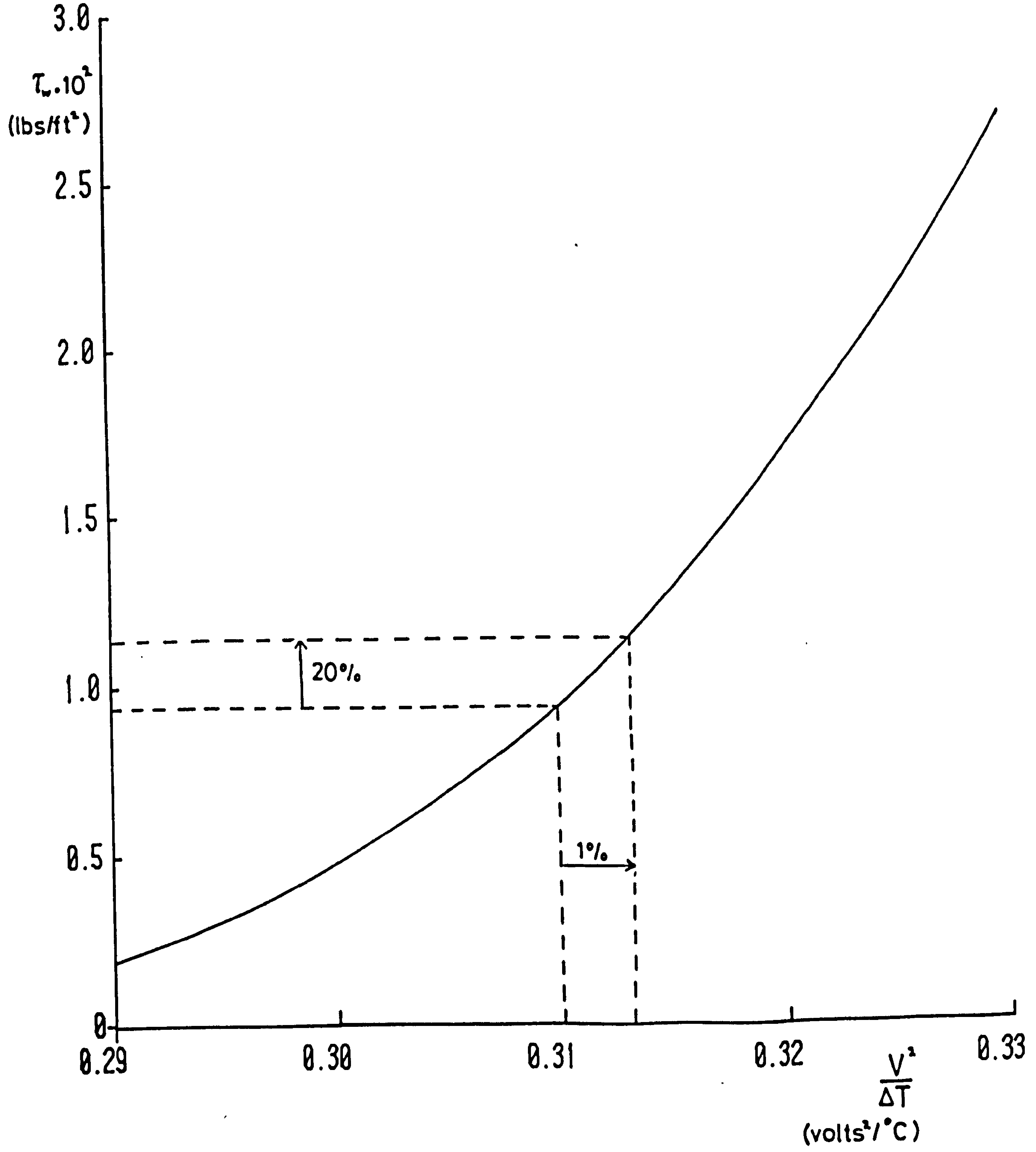

FIG. 1.3 INVERTED CALIBRATION FROM POLL + WATSON 1984

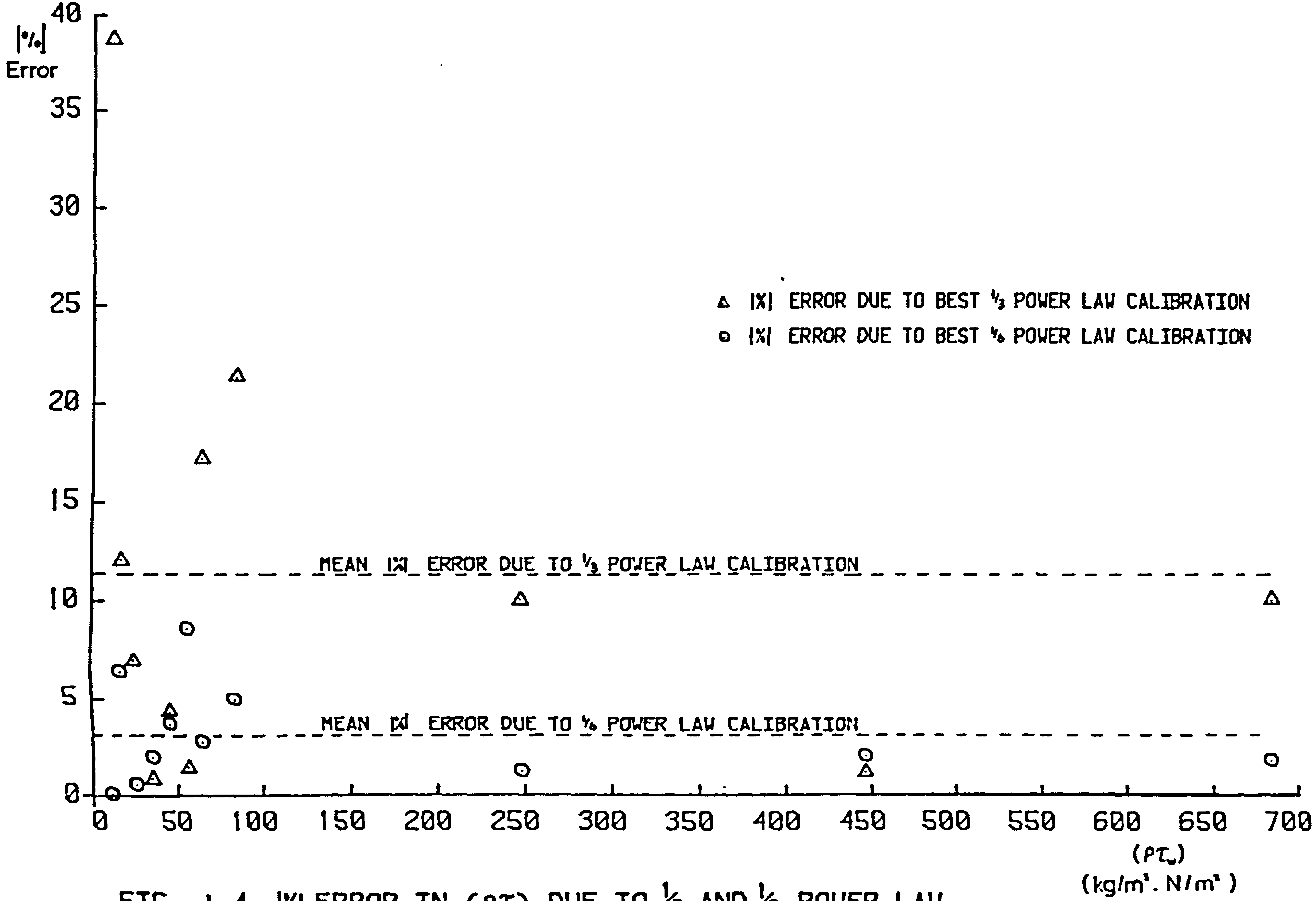

FIG. 1.4 |%| ERROR IN $(\rho\tau_w)$ DUE TO ⅓ AND ⅙ POWER LAW CALIBRATIONS FITTED TO RUBESIN'S RESULTS

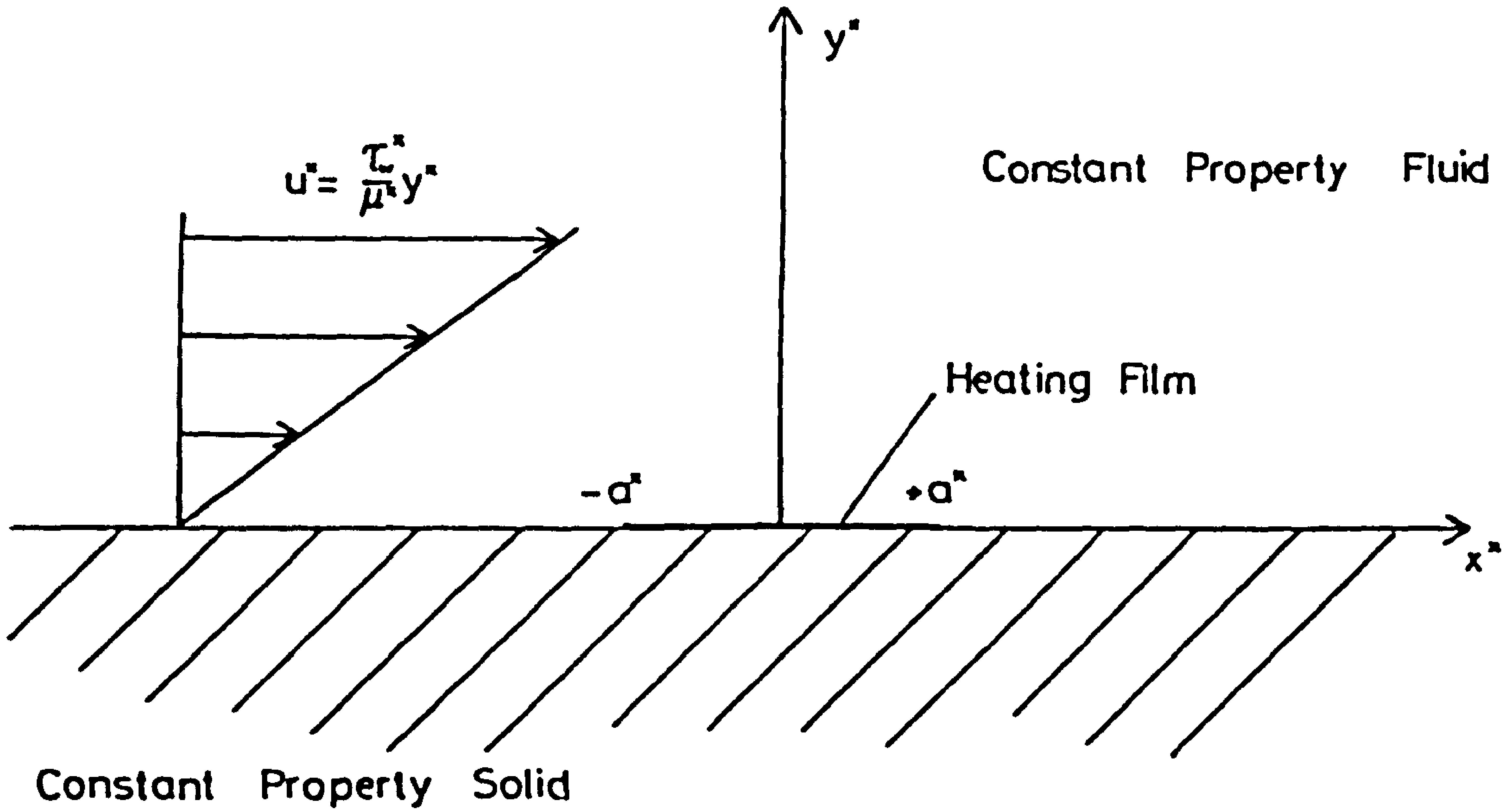

FIG. 3.1 THE HEAT CONDUCTION/CONVECTION PROBLEM

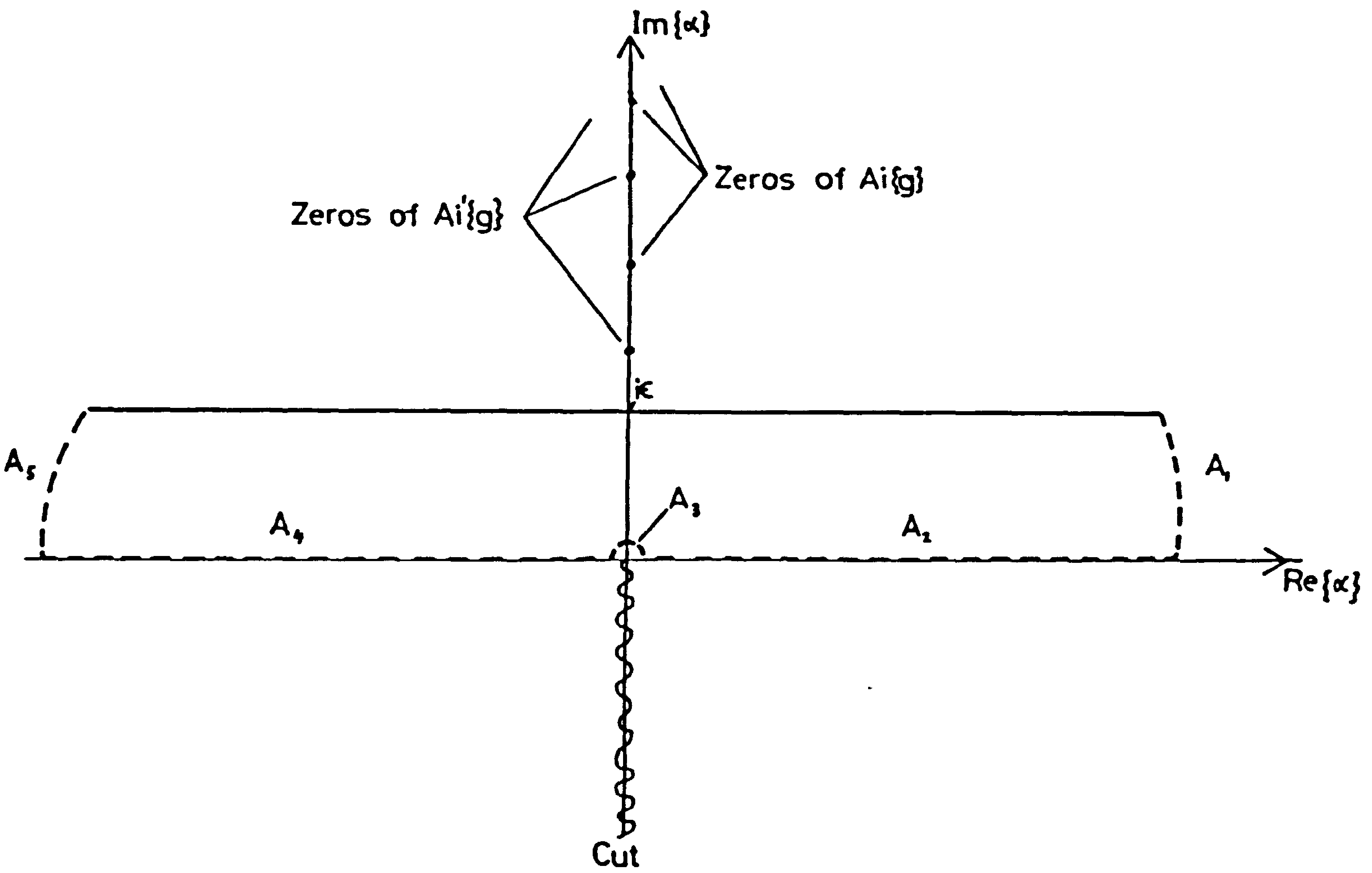

FIG. 3.2 INTEGRATION CONTOUR FOR APPLICATION OF THE FOURIER INVERSE TRANSFORMATION

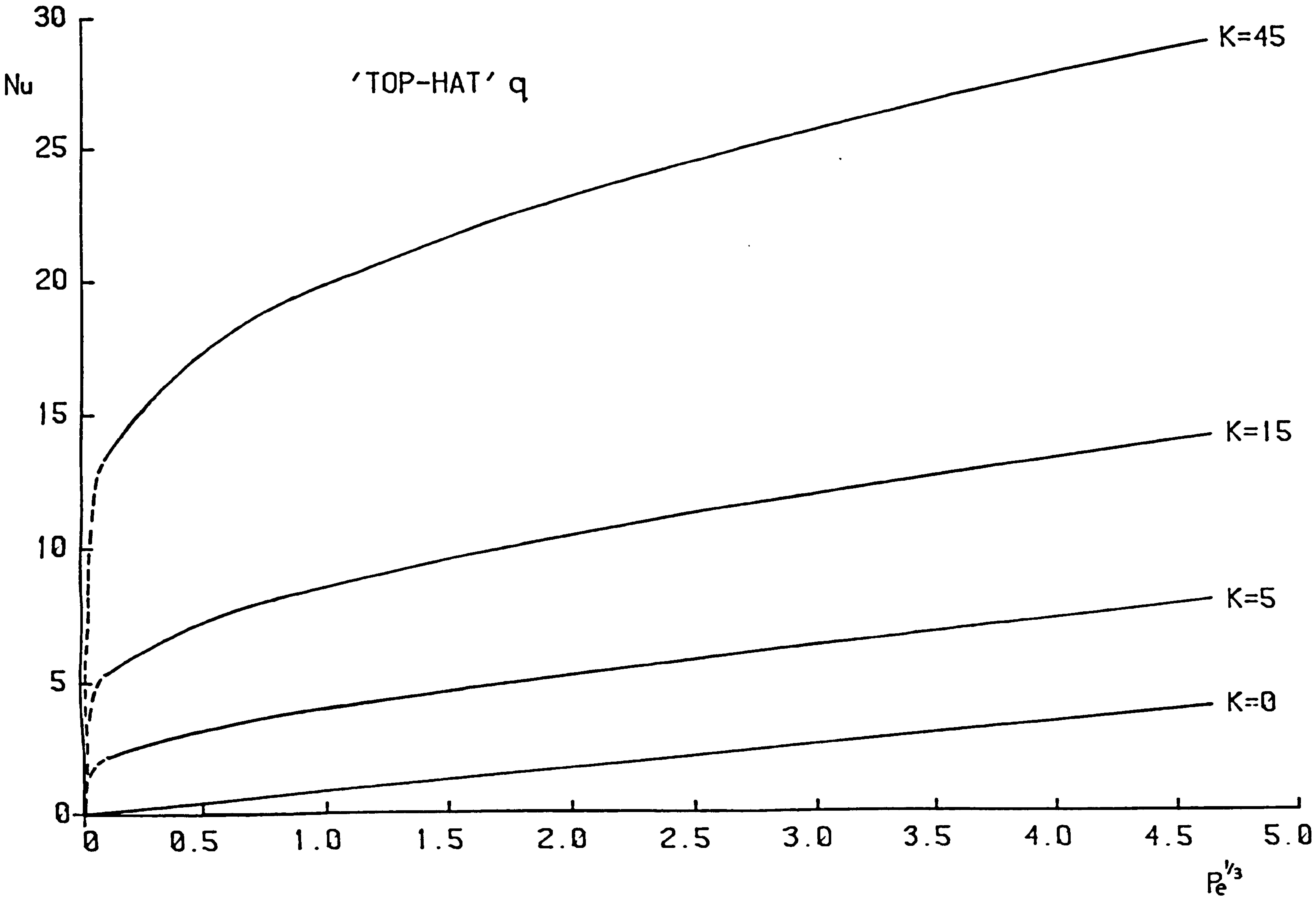

FIG. 3.3 VARIATION OF Nu WITH $P_e^{1/3}$ AND K

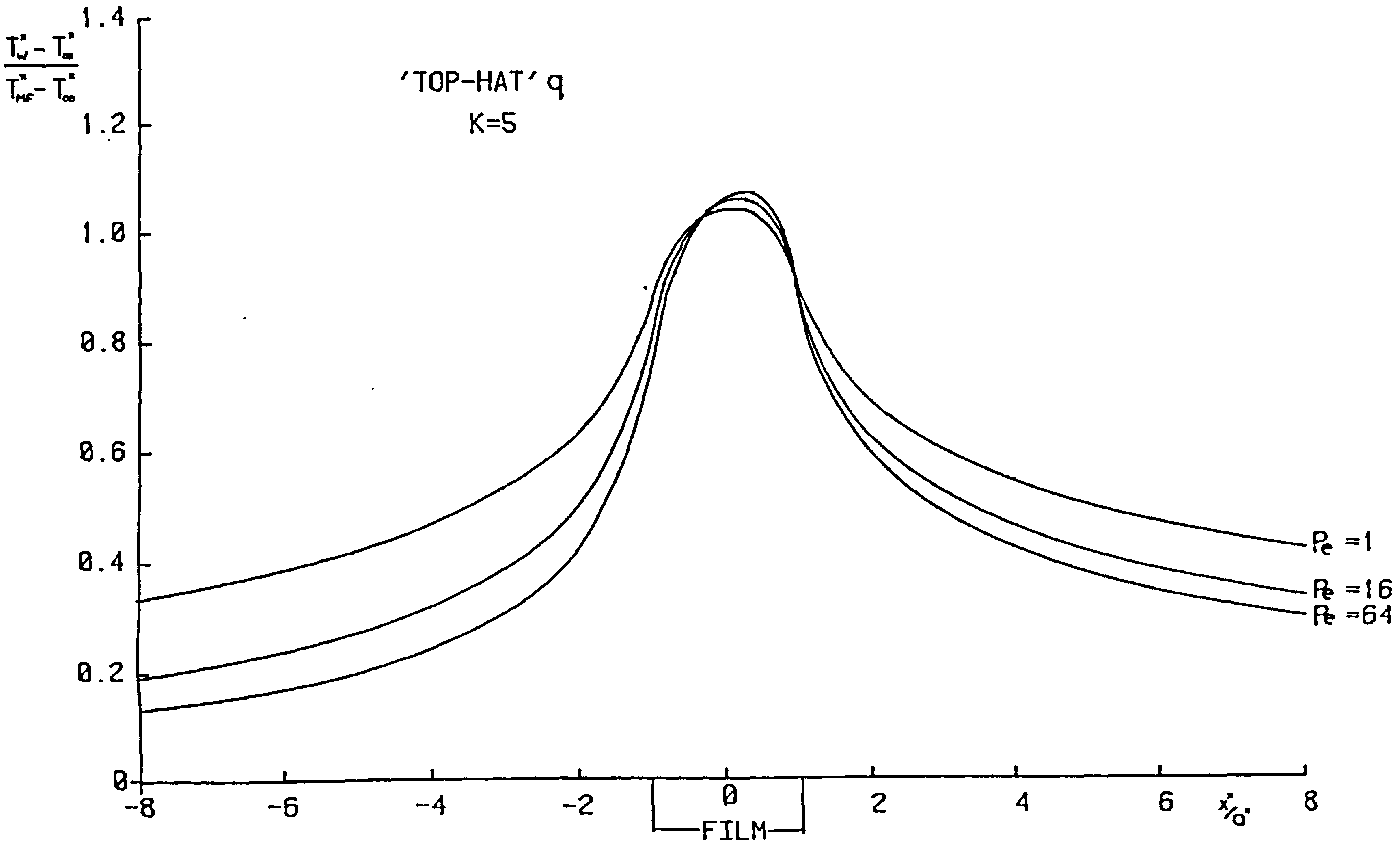

FIG. 3.4 WALL TEMPERATURE DISTRIBUTION - EFFECT OF P_e

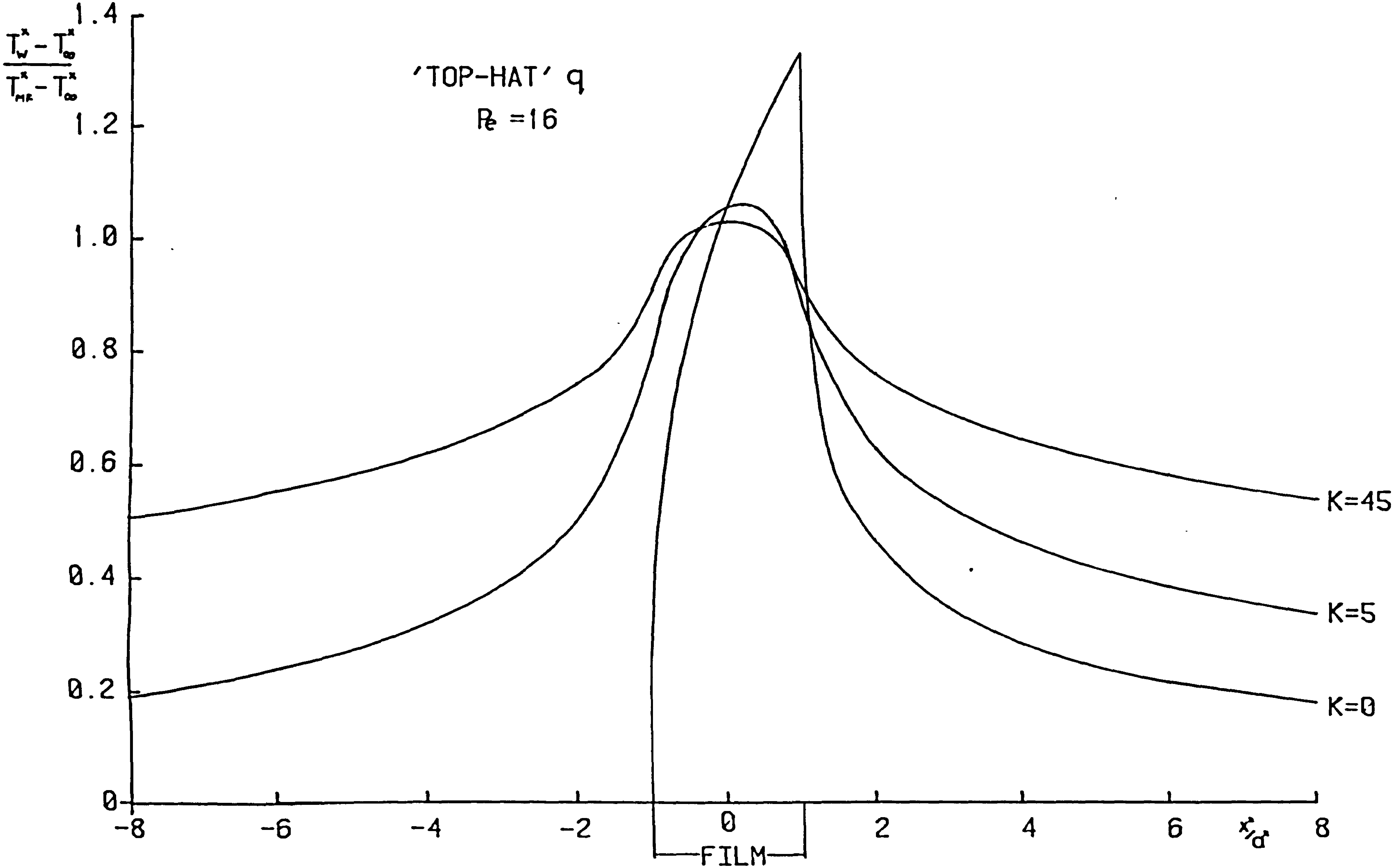

FIG. 3.5 WALL TEMPERATURE DISTRIBUTION - EFFECT OF K

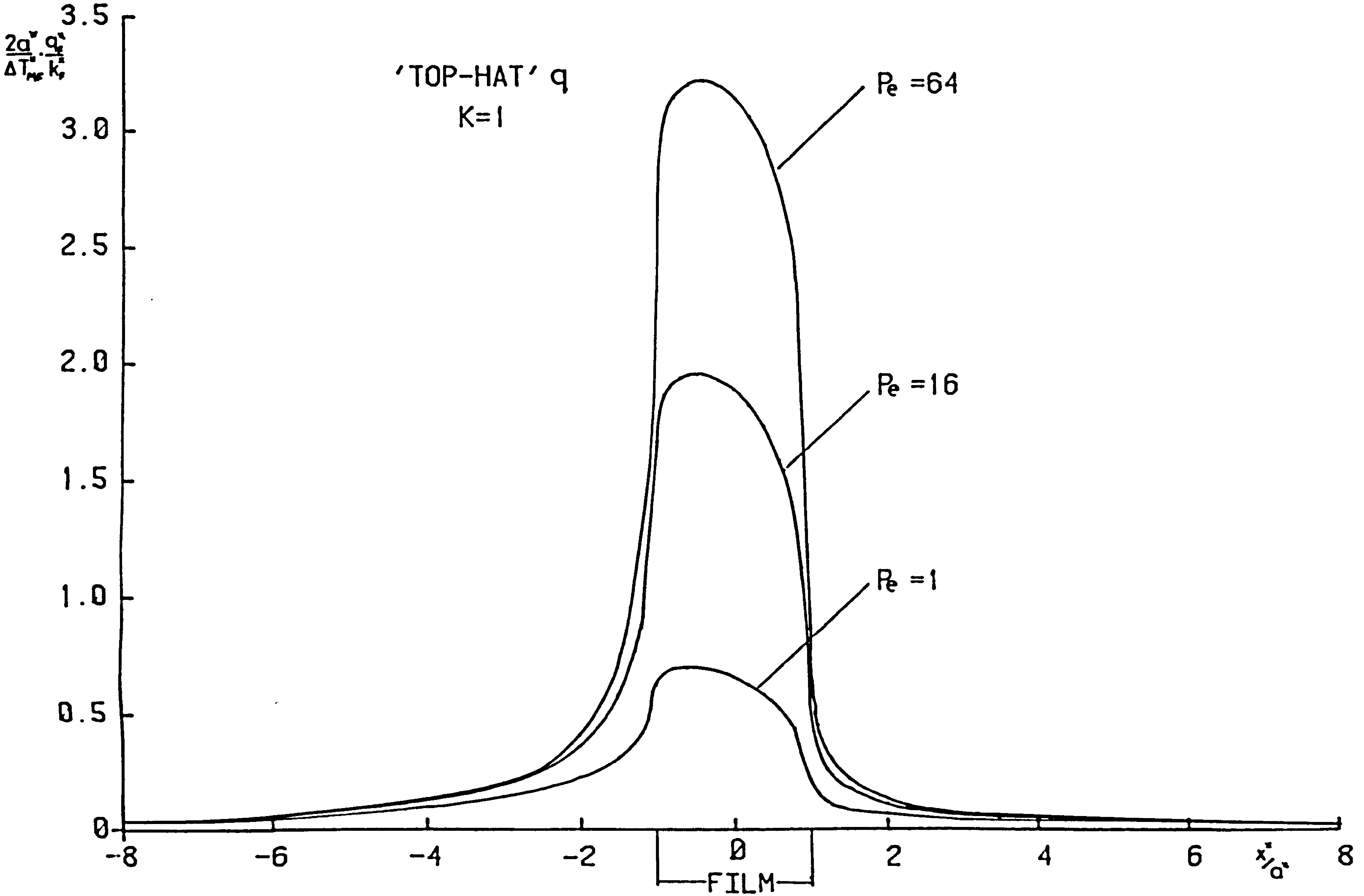

FIG. 3.6 SURFACE HEAT FLUX DISTRIBUTION - EFFECT OF P_e

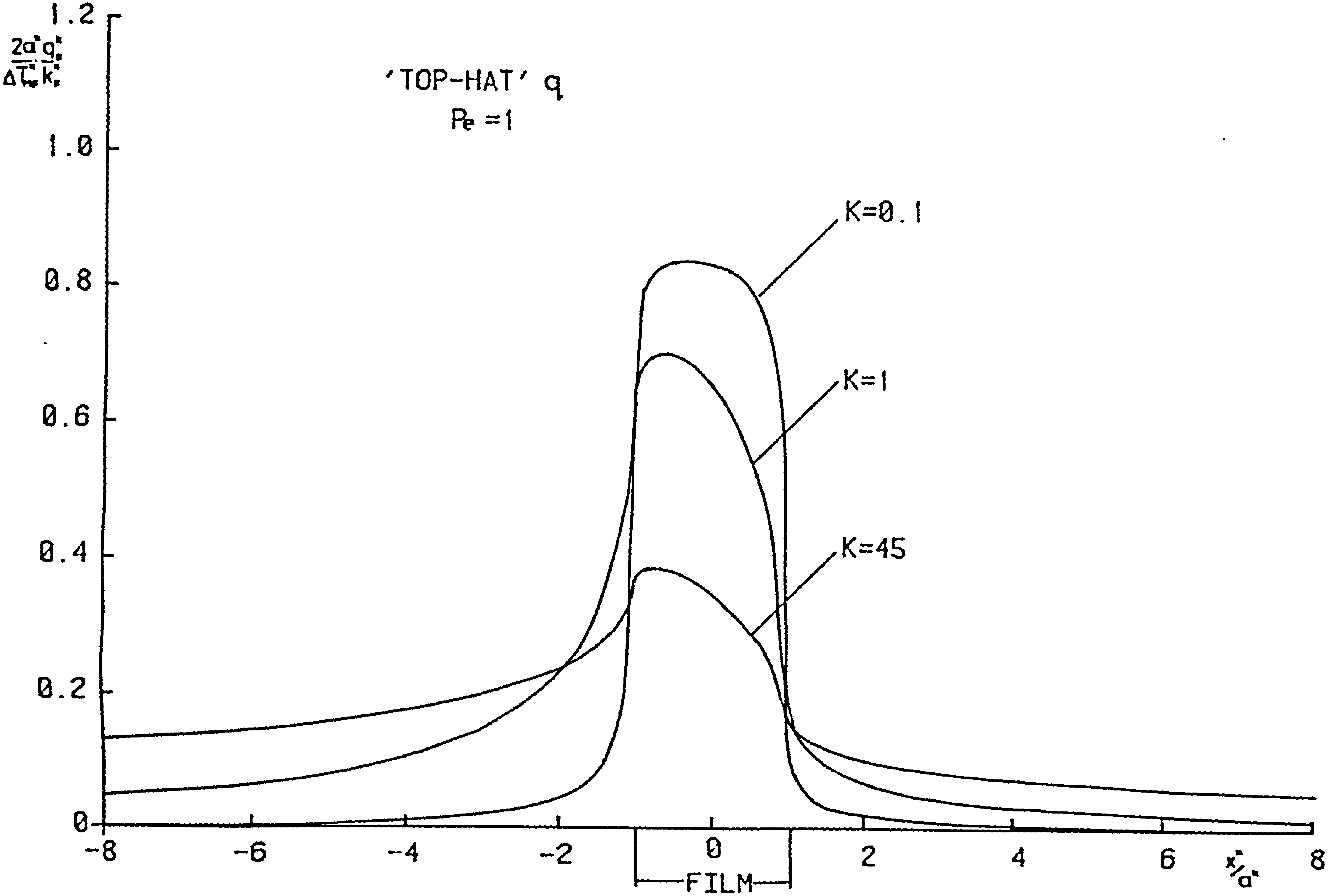

FIG. 3.7 SURFACE HEAT FLUX DISTRIBUTION - EFFECT OF K

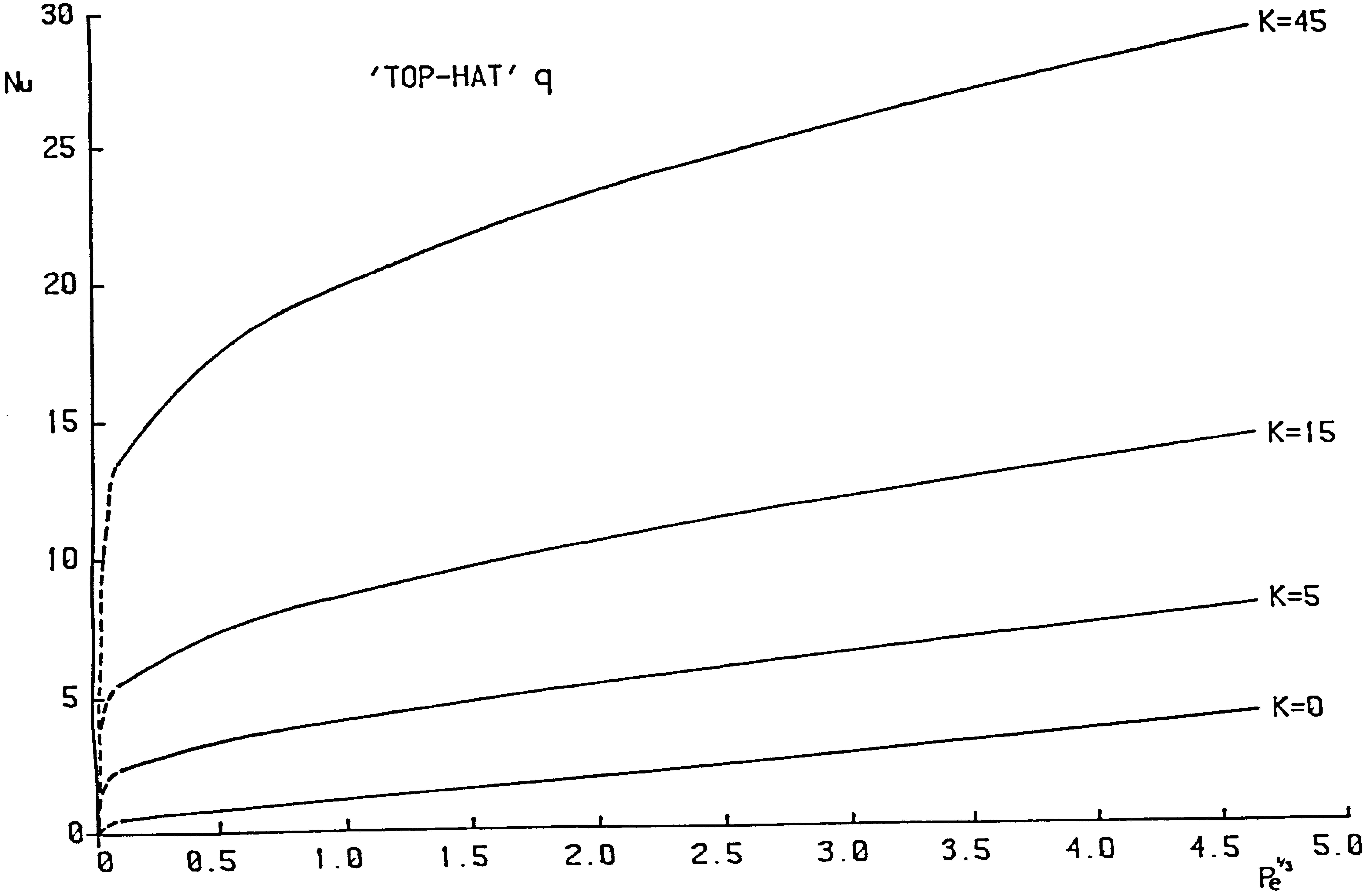

FIG. 3.8 VARIATION OF Nu WITH $Pe^{1/3}$ AND K
(INCLUDING LONGITUDINAL DIFFUSION)

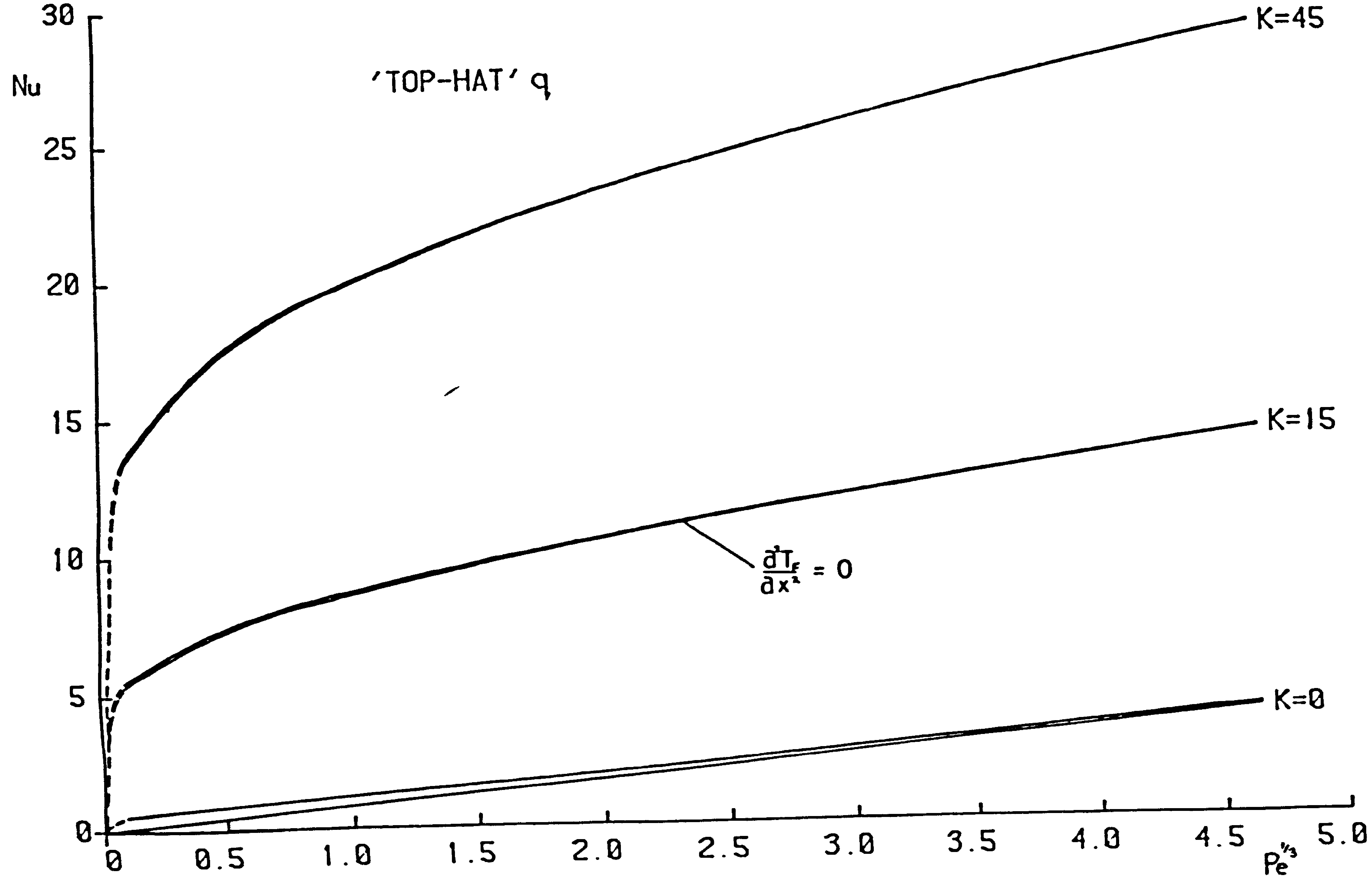

FIG. 3.9 EFFECT OF LONGITUDINAL DIFFUSION UPON THE $Nu - Pe^{1/3}$ RELATIONSHIP

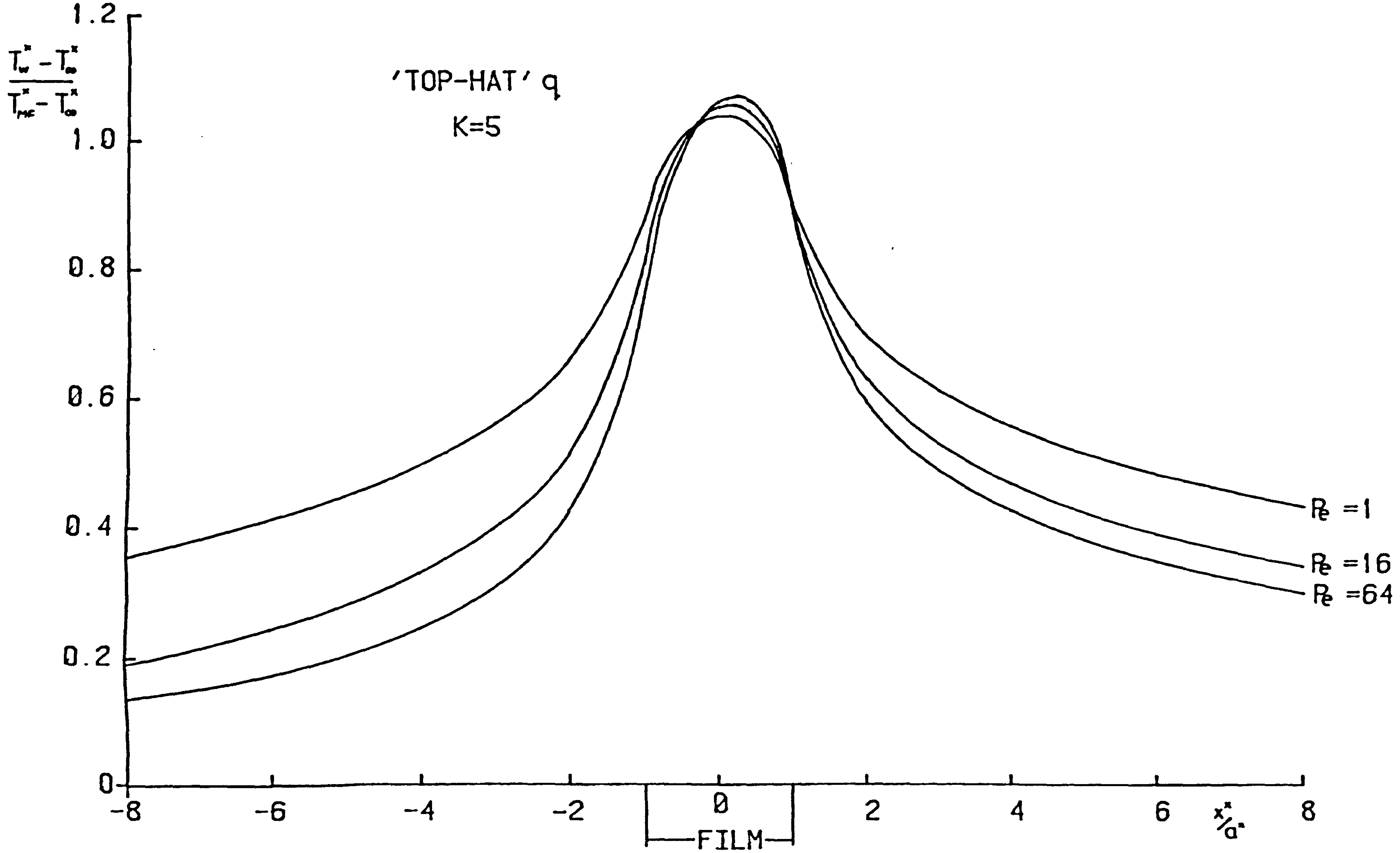

FIG. 3.10 WALL TEMPERATURE DISTRIBUTION - EFFECT OF Pe
(INCLUDING LONGITUDINAL DIFFUSION)

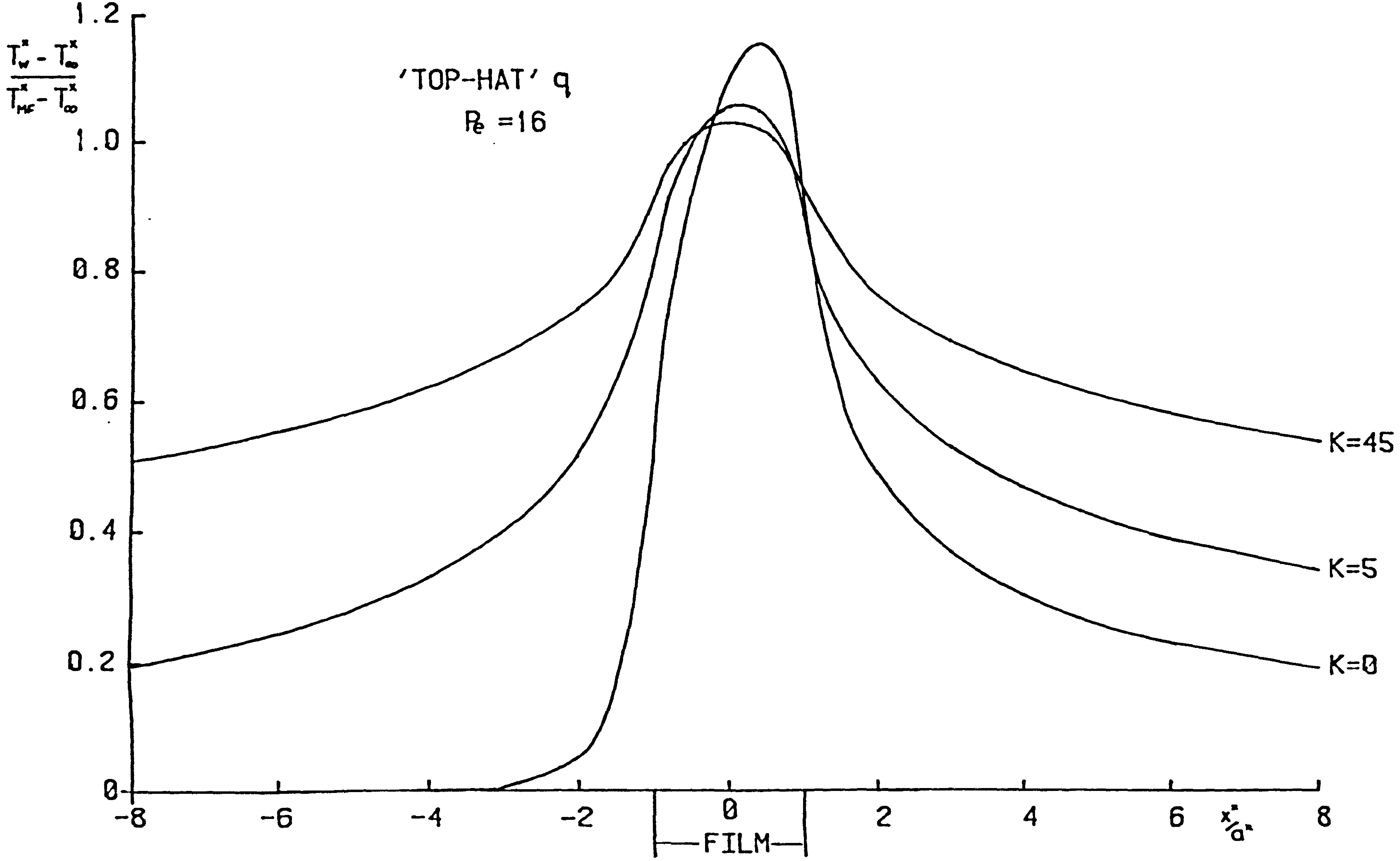

FIG. 3.11 WALL TEMPERATURE DISTRIBUTION - EFFECT OF K
(INCLUDING LONGITUDINAL DIFFUSION)

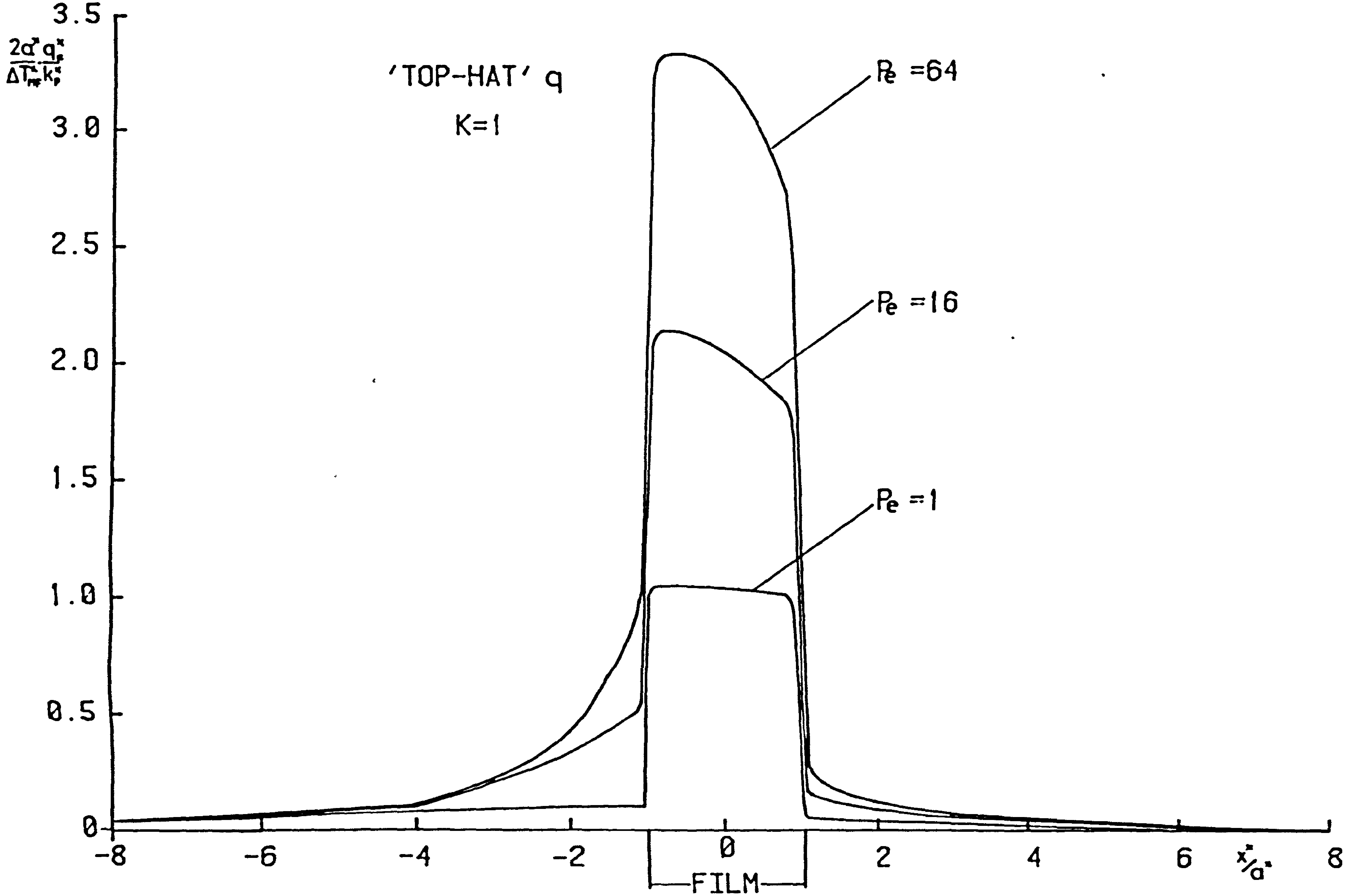

FIG. 3.12 SURFACE HEAT FLUX DISTRIBUTION - EFFECT OF Pe
(INCLUDING LONGITUDINAL DIFFUSION)

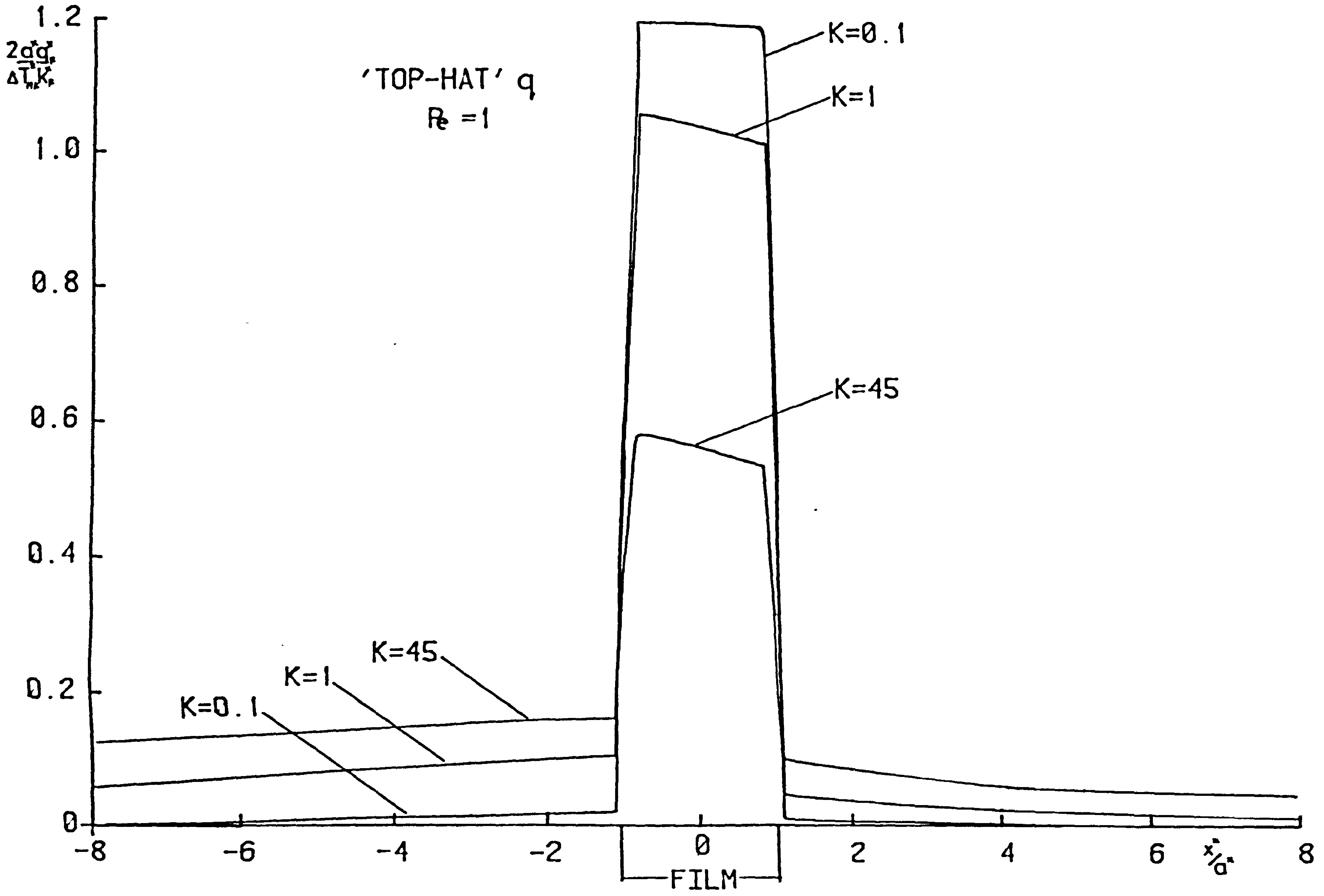

FIG. 3.13 SURFACE HEAT FLUX DISTRIBUTION - EFFECT OF K
(INCLUDING LONGITUDINAL DIFFUSION)

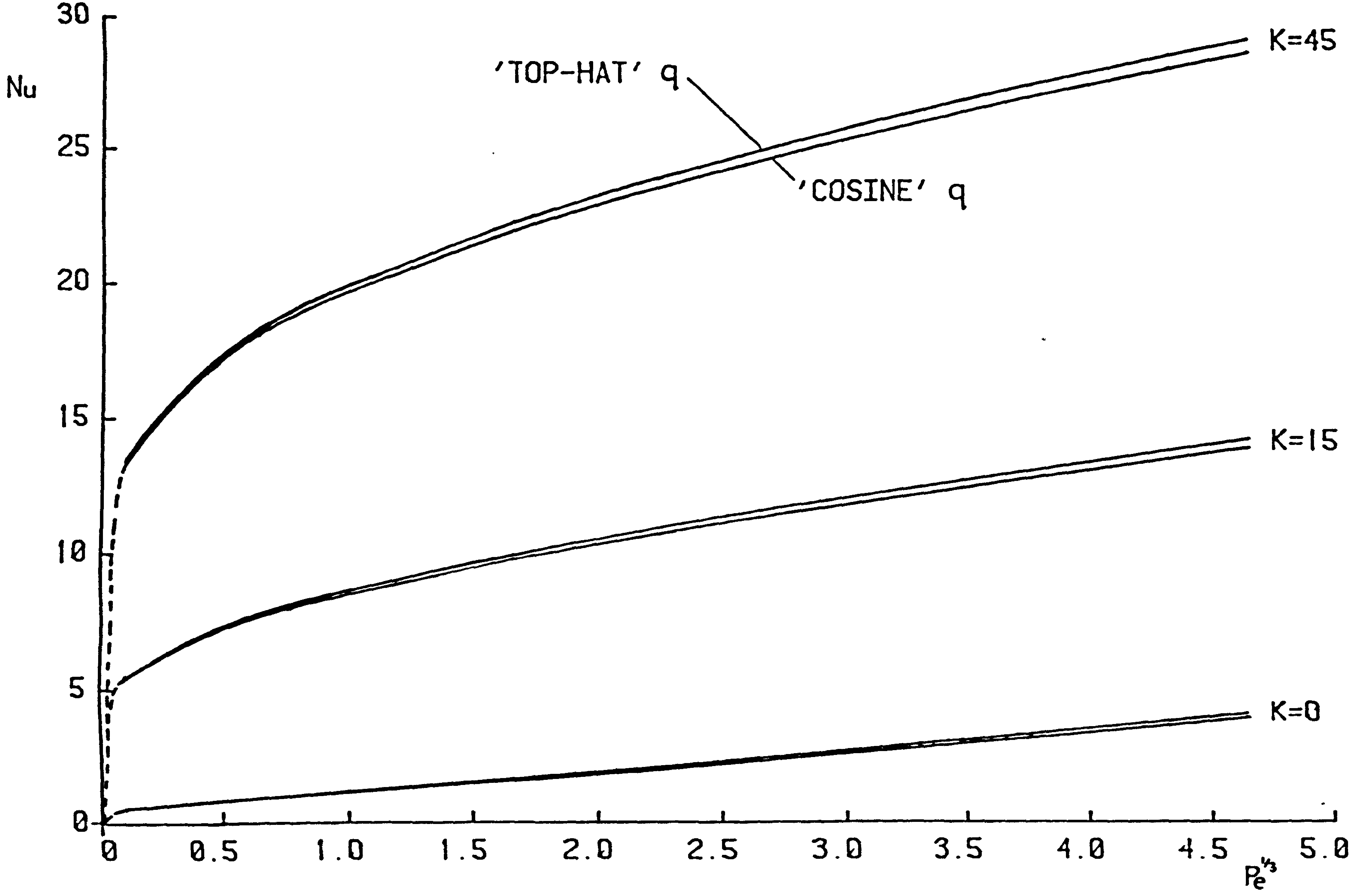

FIG. 3.14 EFFECT OF VARYING q UPON THE Nu - $Pe^{1/3}$ RELATIONSHIP (INCLUDING LONGITUDINAL DIFFUSION)

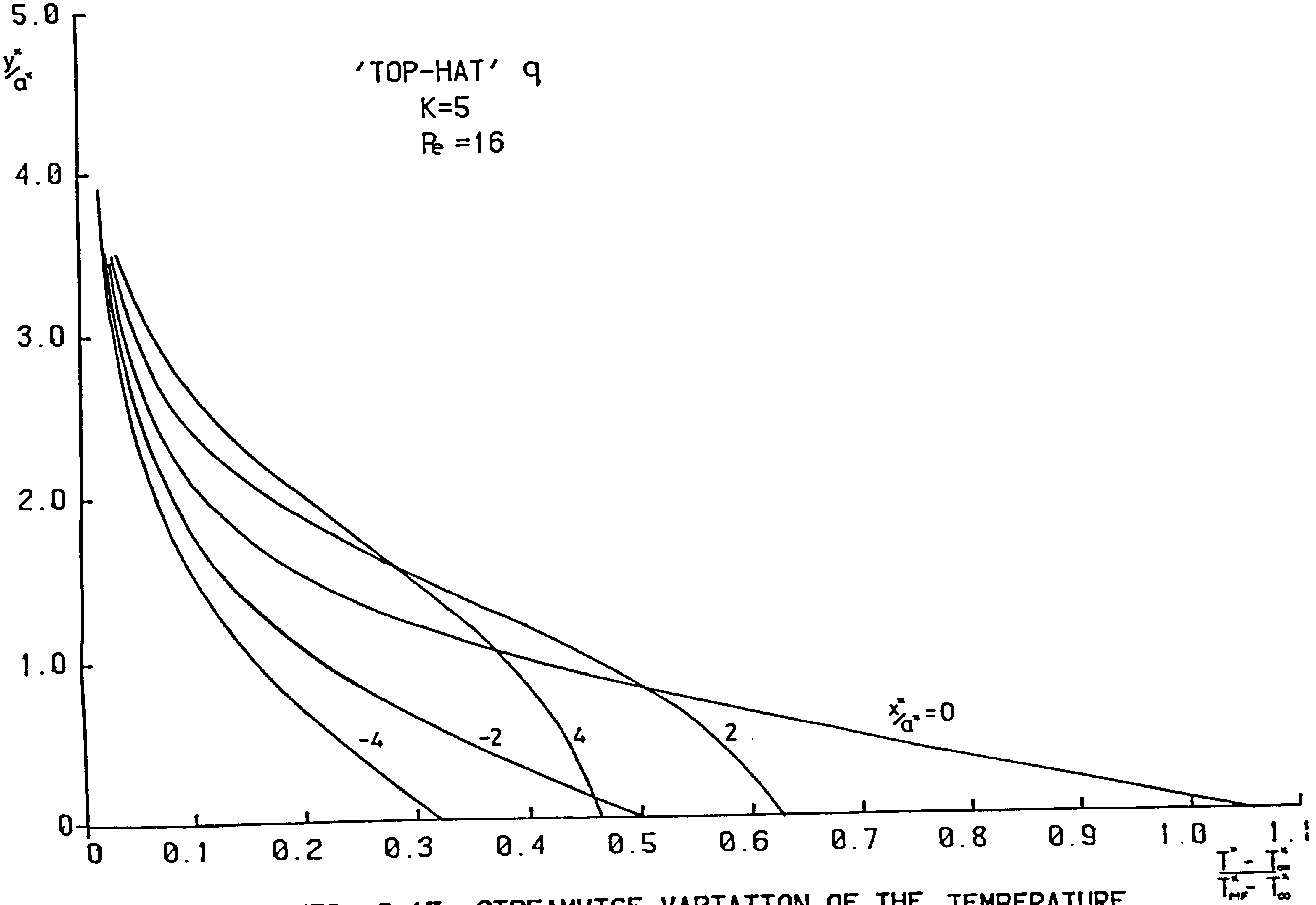

FIG. 3.15 STREAMWISE VARIATION OF THE TEMPERATURE PROFILE IN THE FLUID

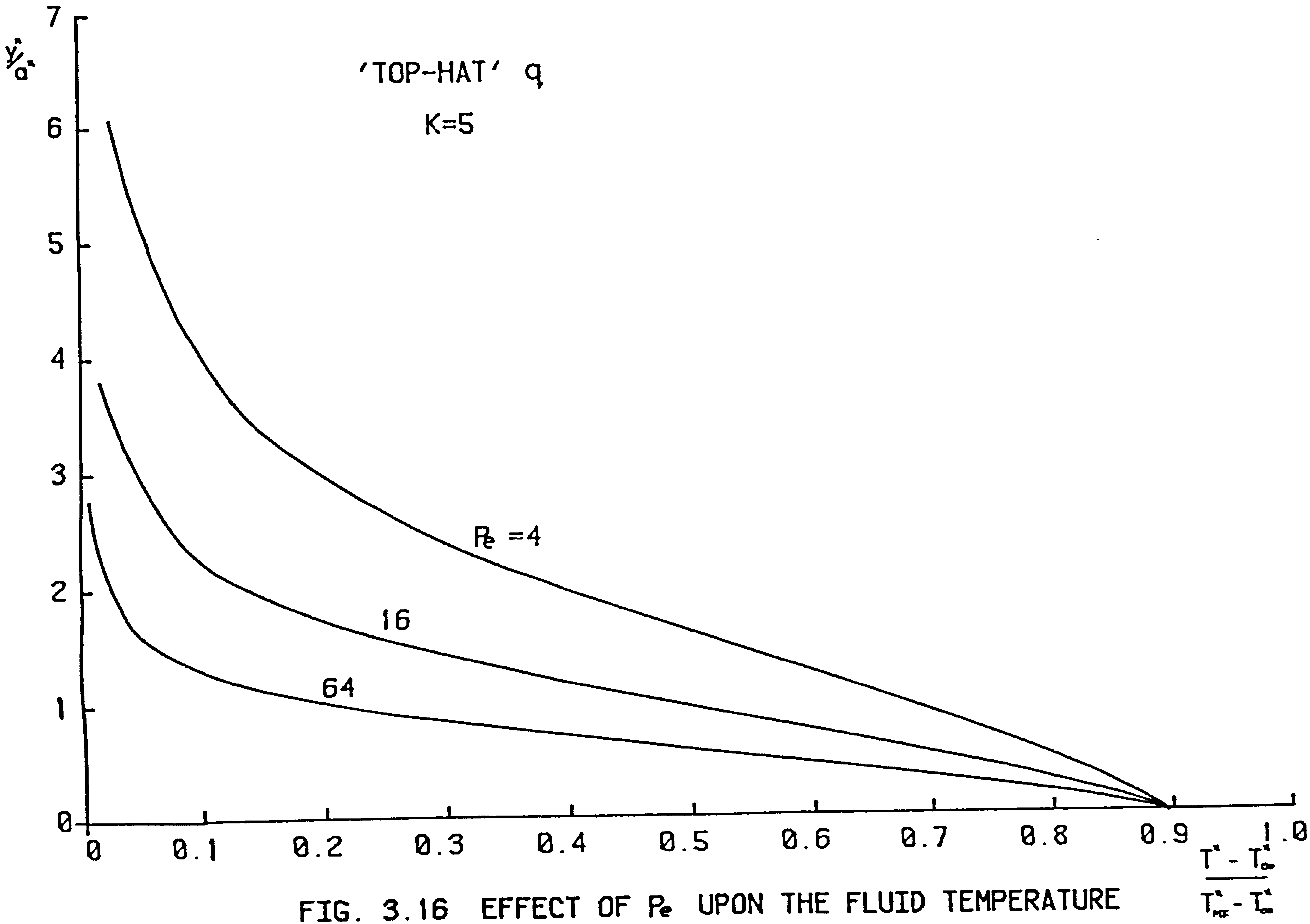

FIG. 3.16 EFFECT OF Pe UPON THE FLUID TEMPERATURE PROFILE AT $x^*/a^*=1$

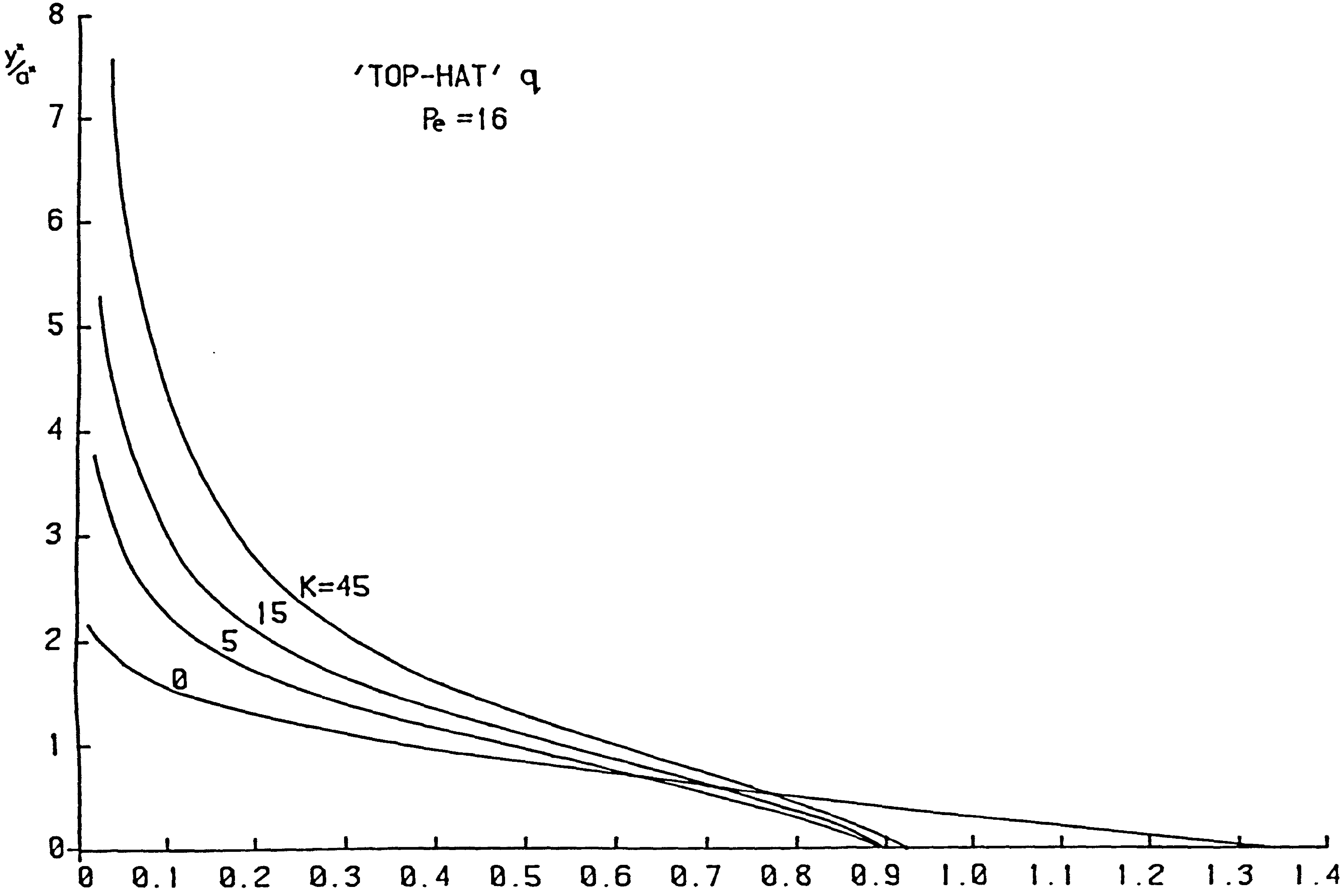

FIG. 3.17 EFFECT OF K UPON THE FLUID TEMPERATURE PROFILE AT $x^*/a^* = 1$

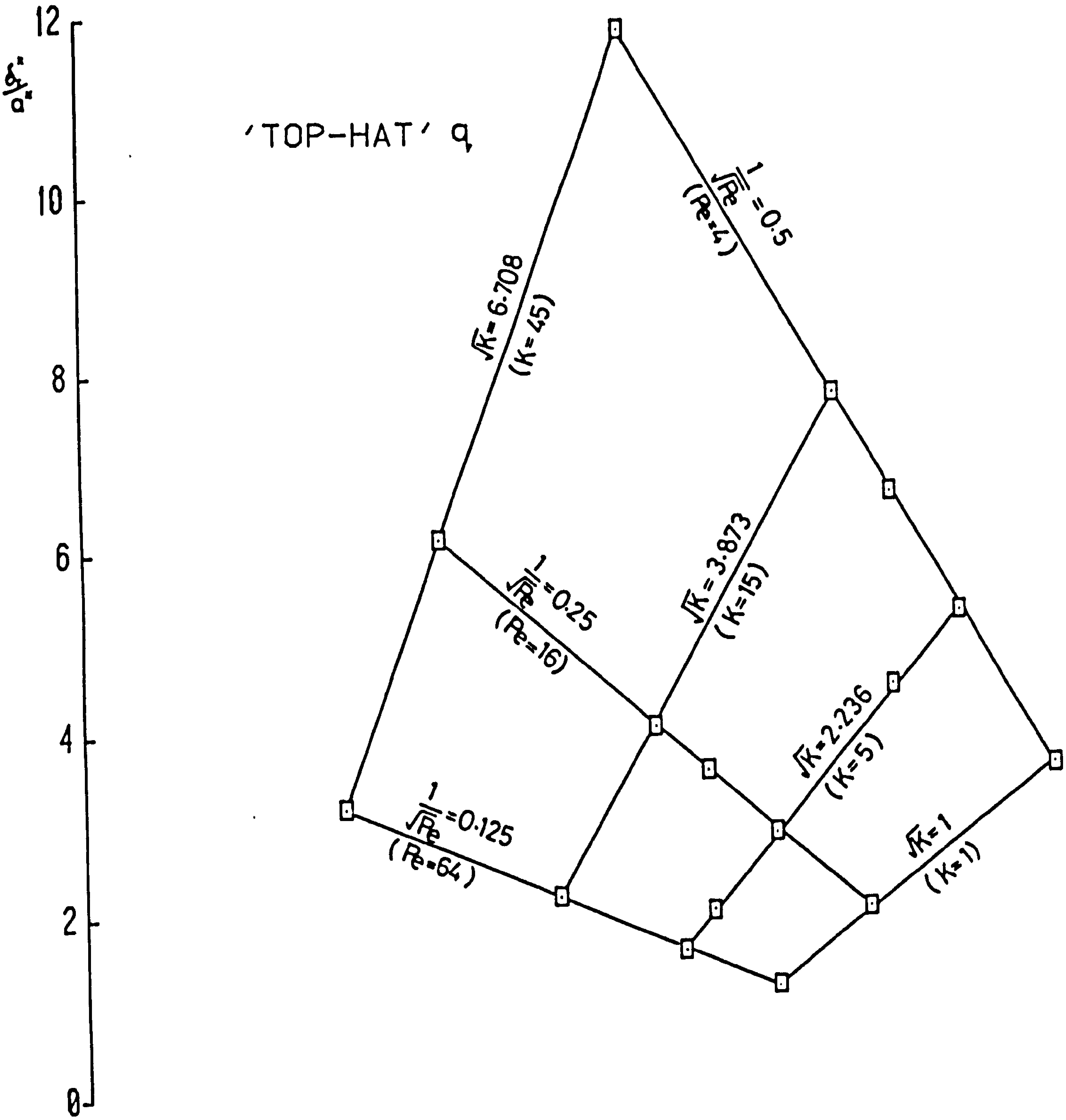

FIG. 3.18 VARIATION OF δ_r^*/a^* WITH $Pe^{-1/2}$ AND $K^{1/2}$
AT $x^*/a^* = 1$

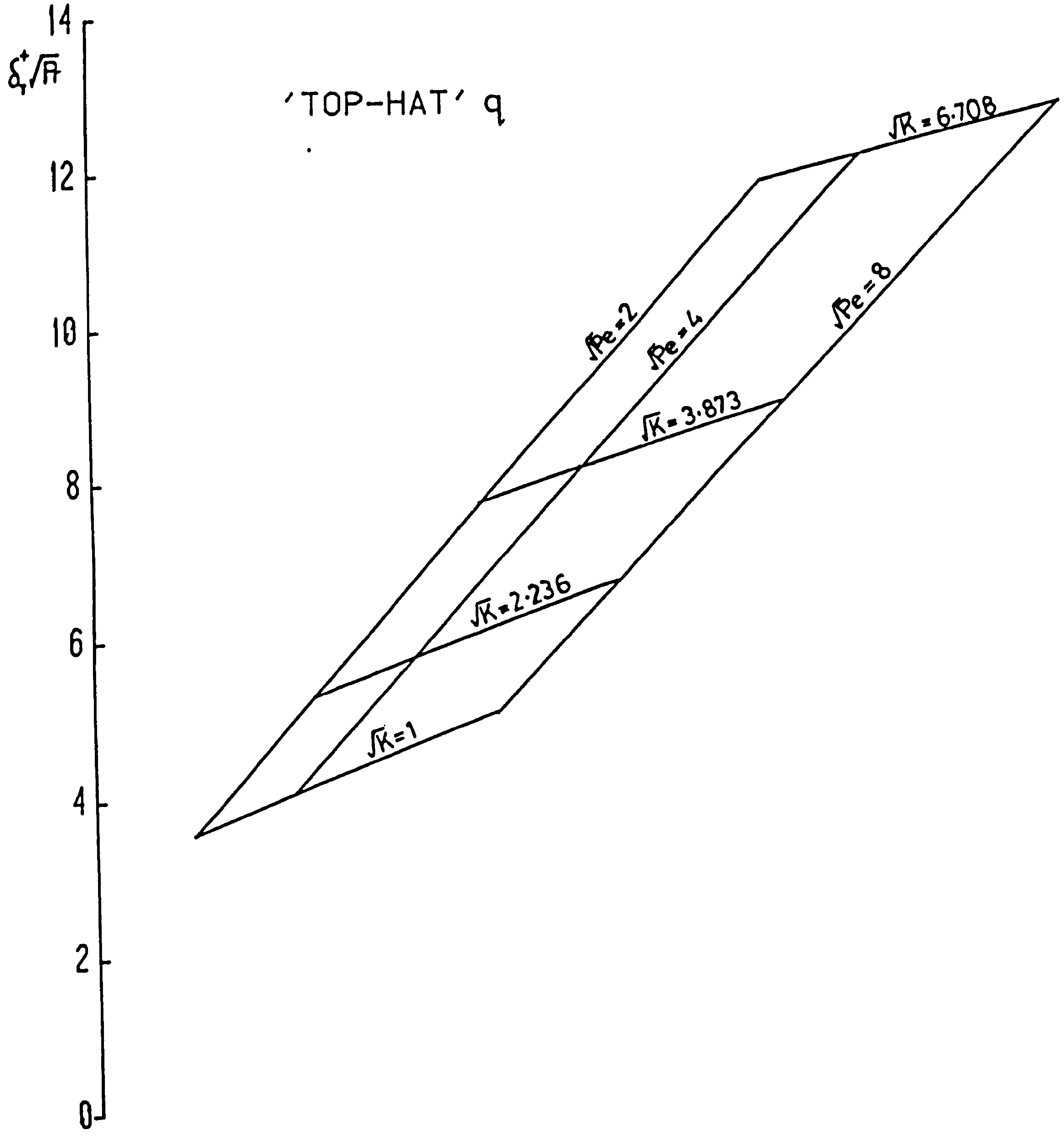

FIG. 3.19 VARIATION OF $\delta_t^+\sqrt{Pr}$ WITH $\sqrt{Pe}$ AND $\sqrt{K}$ AT $x^*/a^*=1$

Flush Mounting Probe

(dimensions in mm)

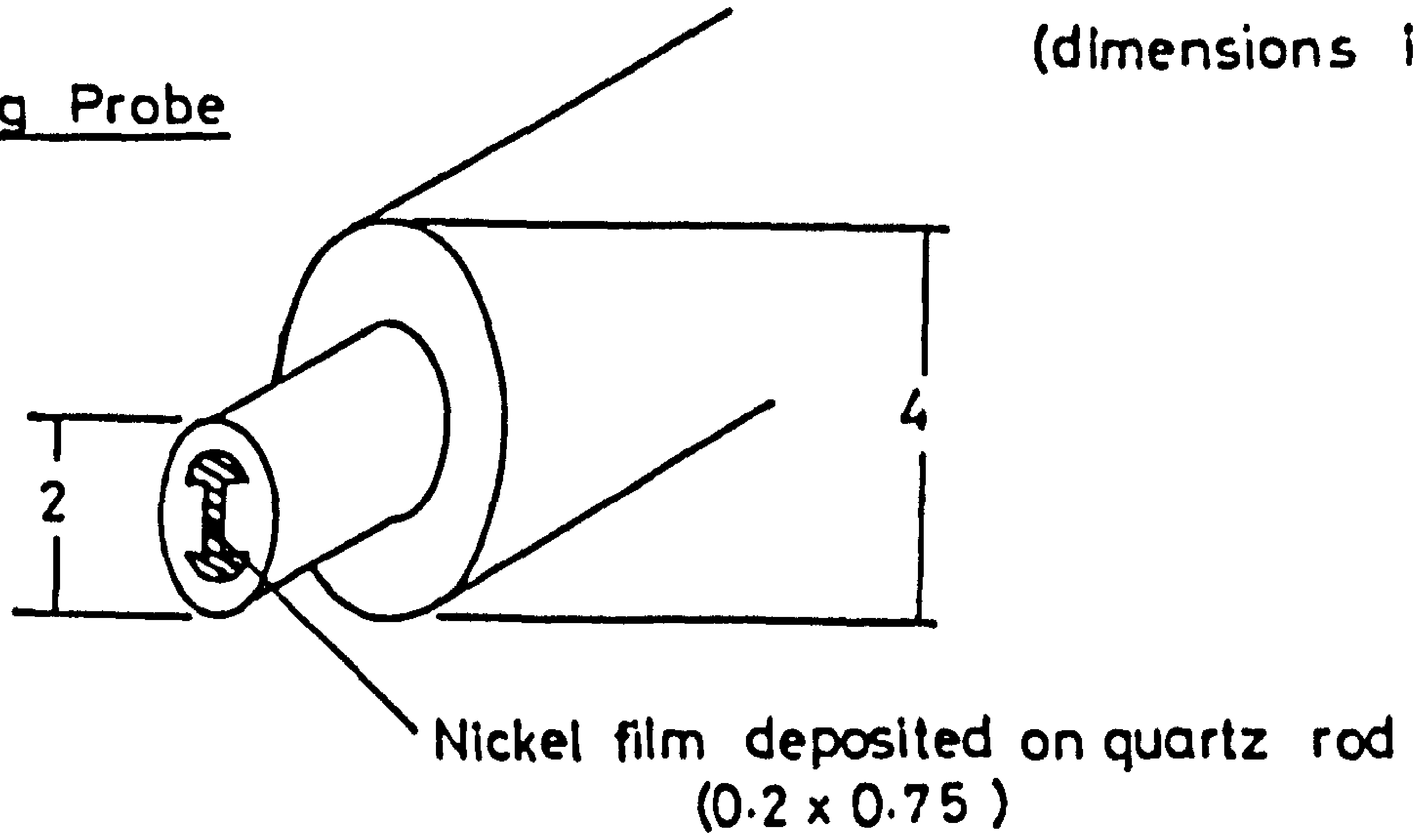

Glue-on Probe

(dimensions in mm)

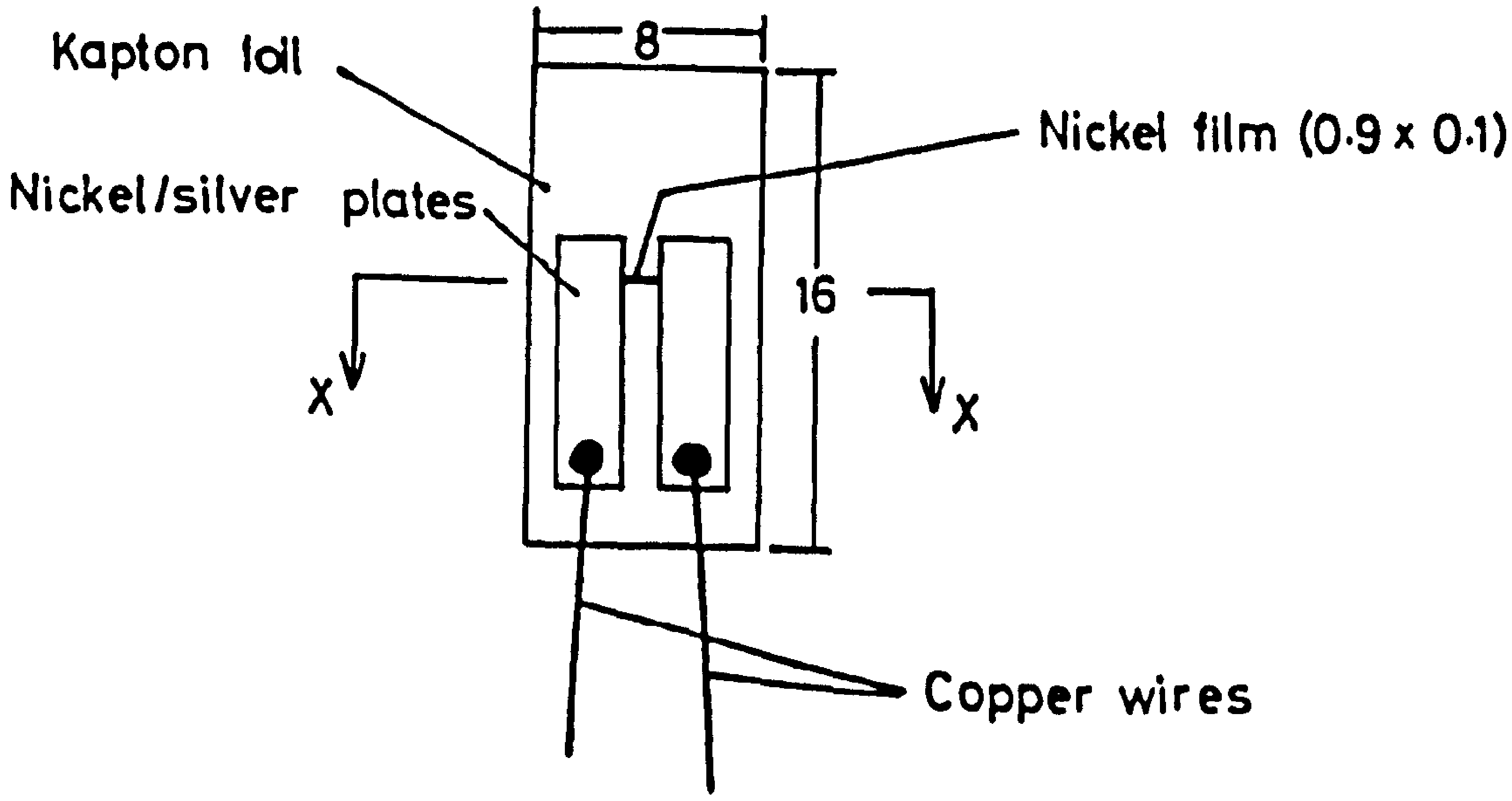

Section XX

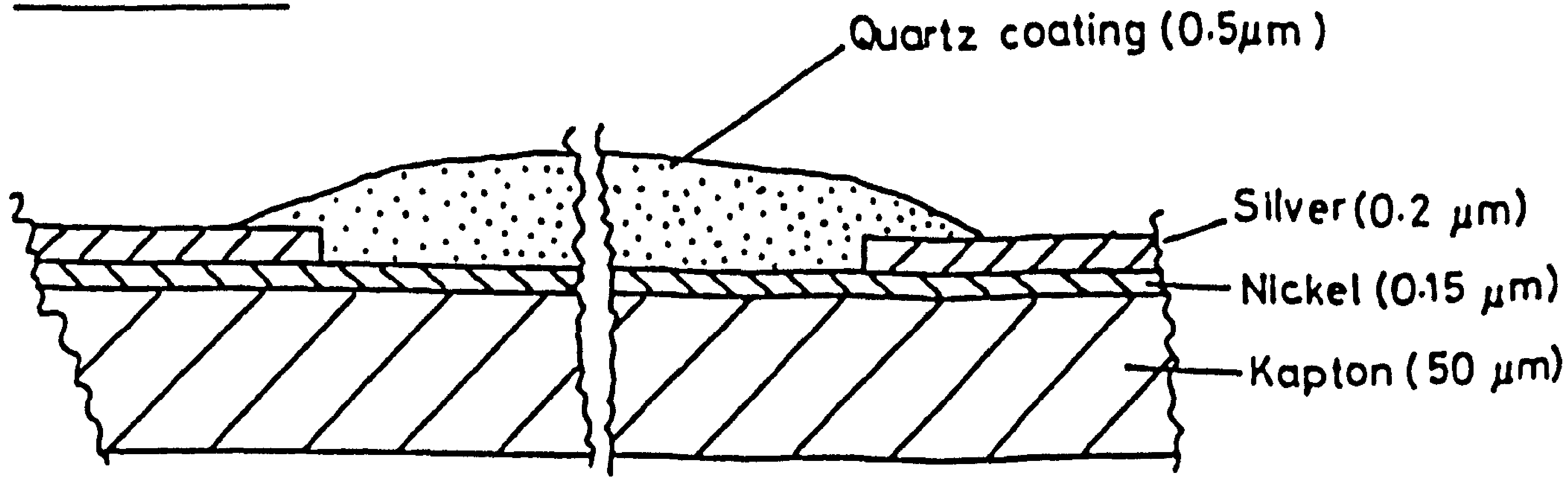

FIG. 4.1 DETAILS OF THE FLUSH MOUNTING AND GLUE-ON PROBES

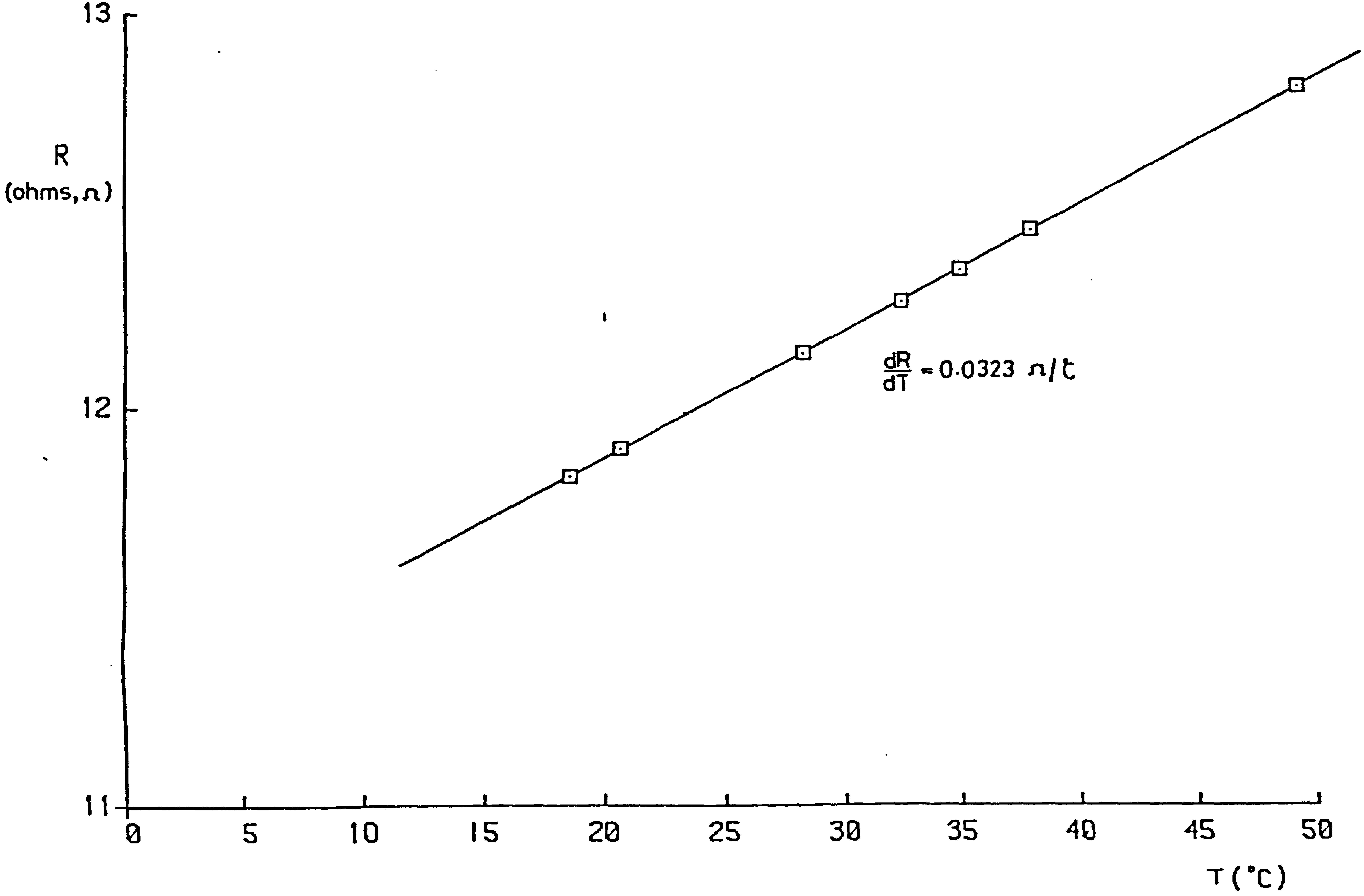

FIG. 4.2 VARIATION OF PROBE RESISTANCE WITH TEMPERATURE

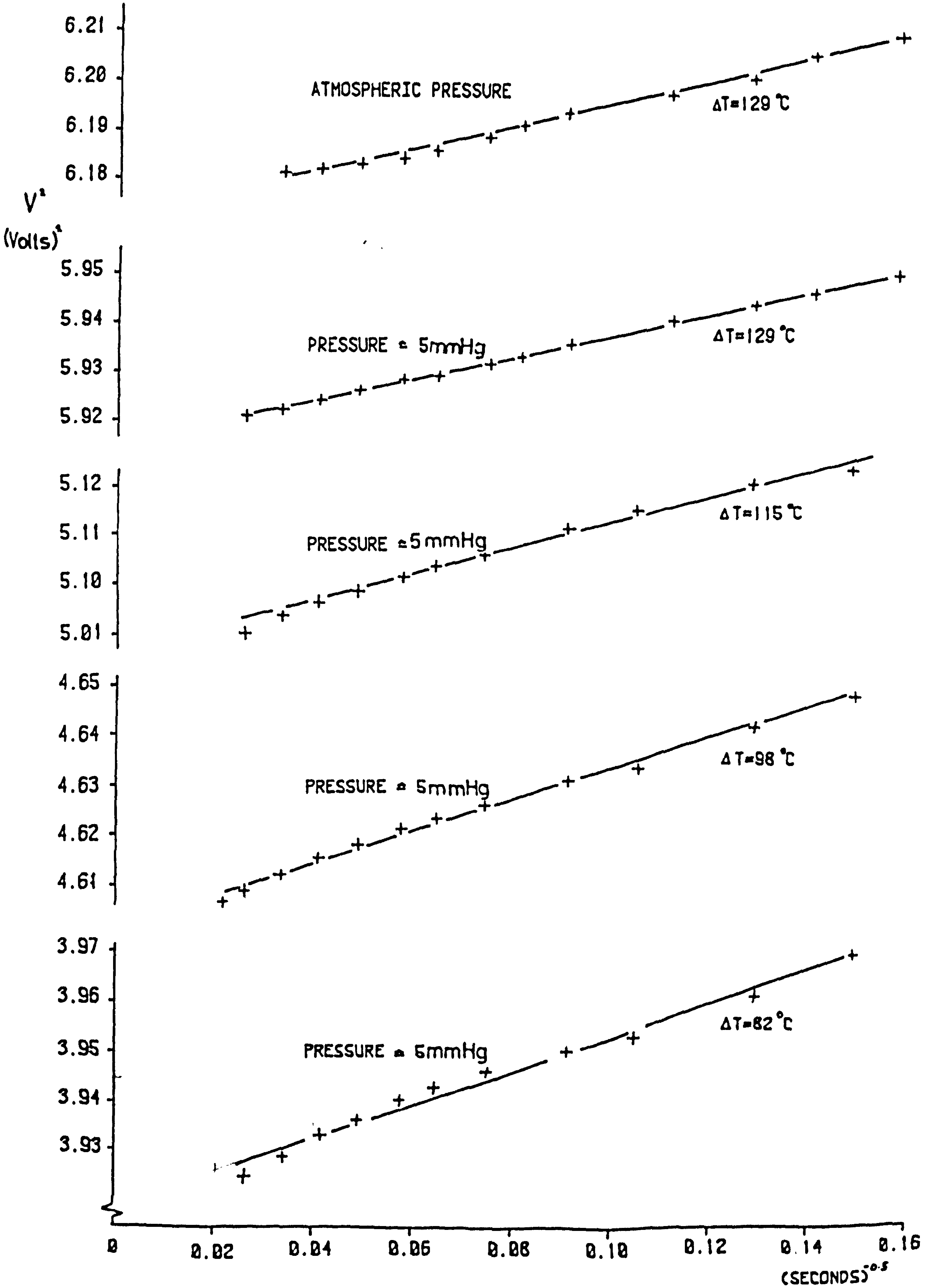

FIG. 4.3 POWER (V^2) VARIATION WITH TIME - SUSPENDED PROBE

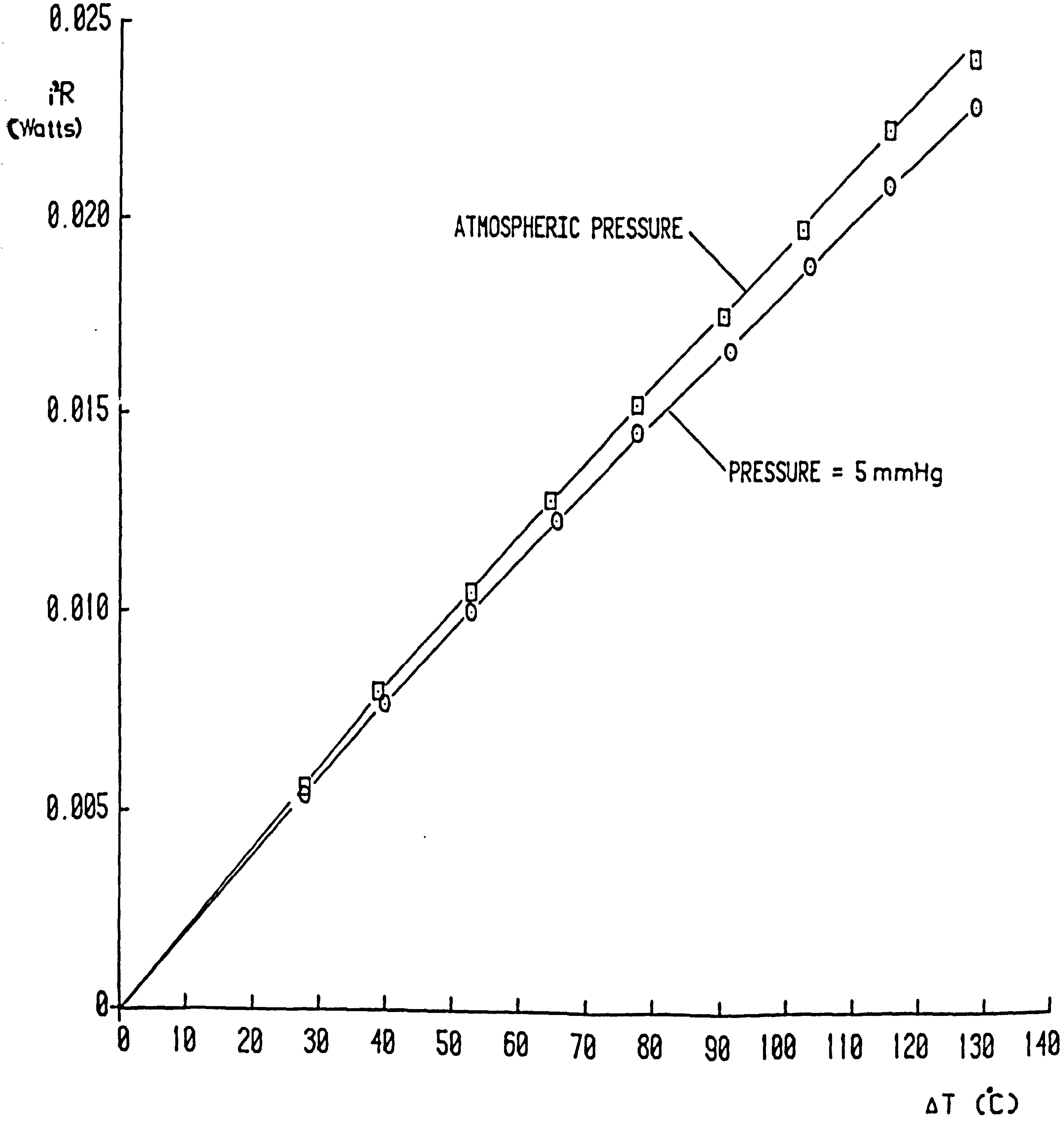

FIG. 4.4 VARIATION OF POWER (i^2R) WITH ΔT - SUSPENDED PROBE

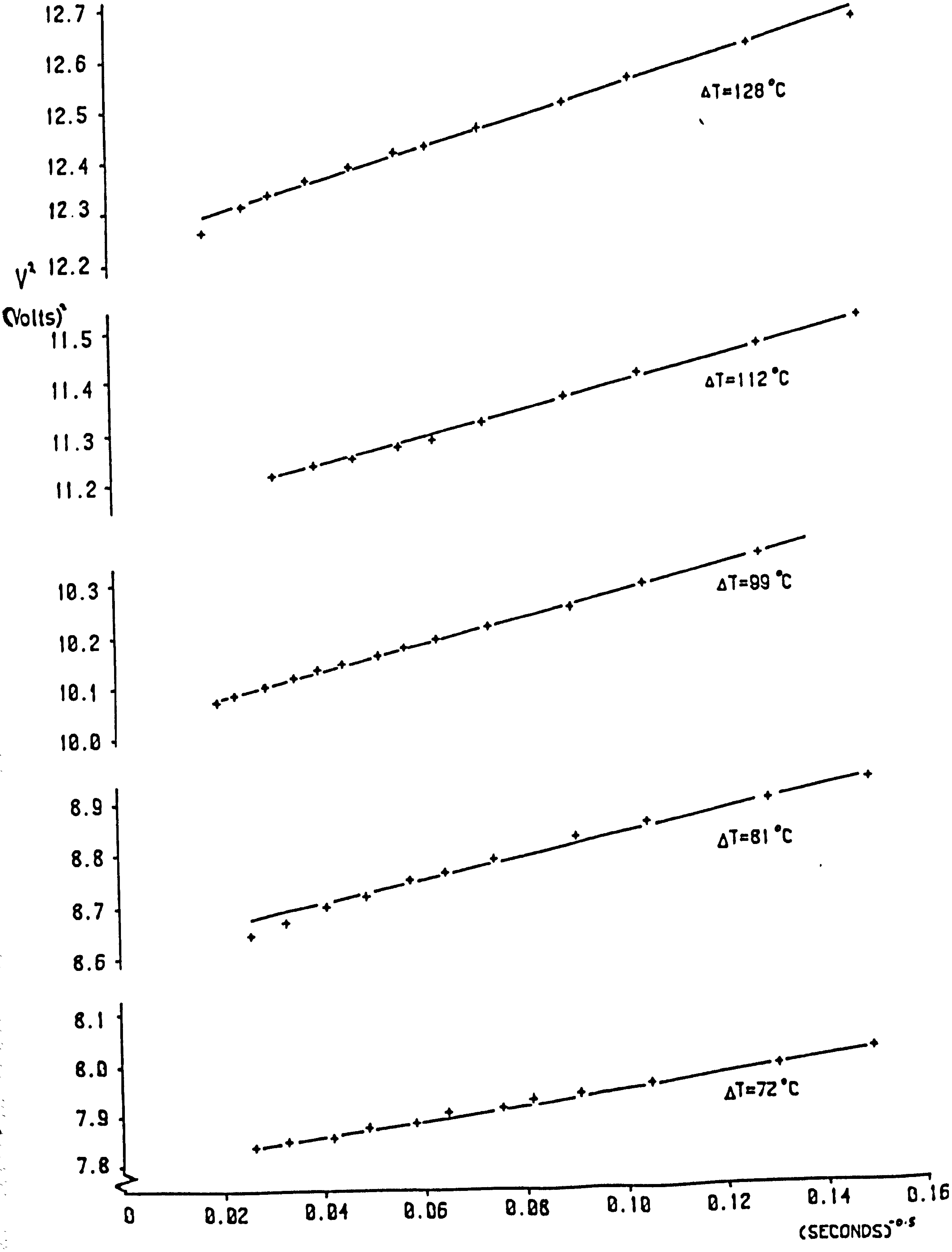

FIG. 4.5 POWER (V^2) VARIATION WITH TIME
- PROBE ON TUFNOL PLATE

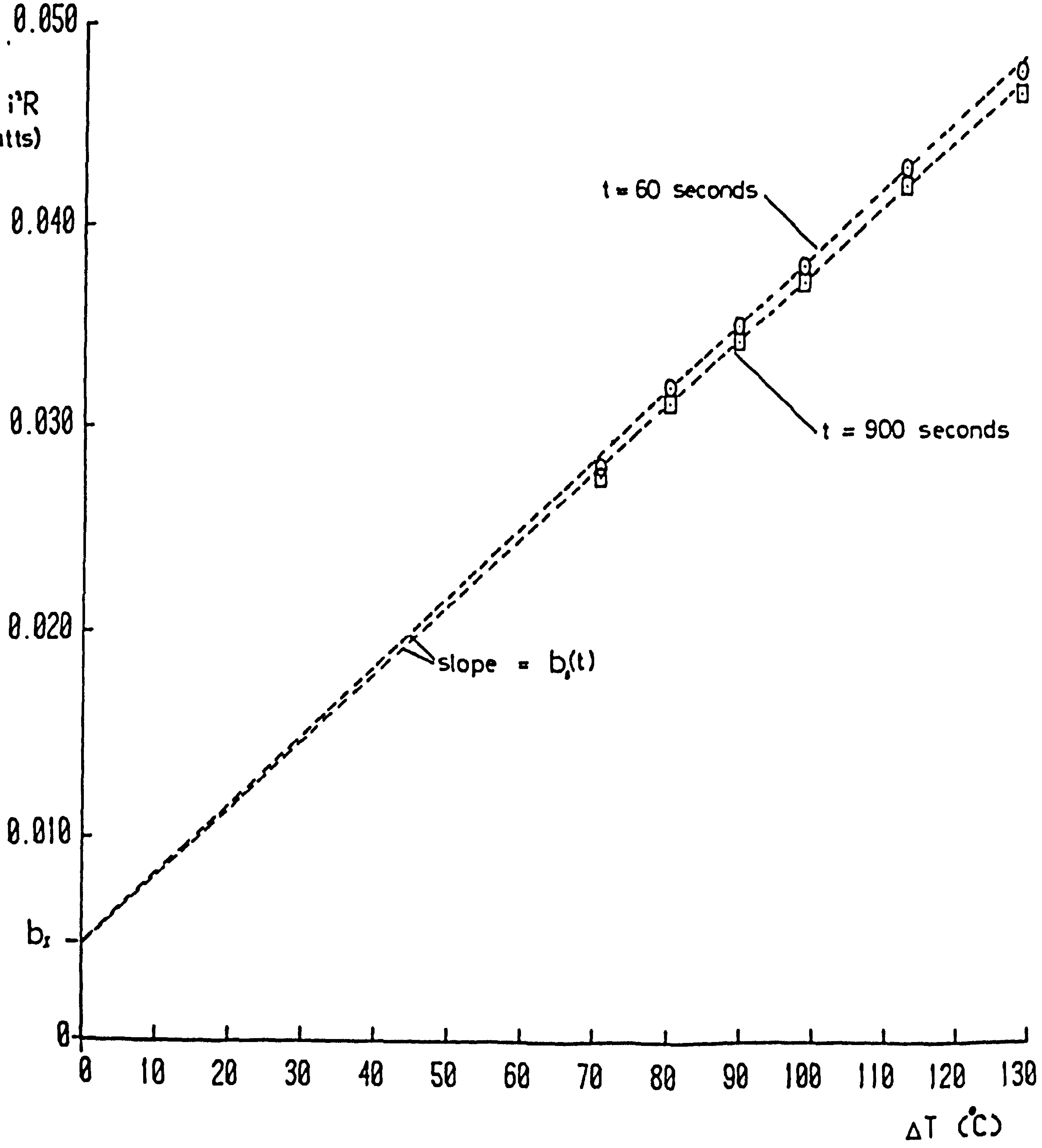

FIG. 4.6 VARIATION OF POWER (i^2R) WITH ΔT AT 2 TIMES

– PROBE ON TUFNOL PLATE

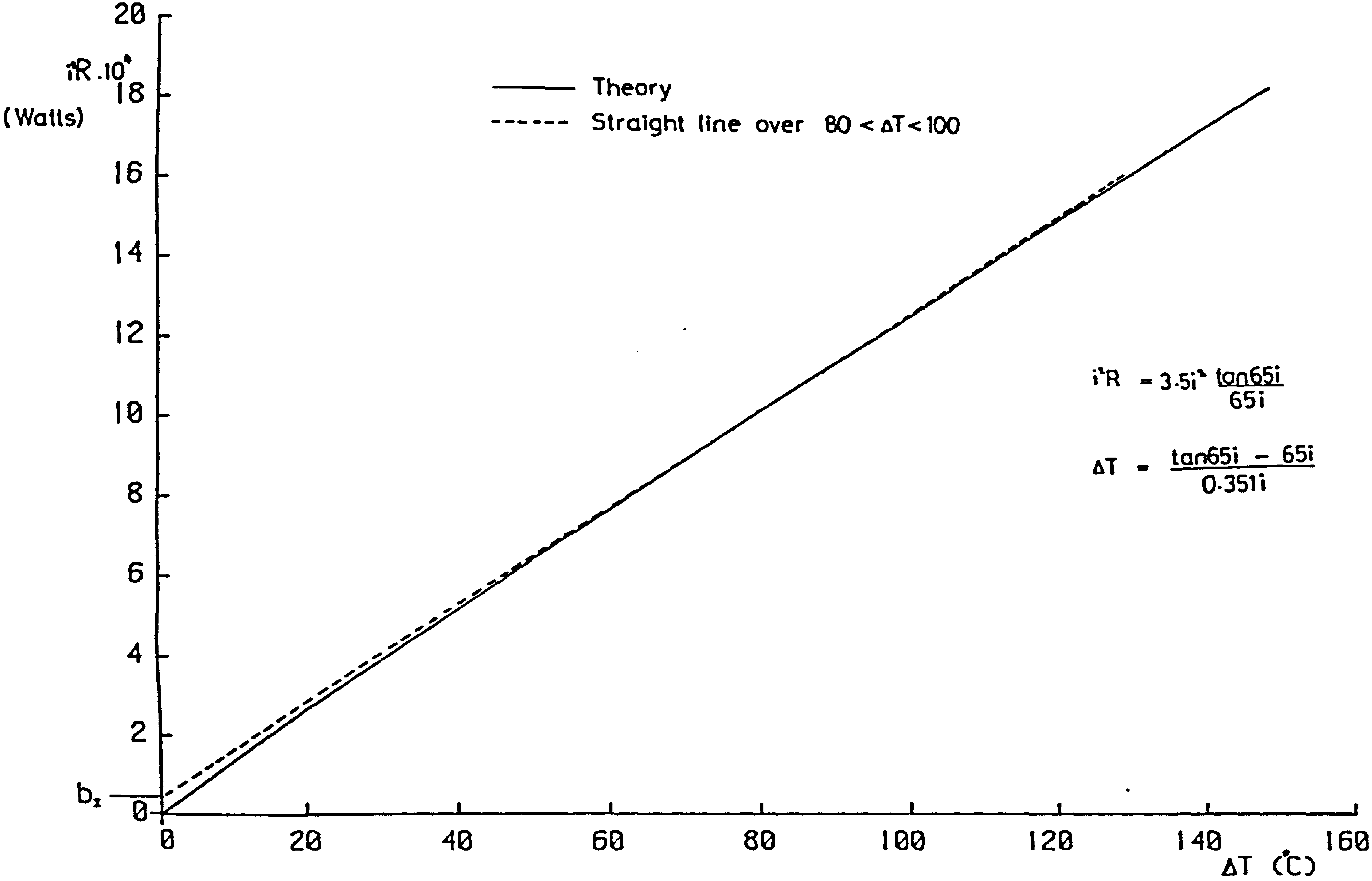

FIG. 4.7 PREDICTED VARIATION OF POWER (i^2R) WITH ΔT FOR THE NICKEL FILM ALONE

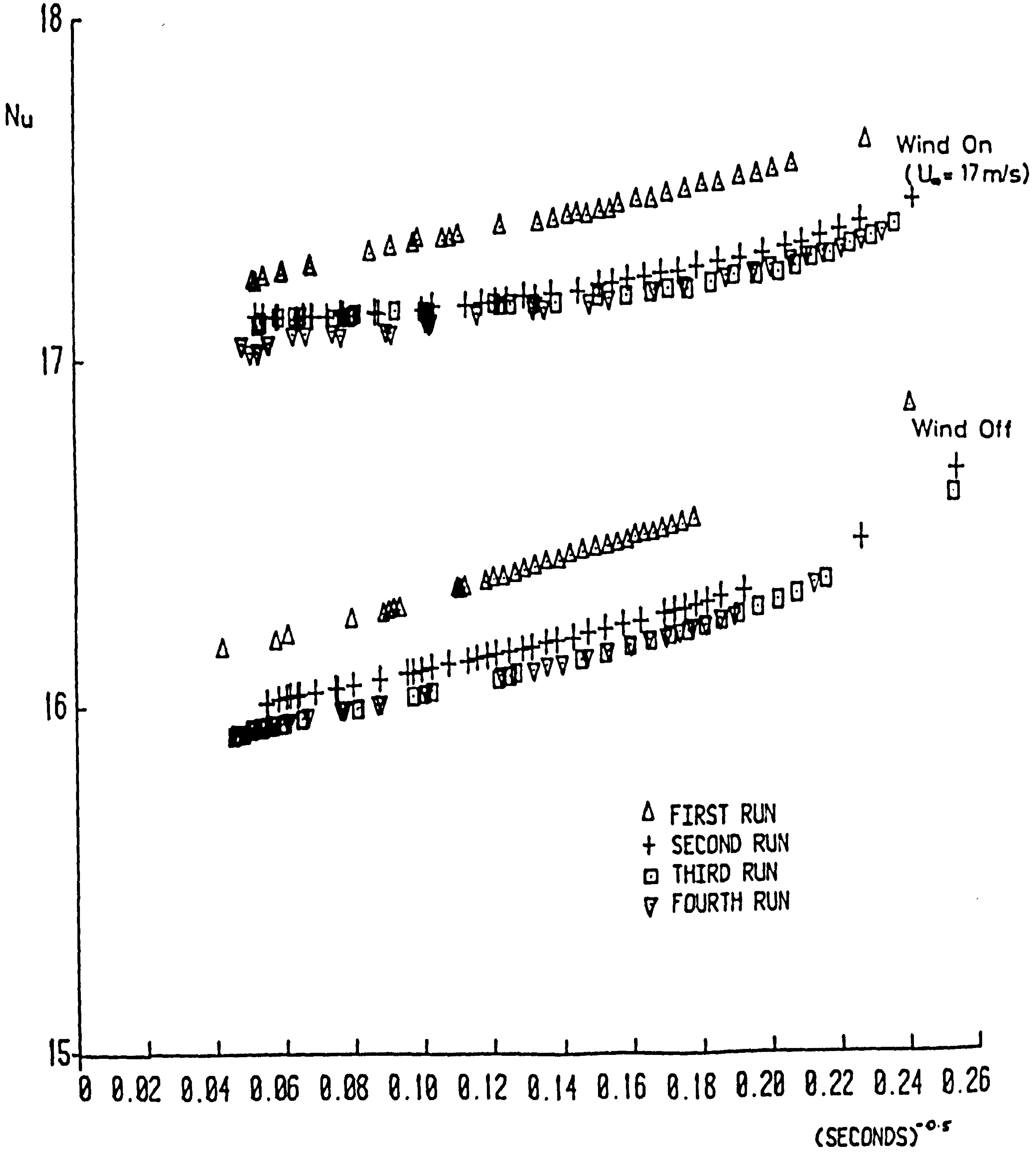

FIG. 4.8 VARIATION OF Nu WITH TIME - WIND ON AND WIND OFF

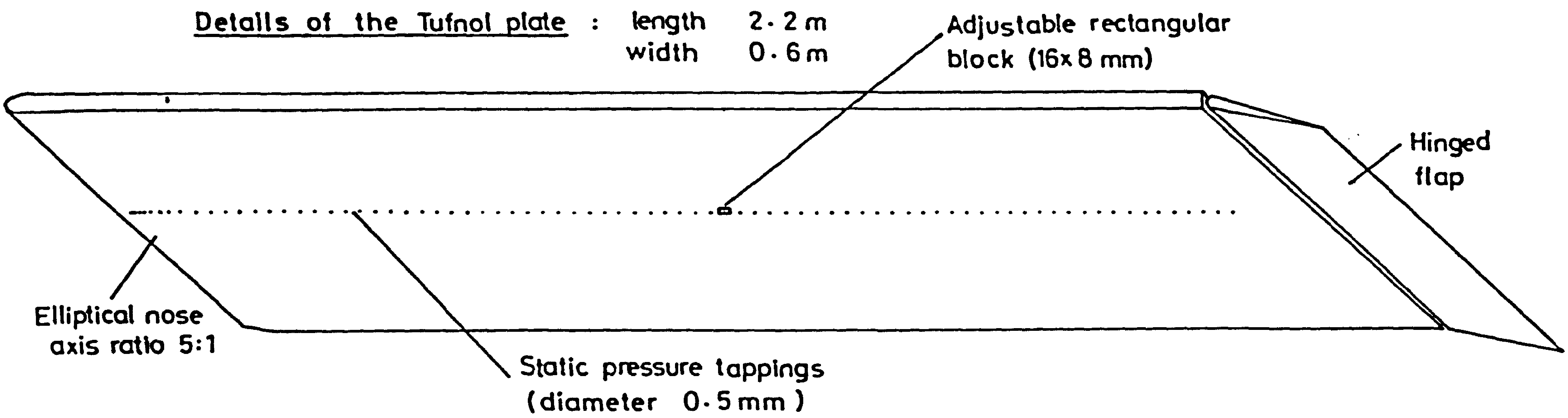

Details of the Tufnol plate : length 2·2 m width 0·6 m

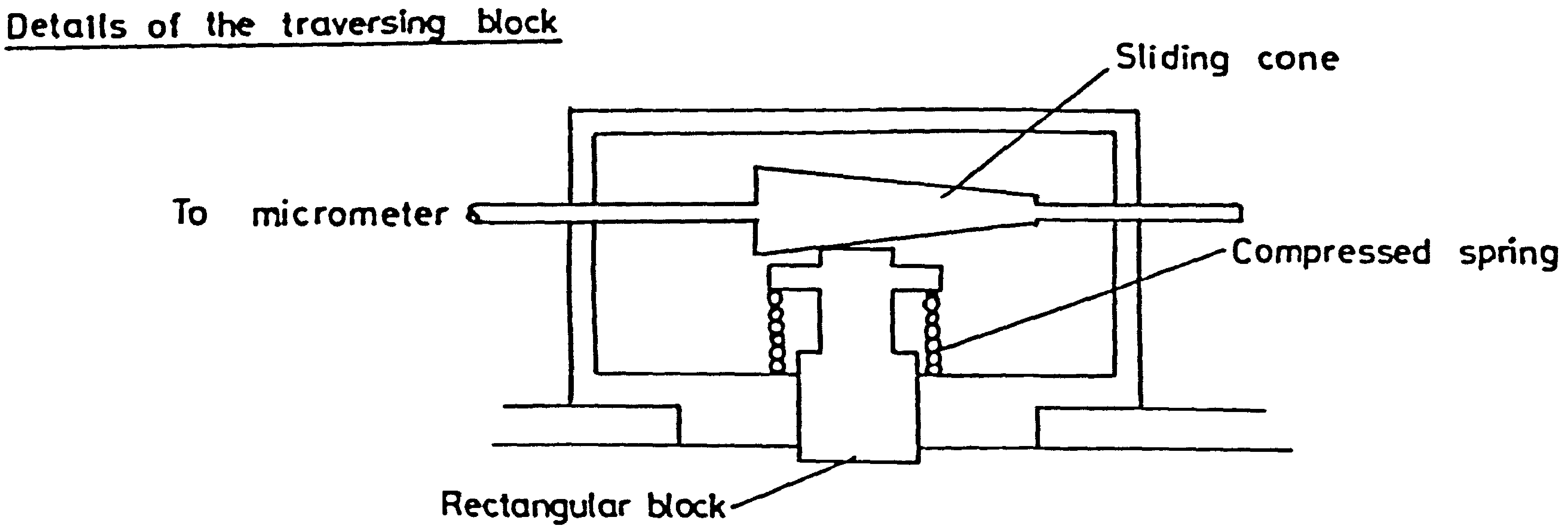

Details of the traversing block

FIG. 5.1 SKETCH OF THE FLAT PLATE MODEL

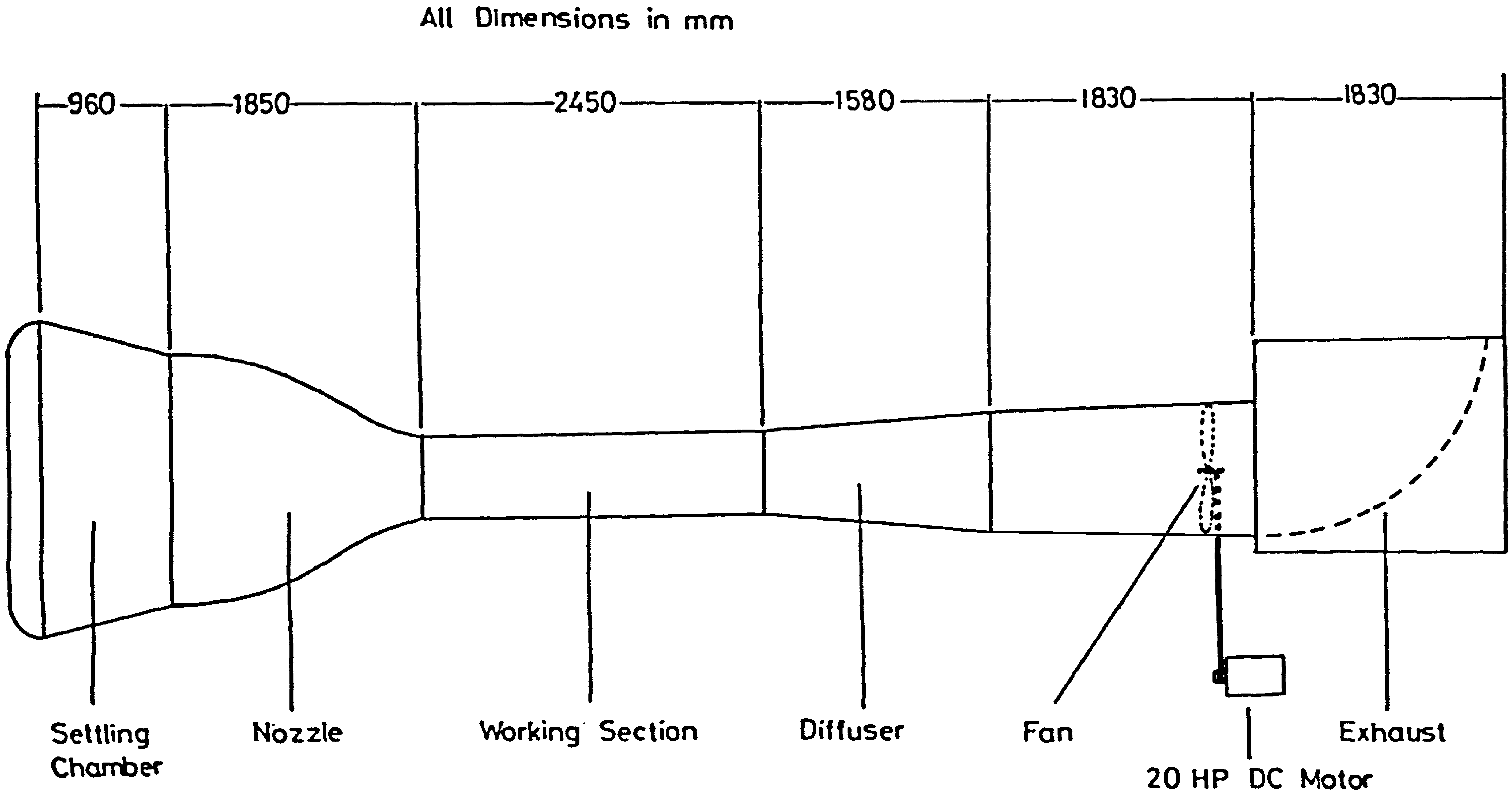

FIG. 5.2 SKETCH OF THE LOW TURBULENCE LOW SPEED WIND TUNNEL

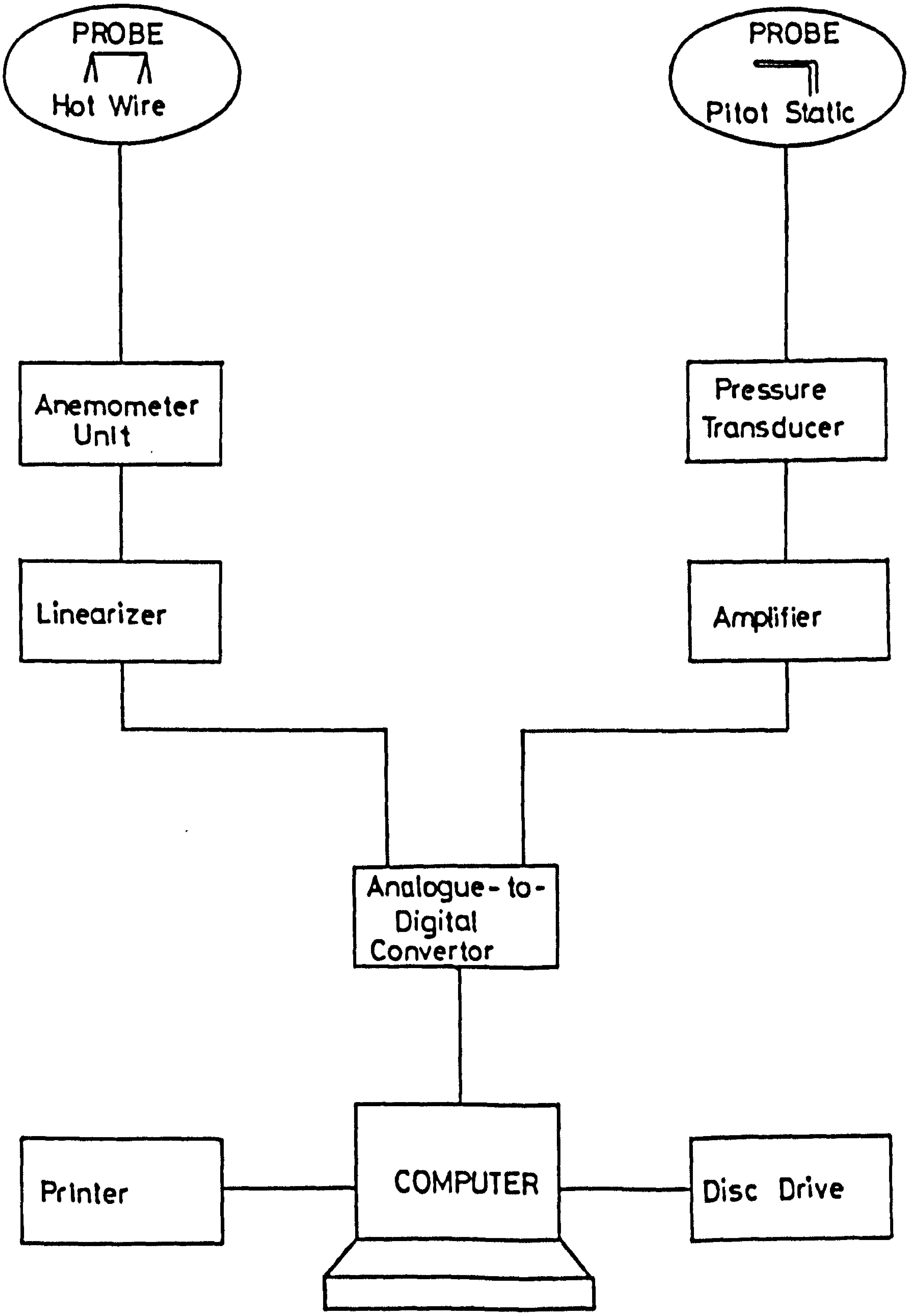

FIG. 5.3 SCHEMATIC DRAWING OF THE DATA ACQUISITION SYSTEM

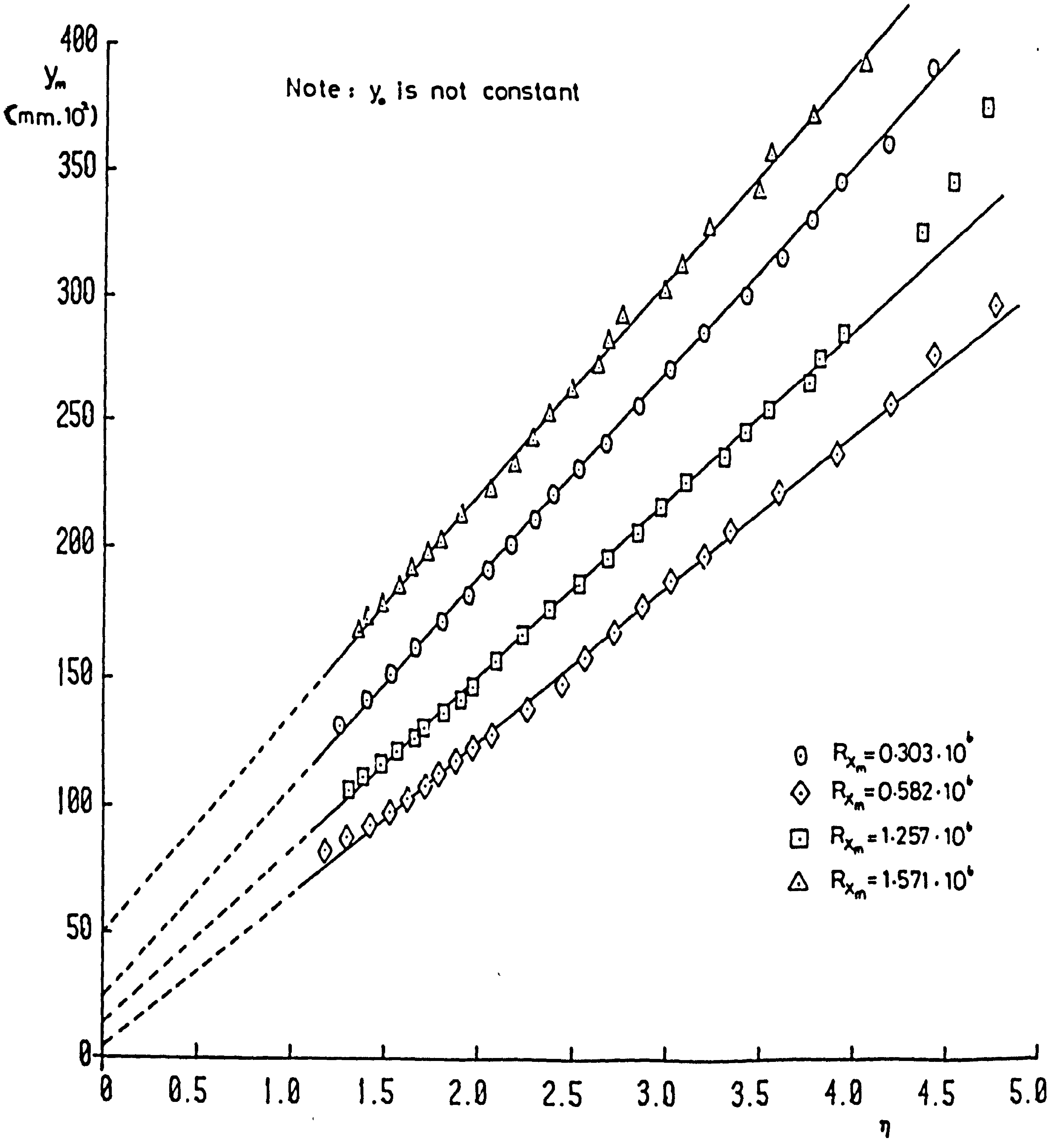

FIG. 5.4 LAMINAR VELOCITY PROFILES - HOT WIRE MEASUREMENTS

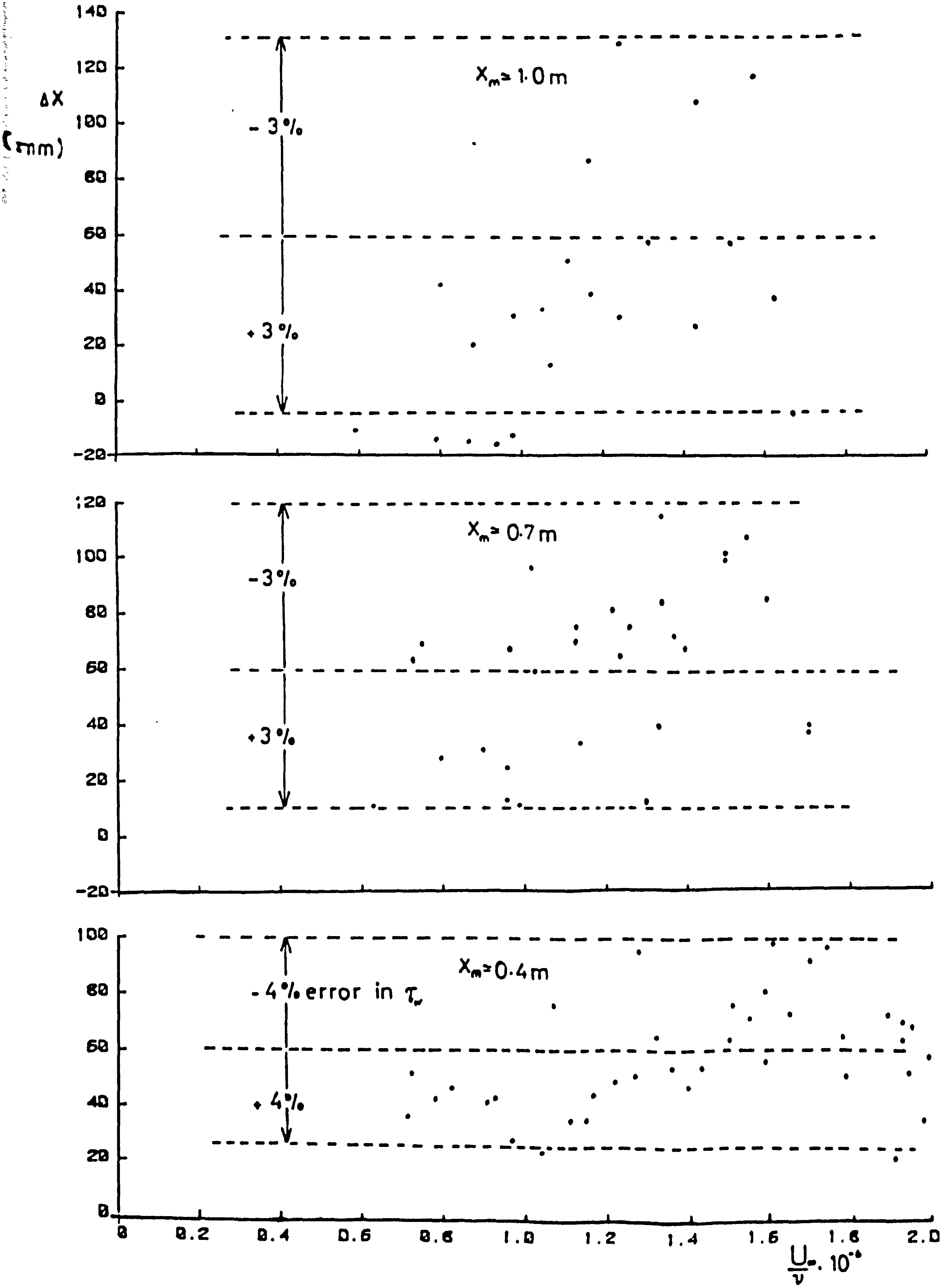

FIG. 5.5 VARIATION OF ΔX WITH UNIT REYNOLDS NUMBER (BASED ON HOT WIRE MEASUREMENTS)

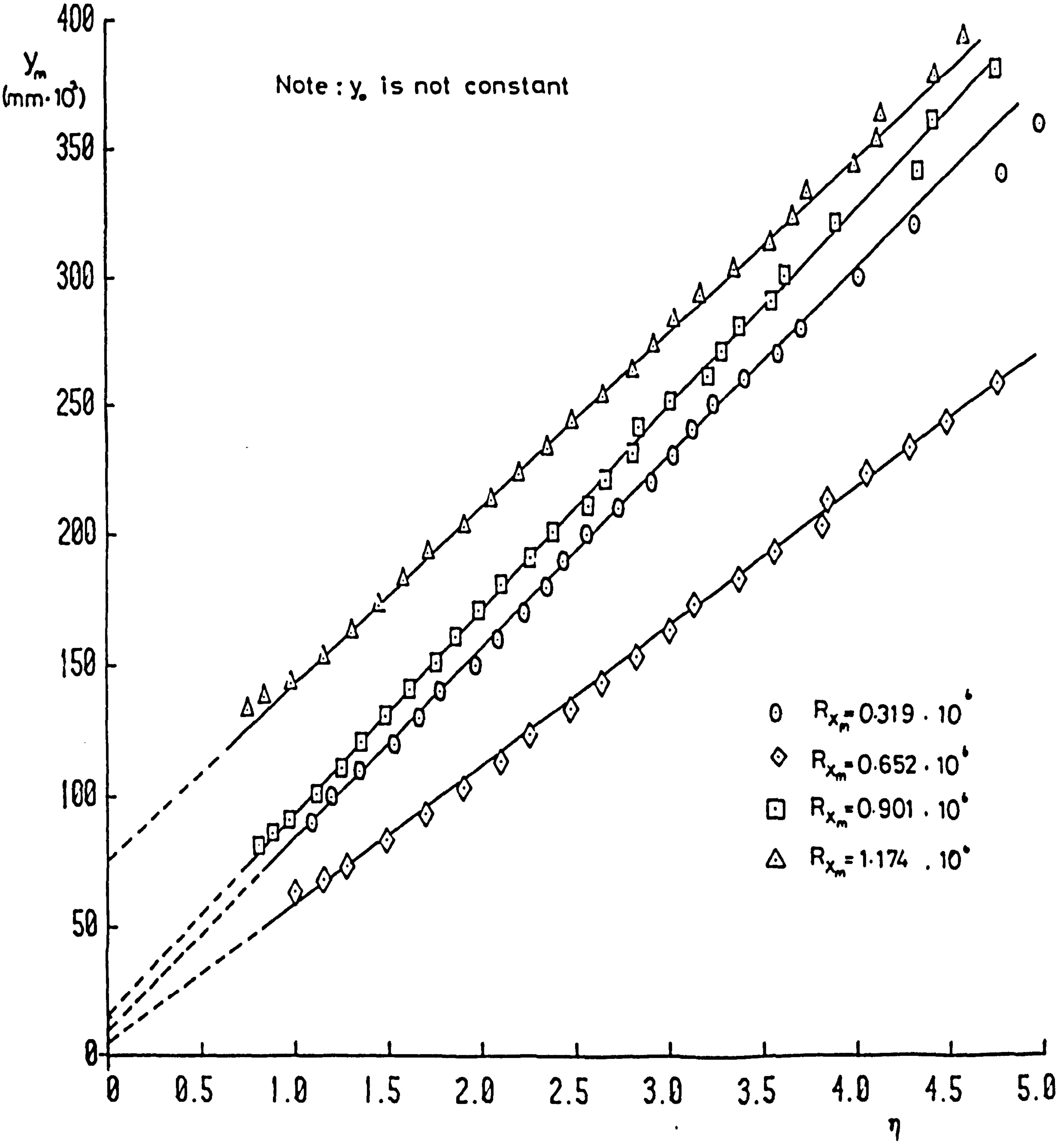

FIG. 5.6 LAMINAR VELOCITY PROFILES – PITOT TUBE MEASUREMENTS

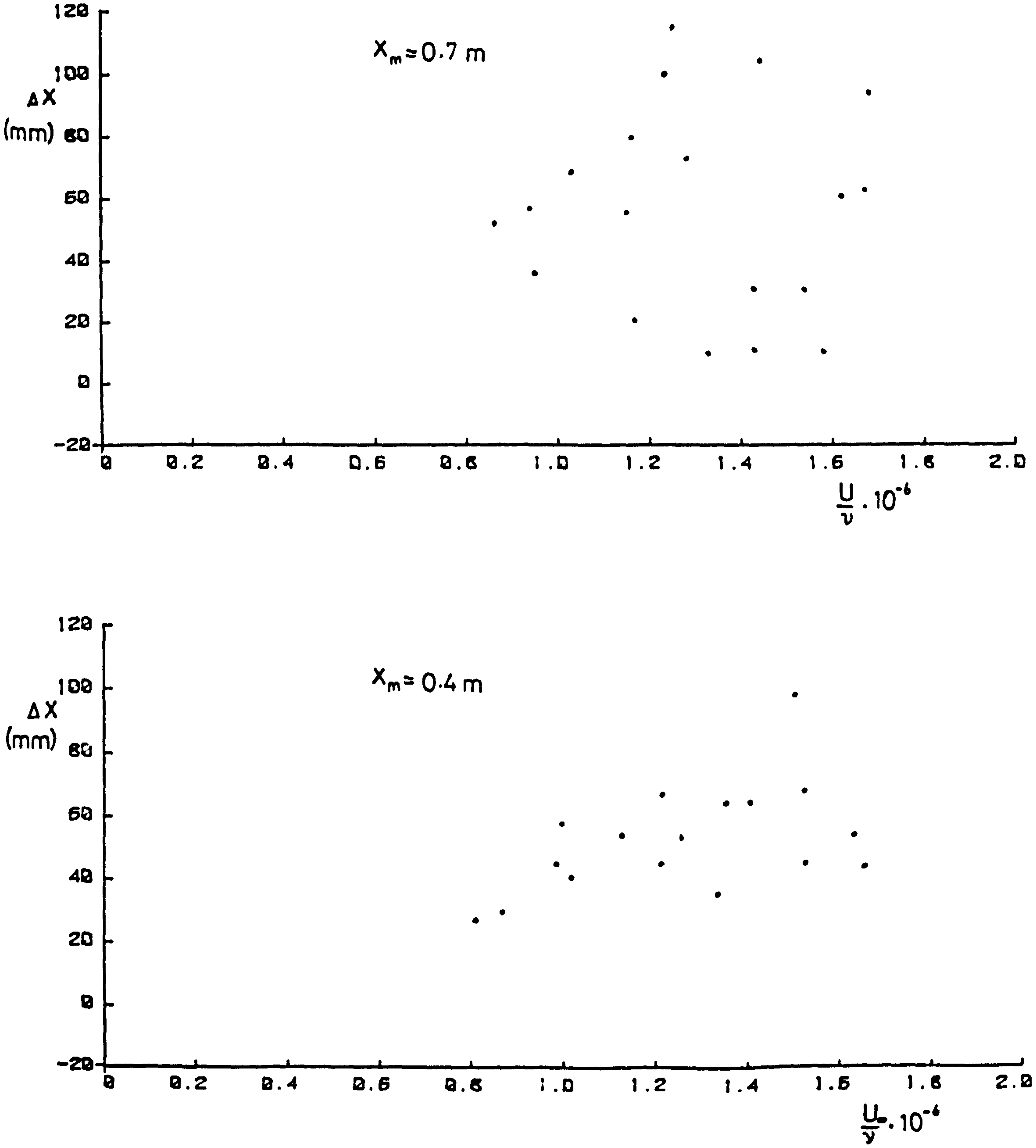

FIG. 5.7 VARIATION OF ΔX WITH UNIT REYNOLDS NUMBER (BASED ON PITOT TUBE MEASUREMENTS)

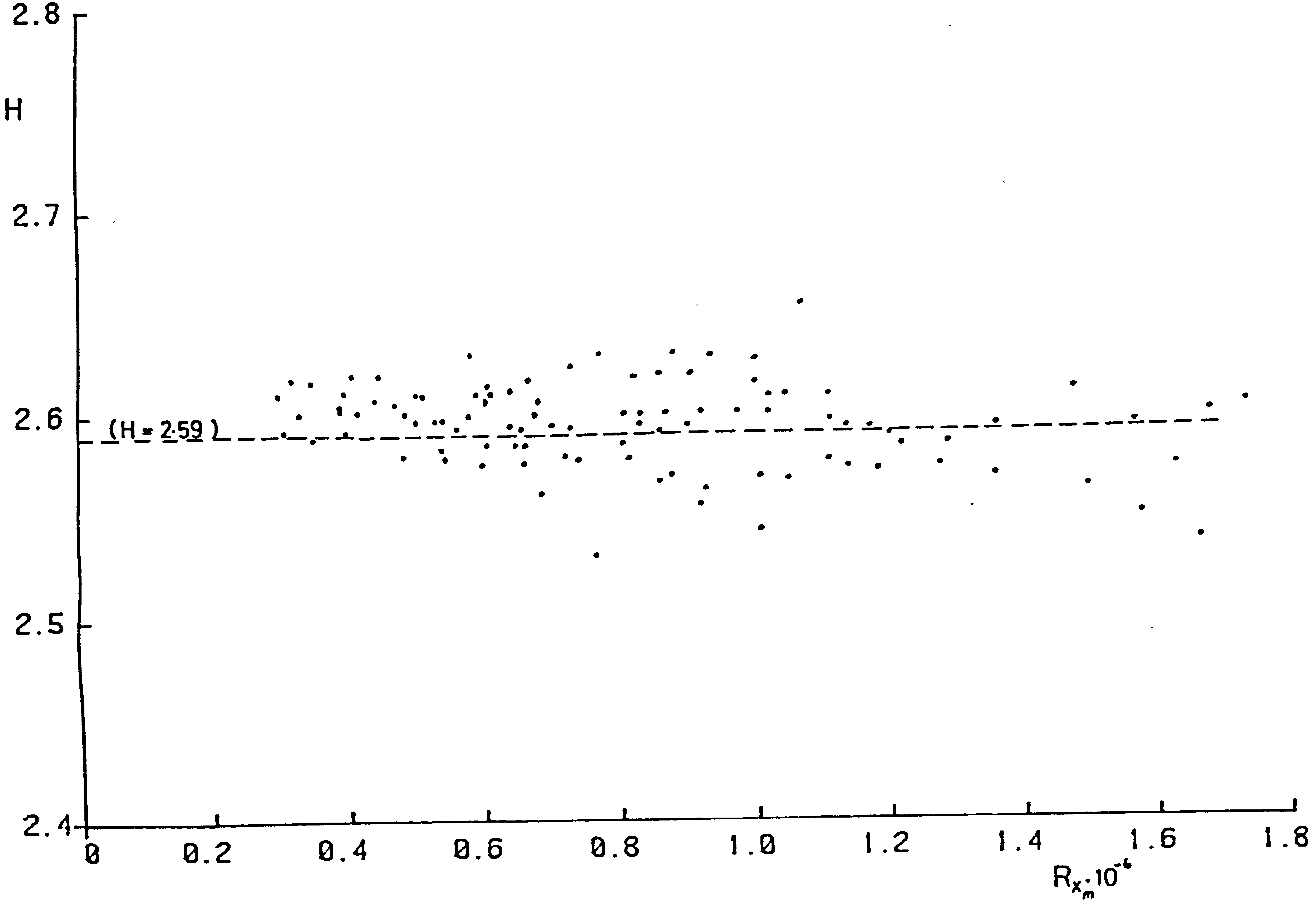

FIG. 5.8 VARIATION OF SHAPE FACTOR (H) WITH REYNOLDS NUMBER

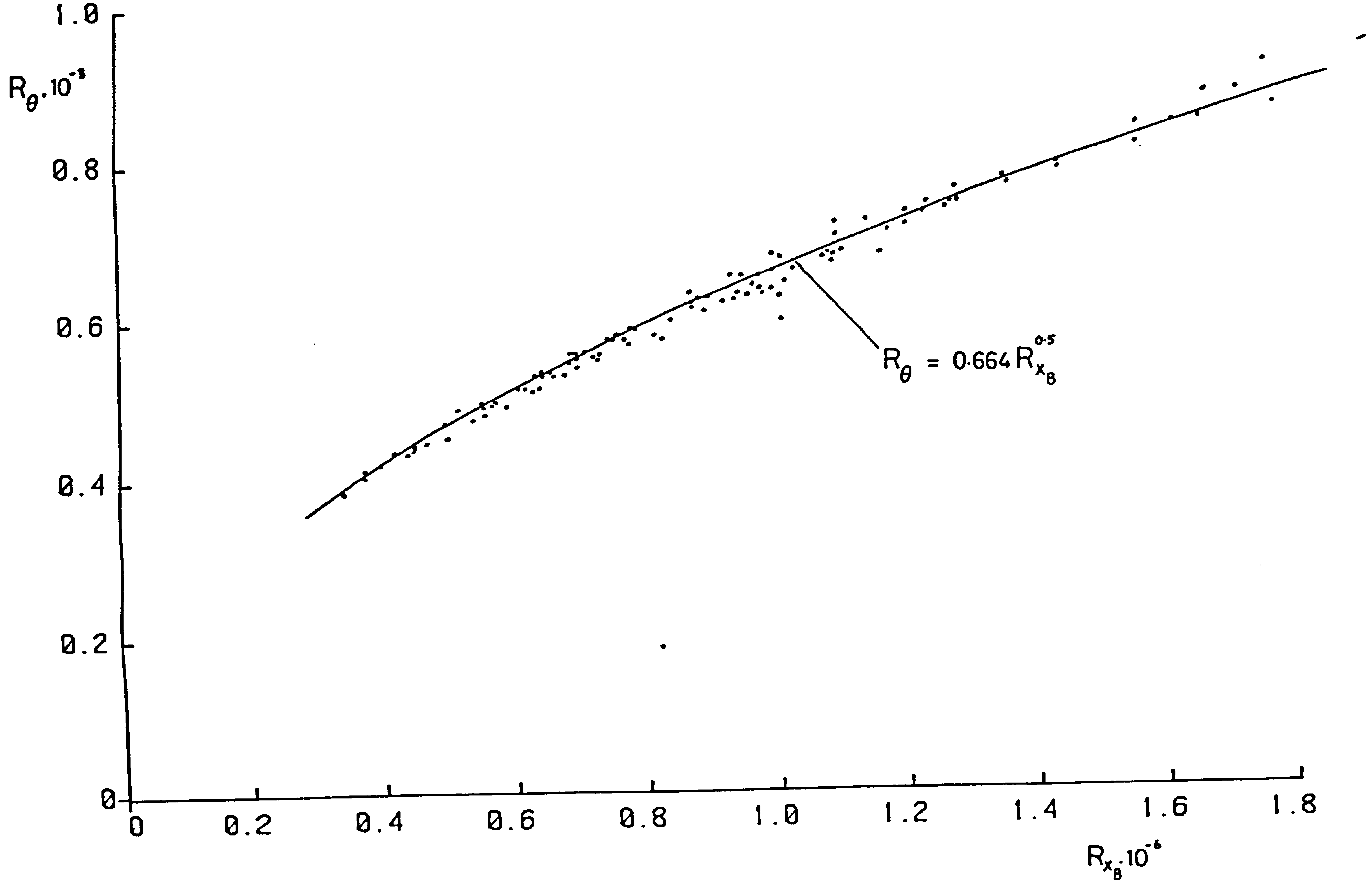

FIG. 5.9 VARIATION OF R_θ WITH R_{x_8}

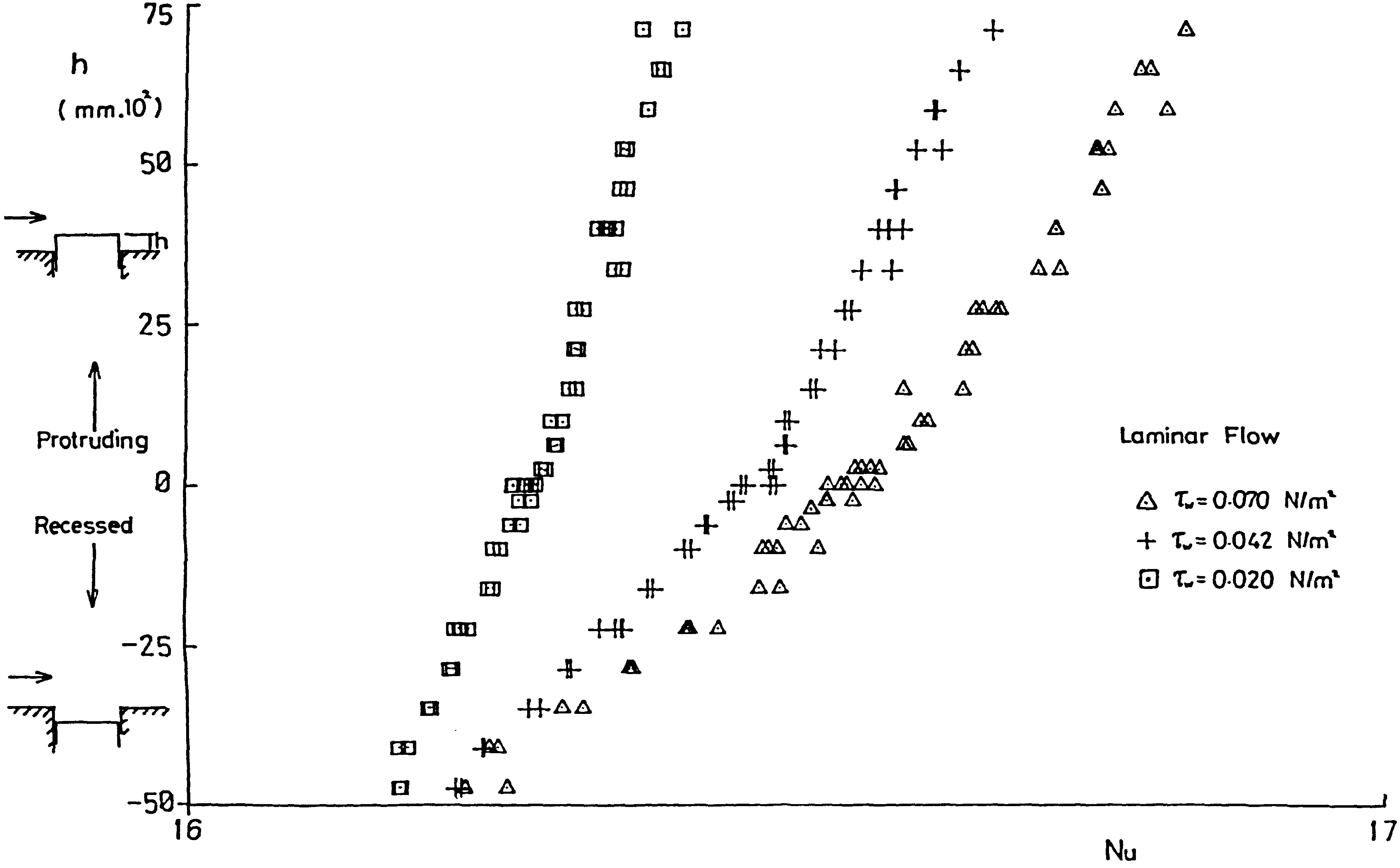

FIG. 5.10 EFFECT OF SURFACE MISALIGNMENT UPON Nu

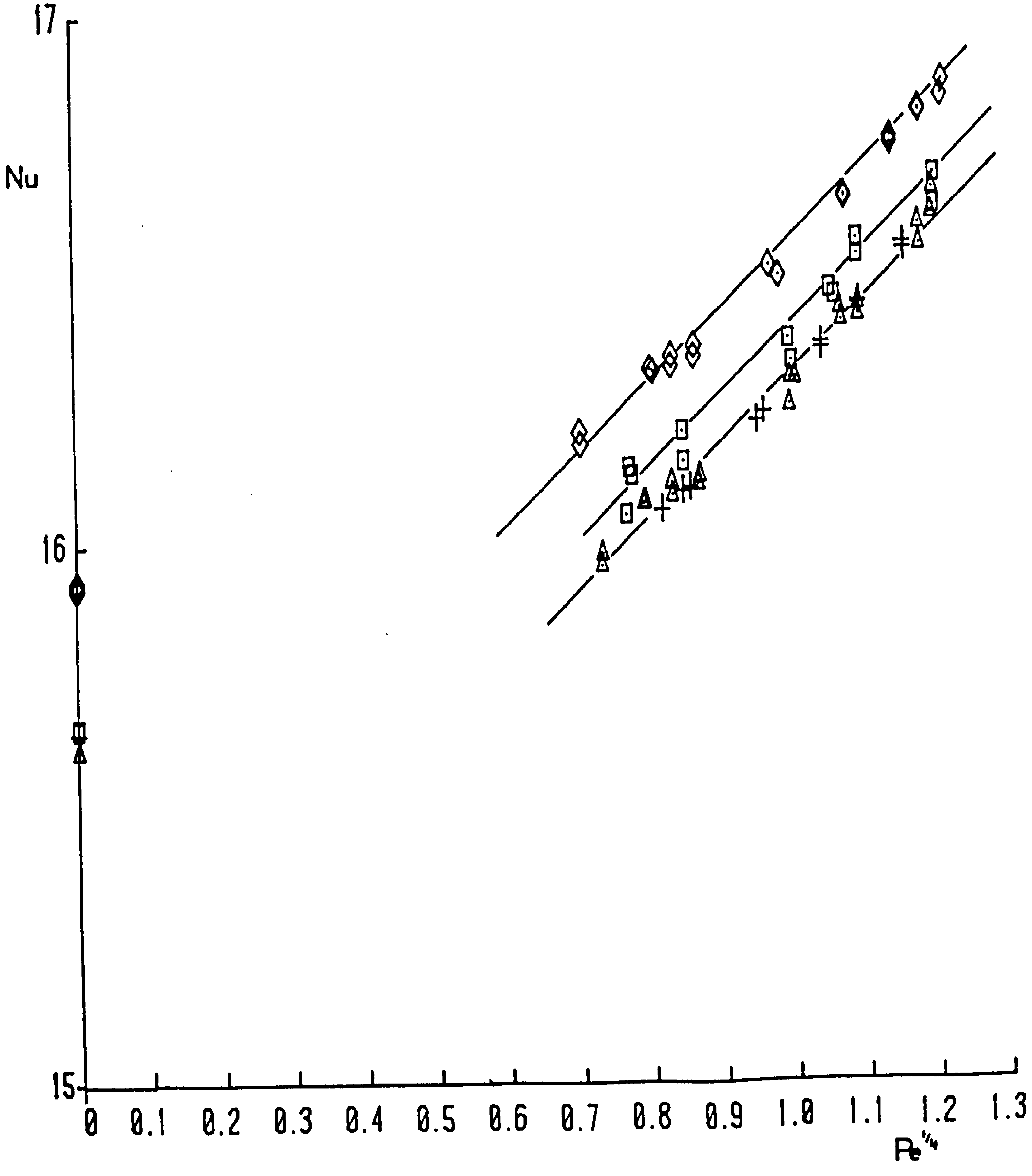

FIG. 5.11 SERIES OF LAMINAR CALIBRATIONS (PROBE FLUSH)

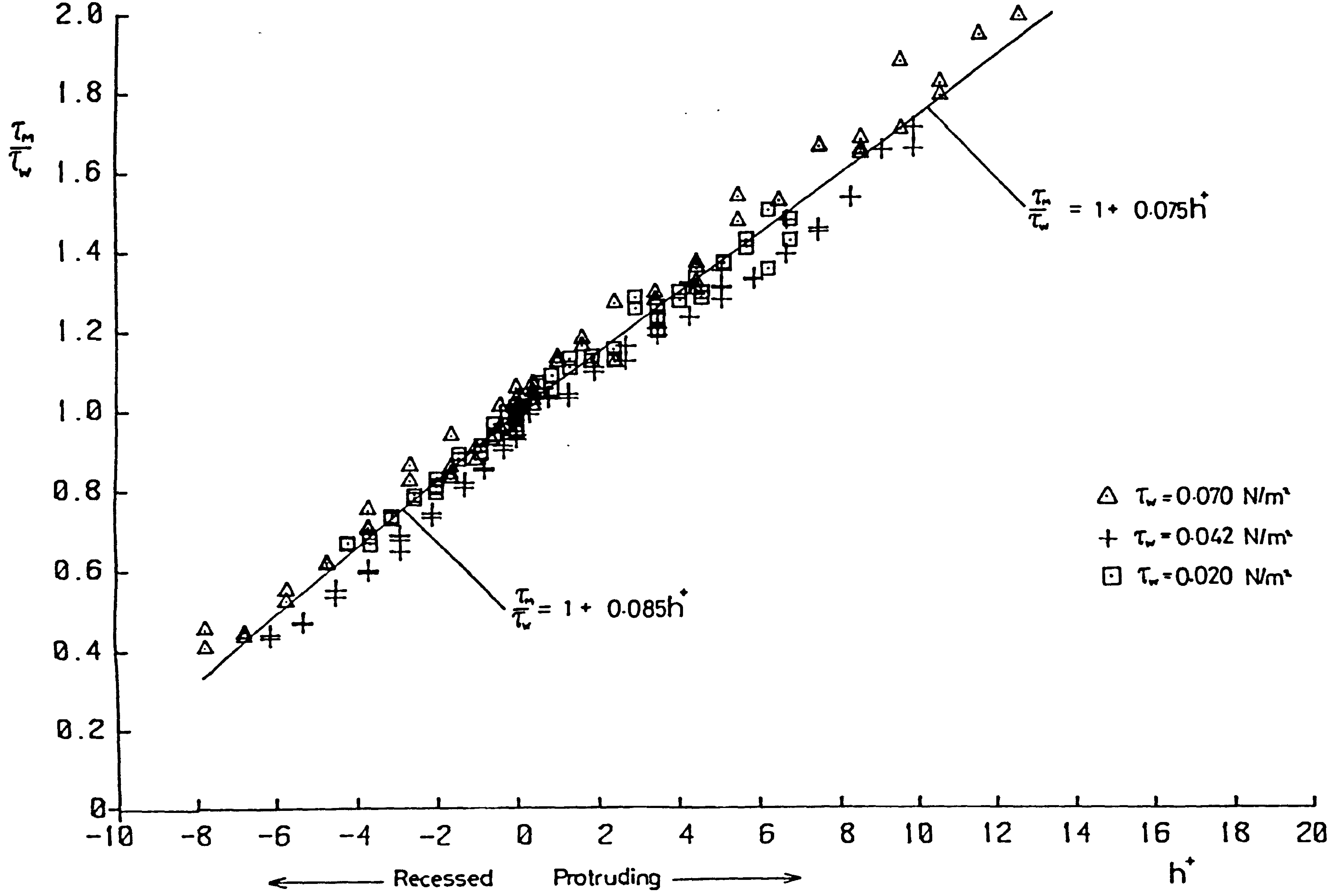

FIG. 5.12 VARIATION OF τ_m/τ_w WITH h^+ (LAMINAR FLOW)

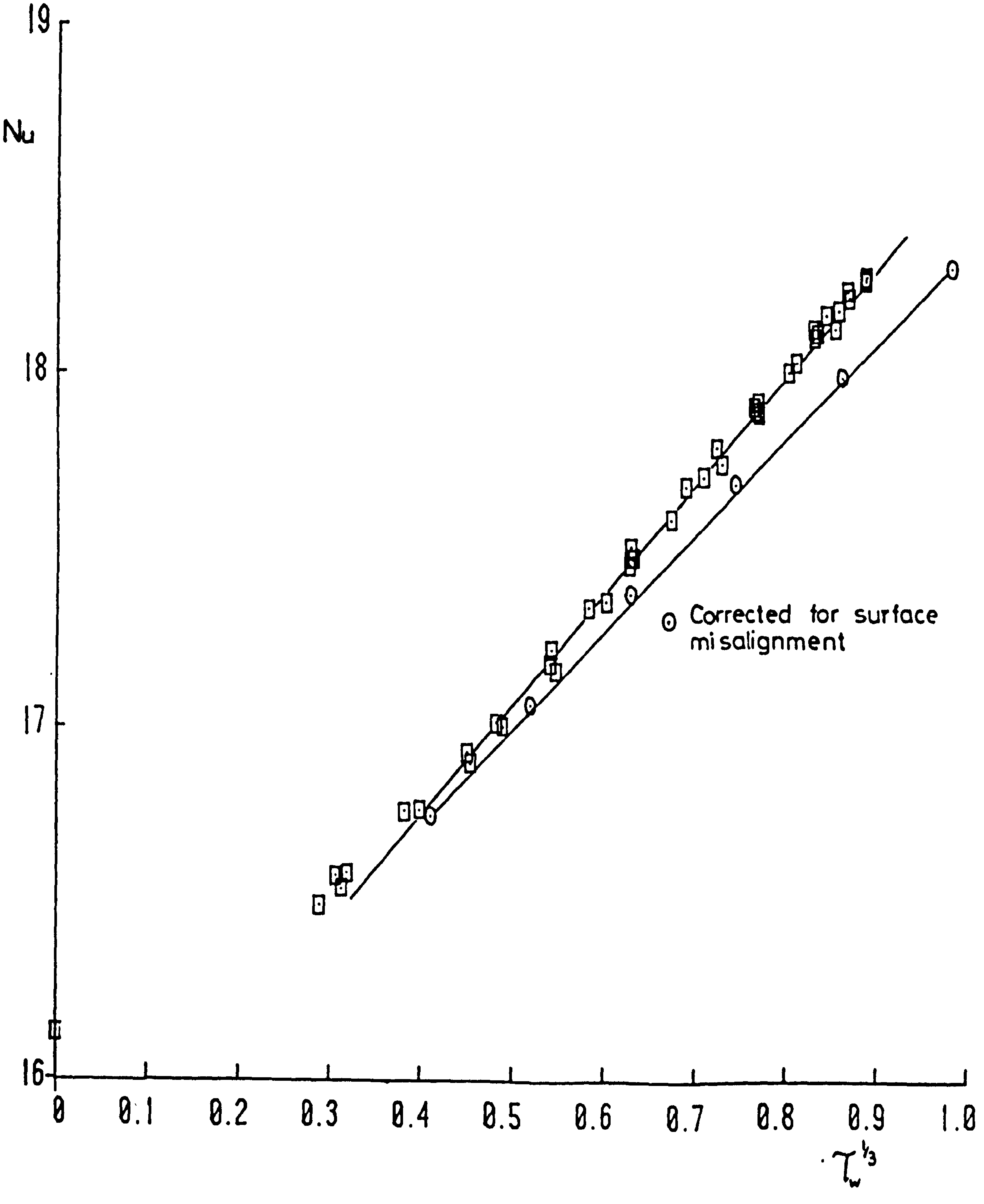

FIG. 5.13 LAMINAR CALIBRATION SHOWING CORRECTION FOR THE SURFACE MISALIGNMENT ERROR

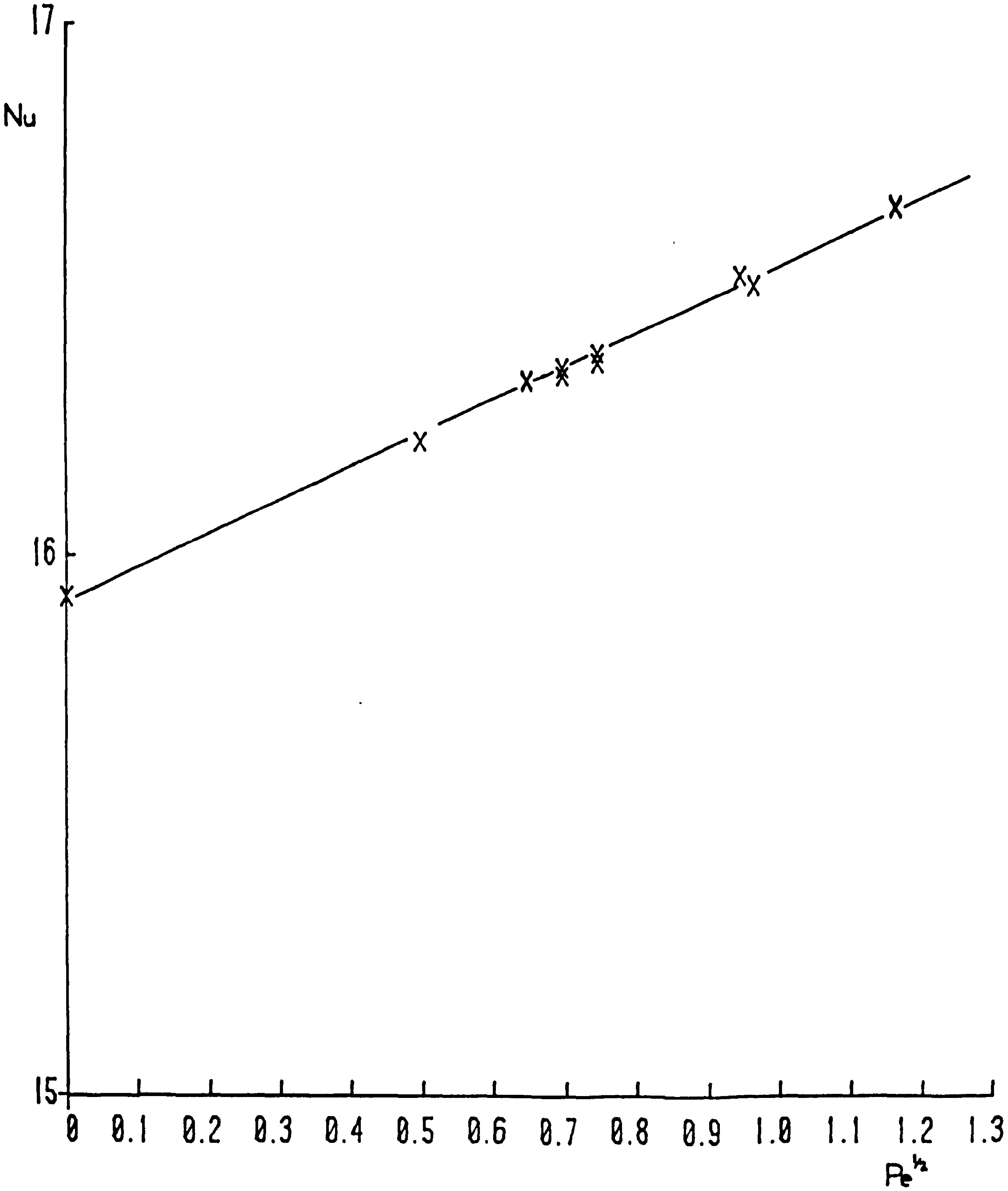

FIG. 5.14 LAMINAR CALIBRATION AT LOW Pe (PROBE FLUSH)

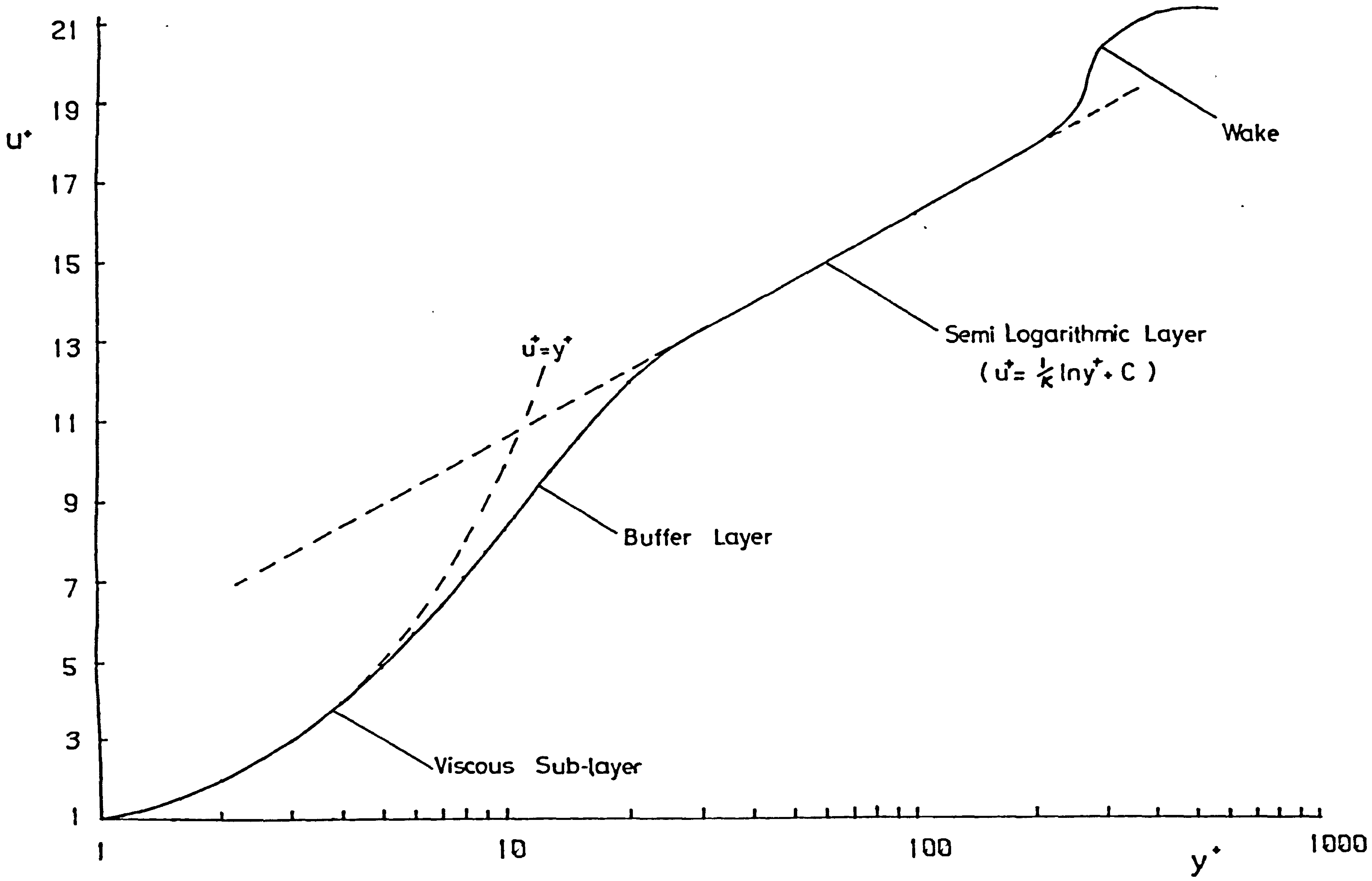

FIG. 6.1 TURBULENT BOUNDARY LAYER MEAN VELOCITY PROFILE

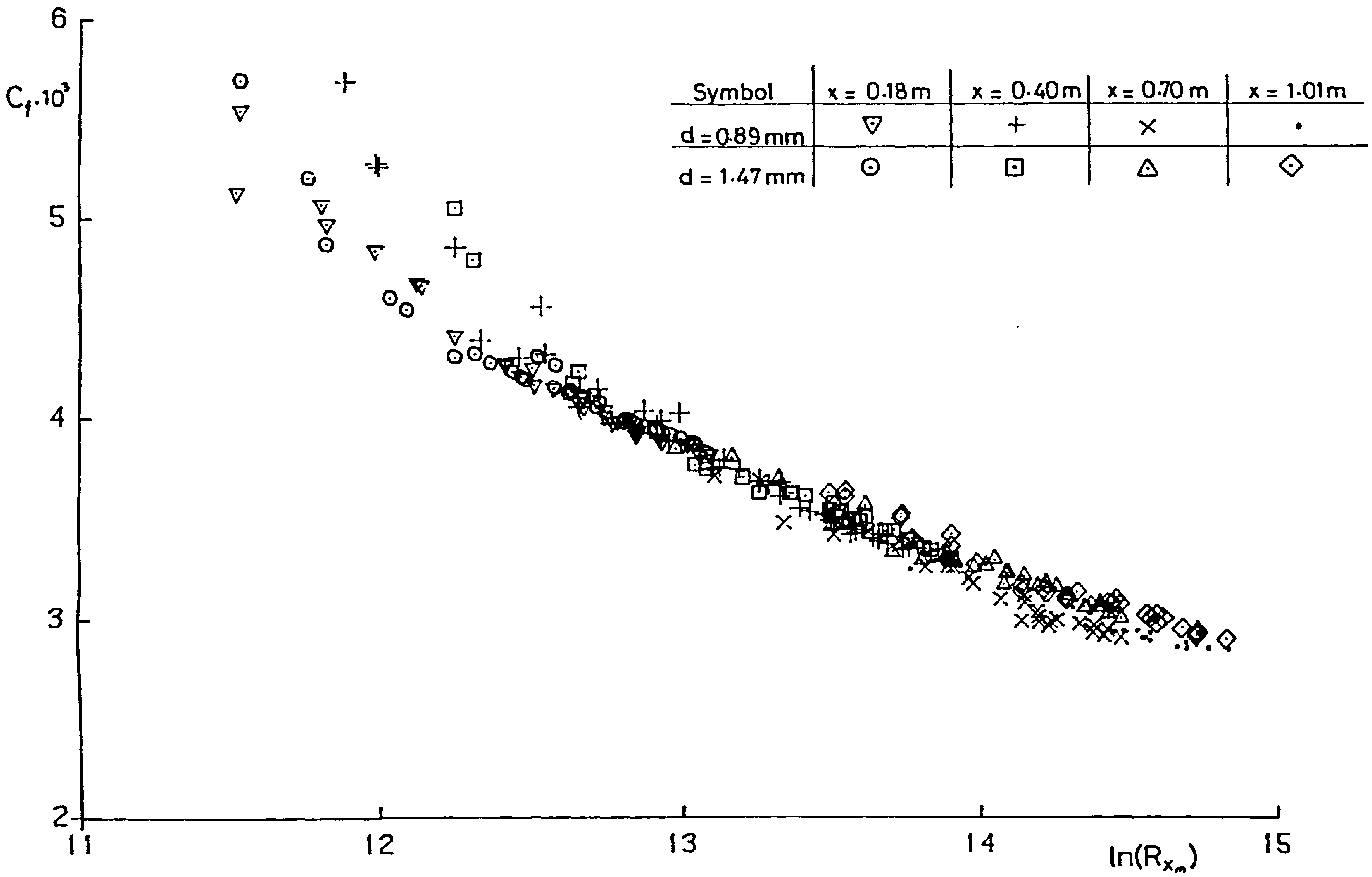

FIG. 6.2 MEASUREMENT OF C_f USING THE PRESTON TUBE TECHNIQUE

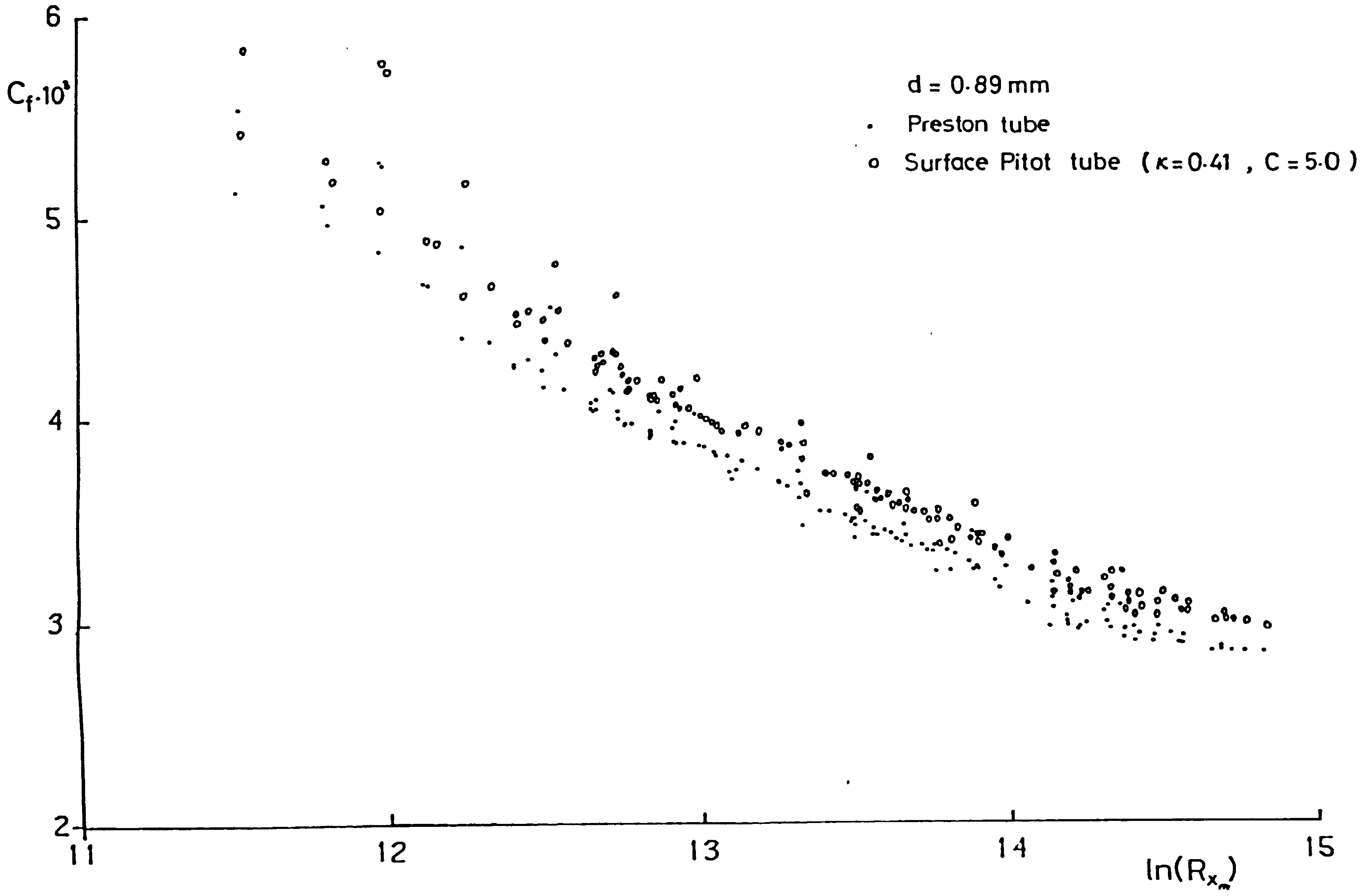

FIG. 6.3 VARIATION OF C_f WITH R_{x_m} DEDUCED FROM THE PRESTON TUBE AND SURFACE PITOT TUBE

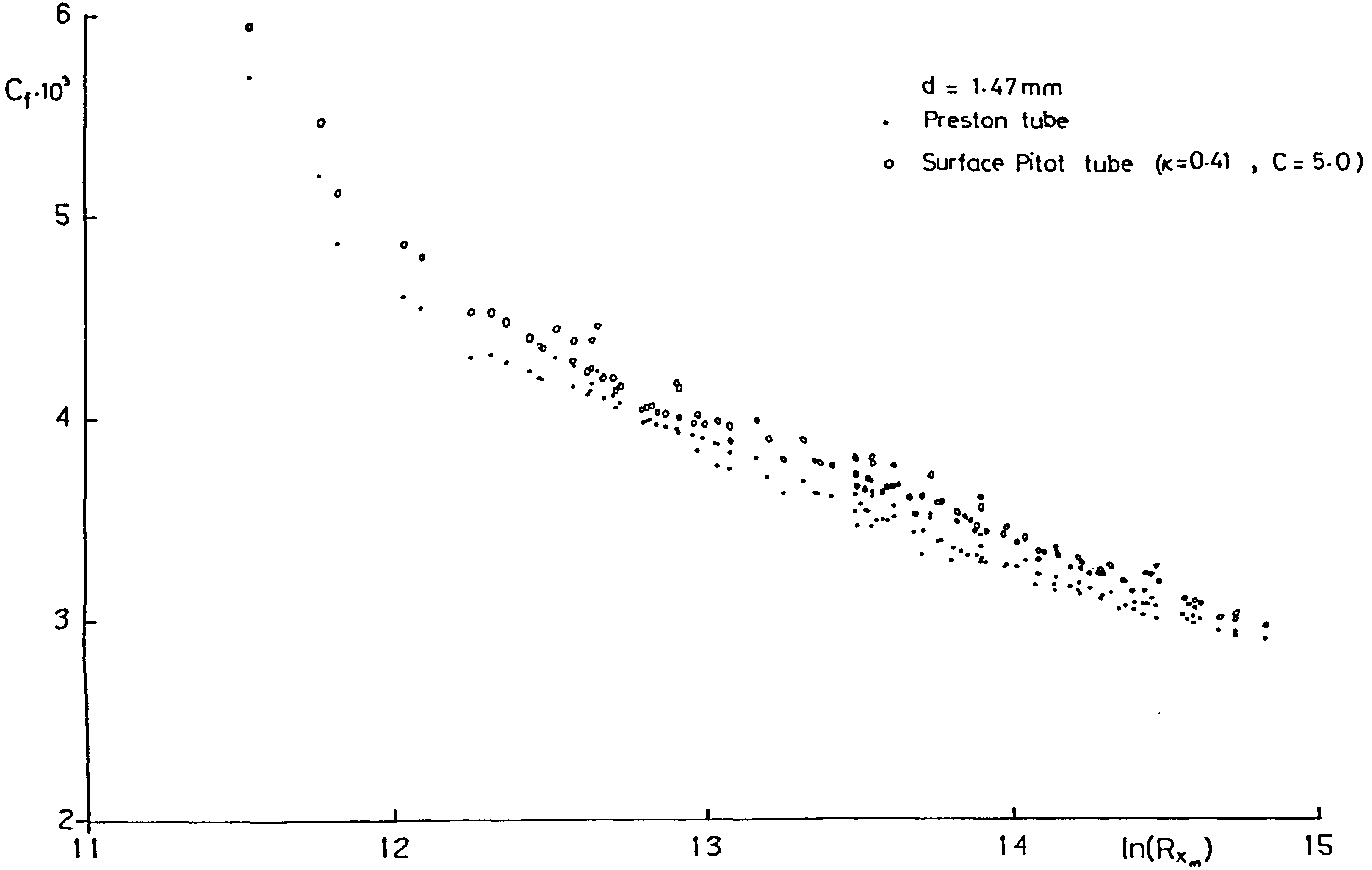

FIG. 6.4 VARIATION OF C_f WITH R_{x_m} DEDUCED FROM THE PRESTON TUBE AND SURFACE PITOT TUBE

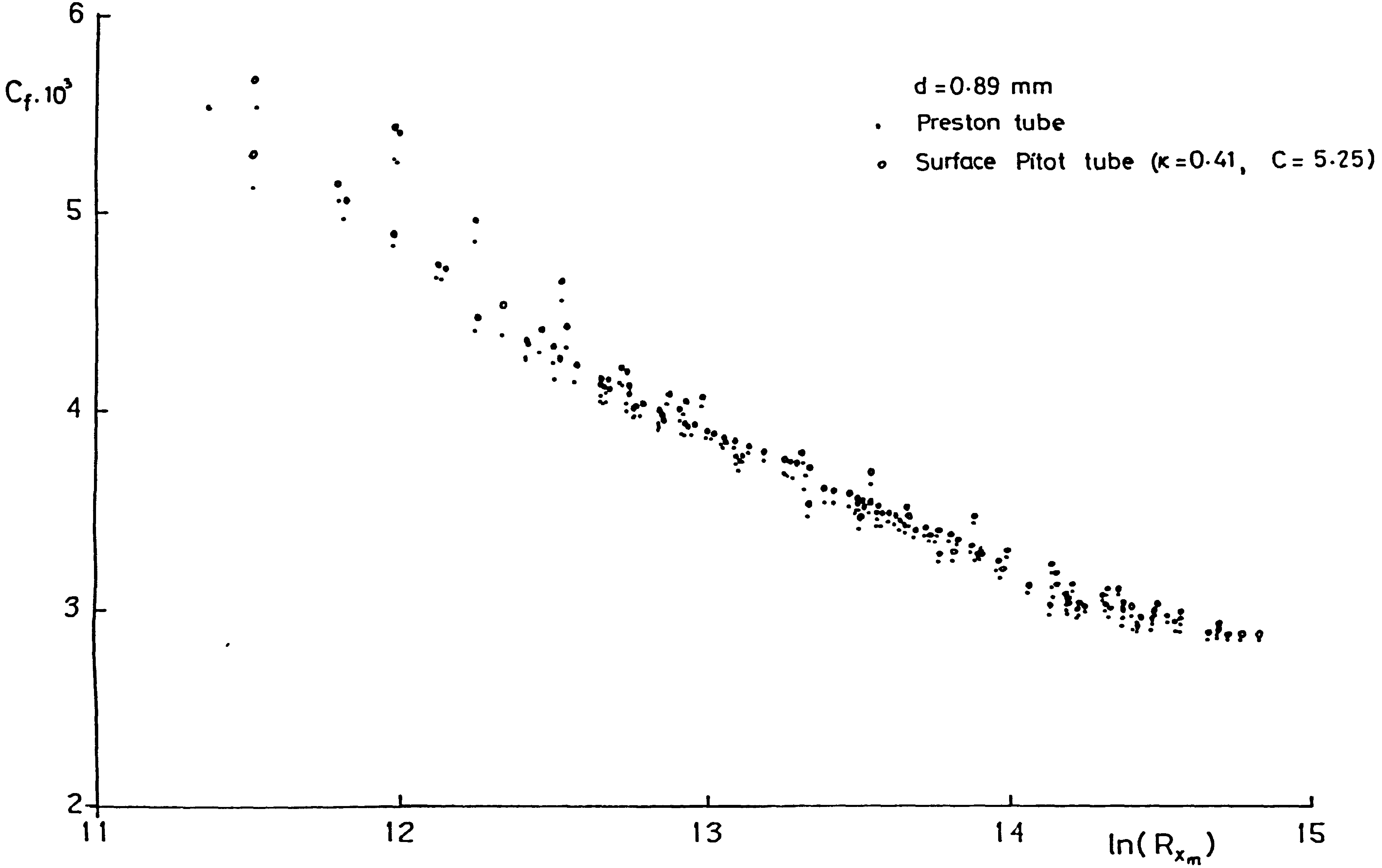

FIG. 6.5 VARIATION OF C_f WITH R_{x_m} DEDUCED FROM THE PRESTON TUBE AND SURFACE PITOT TUBE

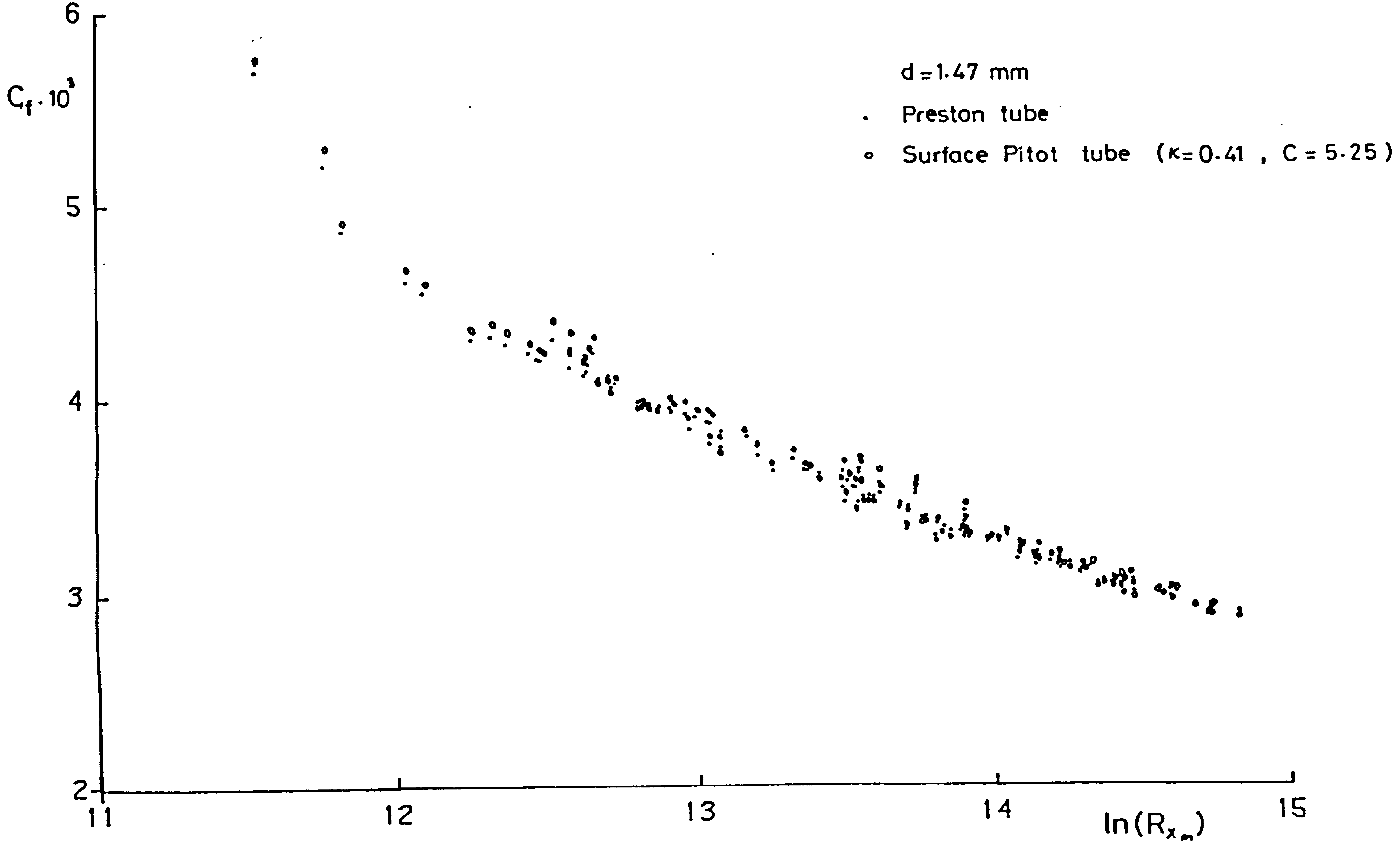

FIG. 6.6 VARIATION OF C_f WITH R_{x_m} DEDUCED FROM PRESTON TUBE AND SURFACE PITOT TUBE

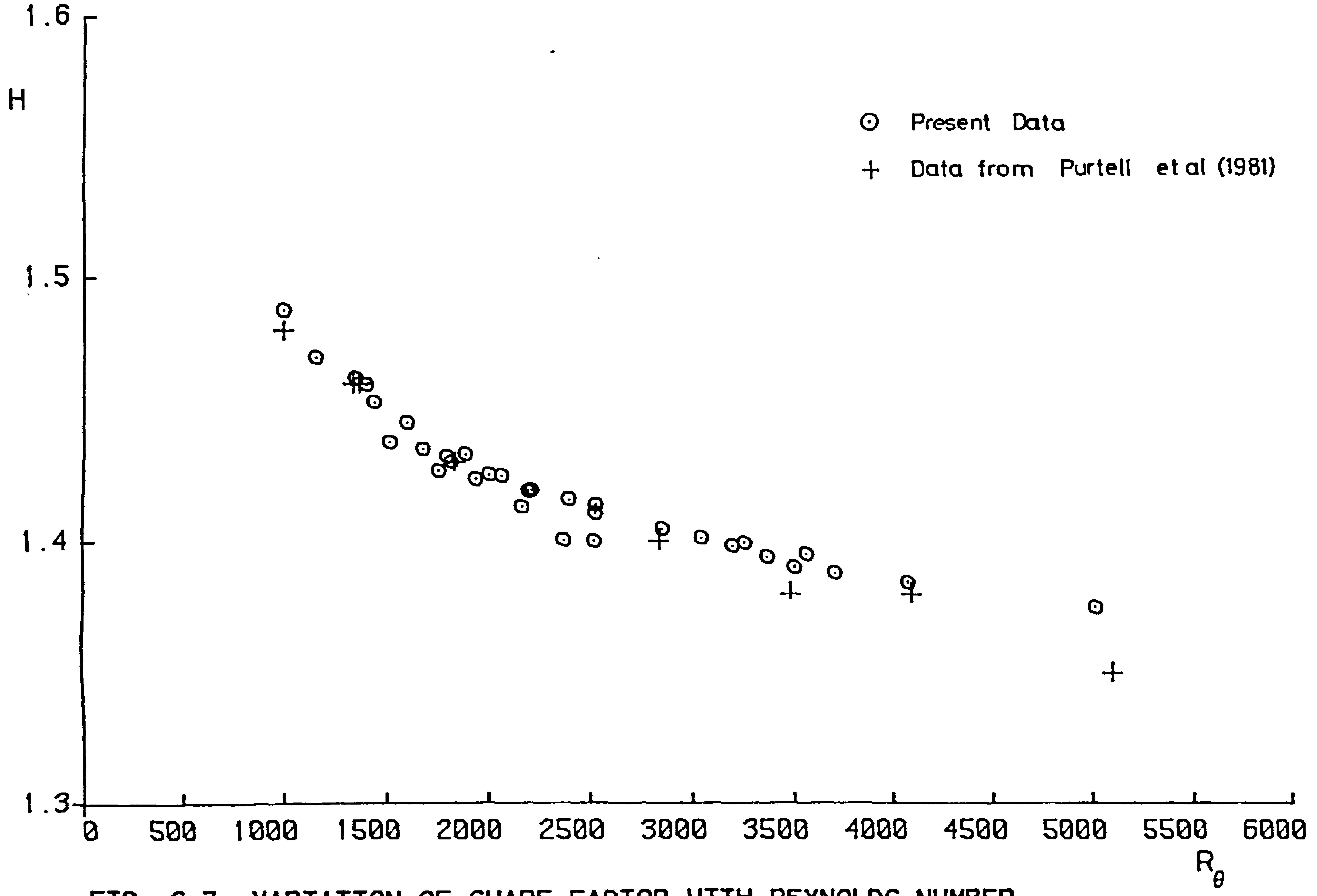

FIG. 6.7 VARIATION OF SHAPE FACTOR WITH REYNOLDS NUMBER

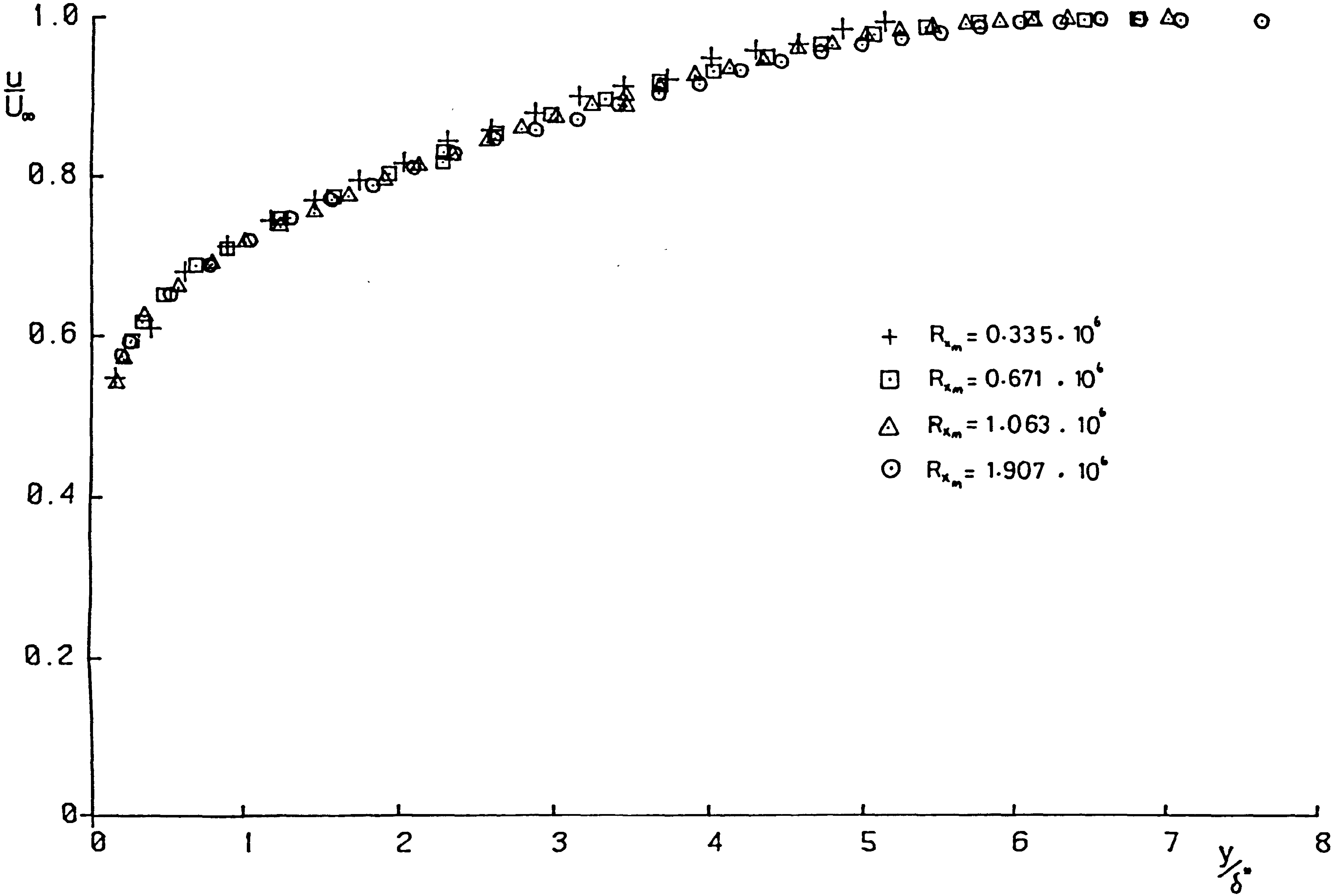

FIG. 6.8 VARIATION OF VELOCITY PROFILE WITH REYNOLDS NUMBER

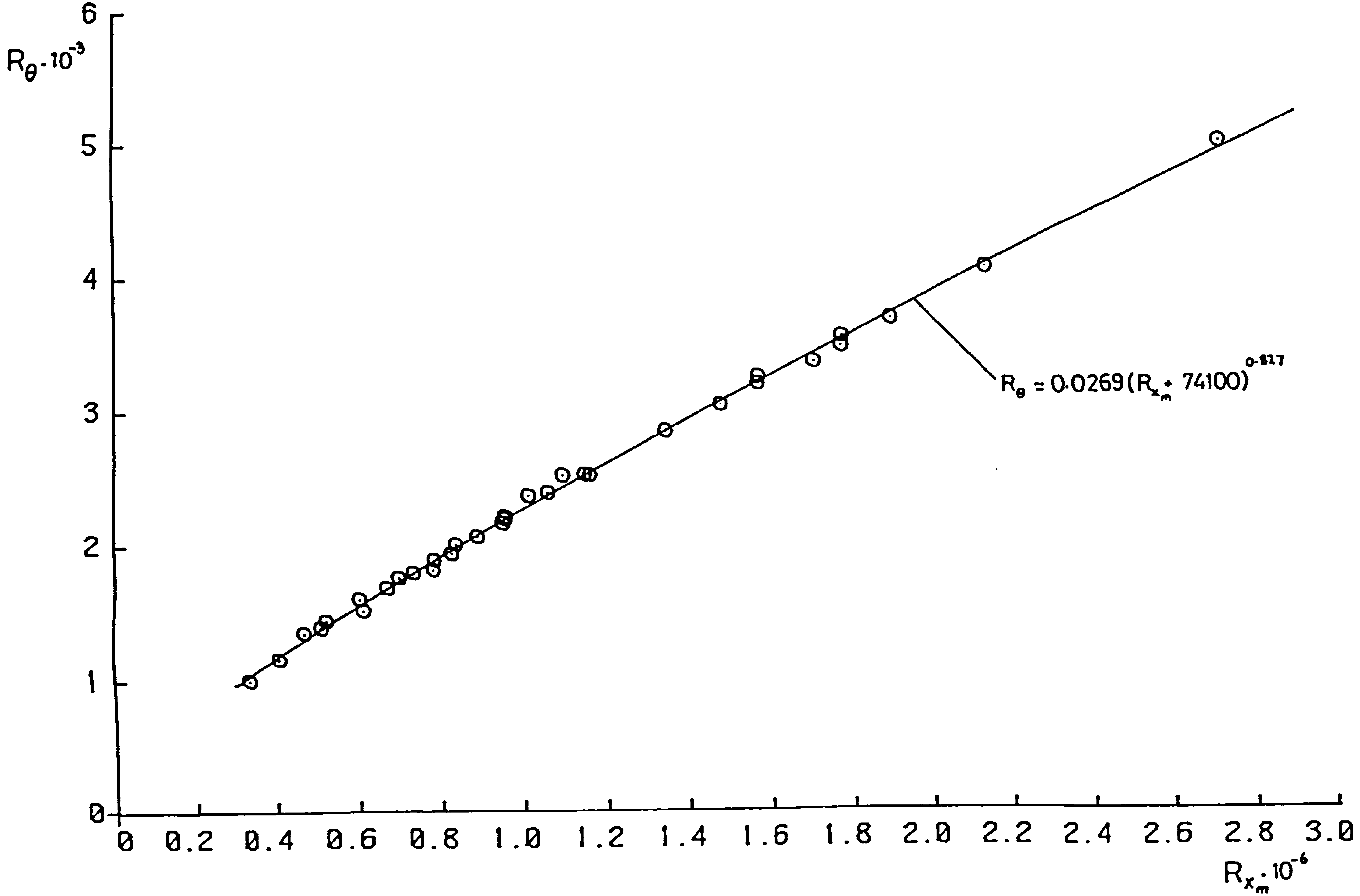

FIG. 6.9 VARIATION OF R_θ WITH R_{x_m}

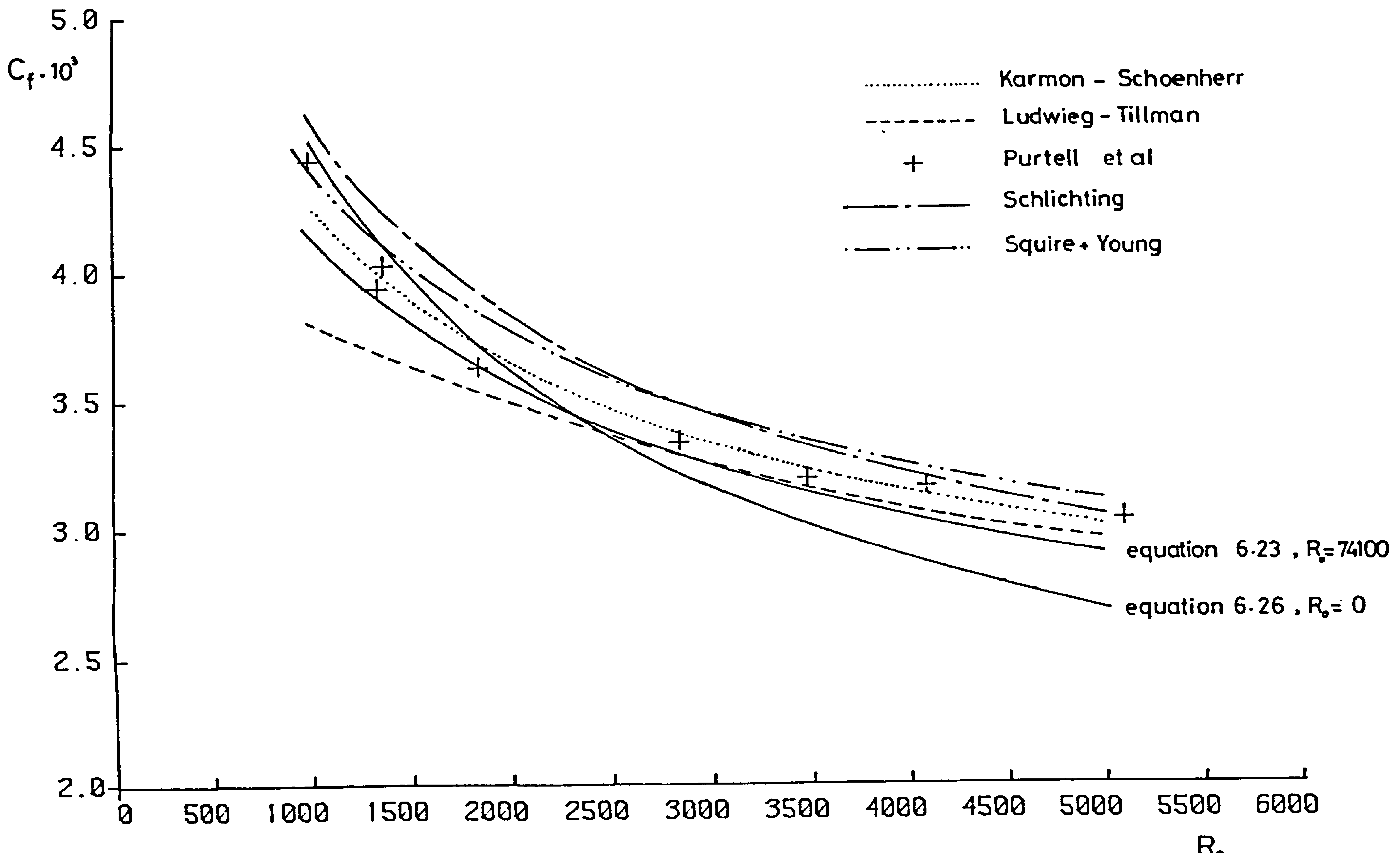

FIG. 6.10 COMPARISON BETWEEN VARIOUS C_f - R_θ RELATIONSHIPS

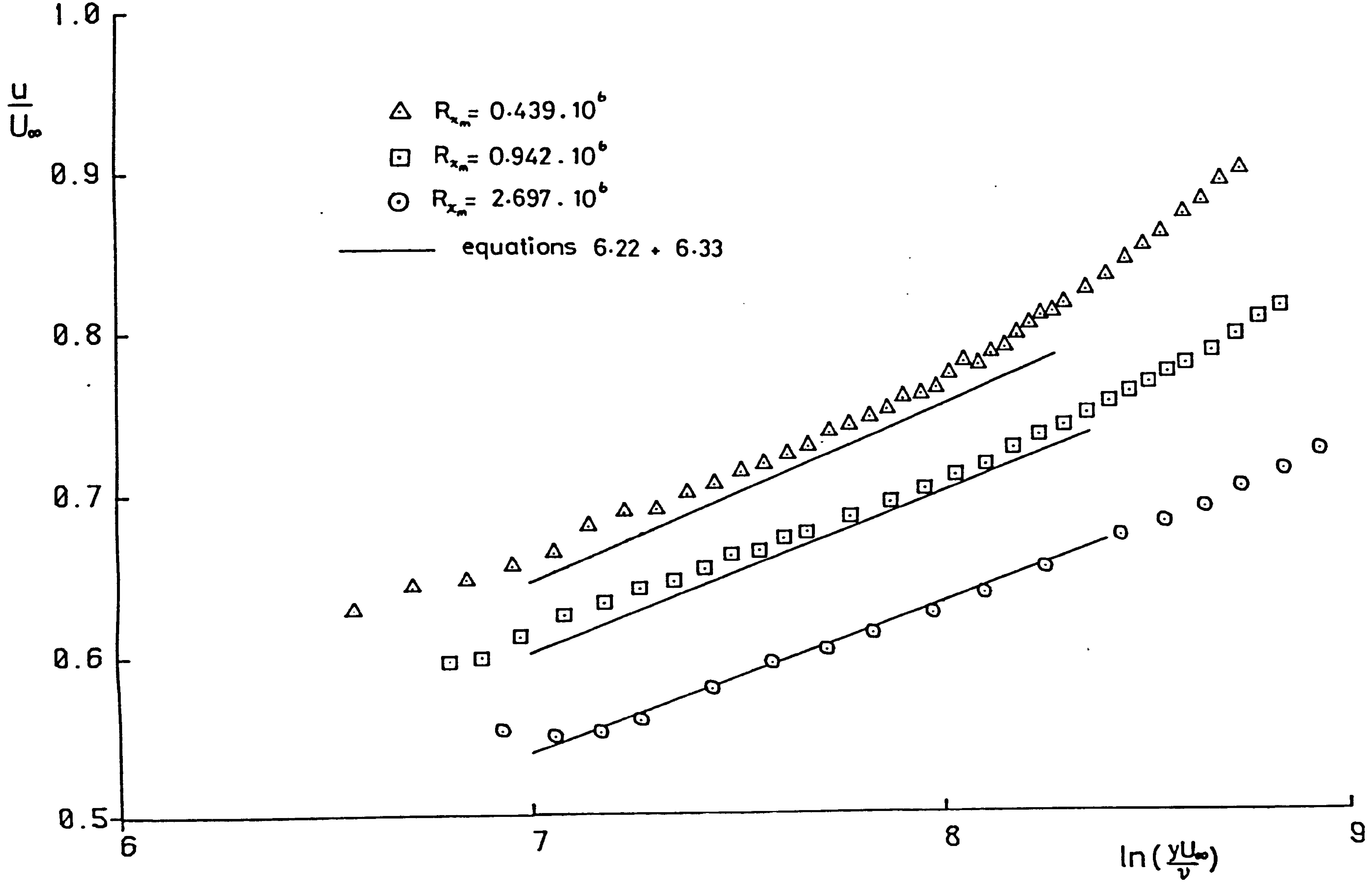

FIG. 6.11 APPLICATION OF CLAUSER'S METHOD

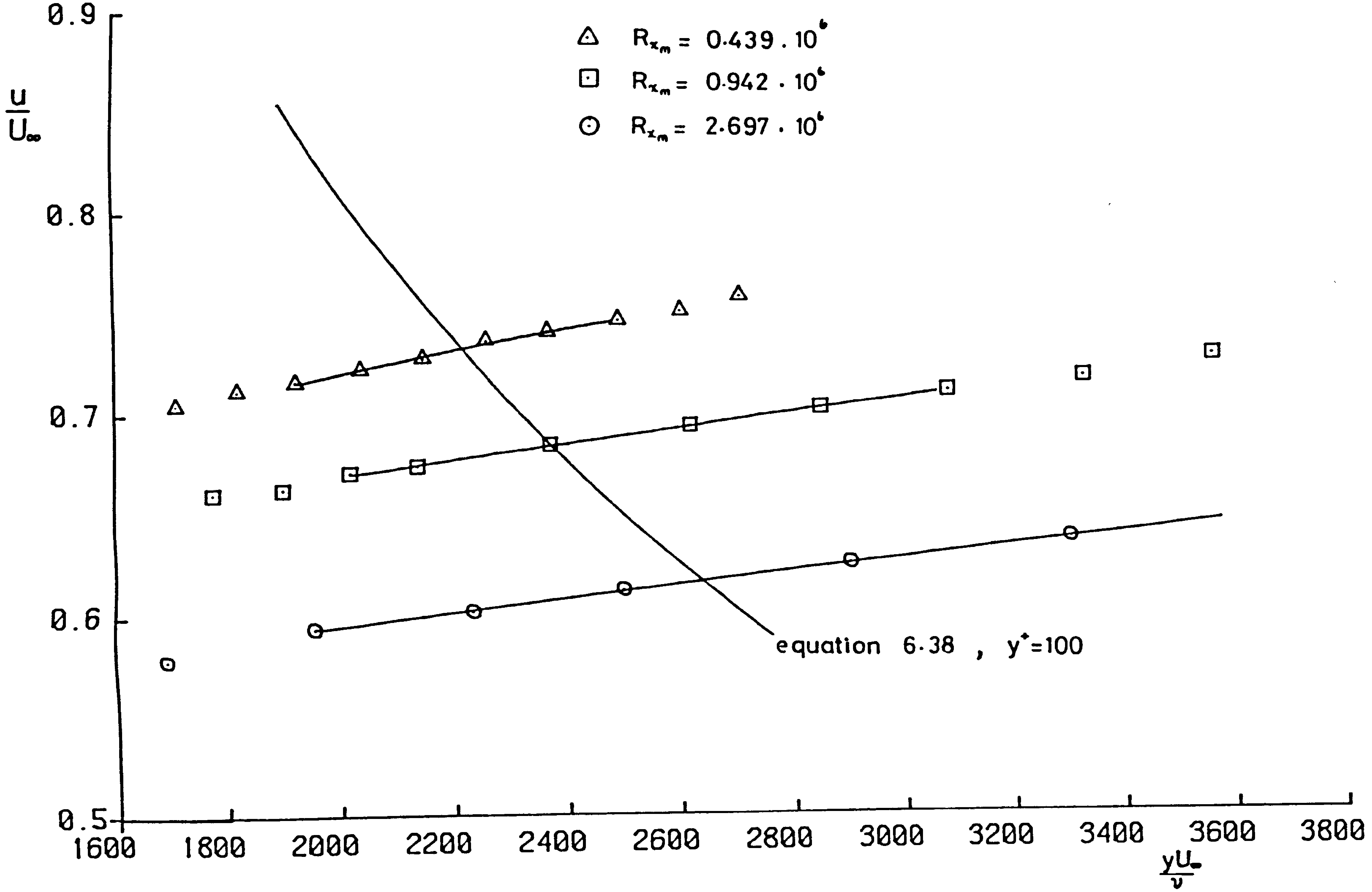

FIG. 6.12 APPLICATION OF BRADSHAW'S METHOD

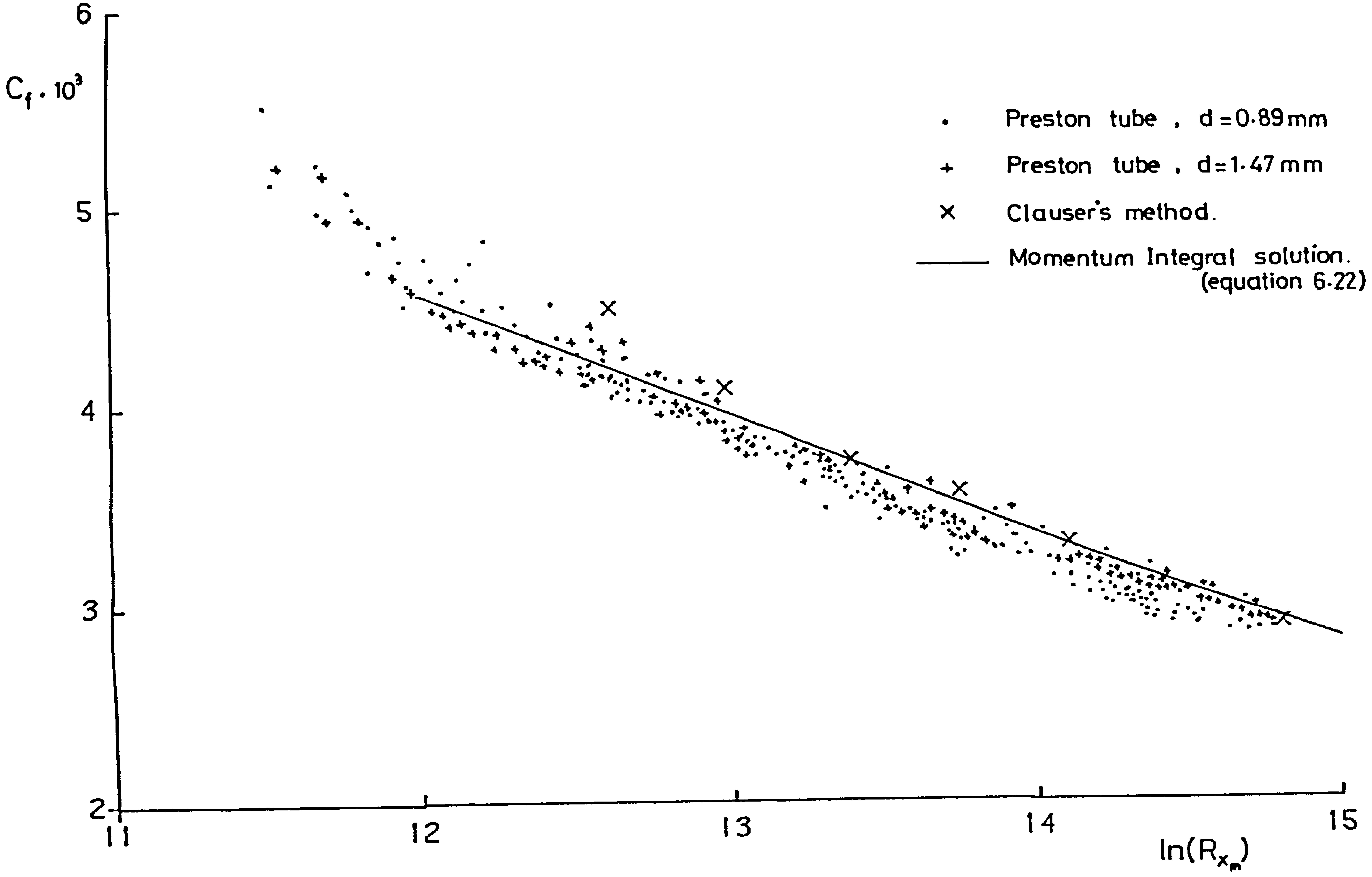

FIG. 6.13 VARIATION OF C_f WITH R_{x_m}

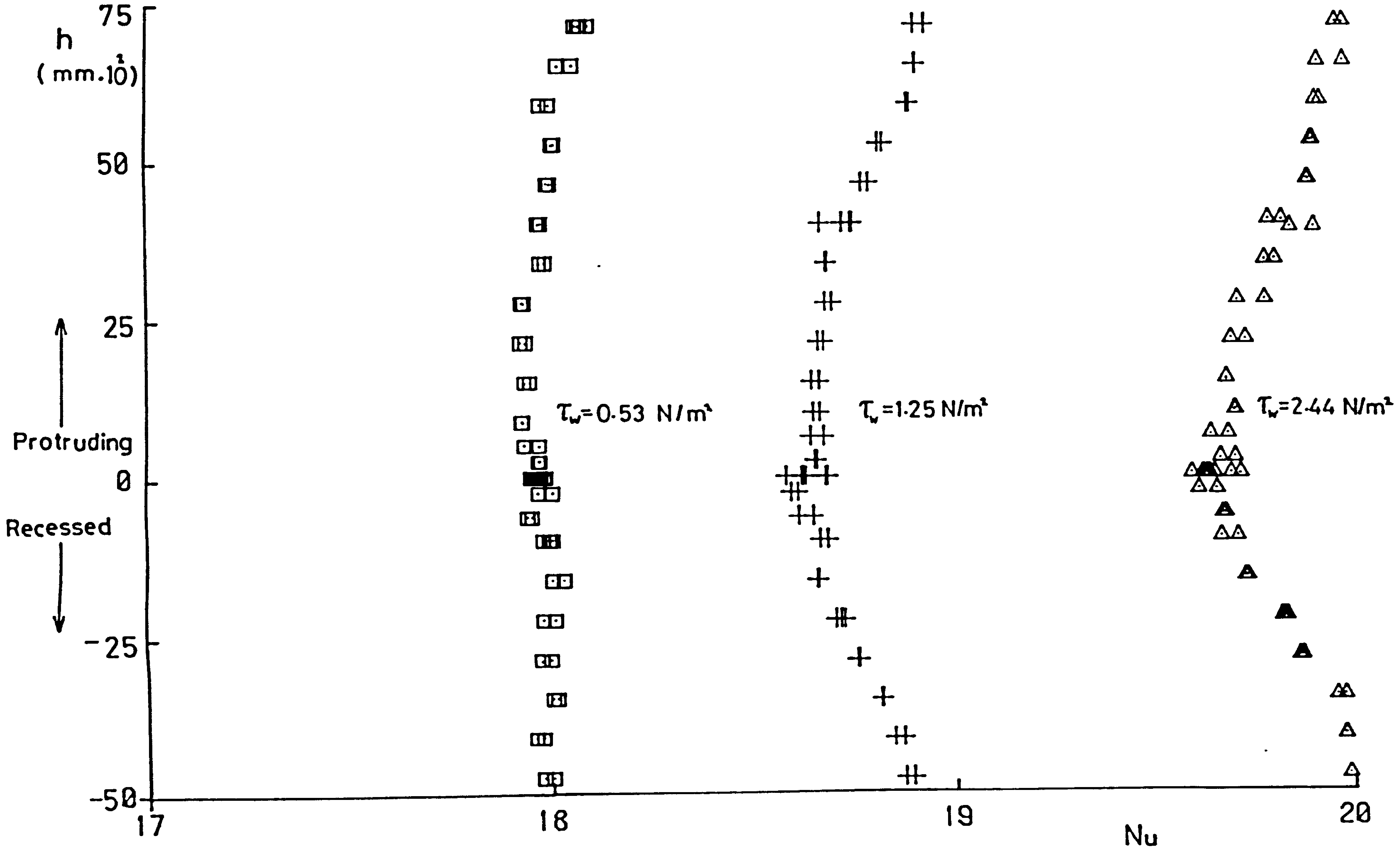

FIG. 6.14 EFFECT OF SURFACE MISALIGNMENT UPON Nu

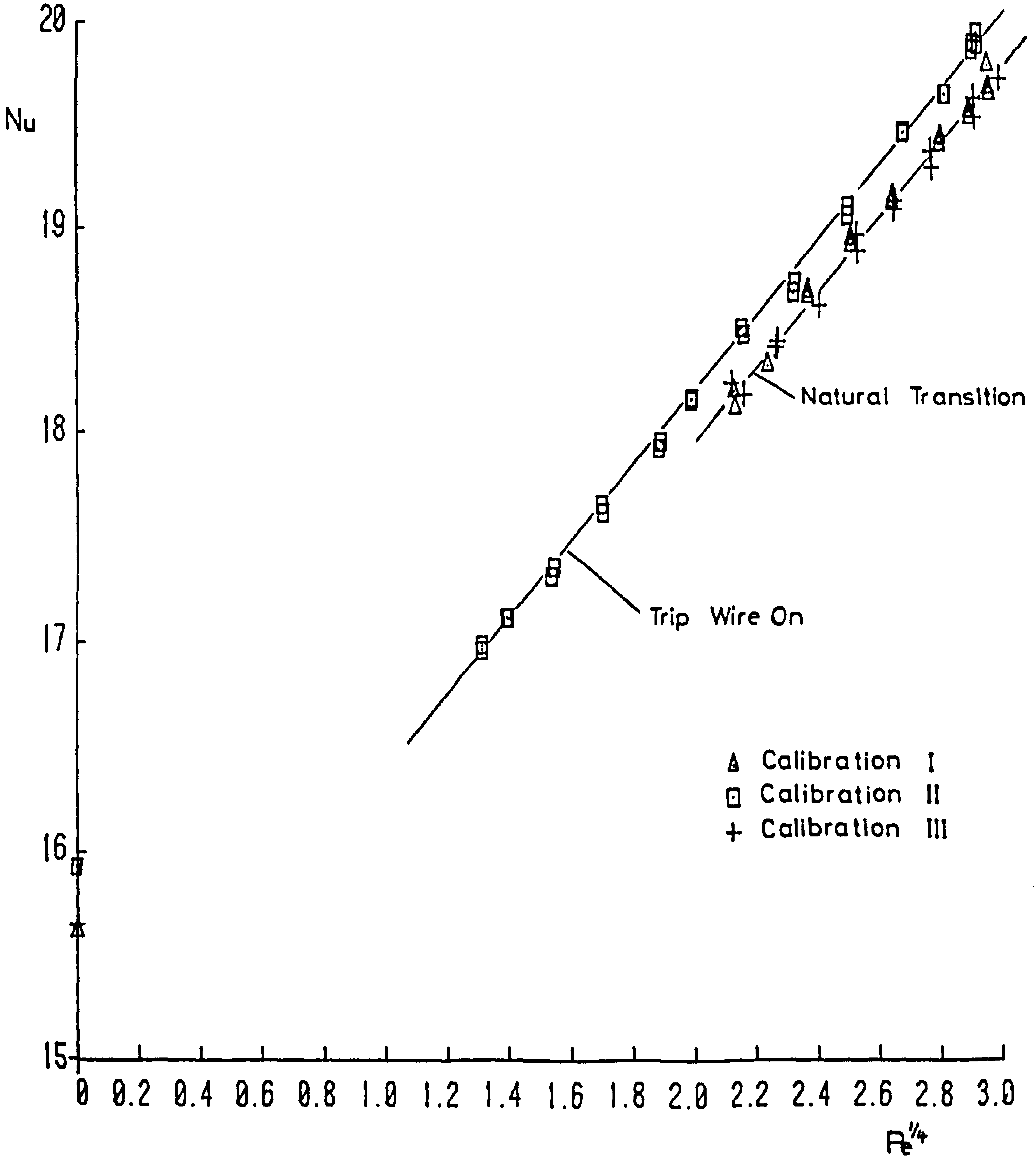

FIG. 6.15 SERIES OF TURBULENT CALIBRATIONS (PROBE FLUSH)

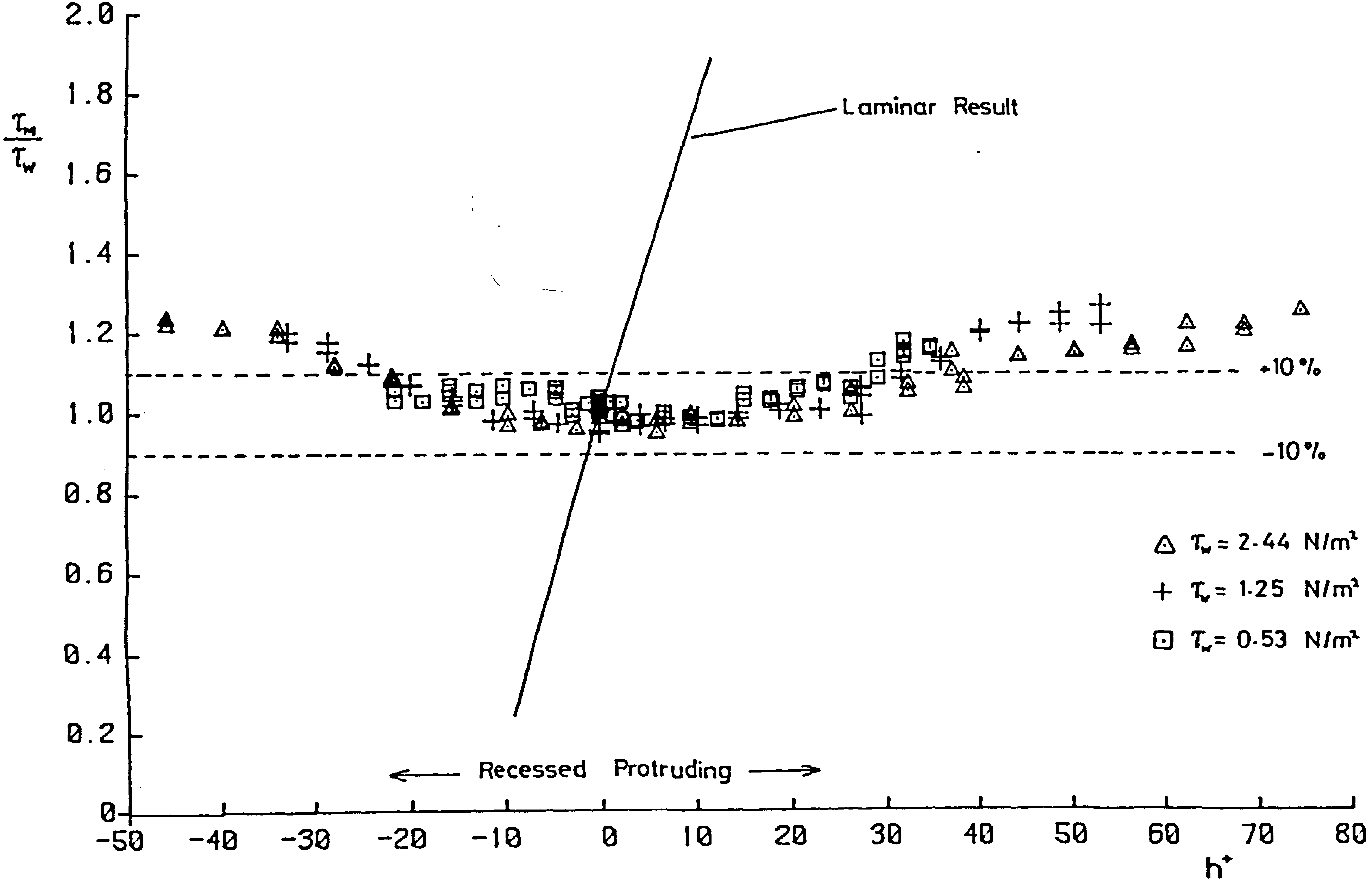

FIG. 6.16 VARIATION OF $\frac{\tau_M}{\tau_w}$ WITH h^+ (TURBULENT FLOW)

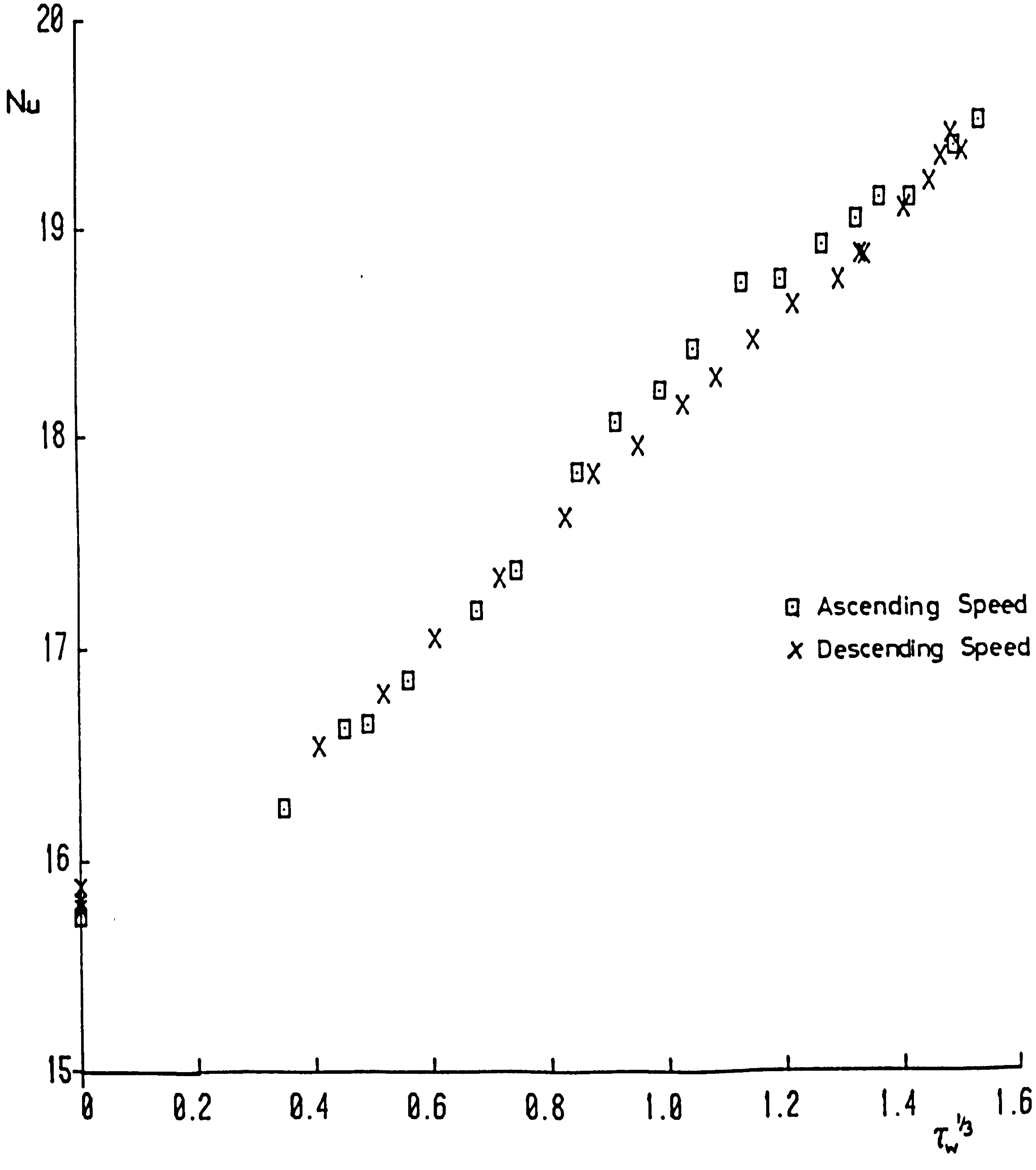

FIG. 6.17 TURBULENT CALIBRATION FOR ASCENDING AND DESCENDING SPEEDS

FIG. 6.18 TIME VARIATION OF Nu FOLLOWING A STEP CHANGE IN U_∞

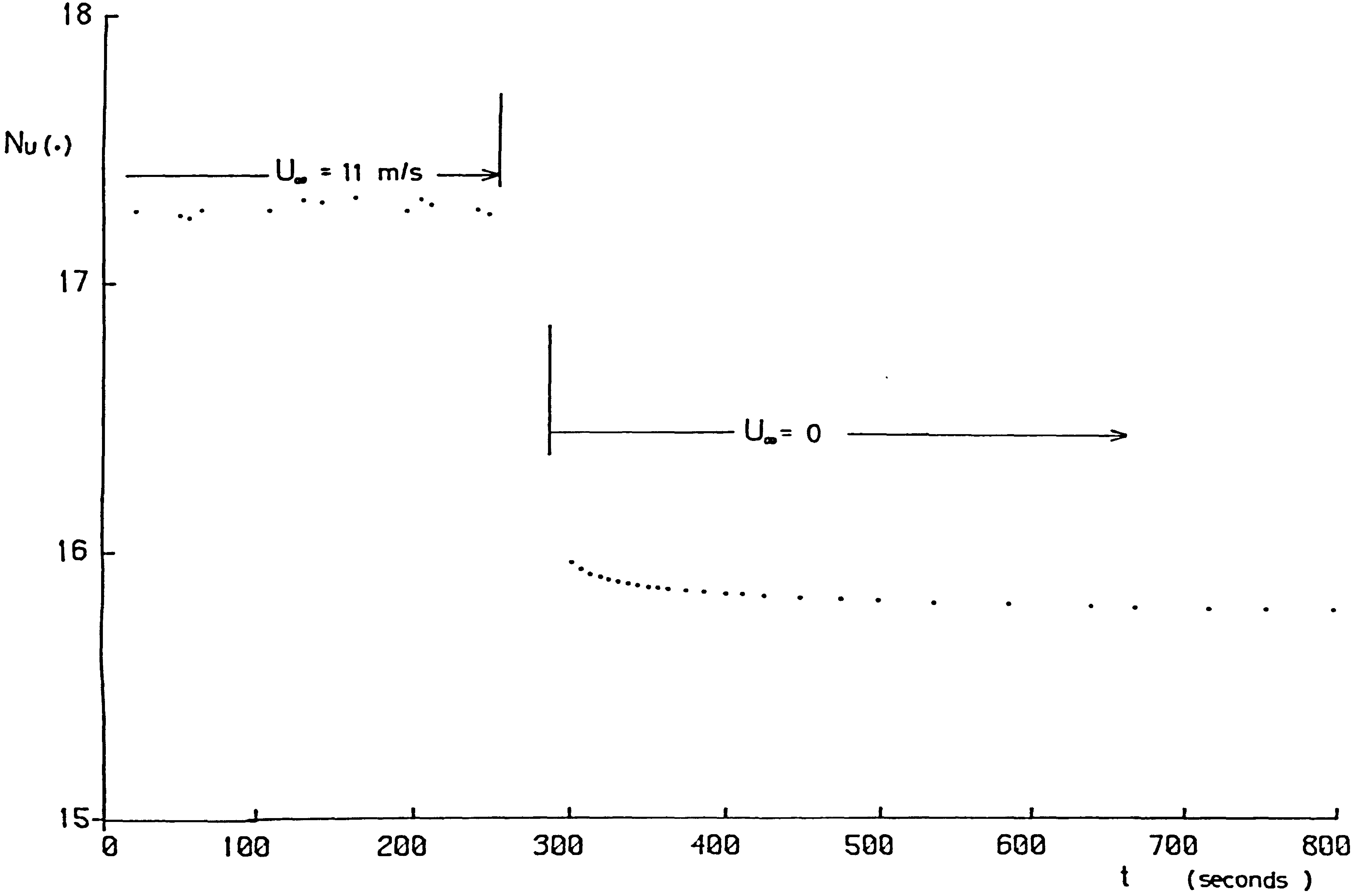

FIG. 6.19 TIME VARIATION OF Nu AFTER STOPPING THE FLOW

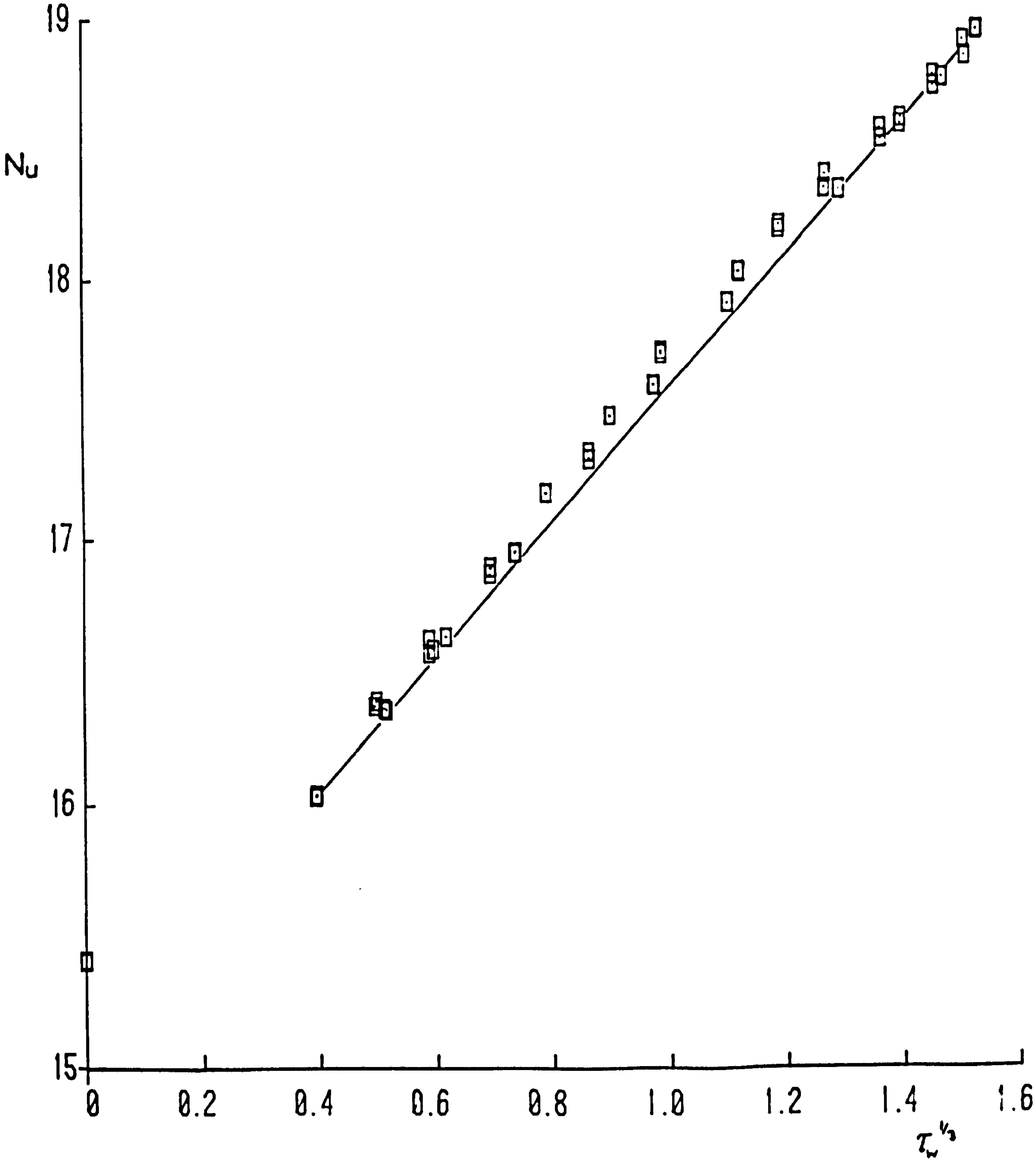

FIG. 6.20 DETAILED TURBULENT CALIBRATION

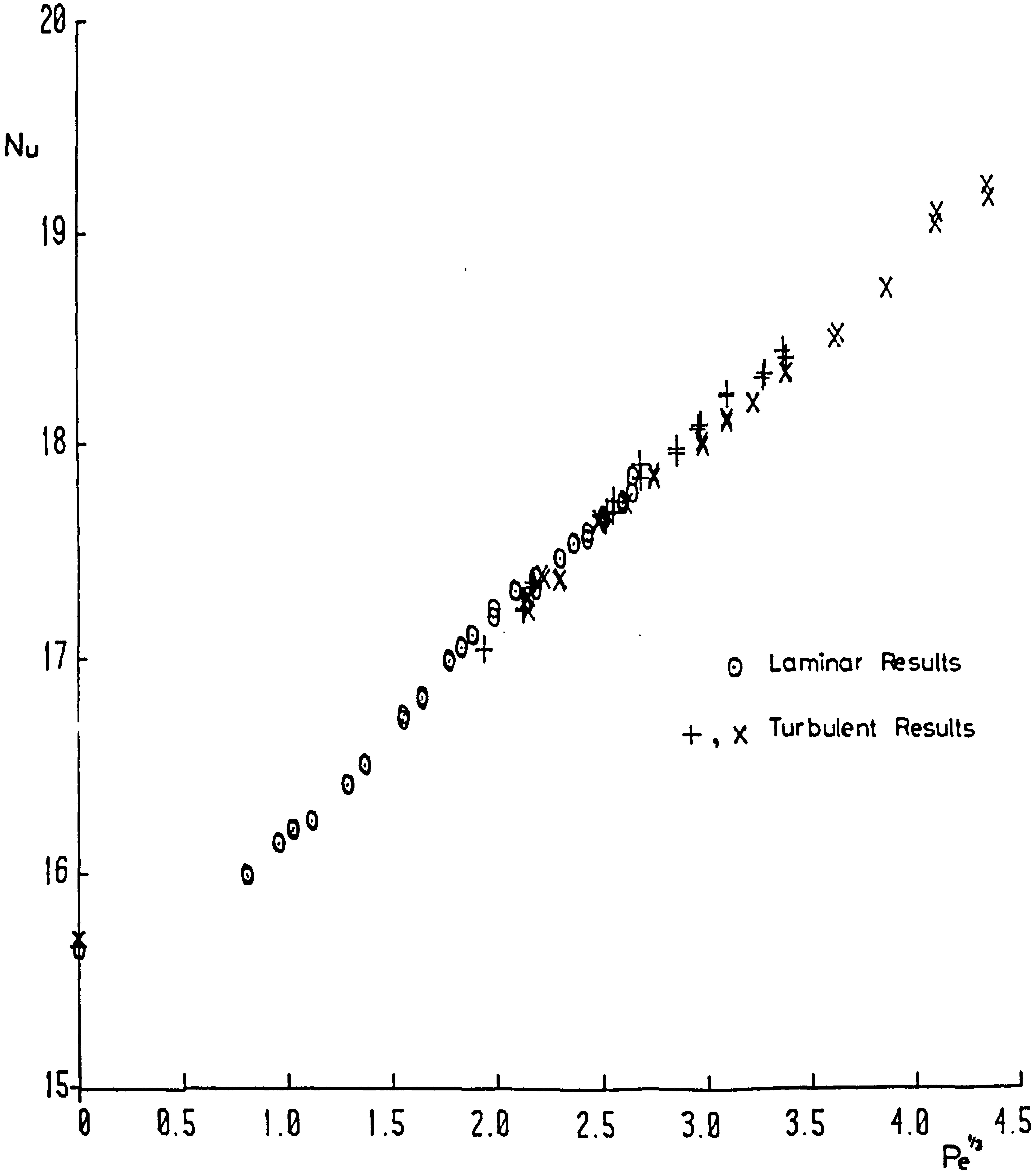

FIG. 6.21(a) LAMINAR AND TURBULENT CALIBRATIONS

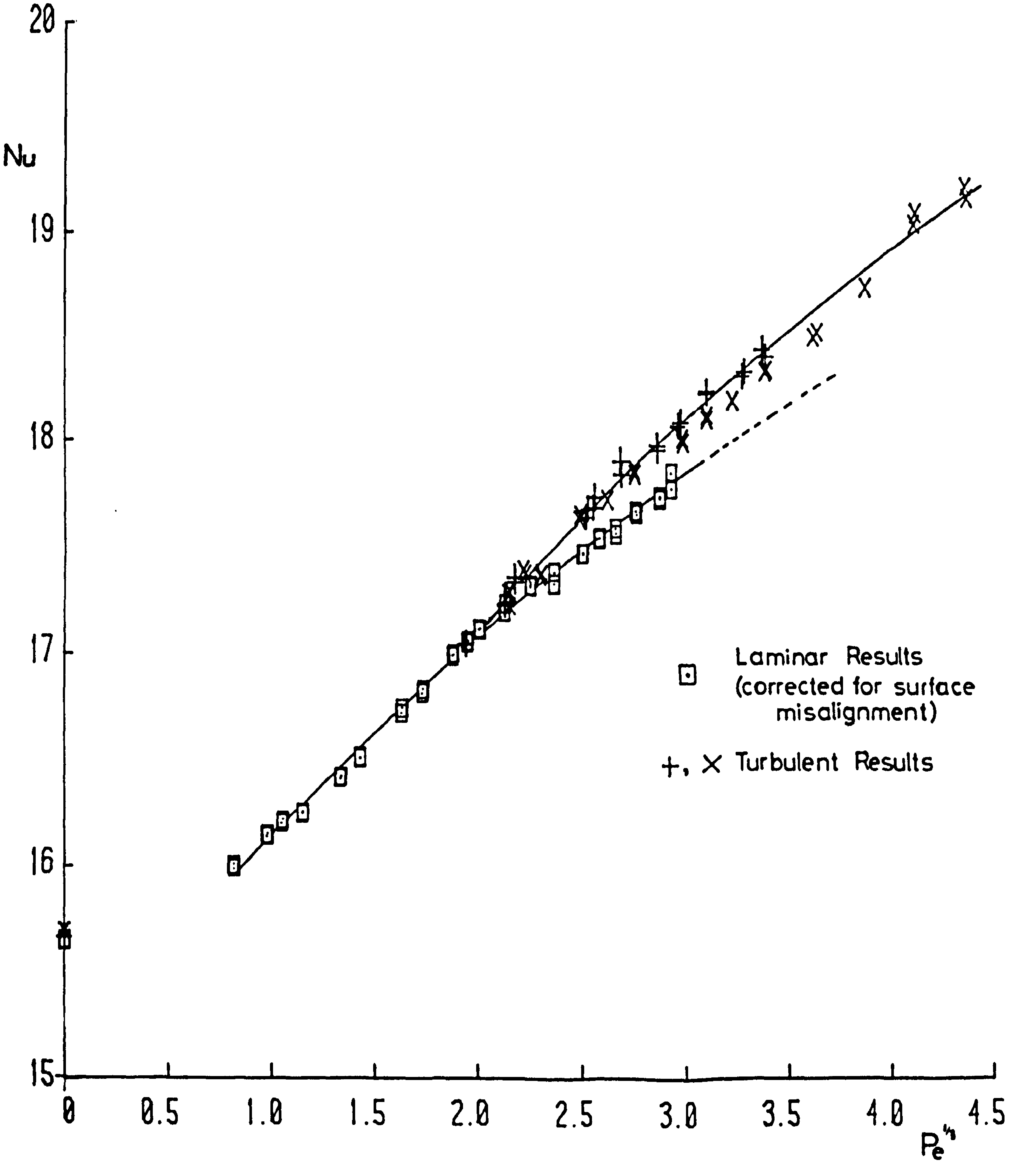

FIG. 6.21(b) LAMINAR AND TURBULENT CALIBRATIONS

(LAMINAR DATA CORRECTED FOR SURFACE MISALIGNMENT)

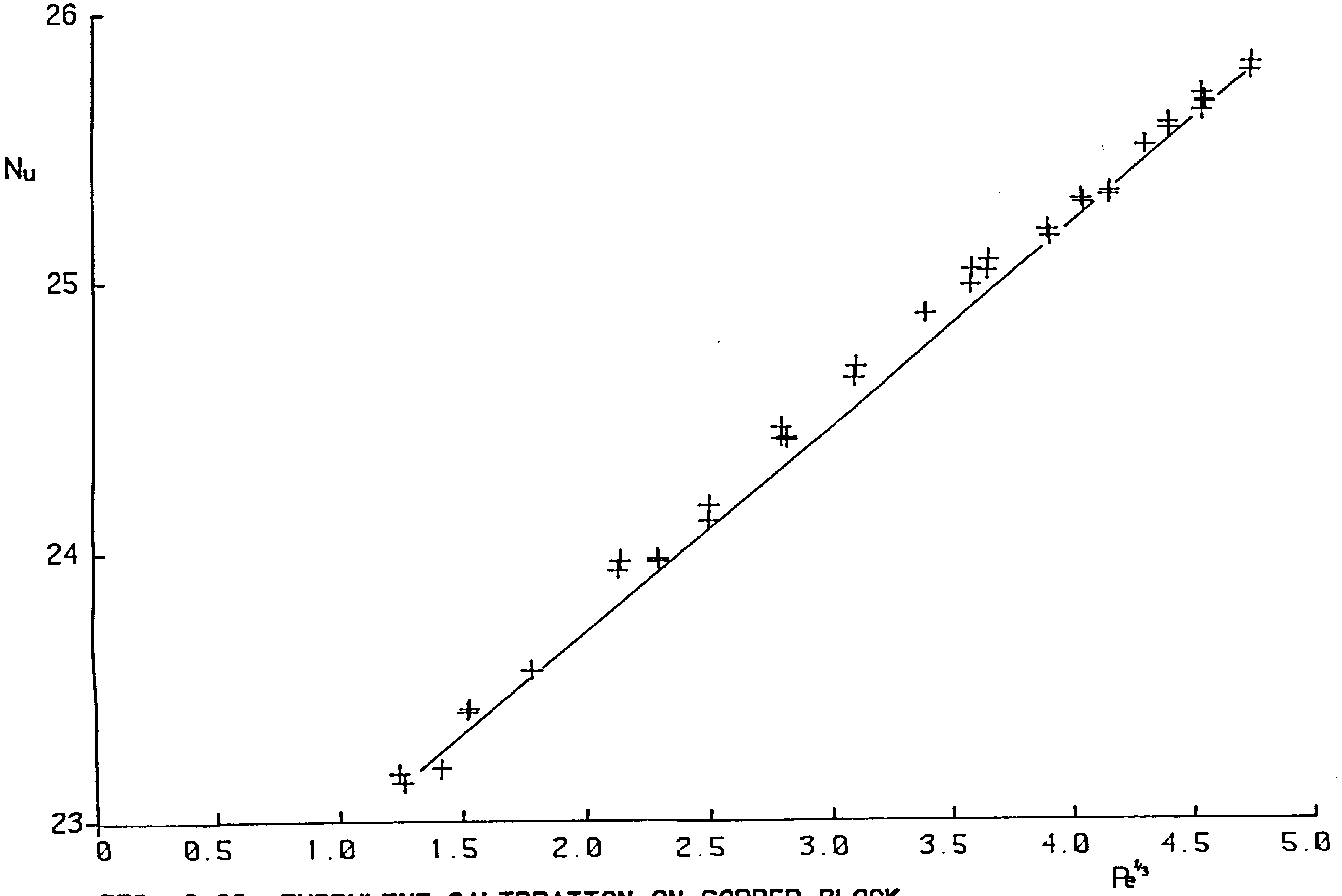

FIG. 6.22 TURBULENT CALIBRATION ON COPPER BLOCK

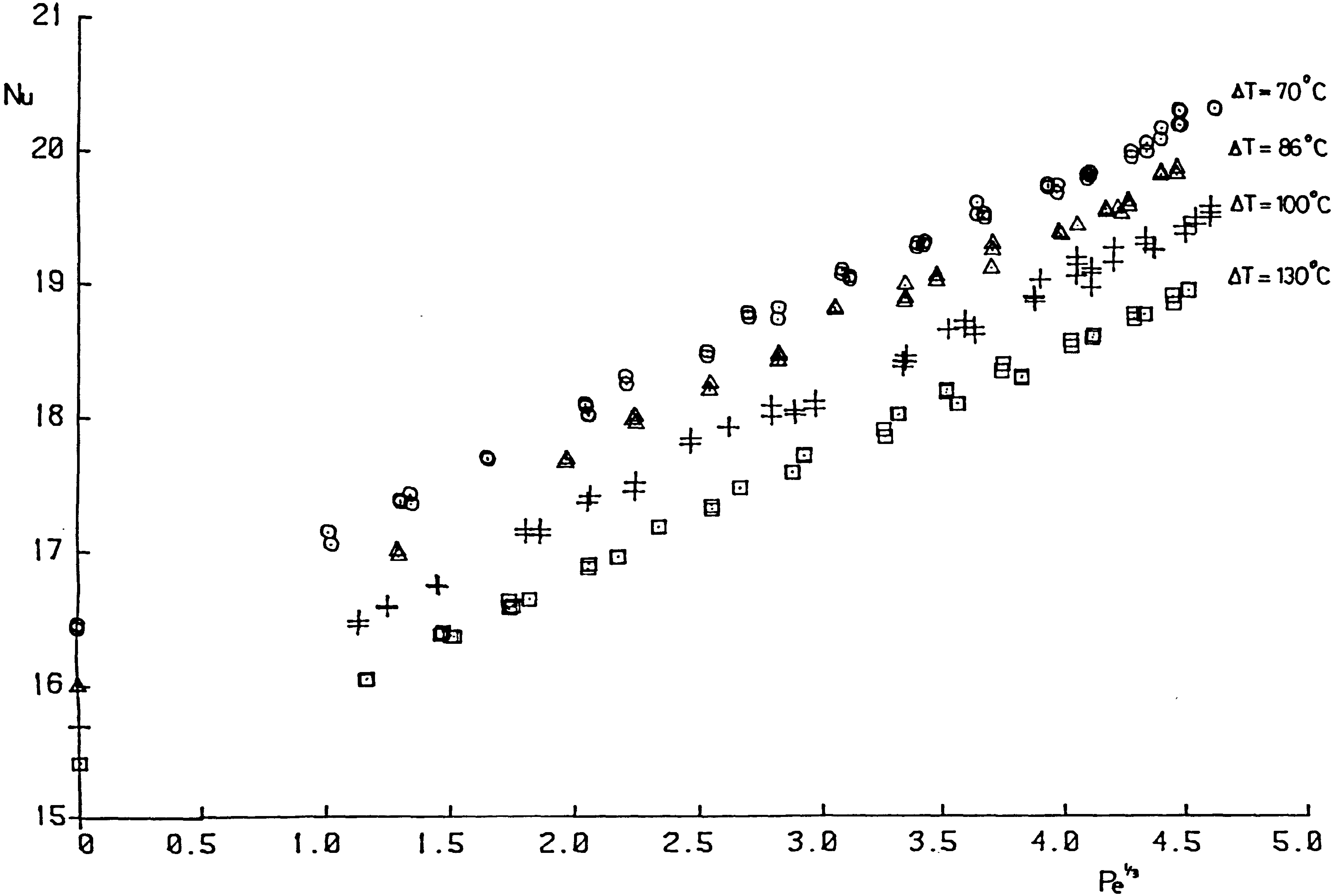

FIG. 6.23 SERIES OF TURBULENT CALIBRATIONS - EFFECT OF ΔT

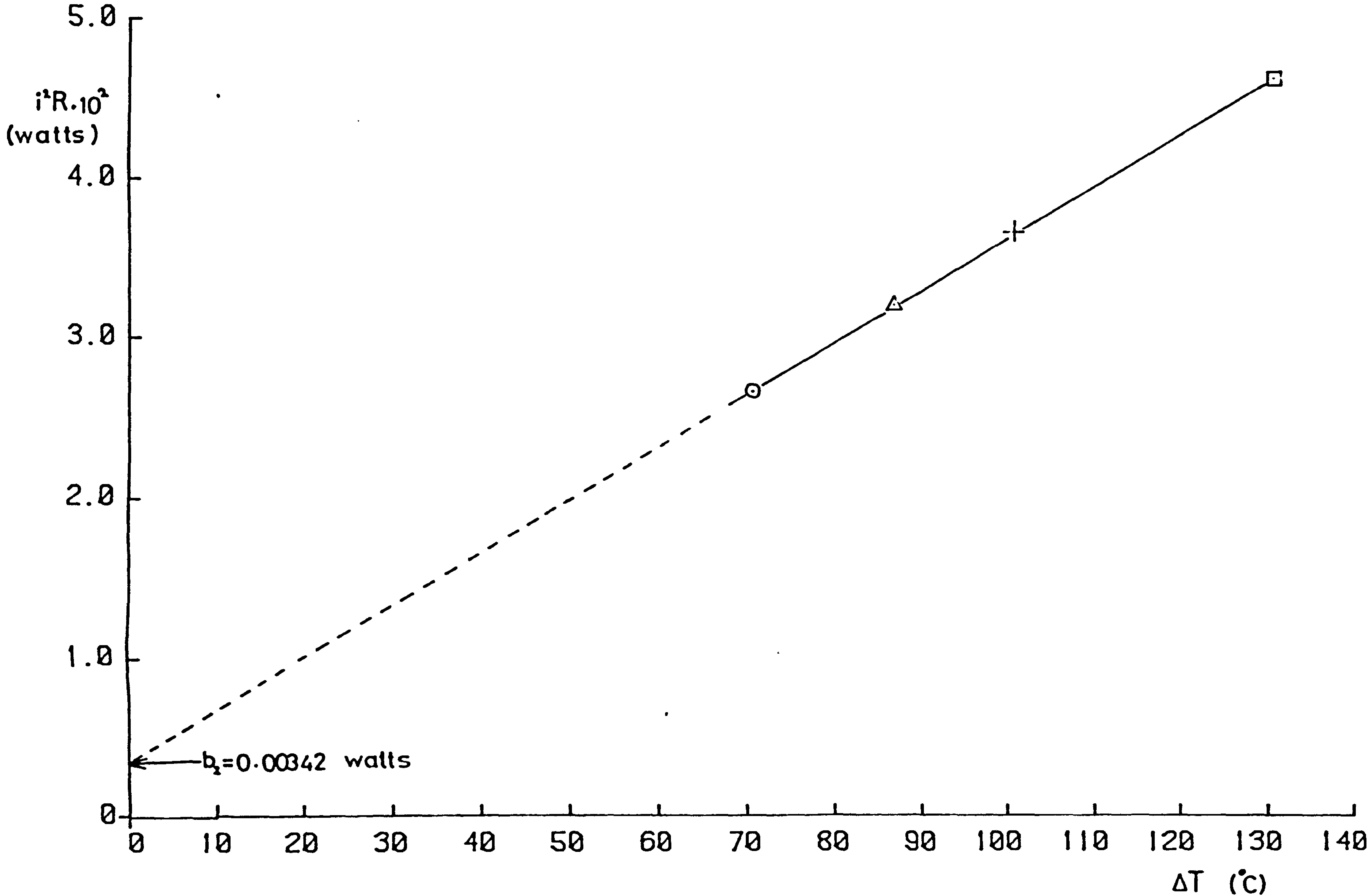

FIG. 6.24 VARIATION OF i^2R WITH ΔT (P_e -0)

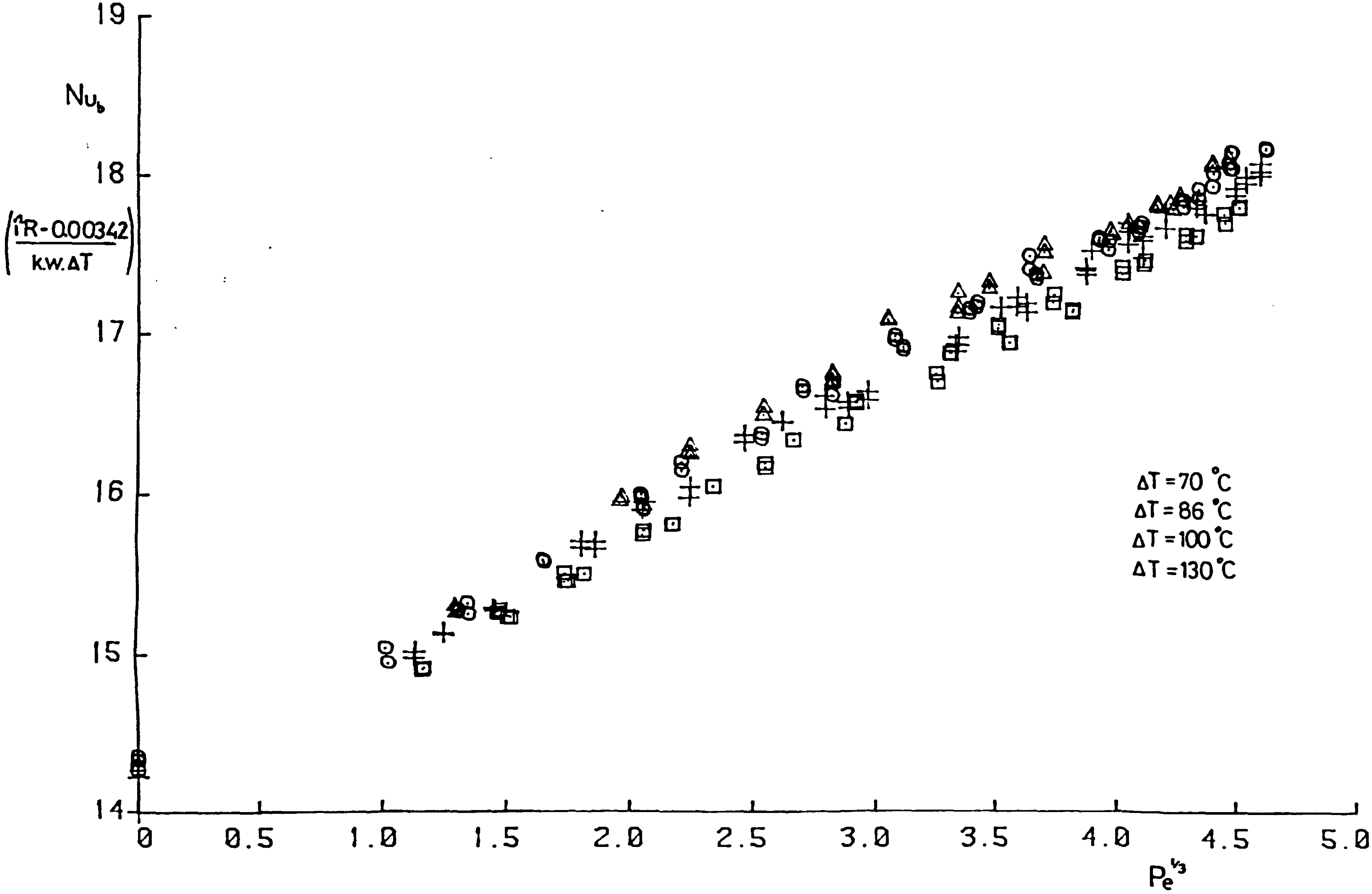

FIG. 6.25 ATTEMPTED NORMALISATION OF TURBULENT CALIBRATIONS

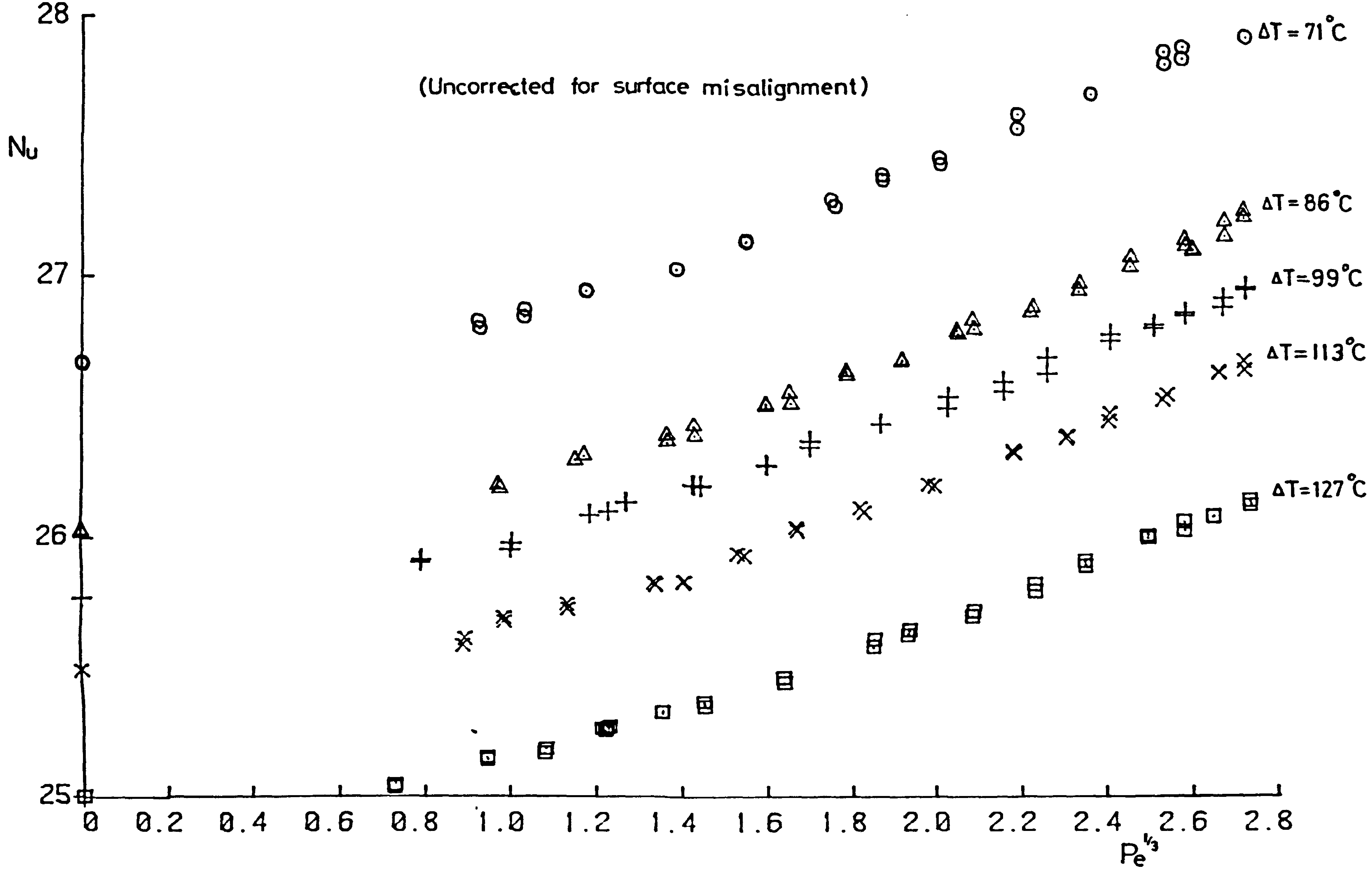

FIG. 6.26 SERIES OF LAMINAR CALIBRATIONS - EFFECT OF ΔT

(PROBE ON COPPER BLOCK)

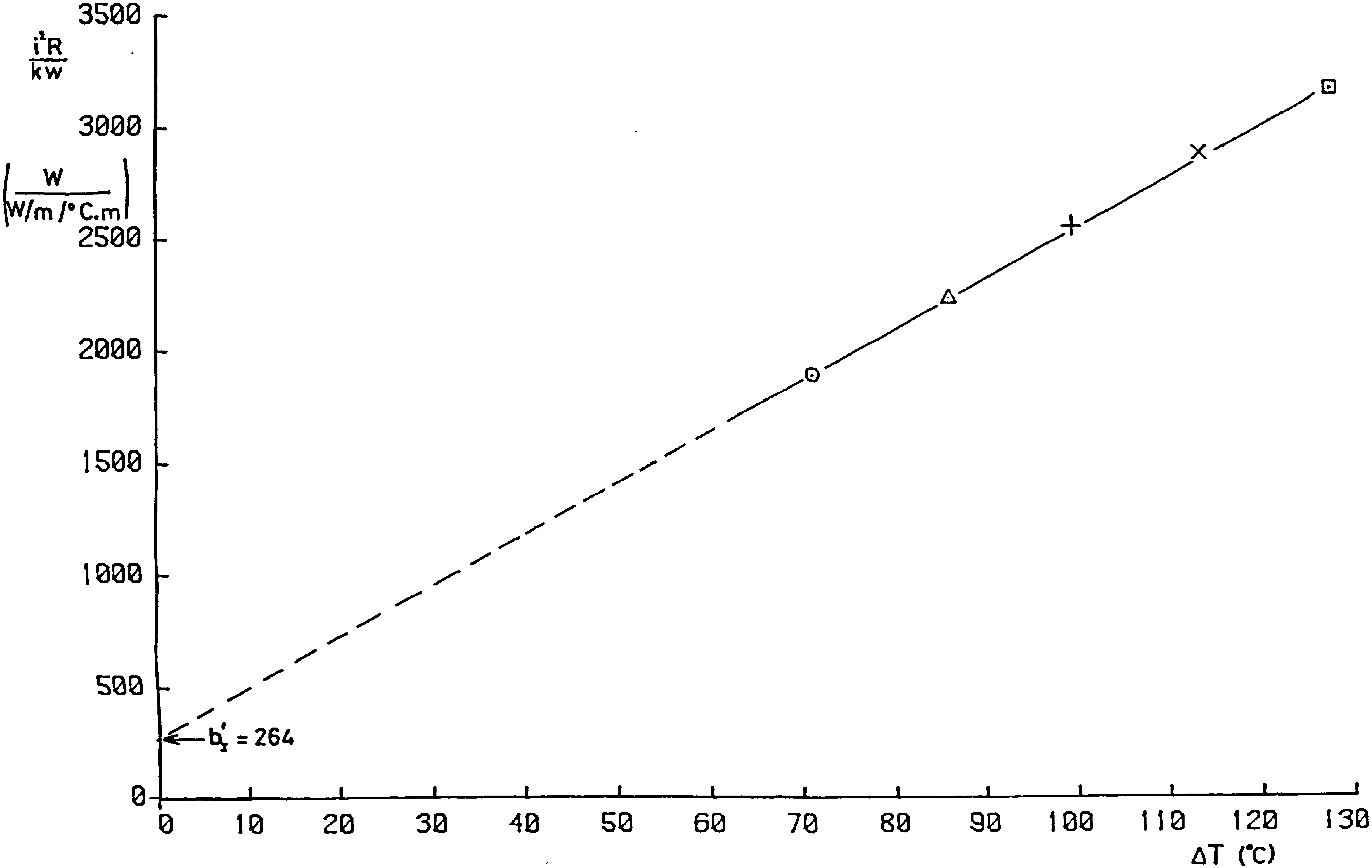

FIG. 6.27 VARIATION OF $\frac{i^2R}{kw}$ WITH ΔT (R_e -0)

(PROBE ON COPPER BLOCK)

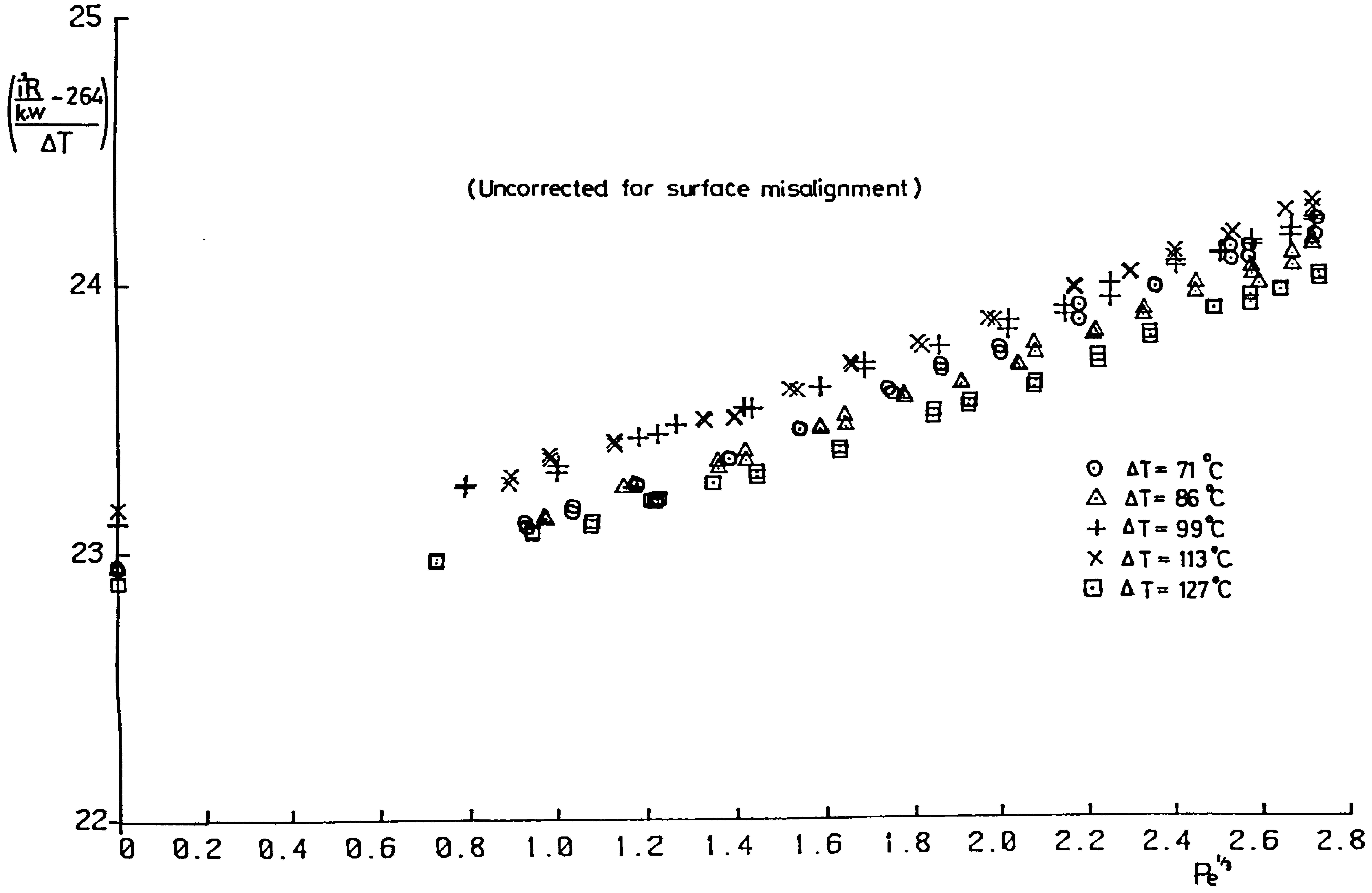

FIG. 6.28 ATTEMPTED NORMALISATION OF LAMINAR CALIBRATIONS

(PROBE ON COPPER BLOCK)